Spectroscopy of non-metallic C_{60} endofullerenes

George Razvan Bacanu[a)]

(*Electronic mail: G.R.Bacanu@soton.ac.uk)

(Dated: 5 August 2025)

C_{60} fullerenes molecules are closed carbon structures hollow inside. Placing an atom or molecule inside the cavity leads to endofullerenes. The encapsulated, endohedral, species display quantisation of their translational degrees of freedom. Such translational eigenstates define the non-bonded (non-covalent) interaction between the host (fullerene) and the guest (endohedral). Encapsulated molecules behave as quantum rotors, displaying essentially free rotation even at cryogenic temperatures. For symmetric molecules, spin isomerism can be observed in the condensed phase.

The translational and rotational motion can interact strongly, leading to translational-rotational coupling, which can couple to the vibrational degrees of freedom. Endofullerenes act as nano-laboratories that isolate the encapsulated atoms/molecules from the environment; ideal for spectroscopic investigations into the quantum behaviour of the endohedral species.

This article is a comprehensive review of all experimental physico-chemical investigations, mostly spectroscopic, of non-metallic C_{60} endofullerenes. In metallic endofullerenes, the endohedral species interacts strongly with the fullerene cage, usually leading to chemical bonding and/or charge transfer. Non-metallic endofullerenes display weaker guest-host interactions, mostly of non-covalent character, that isolate the endohedral species from the environment.

All spectroscopic studies are reviewed, together with experimental techniques related to structure, voltammetry, electron transport, heat capacity, etc. The spectroscopic methods include nuclear magnetic resonance (NMR), electron paramagnetic resonance (EPR), inelastic neutron scattering (INS), Raman, THz & infrared (IR), electronic structure and ionisation techniques. The article is organised in order of ascending energy probed by, or required by, the experimental techniques. Theoretical background is provided for the quantum behaviour and the spectroscopies used to probe them.

CONTENTS

[a)]School of Chemistry, University of Southampton, United Kingdom.

I. INTRODUCTION

Fullerenes represent the third allotropic form of Carbon to be discovered. In 1985, very stable species consisting of 60 and 70 carbon atoms were discovered through the mass spectrometry of laser vaporised graphite.[1] Such species turned out to be the C_{60} and C_{70} fullerene molecules: closed spherical structures composed of only covalently bonded carbon atoms. The structure of the C_{60} fullerene is seen in fig. 1.

The cavity inside the C_{60} cage has a diameter of ~ 3.7 Å and may be occupied by other atomic or molecular species.[2] In the same year that fullerenes were discovered, the first evidence of endofullerene species was discovered for La@C_{60} in mass spectrometry measurements of laser vaporised graphite disks impregnated with Lanthanum.[3] The term **endohedral** is used to describe a species **A** trapped inside a fullerene; with the notation A@C_{60}, where @ denotes that **A** is encapsulated inside C_{60}.

Fullerene molecules are naturally occurring and have been detected in fossil materials, oil, bitumen, etc.[4,5]

Fullerenes have been detected in rock sediments from the Allende and Murchison meteorites.[6] Mass spectrometry analysis of these samples revealed a large family of fullerenes ($C_{60} - C_{250}$). There is evidence that such fullerene molecules contain endohedral noble gas atoms enclosed inside them. The isotopic ratios of the noble gases ^{3}He/^{4}He and ^{36}Ar/^{40}Ar from the meteorite samples differ from the natural isotopic ratios on Earth. Thus, it was concluded that these rock sedi-

ments contain endofullerene molecules of extraterrestrial origin.[6]

C_{60} fullerene molecules have been detected in extraterrestrial space, in diffuse interstellar bands.[7–10] This implies that endofullerenes could also be detected in outer space and could provide assignment of several undetermined diffuse interstellar bands.[7–14]

A. Types of endofullerenes

1. Atomic endofullerenes

Atomic endofullerenes contain a single atom encapsulated inside the fullerene.

a. Noble gas endofullerenes

Noble gas endofullerenes have been extensively studied in the literature. Since the gases are inert, a few different approaches have been used to produce noble gas endofullerenes, sometimes using extreme conditions; see Section I B. Encapsulation of a noble gas atom leads to very stable endofullerene species, for example, $He@C_{60}$ is stable up to 1200 K (similar to C_{60}).[15]

b. Atomic $N@C_{60}$ *endofullerene*

$N@C_{60}$ consists of a bare Nitrogen atom encapsulated inside the C_{60} cage. The valence electrons of Nitrogen half fill the three P orbitals, leading to a spherical electron distribution with no fine-structure interaction. The endohedral N atom has three unpaired electrons with a total electron spin $S = 3/2$.[16]

$N@C_{60}$ is soluble in organic solvents, is stable at room temperature and upon exposure to air.[16] $N@C_{60}$ is stable up to approximately $480 - 500$ K and up to pressures of 0.8 GPa.[17,18] $N@C_{70}$ is less stable, decomposing at ~ 450 K.[19]

c. Atomic $P@C_{60}$ *endofullerene*

$P@C_{60}$ is very similar to $N@C_{60}$. The C_{60} fullerene encapsulates a bare Phosphorous atom − containing three unpaired electrons ($S = 3/2$). $P@C_{60}$ appears to start decomposing at 400 K, being about 100 K less stable than $N@C_{60}$.[19]

2. Molecular endofullerenes

Encapsulation of molecular species inside C_{60} leads to molecular endofullerenes. Some notable examples are $H_2@C_{60}$, $N_2@C_{60}$, $H_2O@C_{60}$, $HF@C_{60}$, $CH_4@C_{60}$, etc. Remarkably, the $HF@C_{60}$ molecule does not possess any of the high reactivity of HF, the fullerene cage acting as a protective barrier.[20]

Recently, the CH_2O molecule was enclosed inside C_{60} fullerene, despite the size of the endohedral species (4.4 Å) being larger than the internal diameter of the cage (3.7 Å).[21]

3. Artificial molecules

Endofullerenes offer the possibility of studying artificial molecules and the non-covalent interactions that govern them. Artificial molecules represent endohedral atoms/molecules that are forced into contact by the confinement and can vibrate/rotate together, analogous to diatomic molecules.[22] Such unconventional systems have been scarcely studied in the literature: $He_2@C_{60}$[23,24], $Ne_2@C_{70}$[22], $(H_2)_2@C_{70}$[25] and $(H_2O)_2@C_{70}$[26]. Fascinatingly, even two distinct species have been inserted inside fullerene cages: $(He \cdot N)@C_{60}$ & $(He \cdot N)@C_{70}$[27], $(H_2 \cdot N)@C_{70}$[28] and $(HF \cdot H_2O)@C_{70}$[29].

Furthermore, dumbbell-shaped dimers of C_{60} endofullerenes have been observed, such as $(He@C_{60})_2$, $(H_2@C_{60})_2$ and $(H_2O@C_{60})_2$.[30–32]

4. Muonium and tritium endofullerenes

Probably the most exotic endofullerenes to be observed contains endohedral muonium (Mu); detected using muon-spin rotation (μSR).[33–35] Muonium is the "hydrogen-like atom" formed between an electron e^- and an anti-muon μ^+ ($Mu = \mu^+ e^-$). Endohedral muonium and the $C_{60}Mu$ radical have been observed for C_{60}, C_{70}, K_4C_{60} and K_6C_{60}.[33–35] There is evidence that tritium C_{60} endofullerene, $^3H@C_{60}$, can be obtained from $^3He@C_{60}$ through a nuclear reaction by neutron irradiation.[36]

5. Metallic endofullerenes

The focus here is on the spectroscopy of non-metallic C_{60} endofullerenes, incorporating atoms or molecules within C_{60}. Metallic endofullerenes are a bit different, usually they have a strong electronic interaction between the endohedral species and the fullerene cage.[37] A selection of references on metallic endofullerenes is given in ref. 37–63.

Of the metallic endofullerenes, Lithium endofullerenes ($Li^+@C_{60}$) are notable examples that have been studied extensively.[37–39,45,48,49,52,53,56–61,63] Other examples are $U@C_{74}$ and $U@C_{82}$[55].

For metallic endofullerenes, multiple metal atoms/ions can be present inside the same cage.[54,62] Cluster endofullerenes being rather common: nitride cluster endofullerenes such as $Sc_3N@C_{80}$[46,54,62], metal carbide cluster endofullerenes such as $Sc_2C_2@C_{84}$[44,54,62], metal oxide/sulfide clusterfullerenes and many others.[46,54,62]

B. Production of endofullerenes

A comprehensive review of the methods used to produce endofullerenes is outside the scope of this article; a brief overview is given below.

1. Vaporisation methods, bottom-up approach

Fullerenes and endofullerenes have been initially obtained through vaporisation methods.[1,3] The vaporisation methods use arc-discharge or laser ablation.[43,51,54,62]

It consists of using graphite rods that, upon vaporisation, produce soot containing fullerene molecules, which sometimes trap endohedral species when forming.[43,51,54,62,64] The endofullerenes need to be purified from the soot and separated, as this method produces large mixtures of (endo)fullerene molecules. In most cases, small quantities of endofullerenes are obtained through such methods.

If the procedure is used on pristine graphite rods in an atmosphere of inert gases, the inert gas will occasionally be trapped by the fullerene molecule upon formation. Small quantities of $He@C_{60}$ and $Ne@C_{60}$ have been obtained in this way.[64]

The method can be used on graphite rods infused uniformly with atoms/ions, in order to trap them inside the fullerene upon formation. This is one of the most popular method for producing metallic endofullerenes.[43,51,54,62]

2. Brute force approach

For the brute force approach, fullerenes are kept under high pressure of the inert gas and at high temperature. Under such extreme conditions, the gas will occasionally penetrate the fullerene cages, or the fullerene chemical bonds break and reform with the gas trapped inside. This brute force approach is mostly applicable to noble gases. Through this method He, Ne, Ar, Kr and Xe endofullerenes (C_{60} and C_{70}) have been obtained in small quantities ($\leq$ mg).[23,65–75] Small quantities of $N_2@C_{60}$ and $CO@C_{60}$ have been obtained, with very low yields, using this brute force approach.[76] The same approach was used to try to make $H_2O@C_{60}$; unfortunately, it was not successful.[76]

3. Ion implantation

The ion implantation method uses ion beams or plasma to insert endohedral species inside the fullerenes. The ions are accelerated to high speeds and impact the fullerene material, inserting themselves into the fullerene molecules without destroying them.[16,37,43,51,54,62,77–81] The yields of such techniques are rather low, but allow the production of $\sim$ mg quantities.

This is the preferred method for synthesising non-metallic bare atom endofullerenes such as $N@C_{60}$, $N@C_{70}$ and $P@C_{60}$.[16,54,77–83] A by-product of the $N@C_{60}$ synthesis is $N_2@C_{60}$, which can be separated in very small quantities through HPLC.[84,85]

Furthermore, ion implantation can be used to obtain alkali metal endofullerenes $M@C_{60}$ (M= Li, Na, K, Rb).[40,42] This method is extensively used to produce lithium endofullerenes such as $Li^+@C_{60}$.[37–39,45,48,49,52,53,56–61,63]

The alternative approach to ion bombardment is to accelerate fullerene ions, such as C_{60}^+, to impact noble gases. Through this method, small quantities of He, Ne and Ar C_{60} endofullerenes have been detected by mass spectrometry.[54,86–90]

4. Molecular surgery

In this context, molecular surgery refers to a chemical synthesis route developed for the production of endofullerenes. Molecular surgery consists of three steps: (1) incision, (2) insertion and (3) suture. (1) consists of a series of chemical reactions applied to the fullerene cage to create an opening in the fullerene surface. (2) the endohedral species are inserted through the opening to form an open cage endofullerene complex. (3) a series of chemical reactions, applied to the open cage endofullerene, close the fullerene cage back to its original form, with the endohedral species fully enclosed. This procedure allows for the production of macroscopic quantities of endofullerenes, mg $-$ g, which is impractical for other synthetic procedures.[54,91–97]

Furthermore, molecular endofullerenes can be obtained with this route, which have molecules as endohedral species. The synthesis of molecular endofullerenes is difficult compared to other "high-energy" routes, because the extreme conditions are likely to destroy the molecules before they are inserted inside fullerenes. For $N_2@C_{60}$ and $CO@C_{60}$ the endohedral molecule can be inserted through the brute force approach, with very low yields, but for $H_2O@C_{60}$ it did not work.[76]

The first successful molecular surgery synthesis of endofullerenes was achieved for the molecular endofullerene $H_2@C_{60}$.[31] Afterwards, the second molecular endofullerene to be synthesised using molecular surgery was $H_2O@C_{60}$.[98] Ever since, the field of molecular surgery has seen immense advancements, now a large selection of C_{60} endofullerenes are available through molecular surgery: $He@C_{60}$[99,100], $Ne@C_{60}$[100], $Ar@C_{60}$[101], $Kr@C_{60}$[102], $HF@C_{60}$[20], $CH_4@C_{60}$[103] and $CH_2O@C_{60}$[21]. Derivatives of C_{60} can also be filled with endohedral species, through molecular surgery, e.g. $H_2@C_{59}N$ and $H_2O@C_{59}N$.[104,105] The paramagnetic NO molecule has been inserted into open cage C_{60} fullerenes.[106,107]

In addition, C_{70} endofullerenes can be obtained through molecular surgery: $He@C_{70}$[99], $H_2@C_{70}$[25]. Furthermore, multiple endohedral species can be inserted in C_{70} due to the larger cage size: $(H_2)_2@C_{70}$[25], $(H_2O)_2@C_{70}$[26], $(HF \cdot H_2O)@C_{70}$[29]. And by coupling molecular surgery with ion implantation, endofullerenes such as $(He \cdot N)@C_{60}$, $(He \cdot N)@C_{70}$ and $(H_2 \cdot N)@C_{70}$ have been obtained.[27,28]

The development of molecular surgery techniques has enabled the field of molecular endofullerenes to explode. Molecular surgery techniques have recently been reviewed.[96] The reader is also advised to check 54,91,93–95,97 for more information on molecular surgery.

C. Applications of endofullerenes

Endofullerenes display peculiar properties. The endohedral species is mostly free to rotate and translate, behaving as if it is in the gas phase even at cryogenic temperatures, despite the fact that the endofullerene material is in the solid (or solution) state.

Investigations of endofullerenes allow for studying molecular confinement, which is possible through other means (e.g. clathrates). However, endofullerenes have the advantage of possessing a very well defined cavity: the cages are rigid and all of the same size, held together by strong covalent carbon-carbon bonds. Thus, endofullerenes act as nano-laboratories which can be used to extract non-covalent interactions between the endohedral species and the cage and between the endohedral species themselves (in the case of multiple encapsulated species). Such experimentally determined interaction potentials can be used as computational benchmarks for quantum chemistry calculations.[108–113] Furthermore, the method shown for the $He@C_{60}$ non-bonded potential gives the entire potential energy surface (within the measured range).[110–112]

Transistors containing a single endofullerene molecule have been produced using $N@C_{60}$ and $H_2O@C_{60}$.[114–116] Such investigations demonstrate that it is possible to construct and control single-molecule transistors for practical applications.

Due to their exquisite electron spin properties, e.g. extremely long relaxation times, $N@C_{60}$ and $P@C_{60}$ have been proposed as ideal qubits for quantum computing – by using the spin states of the unpaired electrons as qubits.[117–124]

These molecules are promising for quantum technologies and could one day lead to an endofullerene-based quantum computer. Furthermore, $^{15}N@C_{60}$ possesses a spin resonance clock transition – making it a suitable condensed matter atomic clock at room temperature.[125]

The ^{3}He chemical shift is sensitive to chemical modifications of the fullerene cage, due to changes in the ring currents. This was utilised to monitor chemical reactions of the fullerene cage through ^{3}He NMR.[66,68] Furthermore, this "spy" property of the endohedral ^{3}He nucleus was utilised to probe magnetic fields inside the $Rb_3@C_{60}$ superconductor; without excessively disturbing the properties of the material.[126]

D. Aim of the article

The aim of this article is to provide a comprehensive review of the experimental spectroscopy of non-metallic C_{60} endofullerenes. The atomic and molecular C_{60} endofullerenes covered here are very stable materials under ambient conditions, similar to empty C_{60} fullerene.

The focus here is on experimental investigations and their interpretations. There are many studies in the literature on computational/theoretical investigations of endofullerenes. Such studies are not covered in this article, unless they are directly related to experimental results. Some computational studies on endofullerenes are given in ref. 127–147.

Metallo-endofullerenes generally have properties different from those of the atomic and molecular endofullerenes covered here. More information about metallo-endofullerenes is found in ref. 37–63.

C_{60} is the smallest stable fullerene molecule, and its endohedral derivatives are the most widely studied. C_{70} endofullerenes have also been studied in the literature, but not to the same extent. This article covers C_{60} endofullerenes; however, some studies on C_{70} endofullerenes are mentioned, if relevant in relation to C_{60} endofullerenes. Furthermore, only fully closed cage C_{60} endofullerenes are covered in this article. Some studies on open cage endofullerenes are given in ref. 97,106,107,148–153. Mostly neutral C_{60} endofullerenes have been studied, with few investigations on charged species.

The entire article is organised in the order of ascending energy. This applies to the theoretical background (section II), the spectroscopic techniques (section III), and the main part of the review (sections V−IX). The order starts with low energy techniques on nuclear spins, then more energetic electron spins, molecular motion (rotations, translations, vibrations), electron motion (excited electronic states) and finally high energy ionisation techniques.

Other techniques are presented in section X, which are strictly speaking not spectroscopical techniques, but provide similar or complementary information. For example, spectroscopic information can be obtained from electron tunnelling and voltammetry measurements. Similarly, information about spin isomers can be obtained from electrical or heat capacity measurements, etc.

This article serves as a comprehensive review of all spectroscopical studies reported in the literature so far, on non-metallic C_{60} endofullerenes. The author apologises if anything has been missed from the literature. Similar compilations/reviews of literature results on C_{60} endofullerenes can be found in ref. 54,97,142,150,151,154–156.

II. THEORETICAL BACKGROUND

Central to non-relativistic quantum mechanics is the Schrödinger equation. The energies (eigenvalues E_a) are calculated using the time independent Schrödinger equation:[157–164]

$$\widehat{H}\,\Psi_a = E_a\,\Psi_a \tag{1}$$

Time evolution of quantum states is obtained from the time dependent Schrödinger equation:[157–164]

$$i\,\hbar\,\frac{d}{dt}\Psi = \widehat{H}\,\Psi \tag{2}$$

Essential to quantum mechanics are the angular momentum operators $\widehat{G}$. In quantum mechanical terms, the angular momentum operators give rise to the eigenstates $|G\,M_G\rangle$ with total angular momentum G and projection of the angular momentum M_G (usually along the z axis):[157–164]

$$\hat{\mathbf{G}}^2\,|G\,M_G\rangle = \hbar^2\,G(G+1)\,|G\,M_G\rangle \tag{3}$$

$$\hat{G}_z\,|G\,M_G\rangle = \hbar\,M_G\,|G\,M_G\rangle \tag{4}$$

$$\hat{\mathbf{G}}^2 = \hat{G}_x^2 + \hat{G}_y^2 + \hat{G}_z^2 \tag{5}$$

The angular momentum operators $\hat{G}_x$, $\hat{G}_y$, $\hat{G}_z$ satisfy the following commutation relations:[157–164]

$$[\widehat{G}_x,\widehat{G}_y] = i\hbar\widehat{G}_z,\quad [\widehat{G}_y,\widehat{G}_z] = i\hbar\widehat{G}_x,\quad [\widehat{G}_z,\widehat{G}_x] = i\hbar\widehat{G}_y \tag{6}$$

Quantisation leads to half-integer angular momentum for nuclear and electron spins ($\widehat{I}$ and/or $\widehat{S}$) or integer angular momentum for: spin, orbital angular momentum ($\widehat{L}$) or molecular rotation angular momentum ($\widehat{J}$).[157–164]

The various quantum phenomena observed and analysed in (endo)fullerenes are given below, in ascending order of the energies involved – this ordering will be used throughout the article. Starting from spin dynamics (nuclear and then electron), then molecular dynamics and finally electronic dynamics.

A. Nuclear spin dynamics

Nuclear magnetic resonance (NMR) is concerned with the interaction of nuclei and their spin with electromagnetic fields. Magnetic interactions are the most common, although electric interactions also occur for quadrupolar nuclear spins ($I > \frac{1}{2}$). Such electromagnetic fields can be generated by an external magnet ($\mathbf{B_0}$) or can be internal to the molecule/material.

The spin of a particle behaves as intrinsic angular momentum of that particle. In quantum mechanics it is described as in eq. 3-6, by replacing $G \rightarrow I$.[158,160,163,165,166] The spin wavefunctions $|I\ M_I\rangle$ are given in terms of Pauli spin matrices. The quantum number $I = 0, \frac{1}{2}, 1, \frac{3}{2}, ..,$ and each I state is $2I+1$ degenerate, from the quantum number $M_I = I, I-1, ..., -I$.[158,160,163,165,166] The hats on the spin operators $\hat{\mathbf{I}}$ will be excluded for the rest of the document.

Nuclear spin interactions are written as Hamiltonian operators ($\widehat{H}_{NMR}$), first in cartesian form eq. 7 and then in spherical tensor notation eq. 8:[158]

$$\widehat{H}_{NMR} = \mathbf{M} \cdot \widehat{\mathbf{O}} \cdot \mathbf{N} = \sum_{i,j=1}^{3} O_{ij}\, M_i\, N_j \tag{7}$$

$$= \sum_{k=0}^{2} \widehat{\mathbf{A}}_\mathbf{k} \cdot \widehat{\mathbf{T}}_\mathbf{k} = \sum_{k=0}^{k_{max}} \sum_{q=-k}^{+k} (-1)^q\, A_{k\ -q}\, T_{k\ q} \tag{8}$$

In cartesian form $\mathbf{M}$ and $\mathbf{N}$ are cartesian vectors (e.g. $\{M_x, M_y, M_z\}$) and $\widehat{\mathbf{O}}$ is a 3×3 cartesian operator (O_{ij} where $i, j = x, y, z$). The vectors $\mathbf{M}$ and $\mathbf{N}$ can be: $\mathbf{I}$ or $\mathbf{S}$ vectors of spin operators $\{I_x, I_y, I_z\}$, or vectors of rotational angular momentum operators $\{J_x, J_y, J_z\}$ or vectors of $\mathbf{B_0}$ the external static magnetic field $\{B_x, B_y, B_z\}$. In spherical tensor form, $\mathbf{A_k}$ and $\mathbf{T_k}$ are spherical tensor operators (space and spin parts respectively). Eq. 8 represents the scalar product of spherical tensors, because the Hamiltonian must be invariant with respect to any general rotation.[158,160,163,165,166]

The space part of the spherical tensors $\widehat{\mathbf{A}}_\mathbf{k}$ (with components A_{kq} where $q = k, k-1, ..., -k$) is obtained from the 3×3 cartesian tensor $\widehat{\mathbf{O}}$ of the respective NMR interaction (e.g. chemical shift, dipole-dipole coupling, etc.) as follows:[158]

$$A_{00} = -\frac{1}{\sqrt{3}} Tr\{\widehat{\mathbf{O}}\}$$
$$A_{10} = -\frac{i}{\sqrt{2}}(O_{xy} - O_{yx})$$
$$A_{1\pm1} = -\frac{1}{2}[O_{zx} - O_{xz} \pm i(O_{zy} - O_{yz})]$$
$$A_{20} = \frac{1}{\sqrt{6}}(3O_{zz} - Tr\{\widehat{\mathbf{O}}\})$$
$$A_{2\pm1} = \mp\frac{1}{2}[O_{xz} + O_{zx} \pm i(O_{yz} + O_{zy})]$$
$$A_{2\pm2} = \frac{1}{2}[O_{xx} - O_{yy} \pm i(O_{xy} + O_{yx})]$$

The spin part of the spherical tensors $\widehat{\mathbf{T}}_\mathbf{k}$ (or the spin-field tensor $\widehat{\mathbf{X}}_\mathbf{k}$) with components T_{kq} where $q = k, k-1, ..., -k$ are obtained in a similar fashion, by combining the cartesian vectors $\mathbf{M}$ and $\mathbf{N}$. The spin spherical tensors $\widehat{\mathbf{T}}_\mathbf{k}$ (for all k ranks) are given for all NMR interactions in table I.

The NMR interactions are briefly discussed below. Nuclear spin interactions can be external (Zeeman & radio frequency pulses) or internal (all interactions from table I)

The Zeeman interaction represents the coupling of nuclear spins with the external magnetic field $\mathbf{B_0}$. The Zeeman interaction is given below, and is identical with the rank $k = 0$ chemical shift interaction, it scales with the gyromagnetic ratio γ.[158,163,165,166]

$$\widehat{H}_{Zeeman} = -\gamma\, \mathbf{B_0} \cdot \mathbf{I} = -\gamma\, B_0\, I_z = \omega_{Larmor}\, I_z \tag{9}$$

The Zeeman energy is given by the energy difference between spin up and spin down states, which scales linearly with B_0, and it gives the spin precession frequency ω_{Larmor} (Larmor frequency).[158,163,165,166] Zeeman is usually the largest interaction (for spin $\frac{1}{2}$ nuclei), resulting in energies in the radio wave regime, MHz. For quadrupolar nuclei ($I > \frac{1}{2}$), the quadrupole interaction can exceed the Zeeman interaction.

Internal spin interactions occur between nuclear spins and magnetic fields generated by the microscopic features of a molecule/material. The internal spin interactions are usually smaller than Zeeman and fall in the kHz – Hz range, but can even be as small as mHz in some cases.[109,158,163,165,166]

The chemical shift also represents the coupling of nuclear spins with the external B_0 magnetic field, except that it also takes into account the magnetic shielding from nearby electrons. The chemical shift has an isotropic rank $k = 0$ part and two anisotropic rank $k = 1, 2$ parts called chemical shift anisotropy (CSA). Usually only the $k = 2$ component is referred to as the CSA since it has direct effects on the NMR spectrum (the $k = 1$ component does not).[158,163,165,166]

The spin-spin couplings, dipole-dipole and J-coupling, represent the direct and indirect (through electrons) magnetic interactions between nuclear spins (magnetic moments).[158,163,165,166]

Spin-rotation represents the coupling of nuclear spins with the molecular angular momentum J.[158,163,165,166]

TABLE I. Expressions for the spin spherical tensor components T_{kq}, in terms of the cartesian vectors. Notation used: $I_\pm = I_x \pm iI_y$. For the chemical shift $B_0 = B_z$. Reproduced from ref. 158.

Interaction	T_{00}	T_{10}	$T_{1\pm1}$	T_{20}	$T_{2\pm1}$	$T_{2\pm2}$
Chemical shift	$-\frac{1}{\sqrt{3}}I_zB_0$	0	$-\frac{1}{2}I_\pm B_0$	$\sqrt{\frac{2}{3}}I_zB_0$	$\mp\frac{1}{2}I_\pm B_0$	0
Dipole-dipole	0	0	0	$\frac{1}{\sqrt{6}}(3I_zS_z-\mathbf{I}\cdot\mathbf{S})$	$\mp\frac{1}{2}(I_zS_\pm+I_\pm S_z)$	$\frac{1}{2}I_\pm S_\pm$
J-coupling	$-\frac{1}{\sqrt{3}}\mathbf{I}\cdot\mathbf{S}$	$-\frac{1}{2\sqrt{2}}(I_+S_-+I_-S_+)$	$+\frac{1}{2}(I_zS_\pm-I_\pm S_z)$	$\frac{1}{\sqrt{6}}(3I_zS_z-\mathbf{I}\cdot\mathbf{S})$	$\mp\frac{1}{2}(I_zS_\pm+I_\pm S_z)$	$\frac{1}{2}I_\pm S_\pm$
Spin-rotation	$-\frac{1}{\sqrt{3}}\mathbf{I}\cdot\mathbf{J}$	$-\frac{1}{2\sqrt{2}}(I_+J_-+I_-J_+)$	$+\frac{1}{2}(I_zJ_\pm-I_\pm J_z)$	$\frac{1}{\sqrt{6}}(3I_zJ_z-\mathbf{I}\cdot\mathbf{J})$	$\mp\frac{1}{2}(I_zJ_\pm+I_\pm J_z)$	$\frac{1}{2}I_\pm J_\pm$
Quadrupole	0	0	0	$\frac{1}{\sqrt{6}}[3I_z^2-I(I+1)]$	$\mp\frac{1}{2}(I_zI_\pm+I_\pm I_z)$	$\frac{1}{2}I_\pm I_\pm$

The quadrupole interaction represents the electric interaction between a non-spherical charge distribution of the quadrupolar nuclei ($I > \frac{1}{2}$) with the electric field gradient (EFG) at the location of the nucleus.[158,163,165,166]

B. Electron spin dynamics

Electron paramagnetic resonance (EPR) concerns the interaction of electron spins with electromagnetic fields. The quantum mechanics for electron spins is the same as for nuclear spins, except that larger energies are involved, because a free electron is about 660 times more magnetic than a proton. Thus, all external and internal EPR interactions are larger for electron spins, usually in the kHz − GHz range. Another distinction is the increased mobility of the electron, compared with the nuclei, because of its much smaller mass.[167–170]

Most EPR interactions have the same form as NMR interactions (section II A), with some different notation. The reader is encouraged to see ref. 167–170 for more detailed descriptions of EPR interactions. The EPR interactions are presented below, with some similarities to the NMR interactions from section II A:[167–170]

- The Zeeman interaction is the same for electron and nuclear spins.
- The g-factor and its anisotropy in EPR are analogous to the chemical shift and its anisotropy (CSA) in NMR.
- The exchange interaction in EPR is analogous to the J-coupling in NMR.
- Dipole-dipole interactions between electron spins have the same form as for nuclear spins.
- Zero field splitting (ZFS) in EPR has two contributions: direct dipole-dipole interaction between electron spins and the interaction of the electron spin with its orbital angular momentum (spin-orbit coupling). ZFS is sometimes referred to as the fine interaction.
- Hyperfine interactions represent the interaction between nuclear and electron spins, which has two main contributions: dipole-dipole interaction between the electron & nuclear spin (anisotropic) and the Fermi contact interaction (isotropic). The Fermi contact contribution depends on the electron spin density at the location of the nucleus. Furthermore, the pseudo-hyperfine interaction involves the interaction of the electron orbital angular momentum with the nuclear spin.
- Quadrupole interactions refer to the interaction of quadrupolar nuclei with the electric field gradient − i.e. NMR interaction. Quadrupole interactions can indirectly lead to changes in the EPR spectra through hyperfine interactions with the electron spins.

C. Quantised translational motion

For any atomic or molecular species, there are 3 translational degrees of freedom. They are often ignored in spectroscopy because for a free species they cannot be probed and they lead to peak broadening (Doppler broadening). Translational degrees of freedom can be used for laser cooling of gas phase species, but do not provide spectroscopic information.

However, in endohedral fullerenes, the translational degrees of freedom are quantised due to the strong confining potential, $V(r)$, which keeps the endohedral species enclosed inside the fullerene molecule. This 3-dimensional confinement leads to a classic quantum mechanical example of a "particle-in-a-box". In this case, the fullerene cage literally acts as an almost spherical box.

The "particle-in-a-box" model assumes zero potential energy inside the box and infinite outside the box − which is unrealistic to model endohedral confinement. This is because the endohedral species has an attractive and/or repulsive interaction potential $V(r)$ with the walls of the cage (box), depending on the distance r from the centre of the cage. In this article, models based on the harmonic oscillator (HO) will be presented. Alternative models use interatomic two-body Lennard-Jones interaction potentials to model the confinement; by summing the 60 interactions with the carbon atoms.[171–176]

The spherically symmetric 3D harmonic oscillator for a single particle is defined by the Hamiltonian:[111,161,162]

$$\widehat{H}_{3D\ HO} = \frac{\hat{p}^2}{2m} + V(r) = \frac{\hat{p}^2}{2m} + V_2\, r^2 = \frac{\hat{p}^2}{2m} + \frac{k}{2}r^2 \qquad (10)$$

where $\hat{p}$ is the linear momentum operator, m is the mass of the particle, r is the radial distance of the particle (in polar coordinates) and V_2 is the HO potential coefficient (or the force constant k of the HO).

The eigenvalues of the 3D HO are given by:

$$E_{3D\ HO} = \hbar\omega(N+\frac{3}{2}) = \hbar\omega(L+2N_r+\frac{3}{2}) \qquad (11)$$

Where ω is the angular frequency of the HO, $\omega = \sqrt{\frac{k}{m}}$, being dependent on the force constant k and the mass m (or reduced mass). The energy depends on the quantum number N, which in turn can be decomposed into the orbital angular momentum quantum number L and the radial quantum number N_r (the number of radial nodes that the wavefunction possesses); both $L = 0, 1, 2, ...$ and $N_r = 0, 1, 2, ...$. Alternatively $N = 0, 1, 2, ...$ which means $L = 0, 2, ..., N$ if N is even or $L = 1, 3, ..., N$ if N is odd. Furthermore, each L state is $2L+1$ degenerate, from the quantum number $M_L = L, L-1, ..., -L$. For both 1D and 3D HO's, the eigenvalues are equally spaced in energy[110,111,161,162]

The wavefunctions $|NLM_L\rangle$ describing the 3D HO are based on Laguerre polynomials for the radial component and spherical harmonics $Y_{LM_L}(\Theta, \Phi)$ for the angular component.[110,111,161,162,177,178]

A model used to realistically describe C_{60} endofullerenes is the spherically symmetric 3D an-harmonic oscillator, which uses the 3D HO as a basis. An-harmonic corrections are included as matrix representations in the 3D HO basis, and the final eigenfunctions and eigenvalues are obtained by diagonalisation of the entire matrix (with corrections included).[110–112,177–179] The most encountered form of the an-harmonic confining potential, used for endofullerenes, is the polynomial potential:[110–112,177–179]

$$V(r) = V_2 r^2 + V_4 r^4 + V_6 r^6 \tag{12}$$

Thus far deviations from spherical symmetry, due to the Icosahedral symmetry of the cage, have only been observed for the $CH_4@C_{60}$ endofullerenes, where a small splitting was observed for the $J = 3$ rotational state.[180] In all other endofullerenes assuming spherical symmetry is appropriate.[133,150,155,177,178,181] Transitions between the translational eigenstates can be probed by various forms of spectroscopy detailed in section III.

D. Molecular rotations

The rotation of a rigid molecule can be described quantum mechanically by the rigid rotor.

1. Rigid rotor

The general Hamiltonian for a freely rotating rigid molecule is:[157,160,162]

$$\widehat{H}_{Rot} = \frac{\widehat{J}_a^2}{2I_{aa}} + \frac{\widehat{J}_b^2}{2I_{bb}} + \frac{\widehat{J}_c^2}{2I_{cc}} = A\,\widehat{J}_a^2 + B\,\widehat{J}_b^2 + C\,\widehat{J}_c^2 \tag{13}$$

Where $\widehat{J}_i$ is the angular momentum operator for molecular rotations about the axis i, I_{ii} are the principal moments of inertia, and A, B, C are the rotational constants.[157,160]

The parameters defining the rotational dynamics are the moments of inertia (rotational constants). If all moments of inertia are different, the rotor is an asymmetric top. If two moments of inertia are the same, the rotor is a symmetric top (can be prolate or oblate). If all moments of inertia are the same, the rotor is a spherical top. And if two moments of inertia are equal and one is zero, that represents a linear rotor ($I_{aa} = 0$, $I_{bb} = I_{cc} \neq 0$), with a simplified equation for the energy:[151,155,157,160,182]

$$E_J = B\,J(J+1) \tag{14}$$

The eigenfunctions $|J\ M_J\rangle$ of a linear rigid rotor are given by spherical harmonics $Y_{JM_J}(\theta, \phi)$ (with associated Legendre functions). Rotational eigenstates are defined by the quantum numbers $J = 0, 1, 2...$ and $M_J = J, J-1, ..., -J$.[157,160,182]

For polyatomic non-linear molecules there are in general 3 quantum numbers: J, M, K for the symmetric top and J, K_a, K_c for the asymmetric top. J is the total angular momentum, M is the projection of J on the space-fixed Z-axis, K is the projection of J on the symmetry axis of the molecule (molecule fixed projection quantum number), for a linear molecule the projection on the molecule fixed axis is zero ($K = 0$), K_a and K_c are the values of $|K|$ the asymmetric top would approach in the limit of a prolate and oblate top respectively.[157,160,182] The quantum numbers can take the following values: $J = 0, 1, 2...$ with $K = J, J-1, ..., -J$ and $M = J, J-1, ..., -J$ (similarly for K_a and K_c). For a symmetric top, the eigenfunctions $|J\ K\ M\rangle$ are the rotation matrices (Wigner D functions) $D^J_{M\ K}(\phi, \theta, \chi)$. And for asymmetric tops, the eigenfunctions are linear combinations of the rotation matrices.[157,160,182]

Transitions between rotational eigenstates can be probed by various forms of spectroscopy, detailed in section III.

2. Non-rigid rotor: centrifugal distortion

The case above applies to the rigid rotor, whereas in reality, molecules are not rigid. As molecules rotate faster and faster (high J quantum numbers), molecular centrifugal distortions appear, written as a modified rotational constant B:[155,157,160,178]

$$B = B_e - D_e\,J(J+1) \tag{15}$$

Where B_e is the undistorted rotational constant and D_e is the centrifugal correction constant, which has the role of reducing the rotational constant as the molecule rotates faster (as it populates high J states).[155,157,160,178]

E. Translation-Rotation coupling

For a system that has quantised rotational and translational degrees of freedom, Translational-Rotational (TR) coupling can occur. Essentially, the interaction potential fullerene−endohedral species depends on the orientation of the endohedral species. For example, the potential energy is different if a diatomic molecule approaches the inner fullerene wall with the interatomic vector (molecule axis) tangential vs. perpendicular to the cage wall.[150,155,157,160,177,178,181,183]

Quantum mechanically there are two sources of angular momentum, rotational (J, M_J) and translational (L, M_L); and they combine together according to the angular momentum coupling rules. The resulting angular momentum is given in terms of bispherical harmonics $F^{LJ}_{\Lambda M_\Lambda}$:[150,155,157,160,177,178,181]

$$F^{LJ}_{\Lambda M_\Lambda}(\Theta,\Phi,\theta,\phi) = \sum_{M_L,M_J} C^{\Lambda M_\Lambda}_{LM_L JM_J}\, Y_{LM_L}(\Theta,\Phi)\, Y_{JM_J}(\theta,\phi) \tag{16}$$

Where $C^{\Lambda M_\Lambda}_{LM_L JM_J}$ are the Clebsch-Gordan coefficients, the spherical harmonics $Y_{LM_L}(\Theta,\Phi)$ are one source of angular momentum (translational orbital angular momentum) and $Y_{JM_J}(\theta,\phi)$ are another source (molecular rotational angular momentum).[150,155,157,160,177,178,181]

The TR coupling can be understood in terms of good and bad quantum numbers. For zero TR coupling, the system can be well described by the rotational (J, M_J) and translational (N, L, M_L) quantum numbers: uncoupled basis $|J\, M_J\rangle \otimes |N\, L\, M_L\rangle$. For finite TR coupling, the system is well described only by N, Λ, M_Λ (good quantum numbers); as J, M_J, L, M_L are no longer good quantum numbers due to mixing. This arises because only the total angular momentum (Λ, M_Λ) is a conserved quantity.[150,155,177,178,181]

1. Potential in terms of bispherical harmonics

Bispherical harmonics can be used as wavefunctions and also as components of the potential. The potential V experienced by the endohedral species can be expanded in multipoles, in terms of the bispherical harmonics $F^{lj}_{\lambda m_\lambda}$ (lowercase letters are used to distinguish potential terms from wavefunctions):[150,155,157,160,177,178,181]

$$V(r,\Omega) = \sum_{n,l,j,\lambda,m_\lambda} V^{ljn}_{\lambda m_\lambda}\, r^n F^{lj}_{\lambda m_\lambda}(\Omega) \tag{17}$$

Where r is the radial distance from the centre of the cage (in polar coordinates), $\Omega = (\Theta,\Phi,\theta,\phi)$ and $V^{ljn}_{\lambda m_\lambda}$ represent the coefficients of the multipole expansion. Setting $j = 0$ in eq. 17 leads to a multipole expansion of the potential energy function for a confined atom, with no rotational degrees of freedom.

In spherical symmetry $\lambda = m_\lambda = 0$, and since $\lambda = |l - j|, ..., l + j$ it means that $l = j$. In I_h symmetry, the allowed values for λ are $\lambda = 0, 6, 10, ...$.[133,150,155] Thus far experimental splittings caused by rank $\lambda = 6, 10, ...$ have only been observed for $CH_4@C_{60}$, where the $J = 3$ rotational state is split in at least two components, see section VII I.[180] For all other C_{60} endofullerenes the spherical symmetry approximation is appropriate.[133,150,155,177,178,181] For homonuclear diatomics all odd$-j$ terms vanish because the molecule is centrosymmetric.[155,181]

The term V^{002}_{00} represents the harmonic term of the potential (V_2 term in section II C). V^{004}_{00} and V^{006}_{00} represent anharmonic corrections of the potential (V_4 and V_6 terms in sections VII A 3 and VII E).

The term V^{222}_{00} is the first non-zero translational-rotational (TR) anisotropic harmonic component of the potential. It takes into account how the potential energy changes when a non-spherical molecule translates inside a spherically symmetric potential. V^{222}_{00} splits states with the same J, N, L quantum numbers but different Λ; since $\Lambda = L + J, L + J - 1, ..., |L - J|$. The anisotropic an-harmonic component of the potential is given by the term V^{224}_{00}.[150,155,177,178,181] For heteronuclear diatomics, the terms V^{111}_{00} and V^{113}_{00} can be non-zero, as these terms vanish for homonuclear diatomics.[155,181]

For non-linear polyatomic molecules, a similar approach can be used, by replacing the spherical harmonics Y with rotational matrices (Wigner D functions), due to the additional rotational degree of freedom.

F. Molecular vibrations

For molecules, the internal degrees of freedom of individual atoms become quantised and lead to molecular vibrations (normal modes of vibration). Normal vibrational modes represent atomic displacements that leave the molecular centre of mass unchanged. For diatomic molecules, the vibration potential has a rather simple expression based on the 1D harmonic oscillator (HO). The Hamiltonian for the 1D HO is the same as the spherically symmetric 3D HO in eq. 10, just that r is replaced by x to represent just one dimension (the interatomic distance):[150,157,160–162]

$$\widehat{H}_{1D\ HO} = \frac{\hat{p_x}^2}{2m} + V(x) = \frac{\hat{p_x}^2}{2m} + V_2\, x^2 = \frac{\hat{p_x}^2}{2m} + \frac{k_x}{2}x^2 \tag{18}$$

The eigenvalues of the 1D HO are given in terms of a single quantum number v:

$$E_{1D\ HO} = \hbar\omega(v + \frac{1}{2}) \tag{19}$$

where ω is the angular frequency of the 1D HO ($\omega = \sqrt{\frac{k_x}{m}}$), and there is a single parameter for the vibration, the force constant k of the molecular bond. The eigenvalues of a 1D HO are equally spaced in energy. The eigenfunctions $|v\rangle$ of the 1D HO are based on Hermite polynomials.[150,157,160–162]

For polyatomic molecules, the vibrational dynamics are more complicated, displaying multiple vibrational modes (normal modes).[157,160–162,182]

1. An-harmonic oscillator (1D)

The harmonic oscillator only describes systems in which the potential energy depends quadratically on position. If the dependence is not strictly quadratic, the vibrational motion corresponds to an anharmonic oscillator. For molecules, atoms in chemical bonds behave purely harmonically only close to the equilibrium position. However, as the atoms move farther apart (closer together), the potential energy decreases (increases) − with respect to the HO model − due to weak attractive forces at large distances (strong repulsive forces at short distances). Thus, an-harmonic corrections are needed in

order to accurately describe vibrating molecules; for this reason the Morse potential can prove more useful than the harmonic oscillator.[157]

An-harmonic corrections can be introduced in eq. 19 by replacing ω with ω_v below:[150,157]

$$\omega_v = \omega_e \left[1 - x_e\left(v + \frac{1}{2}\right)\right] \tag{20}$$

where ω_e is the angular frequency of the HO and the adimensional parameter x_e is the an-harmonic correction. The energy levels of an-harmonic oscillators are no longer equally spaced.

2. Vibrating rotor, Rotation-vibration coupling

Ro-vibrational couplings occur for molecules that can rotate and vibrate at the same time. Intuitively, when a molecule is in an excited vibrational state, this will change the expectation value of the bond lengths (for an-harmonic oscillators, section II F 1) – which in turn will change the moments of inertia. These effects are rather small, and are included as perturbations of the ro-vibrational eigenstates.

Due to such ro-vibrational interactions, the rotational constant B_{RoVib} for a vibrating rotor is adjusted as:[150,157]

$$B_{RoVib} = B_v - D_v\, J(J+1) \tag{21}$$

$$B_v = B_e - \alpha_e(v + \frac{1}{2}) \tag{22}$$

$$D_v = D_e + \beta_e(v + \frac{1}{2}) \tag{23}$$

Where B_e is the undistorted rotational constant, α_e is an anharmonic correction of the rotational constant (as the equilibrium geometry changes upon vibrational excitation due to the bond an-harmonicity), D_e is the correction due to the centrifugal distortion (non-rigid rotor, section II D 2) with β_e representing further corrections of the rotational constant due to the an-harmonicity of the bond.[157] The correction terms α_e, D_e and β_e are small and are sometimes ignored. However, in some cases, higher-order correction terms can be determined if the experimental resolution allows.

The wavefunctions of a vibrating rotor are made up of linear combinations of the free rotor and harmonic oscillator wavefunctions, resulting in the labelling $|v\ J\ M_J\rangle$. Furthermore, if translational degrees of freedom are also quantised, TR coupling can occur (section II E). Then the following labelling is appropriate $|v\ J\ N\ L\ \Lambda\ M_\Lambda\rangle$. In spherical symmetry, all $|v\ J\ N\ L\ \Lambda\rangle$ states are $2\Lambda+1$ degenerate (M_Λ degeneracy).[150,155,177,178,181,183]

G. Electronic dynamics

The simplest case is the hydrogen atom, one electron and one proton, for which the Schrödinger equation has analytical solutions. To model the hydrogen atom, the Schrödinger equation is solved for an electron experiencing the Coulomb potential from a static proton: $V(r) = -\frac{e^2}{4\pi\varepsilon_0}\frac{1}{r}$. The angular part of the wavefunction is given in terms of spherical harmonics Y_{LM_L} (quantum numbers L and M_L) and the radial part in terms of associated Laguerre polynomials (quantum number n).[164]

The eigenvalues of the hydrogen atom (in the absence of other interactions) are given in terms of the quantum number n only:[164]

$$E_n = \left[\frac{m_e}{2\hbar^2}\left(\frac{e^2}{4\pi\varepsilon_0}\right)^2\right]\frac{1}{n^2} \tag{24}$$

Where m_e is the electron mass, e is the electron charge and ε_0 is the vacuum permittivity.

For electronic structure calculations, analytical solutions to the Schrödinger equation exist only for hydrogen-like species (i.e. just one electron). For molecules, numerical quantum chemistry techniques are used to compute molecular orbitals as linear combinations of atomic orbitals, e.g. density functional theory (DFT), Møller–Plesset perturbation theory (MP), coupled-cluster (CC), etc.[184–186]

1. Ionisation

When the excitation energy surpasses the ionisation energy of a given species, ionisation will occur and electrons will be ejected from the species.

H. Spin isomerism

The complete wavefunction of a molecule is given by the product (linear combination) of all components: nuclear spin, rotational, translational, vibrational and electronic wavefunctions:[157,182]

$$\Psi_{tot} = \Psi_{nucl} \otimes \Psi_{rot} \otimes \Psi_{trans} \otimes \Psi_{vib} \otimes \Psi_{elec} \tag{25}$$

In quantum mechanics, the Pauli exclusion principle must be satisfied. The Pauli exclusion principle states that the total wavefunction must be antisymmetric (change sign) with respect to odd permutations of identical fermions (half integer spin) and symmetric with respect to even permutations of fermions. Regarding bosons (integer spin), the total wavefunction is symmetric with respect to any permutations of identical bosons. For symmetric wavefunctions the character is 1 and for antisymmetric wavefunctions the character is -1, with respect to a given permutation.[157,182]

The character (permutation symmetry) of the total wavefunction Ψ_{tot} with respect to permutations of identical particles is given by the product of characters for each component of Ψ_{tot} in eq. 25. For example, if for a given permutation all characters are 1, then Ψ_{tot} is symmetric; alternatively, if one character is -1 and the rest are 1, then Ψ_{tot} is antisymmetric with respect to the given permutation.[157,182]

The most famous example of spin isomerism is the H_2 molecule. In the vibronic ground state, the H_2 vibronic wavefunction is permutation symmetric.[157,182] The translational

wavefunction is unaffected (symmetric) by a permutation of the Hydrogens. Thus, the permutation symmetry of H_2 is determined by the characters of the rotational Ψ_{rot} and nuclear spin Ψ_{nucl} wavefunctions. Ψ_{rot} is symmetric with respect to permutation of the Hydrogens if $J = even$ and is antisymmetric if $J = odd$. H_2 contains two identical spin $I = \frac{1}{2}$ particles which couple to produce two distinct states: singlet S_0 with $I = 0,\ M_I = 0$ (para-H_2) and triplet T_1 with $I = 1,\ M_I = \{-1, 0, 1\}$ (ortho-H_2). Ψ_{nucl} is antisymmetric for para-H_2 and symmetric for ortho-H_2 with respect to permutation of the Hydrogen nuclear spins. In order to satisfy Pauli's exclusion principle for Ψ_{tot}, para-H_2 can only have $J = even$ and ortho-H_2 can only have $J = odd$. Thus, the H_2 molecule has two spin isomers, para-H_2 and ortho-H_2, which behave as two distinct chemical species.[157,182] Fig. 22 displays the energy level diagram for H_2 inside C_{60} (electronic ground state), taking into account spin isomerism.

In free space, conversion between spin isomers is forbidden. However, if intermolecular interactions, collisions, inhomogeneous magnetic fields, etc. are present, then spin isomer conversion is possible. A practical route for obtaining spin isomer conversion is to use paramagnetic catalysts, which can microscopically make the two Hydrogen atoms inequivalent. Paramagnetic species, such as O_2, can create highly local transient magnetic fields that are different for the two ^{1}H nuclei, promoting efficient conversion.[157,182]

The spin-isomerism phenomenon applies to species that have identical nuclei, which can be exchanged by a rotational symmetry operation: H_2, D_2, H_2O, CH_2O, CH_4, etc.

III. SPECTROSCOPIC TECHNIQUES

In this section, a brief overview of the spectroscopic techniques covered in this article is given. The techniques are presented starting from the lowest energy (magnetic resonance of nuclear spins) to the highest (ionisation) - this ordering will be used throughout the article.

A. Spin resonance or spin spectroscopies

At the low energy end, there are two spin resonance techniques: Nuclear Magnetic Resonance (NMR) and Electron Paramagnetic Resonance (EPR). EPR is also known as ESR (Electron Spin Resonance). Both are magnetic resonance techniques that measure spin interactions with magnetic fields and with other spins. The only difference is that NMR concerns nuclear spins, whereas EPR concerns electron spins. The latter is associated with higher energies because electron spins are approximately 1000 times more magnetic than nuclear spins (e.g. ~ 660 times more magnetic than proton spins).

1. Nuclear Magnetic Resonance (NMR)

If one applies an oscillating magnetic field, matching the Larmor frequency, spin flips occur, and magnetic resonance experiments can be performed. Probing energy differences between the spin eigenstates – which in turn will probe the spin interactions of the system, see section II A for NMR interactions. NMR energies are on the order of MHz (Zeeman and quadrupole interactions), but can be much smaller kHz – mHz for internal spin interactions (chemical shift, dipole-dipole, J-couplings, spin rotation).[158,163,165,166,170]

NMR spectra can be simulated using the time dependent Schrödinger equation, eq. 2. In Liouville space notation the NMR signal $S_{NMR}(t)$ is given by:[158,163,165,166]

$$S_{NMR}(t) = \left(Q_{obs} \left| exp(-i\widehat{H}t)\ \rho(0)\right.\right) \tag{26}$$

where the observable $Q_{obs} = -i\ I_-$ and $\rho(0)$ is the density operator of the spin system at time $t = 0$.[158,163,165,166]

NMR experiments are usually performed in the liquid or solid state. Gas phase measurements are less common because of the inherent low sensitivity; although initial NMR measurements were performed on molecular beams. Anisotropic NMR interactions average to zero in isotropic liquids (solutions), because of fast molecular rotations; only isotropic couplings persist. However, in condensed solids, anisotropic interactions are present in full form. A technique called Magic Angle Spinning (MAS) can average rank $k = 2$ interactions to zero and drastically simplify solid state NMR spectra.[158,163]

In between liquids and solids are liquid crystals, representing partially orientated media, which retain anisotropic interactions to some extent. Liquid crystal molecules in the nematic phase align partially with respect to an externally applied magnetic field – which can partially align dissolved molecules. Above a certain temperature, there is no preferential alignment of the liquid crystal molecules (i.e. isotropic phase). All anisotropic NMR interactions are averaged out to zero in isotropic solutions; however, in the nematic liquid crystal solution the alignment averages anisotropic interactions to a non-zero value. The partially averaged couplings are called residual couplings.[158,163]

For the cases discussed here, an interesting question arises: can liquid crystals align C_{60} endofullerenes, which are essentially spherical molecules? It turns out that they can partially align endohedral species, observed in NMR (H_2@C_{60}, HF@C_{60}, H_2O@C_{60}) and EPR (N@C_{60} and N@C_{70}) measurements.

2. Electron Paramagnetic Resonance (EPR)

EPR is analogous to NMR (section III A 1), having the same working principles. The difference is that now electron spins are involved. Because electron spins are more magnetic than nuclear spins, EPR energies are usually larger than NMR and they fall in the microwave GHz range (e.g. electron Zeeman energy is usually in the GHz range). The same is true for internal EPR interactions; they are usually smaller than

electron Zeeman energies but larger than internal nuclear spin interactions, being in the kHz − MHz range (even Hz if the experimental resolution allows).[167–170]

In isotropic solutions, all anisotropic EPR interactions average out to zero. In partially aligned media, liquid crystal solutions, anisotropic EPR interactions are averaged out to a non-zero value, called residual couplings. EPR measurements on the N@C_{60} and N@C_{70} endofullerenes dissolved in liquid crystals display such residual couplings, see section VI A 4. In condensed solids, all EPR interactions, isotropic and anisotropic, are present; the same discussion applies to NMR (section III A 1).

3. Electron nuclear double resonance (ENDOR)

Electron nuclear double resonance (ENDOR) is a magnetic resonance technique which requires irradiation of both electron and nuclear spins. It essentially involves irradiation of nuclear spin transitions and their detection via changes in the EPR signal. Using ENDOR, the interactions between electron and nuclear spins, hyperfine interactions, can be measured. ENDOR can be used to measure very small to large hyperfine and also nuclear quadrupole couplings.[168,169]

B. Molecular motion spectroscopies

In this context, molecular motion means: molecular rotations, molecular translations and molecular vibrations. All can be probed by various forms of spectroscopy, as detailed below.

1. THz or far-Infrared spectroscopy

THz or far-IR spectroscopies use light that have the frequency in the THz range. It measures the absorption of light with respect to its frequency as it passes through a sample. The energy of THz light matches the difference in energies between rotational and translational eigenstates and it induces transitions between them, if they are allowed by the selection rules (usually electric dipole allowed).

In the case of endofullerenes, the translational motion induced dipole moments appear to be strong enough to allow transitions to be observed between translational eigenstates. This is the case for the noble gas C_{60} endofullerenes, for example, which absorb THz light and translationally excite the endohedral noble gas atom (e.g. see section VII A). When the noble gas atom is displaced from the centre of the C_{60} cage (equilibrium position), it induces a dipole moment in the whole endofullerene complex.

The absorption line area S_{fi} used for simulating peak intensities in order to fit the THz and IR spectra is:[111,112,155,177–179,181,187]

$$S_{fi} = N\frac{2\pi^2}{h\varepsilon_0 c_0 \eta}\left(\frac{\eta^2+2}{3}\right)^2 \omega_{fi}\,(p_i - p_f)\,|\langle f|\mu_q|i\rangle|^2 \quad (27)$$

$$\mu_{1q}(r,\beta,\Omega) = \frac{4\pi}{3}\sum_{l,j}\sum_{n} B^{ljn}(\beta)\, r^n\, F^{lj}_{1q}(\Omega) \quad (28)$$

N is the number density of molecules (for $C_{60} = 1.48 \times 10^{27} m^{-3}$), h is the Planck constant, ε_0 is the permittivity of vacuum, c_0 is the speed of light in vacuum, η is the index of refraction, the factor $(\frac{\eta^2+2}{3})$ is the enhancement of electric field felt by the oscillator in a dielectric medium[188], $\omega_{fi} = \frac{(E_f - E_i)}{hc_0}$, E_i and E_f are the eigenvalues of the initial and final states, p_i and p_f are the thermal Boltzmann populations of the initial and final states, and μ_q is the dipole moment (permanent and/or induced). The dipole moment μ_q is a function of the radial distance r from the cage centre, other degrees of freedom β (e.g. interatomic distances for polyatomic endohedrals), and the polar angles Ω. The dipole moment μ_q is given in terms of bispherical harmonics $F^{lj}_{1q}(\Omega)$ (see eq. 16) multiplied by powers of r, weighed by the coefficients $B^{ljn}(\beta)$.

For transitions of ro-translational states $|J\ N\ L\ \Lambda\ M_\Lambda\rangle$, the selection rule applies to the total angular momentum quantum number $\Delta\Lambda = 0, \pm 1$. For the quantum numbers J, N, L the selection rules depend on the system, e.g. usually $\Delta J = \pm 1$ but for homonuclear diatomics $\Delta J =$ even and $\Delta L =$ odd.[155,177,178,181]

2. Infrared spectroscopy

Infrared (mid-IR and IR) spectroscopy uses IR light to probe vibrations of molecules (normal modes). It is more energetic than THz spectroscopy (previous section), with visible light usually representing the upper limit. Vibrational excitation is accompanied by ro-translational excitations, for $|v\ J\ N\ L\ \Lambda\ M_\Lambda\rangle$ states, if the selection rules allow it. IR matrix elements and the ro-translational selection rules are the same as for THz spectroscopy (section III B 1). Furthermore, for vibrational excitations, the selection rule for a harmonic oscillator (section II F) $\Delta v = \pm 1$ applies. However, an-harmonic corrections can relax the selection rule and allow overtone transitions to be observed.[157]

3. Raman spectroscopy

Raman spectroscopy is complementary to IR in terms of the information obtained. As a sample is illuminated with IR/visible/UV light, the photon is inelastically scattered by the sample, and it can lose or gain energy in the process. Raman spectroscopy makes use of the energy transfer to build up the spectrum: Stokes and anti-Stokes sides corresponding to photon energy loss and energy gain respectively. With Raman, ro-vibrational states can be spectroscopically probed. However, translational states in endofullerenes have not yet been observed with Raman spectroscopy.

The intensities of Raman lines are related to the change in polarisability during a vibration/rotation. Raman selection rules for molecular rotations are $\Delta J = 0, \pm 2$ and for molecular vibrations $\Delta v = \pm 1$.[157]

For the endofullerenes relevant to this article, Raman spectroscopy was mainly used to probe the fullerene cage vibrations. Raman signals for the endohedral species have not yet been observed for fully closed C_{60} endofullerenes, and the reason is unknown at the moment.

4. Inelastic neutron scattering

Inelastic Neutron Scattering (INS) is complementary to IR spectroscopy (far-IR, mid-IR and IR) and analogous to Raman. However, the mechanism and selection rules are completely different. INS uses neutrons rather than light, and it makes use of the energy transfer between the neutron and the sample to build the INS spectrum. The sample can gain energy (neutron energy loss) or lose energy (neutron energy gain), depending on whether the sample has populated excited states or not. It probes the same eigenstates (rotational, translational and vibrational) as IR and/or Raman, and the energies involved can vary between fractions of meV to eV.

Neutron scattering experiments are characterised by the differential scattering cross section $\frac{\partial^2\sigma}{\partial\Omega\partial\omega}$, which gives the fraction of neutrons with energy E_i being scattered into an element of the solid angle Ω with an energy change $\hbar\,\partial\omega$.[159,172,173,183,189–193] The expression used to simulate neutron scattering experiments is:

$$\frac{\partial^2\sigma}{\partial\Omega\partial\omega} = \frac{k_f}{k_i}\sum_{i,f} p_i\,|\langle i|\widehat{V}_{INS}|f\rangle|^2\;\delta(\hbar\omega - E_i + E_f) \tag{29}$$

$$\widehat{V}_{INS} = \sum_{\alpha} exp(i\boldsymbol{\kappa}\cdot\mathbf{r}_\alpha)\;\left(b_\alpha^{coh} + \frac{2\,b_\alpha^{incoh}}{\sqrt{I_\alpha(I_\alpha+1)}}\frac{\boldsymbol{\sigma}_\mathbf{n}}{2}\cdot\mathbf{I}_\alpha\right) \tag{30}$$

Where the energy and wavevector for the incident neutron are E_i and $\mathbf{k_i}$ and for the scattered neutron are E_f and $\mathbf{k_f}$, the neutron energy transfer is $\hbar\omega = E_i - E_f$, the neutron momentum transfer is $\hbar\boldsymbol{\kappa} = \hbar\mathbf{k_i} - \hbar\mathbf{k_f}$ and p_i is the statistical weight of the initial state $|i\rangle$. $\widehat{V}_{INS}$ is the interaction potential causing transitions, α is a label for the nuclei present, $\mathbf{r}_\alpha$ is the position of nucleus α, $\frac{\boldsymbol{\sigma}_\mathbf{n}}{2}$ is the spin $\frac{1}{2}$ of the neutron, $\mathbf{I}_\alpha$ is the spin of nucleus α, b_α^{coh} and b_α^{incoh} are the coherent and incoherent scattering lengths of nucleus α.[159,172,173,183,190–193] The term $exp(i\boldsymbol{\kappa}\cdot\mathbf{r}_\alpha)$ is a plane wave which can be expanded into an infinite series of spherical waves (plane wave expansion). The series, in principle, is a linear combination of spherical harmonics with ranks ranging from zero to infinity. For this reason, it is said that INS does not have selection rules, besides very few exceptions. One such exception has arisen from INS of endofullerenes, see section IV B. For more information on neutron scattering see refs. 159,172,173,183,190–193.

A huge advantage of neutron scattering techniques is that transitions between spin isomers (section II H) can be excited. Because the neutron is magnetic (spin $\frac{1}{2}$), it can flip one nuclear spin in the sample as it passes through; this changes the nuclear spin state, which can belong to a different spin isomer. Thus, exact energy differences between spin isomers can be measured directly.

C. Electronic spectroscopies

Electronic states can be excited by more energetic light, corresponding to the visible and ultraviolet ranges. Such an excitation will change the electronic structure, and it is usually accompanied by vibrational, rotational (and translational) excitations. For this reason, such transitions are called ro-vibronic (and translational) transitions.

Electronic transitions usually have intensities proportional to the Franck-Condon principle; which is the overlap between the initial and final wavefunctions.[157] Electronic motion is much faster than nuclear motion, due to much smaller mass, thus as ro-vibronic transitions occur, nuclei cannot adjust immediately – and the intensity of such transitions is proportional to the overlap of the two wavefunctions.[157] UV-vis is a typical example of electronic spectroscopy that is routinely performed. Other techniques usually employ laser excitation to drive electronic transitions; i.e. vibronic transitions, and additionally they can be accompanied by translational excitation.

D. Ionisation spectroscopies and techniques

When the energy of incident light surpasses the binding energy of a given atomic shell the light is absorbed, and the excess energy will be transferred to an electron in that shell. This will expel the electron, leaving a hole behind in the ionised atom. This process is called *photoelectric absorption* and the ejected electron is called a *photo electron*. The minimum energy at which photoelectric absorption occurs is called the absorption edge because of the drastic step-like increase in the absorption cross section. Such energies usually fall in the X-ray regime, and X-ray absorption spectroscopy is usually called XPS (X-ray Photoelectron spectroscopy).[194] Useful information can be obtained from the details of the emitted photo electron, energy, momentum, etc.

If the hole left by the photo electron is in the inner atomic shell, an electron from an outer shell can relax to fill the inner shell hole, with a net release of energy. If the energy is released as radiation, the process is called fluorescence. The released energy can also be used to eject another electron from an outer shell, this is called the *Auger process* and the expelled electron is called *Auger electron*.[194]

1. Valence band X-ray photoemission spectroscopy (VB-XPS)

Valence-band X-ray photoemission spectroscopy (VB-XPS) is an XPS technique used for electrons in the valence

shell. VB-XPS measures the ionisation energy of a given valence electron.[194,195]

2. *Extended X-ray absorption fine structure (EXAFS)*

Extended X-ray absorption fine structure (EXAFS) represents oscillations in the X-ray absorption spectrum, when the X-ray energy surpasses the absorption edge (binding energy of a given atomic shell). The oscillations arise from the interference of the ejected photoelectron's wavefunction, at the location of the absorbing atom, with its own reflection (backscattering) from the neighbouring atoms. Modelling the EXAFS response can give highly accurate interatomic distances, as the interference depends on the atomic distances and the wavelength of the ejected photo-electron.[194,196]

3. *Normal incidence X-ray standing wave (NIXSW)*

NIXSW is a technique that measures the distance of a given atom adsorbed on a surface away from the surface layer. NIXSW creates an X-ray standing wave as the incident wave (normal to the surface) interferes with the wave reflected off the surface layer. By scanning the incident X-ray energy, the position of an (absorbing) atom of interest, away from the surface layer, can be measured from the known change in the period/wavelength of the X-ray standing wave.[197,198]

4. *Confinement resonances photoionisation*

In the case of endofullerenes, confinement resonances arise when a confined atom is ionised and the emitted photoelectron's wavefunction interferes with itself. The photoelectron transmitted through the fullerene cage interferes with its own reflection with the inner and outer fullerene wall, giving rise to confinement resonances.[199–201] The confinement resonance can be observed if the photon energy is scanned (above the ionisation energy) in the energy range where the photoionisation cross section does not change much with the energy of the photon.[201]

E. Other techniques

In some cases non-spectroscopic techniques have been used to investigate endofullerenes, section X. Where such techniques are used, a brief description is given in the relevant section.

IV. BACKGROUND: C_{60} FULLERENES & ENDOFULLERENES

A. C_{60} structural considerations

Fullerene molecules are made of only carbon atoms, covalently bonded in a closed structure. In order to produce a closed convex structure, pentagonal faces are required; hexagonal and heptagonal faces lead to planar and concave structures, respectively.[2] Fullerene molecules built up from only pentagonal and hexagonal faces must satisfy Euler's theorem for polyhedra; which states that there must be 12 pentagonal faces and an arbitrary number of hexagonal faces.[2] Furthermore, due to chemical bond strain, fullerenes satisfy the isolated pentagon rule: pentagonal faces must not share an edge between them, as it would induce too much strain and the molecule would be energetically unfavourable. From such arguments, it is apparent why C_{60} is the smallest stable fullerene molecule.[2]

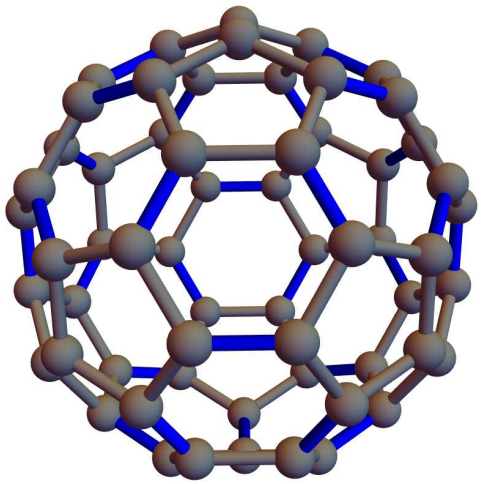

FIG. 1. Structure of the C_{60} fullerene. Single bonds (gray) are between a hexagon and a pentagon (HP bond) and double bonds (blue) are between two hexagons.

The structure of C_{60} fullerene is seen in fig. 1. It represents a truncated icosahedron shape, composed of 60 vertices (carbon atoms) arranged in 12 pentagonal and 20 hexagonal faces. There are 90 edges (chemical bonds): 60 shared between a hexagon and a pentagon (HP single bond) and 30 shared between two hexagons (HH double bonds). The HP single bond is 1.46 Å and the HH double bond is 1.40 Å.[2] Because the two types of bonds in C_{60} are not equal, the C_{60} molecule is *not* a regular truncated icosahedron.[2]

Important pieces of evidence for the structure of C_{60} are the ^{13}C solution and solid state NMR spectra.[202–204] The spectra

consist of a single peak at ambient conditions, plus small side peaks (see below), see main C_{60} peak in fig. 2 for the solution state NMR spectrum. This proved that the C_{60} structure is highly symmetric, as it contains 60 carbon atoms, but all of them are chemically equivalent, leading to a single peak in the NMR spectrum.[202–204] It turns out that when one looks very closely at the fine structure of the ^{13}C NMR (high-resolution) solution state spectrum of C_{60}, two extra resonances are observed. Displaying very small intensities due to low-abundant isotopomers with two adjacent ^{13}C nuclei[205], described next in section IV A 1.

1. C_{60} *NMR fine structure, HP and HH isotope shifts*

Close inspection of the ^{13}C solution state NMR spectrum of C_{60} reveals two small additional peaks on the shielding (upfield) side of the main C_{60} peak. This is shown in fig. 2 where two small peaks labelled HP and HH are seen, shifted away from the main peak by 12.6 ppb ($^1\Delta_{HP}$) and 20.0 ppb ($^1\Delta_{HH}$) respectively.[110,205]

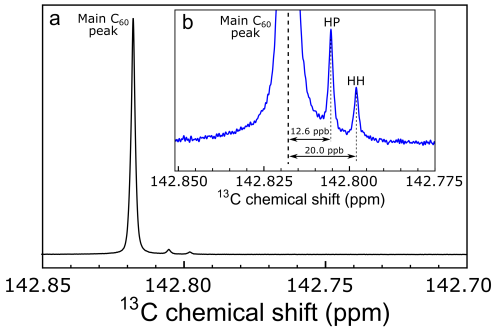

FIG. 2. (a) ^{13}C solution NMR spectrum of 25 mM C_{60} in deuterated orthodichlorobenzene (ODCB-d_4), at a magnetic field of 16.45 T and a temperature of 295 K (sum of 856 transients). The main C_{60} peak is at 142.818 ppm relative to TMS. (b) Expanded view of the base of the main C_{60} peak, showing the assignment of the side peaks to ^{13}C pairs sharing either a HP (hexagon-pentagon) or a HH (hexagon-hexagon) bond. The secondary ^{13}C isotope shifts are $^1\Delta_{HP} \simeq 12.6$ ppb for a HP $^{13}C_2$ pair and $^1\Delta_{HH} \simeq 20.0$ ppb for a HH $^{13}C_2$ pair. Open access reprint from the PCCP Owner Societies (ref. 205): G. R. Bacanu *et al.*, Phys. Chem. Chem. Phys., **22**, DOI: 10.1039/D0CP01282C, 2020; licensed under a Creative Commons Attribution-Non Commercial 3.0 Unported Licence (CC BY-NC) license.

The integrated amplitudes of the two side peaks, relative to the main ^{13}C peak are HP = 1.63 ± 0.15% and HH = 0.81 ± 0.08%. Furthermore, the relative ratio of the peak amplitudes is HP : HH = 2 : 1. These peaks were shown to arise due to the NMR secondary isotope shift, when two ^{13}C's are adjacent in the C_{60} cage.[110,205] The secondary isotope shift in NMR is a change in the chemical shift experienced by a nuclear spin when one of the neighbouring atoms is substituted by one of its isotopes.[205–207]

For C_{60} there are 90 bonds in total, 60 "single bonds" between a hexagon and a pentagon (HP) and 30 "double bonds" between a hexagon and a hexagon (HH), in relative ratio 2:1.[2] It was shown that when two ^{13}C's are adjacent along a HP (or HH) bond it leads to the observed HP (or HH) peak.[205] The HH peak is shifted by a larger amount because the HH "double bond" is stronger and the secondary isotope shift is affected more by a change in mass of the constituent atoms. ^{13}C-^{13}C J-couplings do not generate spectral splitting because the two carbon atoms are magnetically equivalent if they are adjacent along HP or HH bonds.

A model explaining the observed intensities, making use of the measured shifts, was developed and further tested on ^{13}C enriched C_{60} – with an excellent match to experiment.[110,205] Furthermore, the isotope shifts decrease (linearly) in magnitude with increasing temperature, consistent with the expected trend.[110,205]

2. C_{60} *merohedral disorder*

The C_{60} fullerene exhibits a rich set of exquisite properties. C_{60} fullerene molecules rotate freely in the lattice at room temperature, which makes C_{60} a plastic solid.[204,208,209] At room temperature, the C_{60} lattice is fcc (face-centred-cubic) with $Fm\bar{3}m$ space group.[2,210,211]

As the temperature is lowered, at ~ 260 K a phase transition occurs to a primitive cubic lattice with the $Pa\bar{3}$ space group (S_3 point group).[2,204,208–211] A large drop in the lattice constant is seen at this $Fm\bar{3}m \rightarrow Pa\bar{3}$ phase transition.[2,210] Furthermore, a large drop in the ^{13}C T_1 is observed at this $Fm\bar{3}m \rightarrow Pa\bar{3}$ phase transition.[208]

In this $Pa\bar{3}$ phase, C_{60} is in a "ratcheting" phase where it is still rotating but no longer freely, it jumps (ratchets) in between symmetry equivalent positions.[204,208,209] If the temperature is lowered even further, at 90−100 K another phase transition occurs, and the C_{60} molecules lose their rotational mobility, being "frozen" in the lattice.[204,208,209] The space group $Pa\bar{3}$ does not change with this second phase transition.[2,210,211]

In the low temperature phase, $Pa\bar{3}$, there is another aspect, orientational disorder or merohedral disorder. Two distinct orientations of the C_{60} with respect to the crystallographic axis, called P and H, can be disentangled using diffraction measurements.[2,210,211] The P orientation has the pentagonal faces (electron deficient) on one C_{60} facing the double bonds (electron rich) on a neighbouring C_{60}; whereas in the H orientation the hexagonal faces (electron rich) are facing the double bonds (electron rich). From this simple electrostatic argument the P orientation is observed to be lower in energy (more stable). This is also observed in the relative ratios of the P and H orientations, where below $90-100$ K the ratio is locked to approximately P : H = 85 : 15. As the temperature is increased close to the ~ 260 K $Pa\bar{3} \rightarrow Fm\bar{3}m$ phase transition, the P : H ratio approaches 1:1.[2,210,211]

The P : H ratio is also sensitive to the applied pressure. If C_{60} is pressurised in the "ratcheting" phase, the P : H ratio changes, increasing the ratio of H orientations.[2,212]

B. INS selection rule: unique for C_{60} endofullerenes

A novel selection rule was found for INS (Inelastic Neutron Scattering) of C_{60} endofullerenes. Initially, when a diatomic molecule is confined in C_{60}.

1. INS selection rule: numerical approach

It arises when the rotational angular momentum J and the orbital angular momentum L couple together to give the total angular momentum $\Lambda = L+J, L+J-1, ..., |L-J|$.[172–175,189,213,214] The selection rule states that a given INS transition $N',J',L',\Lambda' \rightarrow N,J,L,\Lambda$ is forbidden if the following are satisfied:[213,215]

$$\Lambda' = 0$$
and
$$\Lambda - L - J = \text{odd integer}$$

The quantum number N does not play a role in the selection rule. Furthermore, the nuclear spin component of the INS transition (see eq. 29−30) does not influence the selection rule at all. The selection rule only involves spatial quantum states.[172–176,189,213]

The selection rule was shown to hold for INS of H_2@C_{60}, HD@C_{60} and HF@C_{60}.[172–175,213] The forbidden transitions for H_2@C_{60} are shown to have intensities up to 1% of the allowed transitions.[174]

The selection rule is valid if the N,L,J and Λ used to describe the system are good quantum numbers. This is the case for homonuclear diatomics like H_2@C_{60}. Although, for HD@C_{60} and HF@C_{60} the N,L,J are not good quantum numbers due to strong mixing, and only Λ is a good quantum number.[172–176,213] In some cases, however, the states that are mixed into the eigenstates (involved in the transition) each satisfy the selection rule separately, and this will make the selection rule valid for the mixed eigenstate as well.[173,175,213]

Upon symmetry breaking interactions (section IV C) a given $|vJNL\Lambda\rangle$ TR level is split into $2\Lambda+1$ components, based on the $|M_\Lambda|$ quantum number. The selection rule makes transitions to $M_\Lambda = 0$ states forbidden. However, transitions to $|M_\Lambda| > 0$ states acquire small non-zero intensities − although the transitions are not guaranteed to be observable in the spectrum.[175]

2. INS selection rule: group theory approach

The INS selection rule can be elegantly derived in a general form using group theory.[216,217] One can calculate if any transition $\langle\Psi_f|\widehat{V}_{INS}|\Psi_i\rangle$ (see eq. 29-30) is forbidden or allowed by using the triple direct product of the irreducible representations (irreps) of the eigenstates and the INS transition operator ($\widehat{V}_{INS}$):[216,217]

$$\Gamma = \Gamma(\Psi_f) \otimes \Gamma(\widehat{V}_{INS}) \otimes \Gamma(\Psi_f) = a_0\Gamma^0 \oplus a_1\Gamma^1 \oplus ....$$

The direct product Γ can be reduced to a direct sum of irreducible representations Γ^i, where the totally symmetric irreducible representation is Γ^0. The selection rule states that transitions are forbidden if the direct sum of irreducible representations does not contain Γ^0 (i.e. $a_0 = 0$).[216,217]

The challenging part of this approach is to treat all irreps under the same group. In a rigorous treatment, the largest common subgroup between $\langle\Psi_f|$, $\widehat{V}_{INS}$ and $|\Psi_i\rangle$ needs to be found, and all representations must be expressed using this group. This approach leads to the analogous selection rule, seen in the previous section, between states labelled by N, J, L and Λ for diatomic molecules confined **inside a perfect sphere**, transitions are forbidden if:[216,217]

at least one $\Lambda = 0$
and
$(J+L-\Lambda)$ changes from even to odd (or vice − versa)

Using the "spectroscopic parity", INS selection rules are also derived for H_2O@sphere and CH_4@sphere using this group theoretical approach.[217] Furthermore, a selection rule for pure rotational transitions is derived for H_2O@sphere, which proves that TR coupling is actually not necessary for the INS selection rule to be valid.[217]

Such selection rules are valid for spherical symmetry, describing the C_{60} endofullerenes using the spherical point group K_h. However, the true symmetry group of C_{60} is I_h (Icosahedral) and not K_h. Strictly speaking, the correct symmetry group for endofullerenes of C_{60} is $I_h^G = I_h \otimes G$ where G is the symmetry group of the endohedral species.[216] When using the I_h group, it turns out there are no rigorous INS selection rules for C_{60} endofullerenes within I_h symmetry; the forbidden transitions actually have very small non-zero intensities. However, since C_{60} is nearly spherical, any orientation is close to an equivalent orientation, which makes the INS selection rules essentially valid for practical purposes. Such "forbidden" transitions would have a negligible intensity with respect to the INS sensitivity.[216,217]

C. C_{60} endofullerene symmetry breaking phenomena

In many spectroscopic investigations of C_{60} endofullerenes additional symmetry breaking effects are observed. Small splittings are observed for the $\Lambda = 1$ ro-translational states. This is not possible within the I_h symmetry of C_{60}, because only ro-translational states with $\Lambda \geq 3$ would be split.[134,181,183]

Such small splittings have been observed in He@C_{60}[110–112], H_2@C_{60}[92,150,177,178,181,192,218,219], HF@C_{60}[20] and H_2O@C_{60}[187,193,220–222]. Furthermore, fine structure couplings are observed in EPR measurements on solid N@C_{60}, which are not possible in I_h symmetry.[83,223]

The low temperature phase of the C_{60} crystal has local S_6 point group symmetry[2], which can lead to such splittings of $\Lambda = 1$ states. Many studies have suggested that the source of this symmetry breaking is due to the crystal

field effects of the C_{60} lattice.[83,92,177,181,187,192,219,220,223] Taking it further, merohedral disorder of the C_{60} lattice (section IV A 2) has been suggested to be the cause of the crystal field.[83,92,110,112,187,214,219,224,225] Other studies suggested that distortion of the C_{60} cage may be responsible for the symmetry breaking.[20,193,220,221,226] Some interpretations of the symmetry breaking mechanism are given below.

1. Symmetry breaking: merohedral disorder

An interpretation of the symmetry breaking effects, observed for C_{60} endofullerenes, is presented for $H_2@C_{60}$, $HF@C_{60}$ and $H_2O@C_{60}$ in terms of merohedral disorder of the C_{60} lattice (section IV A 2).[175,176,214,224,225] This considers a lattice fragment of rigid C_{60} molecules, with one central C_{60} surrounded by 12 nearest neighbours, with all cages in either the P or the H orientation (100% pure P or H orientations).[175,176,214,224,225]

The charge distribution for the central C_{60} (with 12 nearest neighbours), computed with DFT, is expanded in spherical multipoles. The lowest non-zero rank is $\ell = 2$ (electric field gradient = quadrupole terms).[175,176,214,224,225] For an isolated C_{60} with I_h symmetry rank ℓ or $\lambda = 2$ is impossible, the lowest non-zero ranks are $= 6, 10, ...$[133,150,155] The electric field gradient (EFG) $I^{(2)}_m$ couples to the molecular electric quadrupole moment of the endohedral species $Q^{(2)}_m$ (both ranks $\ell = 2$), giving the quadrupole interaction V_{quad}:[224]

$$V_{quad} = \sum_{m=-2}^{2} (-1)^m \, I^{(2)}_{-m} \, Q^{(2)}_m \tag{31}$$

Rank $\ell = 2$ interactions can split $\Lambda = 1$ ro-translational states.[175,176,214,224,225]

Calculations on 100% pure P and H orientations of the 12 nearest neighbours give an EFG for P more than an order of magnitude larger than for H.[224] Furthermore, the calculated splittings for P are approximately 30 times larger than for H.[175,176,214,224,225] Thus, within this model the symmetry breaking splittings arise mainly from the P orientation, with H orientation splittings being negligible.[224] Such calculations for P give splittings of the $J = 1$ rotational states of ~ 1 cm^{-1} for $H_2@C_{60}$ and ~ 4 cm^{-1} for $HF@C_{60}$ & $H_2O@C_{60}$.[214,224]

The same type of calculation for the pure translational states, orbital angular momentum $L = 1$ ($\Lambda = 1$ and $J = 0$), gives splittings about one order of magnitude smaller than for the pure rotational states.[225] Spectra simulated considering 15% H and 85% P contributions give a good match to the experiment.[214,225]

2. Symmetry breaking: C_{60} cage distortion

An alternative interpretation of the symmetry breaking invokes a Jahn-Teller (JT) distortion of the C_{60}.[226] The observed splittings of the $J = 1$ rotational states can be explained by the endohedral species experiencing a spheroidal $D_{\infty h}$ environment. This could be achieved through a JT distortion of the fullerene cage of D_{5d} or D_{3d} symmetry, distortion coinciding with the 5 or 3-fold axis, respectively.[226] For such a JT effect, charge transfer between the endohedral species and the cage should be present and also stabilisation effects from cooperative interactions of the fullerene molecules.[226]

Using group theory, a potential satisfying the S_6 symmetry (and I_h) can be constructed from a linear combination of symmetry-adapted rotational and translational states.[227] Such a spheroidally distorted potential can be constructed using only two terms. This potential is in the general form, which can explain the observed splittings in $H_2O@C_{60}$ without making explicit assumptions about the system.[227]

However, making use of this approach does not exclude the electrostatic mechanism mentioned above (section IV C 1). It is possible that such distortions of the cages are in addition to the electrostatic interactions with the nearest C_{60} neighbours. In order to elucidate the effect and disentangle between the two, further high-resolution experiments and calculations involving higher excited states are required.[214,224–227]

A related approach includes an additional C_{3i} potential to the I_h potential provided by C_{60}.[228] Such a term can be regarded as arising from the induction interaction of the HF quadrupole with the effective polarisability of C_{60}. This term is much larger than the analogous term arising from the interaction of the quadrupoles of HF and C_{60}.[228]

Another related approach uses quantum chemistry calculations, in which the fullerene cage is elongated or compressed. A compression/elongation of $\sim 1\%$ gives the splitting of the $J = 1$ rotational state observed for $H_2O@C_{60}$.[229]

3. Symmetry breaking: off-centre endohedral

To explain the symmetry breaking effect, a different approach involves the position of the endohedral molecule within the fullerene cage. Through non-covalent interactions with the fullerene cage or nearest neighbours, the position of the endohedral species could be displaced from the centre.[229] The splitting of the $J = 1$ rotational state observed for $H_2O@C_{60}$ can also be explained by assuming an off-centre position for the endohedral H_2O molecule.[229]

D. Photo excited C_{60}: electronic triplet state

The C_{60} molecule can be excited to an electronic triplet state by strong laser irradiation; and the same can be achieved for endofullerenes of C_{60}. Initially, the laser populates an excited electronic singlet state S_1 of the cage, which then through an intersystem crossing (ISC) mechanism is converted to the electronic triplet state T_1; with different transition amplitudes for the triplet sublevels (T_{10}, T_{1+1}, T_{1-1}). Thus, the triplet sublevels become unequally populated. The electronic triplet state T_1 then decays to the ground electronic single state S_0 with its characteristic decay constant (electronic triplet state lifetime).[230] Transient absorbance decay kinetics measure the photo excited electron triplet state lifetime of C_{60} (endo)fullerenes.[73,231,232]

Furthermore, time-resolved EPR measurements can be performed on the C_{60} (endo)fullerene photo excited electronic triplet state, if the triplet lifetime is long enough; see section VI F 2.

V. NMR

NMR measurements are extremely useful for investigating endofullerenes. Many results have been published on the NMR of endofullerenes, characterisation, unusual relaxation properties, unusual NMR interactions, endohedral shifts, nuclear spin isomers, quantum rotor induced polarisation, etc.

In all endofullerenes discussed here, encapsulation inside the C_{60} cage causes a change in the chemical shift of the endohedral species. In all cases shielding of the chemical shift occurs, in some cases even pushing the chemical shift to negative values. This is a clear indication that encapsulation has taken place: as the fullerene shields the endohedral species from the environment, it also shields the chemical shift.

A. ^{13}C NMR aspects of C_{60} endofullerenes

1. ^{13}C Endohedral shifts

Upon encapsulation of an endohedral species within C_{60}, the ^{13}C chemical shift of C_{60} changes, usually in the deshielding direction. This change in chemical shift is referred to as the (^{13}C) endohedral shift. ^{13}C endohedral shifts for $H_2@C_{60}$ and $H_2O@C_{60}$ are shown in fig. 3, where the ^{13}C chemical shifts of the endofullerenes are deshielded with respect to empty C_{60}. In the solution state, all carbon atoms of the endofullerene are still chemically equivalent, i.e. the cage retains icosahedral symmetry upon encapsulation.

The endohedral shift can be understood by at least two mechanisms: (i) electronic changes induced in the cage by interacting with the electrons and nuclei of the endohedral species (direct interaction) and (ii) geometric changes of the cage induced by the endohedral species (indirect interaction)[21]. Both mechanisms can modify the electronic structure of the cage and lead to changes in the shielding = changes in the ^{13}C chemical shift.

The endohedral shifts seem to follow the general trend of increasing in magnitude with increasing size of the endohedral species. Endohedral shifts of C_{60} endofullerenes measured by ^{13}C solution state NMR are presented in table II. No ^{13}C resonance was detected for $N@C_{60}$, due to line broadening and paramagnetic shifts caused by the unpaired electrons.[232]

2. ^{13}C NMR fine structure: HP & HH side peaks

High resolution ^{13}C solution state NMR of C_{60} reveals two small additional peaks on the shielding (upfield) side of the main C_{60} peak. This is shown in fig. 2 (also in fig. 3) where two additional small peaks labelled HP and HH are seen. The peaks arise due to the NMR secondary isotope shift, when two

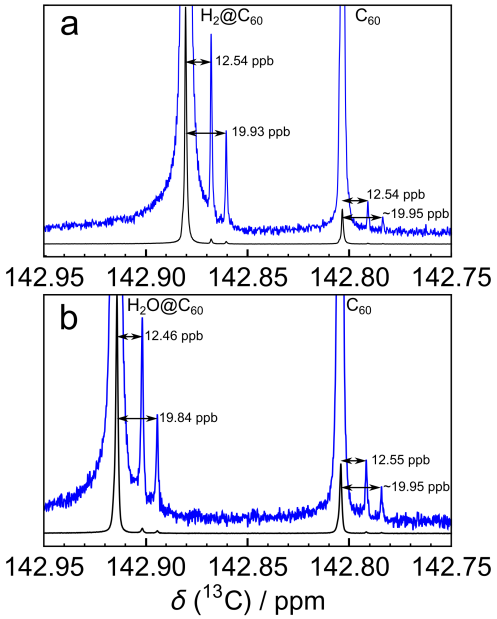

FIG. 3. ^{13}C solution NMR spectra of ~25 mM solutions of (a) $H_2@C_{60}$ (filling factor 87.7%, sum of 416 transients) and (b) $H_2O@C_{60}$ (filling factor 78.6%, sum of 272 transients), in ODCB-d_4 at a temperature of 298 K. For each species, a pair of side peaks on the shielding side of the main ^{13}C peak is clearly visible. Open access reprint from the PCCP Owner Societies (ref. 205): G. R. Bacanu *et al.*, Phys. Chem. Chem. Phys., **22**, DOI: 10.1039/D0CP01282C, 2020; licensed under a Creative Commons Attribution-Non Commercial 3.0 Unported Licence (CC BY-NC) license.

^{13}C's are adjacent in the C_{60} cage; see section IV A 1 for more information.[110,205]

Upon encapsulation, the ^{13}C chemical shift of the endofullerene cage changes due to the ^{13}C endohedral shift (section V A 1). The HP & HH isotope shifted peaks follow the main ^{13}C peak of the respective endofullerene, see fig. 3 for $H_2@C_{60}$ and $H_2O@C_{60}$.[101,205] There are small differences between the HP & HH isotope shifts ($^1\Delta_{HP}$ & $^1\Delta_{HH}$) of endofullerenes and empty C_{60}. Generally, the isotope shifts decrease slightly in magnitude as the endohedral species increases in size, see Table III.

3. ^{0}J-couplings in C_{60} endofullerenes

Internuclear J-couplings have been observed, in solution state NMR, between the endohedral species and the ^{13}C nuclei of the C_{60} cage that encloses it. The nuclei involved in the interaction are not chemically bonded together, which leads to a "non-bonded" ^{0}J-coupling. The prefix "0" in the ^{0}J symbol

TABLE II. ^{13}C endohedral shift of C_{60} endofullerenes, measured by solution state NMR.

Species	^{13}C Endohedral shift	Solvent	Reference
$^4He@C_{60}$	0.02 ppm	ODCB-d_4	99
	24.781 ± 0.001 ppb	ODCB-d_4	100
$^3He@C_{60}$	24.628 ± 0.001 ppb	ODCB-d_4	100
$Ne@C_{60}$	23.617 ± 0.002 ppb	ODCB-d_4	100
$HF@C_{60}$	0.05 ppm	toluene-d_8	20
$H_2@C_{60}$	0.078 ppm	ODCB-d_4	31
$H_2O@C_{60}$	0.11 ppm	ODCB-d_4	98
$Ar@C_{60}$	0.17 ppm	benzene-d_6	233
	0.18 ppm	ODCB-d_4	101
$Kr@C_{60}$	0.39 ppm	benzene-d_6/h_6 (1:1)	73
	390 ± 1 ppb	ODCB-d_4	102
$CH_4@C_{60}$	0.52 ppm	ODCB-d_4	103
$CH_2O@C_{60}$	0.684 ppm	ODCB-d_4	21
$Xe@C_{60}$	0.95 ppm	benzene-d_6/h_6 (1:1)	75

indicates the absence of a formal chemical bond, as the notation makes use of the usual J-coupling nomenclature: $^nJ_{AX}$ represents a J-coupling between nuclei "A" and "X" separated by "n" covalent bonds.[21,109,110]

The magnitudes of the observed ^{0}J-couplings are very small, around 70 mHz.[21,109,110] Thus far, evidence of ^{0}J-couplings has been observed for: $^3He@C_{60}$ ($^0J_{HeC}$ section V B 2), $CH_4@C_{60}$ ($^0J_{HC}$ section V G 1) and $CH_2O@C_{60}$ ($^0J_{HC}$ section V H 1).

Observation of such an effect proves that for J-couplings to form, confinement to a small region of space is required but chemical bonding is not. The confinement facilitates orbital overlap between the endohedral species and the enclosing fullerene cage, which enables ^{0}J-couplings to be observed.[21,109,110] A prerequisite for the observation of such small J-couplings is that the NMR relaxation times are sufficiently long. Since the coupling is very small, the nuclei involved must have a long enough T_1 spin-lattice relaxation time to allow for the coupling to be observable (roughly larger than $1/^0J_{HeC}$).[21,109,110]

B. $^3He@C_{60}$ NMR

1. $^3He@C_{60}$ solution NMR

The ^{3}He chemical shift of $^3He@C_{60}$ is -6.30 ± 0.15 ppm in 1-methylnaphthalene, with respect to dissolved ^{3}He gas.[65] In THF-d_8 the ^{3}He chemical shift is -6.403 ppm.[23] Remarkably, two Helium atoms can be observed inside C_{60}, with $^3He_2@C_{60}$ having the same ^{3}He chemical shift of -6.403 ppm (THF-d_8).[23]

In contrast, the ^{3}He chemical shift of $^3He@C_{70}$ is -28.8 ± 0.2 ppm in 1-methylnaphthalene,[65] and -28.716 ppm in methylnaphthalene:CD_2Cl_2 = 3:1 (with respect to dissolved ^{3}He gas).[71] Furthermore, the ^{3}He chemical shift of the bis species $^3He_2@C_{70}$ is -28.702 ppm in methylnaphthalene:CD_2Cl_2 = 3:1.[71] Such changes in the ^{3}He chemical shifts have been exploited to monitor chemical reactions of the fullerene cage. The ^{3}He chemical shift is sensitive to chemical modifications of the fullerene cage, due to changes in the ring currents.[66,68]

For $^3He@C_{60}$ the ^{3}He T_1 spin lattice relaxation time has been measured to be around $300-500$ s, in a range of solvents and temperatures.[72] The ^{3}He T_1 was measured to be 365 ± 41 s at 298 K in ODCB-d_4 (degassed by bubbling N_2 gas).[109] For ^{13}C (endohedral) chemical shifts see section V A 1.

2. $^0J_{HeC}$ in $^3He@C_{60}$

An internuclear NMR ^{0}J-coupling (see section V A 3) has been observed in $^3He@C_{60}$ between the endohedral ^{3}He nucleus and one ^{13}C nucleus part of the fullerene cage.[109,110] This is shown as splitting of the ^{13}C resonance for $^3He@C_{60}$ in fig 4 a and b, with a magnitude of 77.5 ± 0.2 mHz (at 340 K in ODCB-d_4).[109,110] The splitting is absent in the $^4He@C_{60}$ isotopomer, fig 4 c and d, because the ^{4}He nucleus has zero nuclear spin so it cannot exhibit J-couplings.

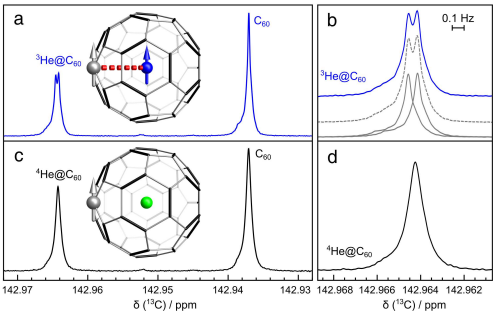

FIG. 4. **(a)** ^{13}C solution NMR spectra of ~25 mM $^3He@C_{60}$ (43% filling factor) in ODCB-d_4 at 340 K and 16.45 T, using a Bruker AVANCE NEO console and a TCI prodigy 5 mm cryoprobe (average of 40 transients). **(b)** Blue line: expansion of the ^{13}C peak of $^3He@C_{60}$; Dashed grey line: Best fit to two shifted spectral components, each with a shape matching the ^{13}C peak of C_{60}; Solid gray lines: individual spectral components. **(c)** ^{13}C solution NMR spectra of ~25 mM $^4He@C_{60}$ (41% filling factor) in ODCB-d_4 (average of 32 transients); all other conditions are the same as in **(a)**. **(d)** Expansion of the ^{13}C peak of $^4He@C_{60}$. Reprinted with permission from (ref. 109) Bacanu *et al.*. J. Am. Chem. Soc., **142**, 16926–16929, (2020). Copyright 2020 American Chemical Society.

Minor $^{13}C_2$ isotopomers give rise to two side peaks, HP & HH, on the main ^{13}C resonance due to the secondary isotope shift (sections IV A 1 and V A 2). In $^3He@C_{60}$, these side peaks are also split by this ^{0}J-coupling (see SI of ref 109).

The splitting is attributed to a "non-bonded" $^0J_{HeC}$-coupling between the nuclear spin $I = 1/2$ nuclei ^{3}He and ^{13}C. The existence of such a J-coupling is quite remarkable; it is the first direct spectroscopic observation of a J-coupling involving the ^{3}He nucleus, for the very simple reason that Helium does not form covalent bonds. This proves that for J-couplings to

TABLE III. One bond secondary isotope shifts for the HP and HH side peaks ($^1\Delta_{HP}$ and $^1\Delta_{HH}$) for C_{60} and endofullerenes of C_{60}, acquired at 298 K in ODCB-d_4.

Species	C_{60}	$H_2@C_{60}$	$Ne@C_{60}$	$Ar@C_{60}$	$H_2O@C_{60}$	$Kr@C_{60}$
$^1\Delta_{HP}$/ ppb	12.56 ± 0.01	12.54 ± 0.03	12.53 ± 0.01	12.50 ± 0.01	12.46 ± 0.02	12.45 ± 0.01
$^1\Delta_{HH}$/ ppb	19.98 ± 0.02	19.93 ± 0.05	19.94 ± 0.03	19.86 ± 0.02	19.84 ± 0.04	19.77 ± 0.02
Reference	205	205	100	101	205	102

TABLE IV. ^{3}He NMR chemical shifts (in ppm) of endohedral mono- & bis-helium fullerenes and fullerene hexaanions, relative to ^{3}He gas in THF-d_8. Reproduced from ref. 23.

	A = ^{3}He	A = ^{3}He$_2$
$A@C_{60}$	−6.403	−6.403
$A@C_{60}^{6-}$	−49.266	−49.173
$A@C_{70}$	−28.821	−28.807
$A@C_{70}^{6-}$	+8.198	+8.044

form, confinement to a small region of space is required, but chemical bonding is not.

In order to observe small J-couplings the relaxation times must be long enough (roughly larger than $1/^0J_{HeC}$). All requirements are satisfied for $^3He@C_{60}$ where the ^{3}He T_1 = 365 $\pm$ 41 s and for ^{13}C T_1 = 16.83 $\pm$ 0.04 s.[109]

The magnitude of the $^0J_{HeC}$-coupling increases linearly with temperature (between $260-340$ K), see ref 109. The enclosed Helium atom behaves akin to a "particle-in-a-box", it exhibits translational quantisation (section II C) which leads to well defined translational eigenstates. The ground state translational wavefunction is strongly localised at the centre of the fullerene cage, but excited states have an increasingly large probability close to the "inner box edge". Thus, as the temperature increases, the excited states become more populated and the ^{3}He atom gets closer to the fullerene wall on average; leading to an overall increase in the magnitude of the $^0J_{HeC}$-coupling.[109]

The $^0J_{HeC}$ can be estimated by quantum chemistry calculations, giving reasonable agreement with the experiment.[109] Thus, showing that ^{0}J-couplings can be used to benchmark quantum chemistry algorithms involving calculation of NMR parameters for non-bonded systems.

3. $^3He@C_{60}^{6-}$ & $^3He@C_{70}^{6-}$ solution NMR

The cages of $^3He@C_{60}$ and $^3He@C_{70}$ endofullerenes can be reduced to the hexanion forms, $^3He@C_{60}^{6-}$ and $^3He@C_{70}^{6-}$, using strong reducing agents.[23,72] The ^{3}He chemical shifts for these compounds change in peculiar ways, with explicit values in table IV.[23,72] The reduction of C_{60} deshields the ^{3}He chemical shifts further, whereas for C_{70} strong shielding occurs after reduction, which actually pushes the ^{3}He chemical shift to positive values. This observation applies to both the mono- and bis-Helium endofullerenes, see table IV.[23,72]

4. $^3He@C_{60}^{3-}$ solid state NMR

^{3}He NMR measurements have been performed on the $Rb_3(^3He@C_{60})$ endofulleride material, in the solid state at cryogenic temperatures.[126] The endofulleride has 3 negative charges ($^3He@C_{60}^{3-}$) from the three Rubidium ions. This material becomes superconducting at low temperatures (<30 K) and the endohedral ^{3}He is used to probe the phenomenon; because it can act as an observer without appreciably changing the properties of the material. The ^{3}He NMR signal is strongly influenced by the magnetic fields in the centre of the cage, induced by the conducting and superconducting phases. The ^{3}He T_1 displays an anomalous dependence on the spectral frequency in the superconducting state; and surprisingly such behaviour persists at higher temperatures, well above the superconducting transition.[126]

C. $Kr@C_{60}$ NMR

^{83}Kr NMR measurements were performed on $Kr@C_{60}$.[102] ^{83}Kr is 11.58% naturally abundant, with a nuclear spin $I = 9/2$. The ^{83}Kr chemical shift of $Kr@C_{60}$ was measured to be 64.3 $\pm$ 0.1 ppm (in ODCB-d_4 at 298 K); using the IUPAC unified referencing scale (with an updated Ξ parameter for ^{83}Kr).[102] Kr gas dissolved in the same sample had the ^{83}Kr chemical shift deshielded by 39.5 ppm with respect to $^{83}Kr@C_{60}$. In benzene-d_6 the ^{83}Kr chemical shift of $Kr@C_{60}$ is the same, but the dissolved Kr gas is deshielded by 32.7 ppm with respect to $Kr@C_{60}$.[102]

The shielding effect of the C_{60} cage is observed in the ^{83}Kr chemical shifts but also in the T_1 spin-lattice relaxation times. The ^{83}Kr T_1 for dissolved Kr gas was 31 $\pm$ 2 ms and for $^{83}Kr@C_{60}$ it was 860 $\pm$ 24 ms. The $\sim$28-fold increase in relaxation time upon encapsulation demonstrates how the fullerene cage protects the endohedral Kr atom from the environment.[102]

For ^{13}C (endohedral) chemical shifts see section V A 1. The cage ^{13}C NMR signal of $Kr@C_{60}$ displays side peaks (HP & HH), arising from secondary isotope shifts when two ^{13}C's are adjacent.[205] Measured shifts and more details are shown in section IV A 1 and V A 2.

D. $H_2@C_{60}$ NMR

NMR investigations have been performed on $H_2@C_{60}$ in the solution and solid state.

1. H_2@C_{60} *solution NMR*

The ^{1}H chemical shift of $H_2@C_{60}$ is -1.44 ppm in ODCB-d_4, shielded by 5.98 ppm with respect to dissolved free H_2.[31,234] For ^{13}C (endohedral) chemical shifts see section V A 1. The cage ^{13}C NMR signal of $H_2@C_{60}$ displays two side peaks in the fine structure, HP & HH, arising from secondary isotope shifts when two ^{13}C's are adjacent.[205] Measured shifts and more details are shown in section IV A 1 and V A 2.

The ^{1}H T_1 of $H_2@C_{60}$ is solvent dependent, varying from 0.118 s in benzene to 0.046 s in CCl_4. Furthermore, the ^{1}H T_1 of H_2 dissolved in the same solvent as $H_2@C_{60}$ is $10-20$ times longer, but the T_1 ratios in the same solvent are rather similar.[235] The ^{1}H T_1 in toluene-d_8 was measured with temperature; it had a maximum of ~ 0.12 s at 240 K and a minimum of ~ 0.09 s at 200 K and 330 K. In other solvents, only a monotonic decrease in ^{1}H T_1 was observed with increasing temperature.[235] In $H_2@C_{60}$ the dipole-dipole and spin-rotation relaxation mechanisms are shown to be the dominant mechanisms.[235,236]

a. Paramagnetic spin-lattice relaxation of $H_2@C_{60}$

The ^{1}H spin-lattice relaxation rates ($1/T_1$) of H_2 and $H_2@C_{60}$ were measured in toluene-d_8, in the presence of nitroxide radicals containing unpaired electrons. The relaxation rates are linearly dependent on radical concentration, with the paramagnetic relaxation effects enhanced 5-fold for $H_2@C_{60}$ compared with H_2 under the same conditions.[237] It appears that the encapsulation does not magnetically shield the endohedral H_2 from the environment. On the contrary, it seems that the interaction with paramagnets is stronger for $H_2@C_{60}$ than for dissolved free H_2, based on the achievable intermolecular distance in solution between H_2 and the unpaired electrons.[237]

Similar enhanced relaxation rates are achieved by covalently attaching nitroxide radicals to the $H_2@C_{60}$ cage.[238]

b. Comparison with HD@C_{60}

The secondary NMR isotope shift between $H_2@C_{60}$ and HD@C_{60} observed for the ^{1}H resonances ($^1\Delta$H(D)) is approximately 36 ppb at room temperature (toluene-d_8). Smaller by 1-2 ppb than the free forms of H_2/HD dissolved in toluene-d_8, and about 6 ppb smaller than the calculated values for gas phase H_2/HD. This isotope shift decreases by ~ 3 ppb when going from 200 K to 340 K.[239]

The one bond J-coupling in HD@C_{60} ($^1J_{HD}$) was measured to be $\sim$41.7 Hz (in toluene-d_8) and temperature independent. However, $^1J_{HD}$ is smaller by $\sim$2% when encapsulated in C_{60} compared to free HD dissolved in toluene-d_8.[239]

The ^{1}H T_1 of HD@C_{60} in toluene-d_8 decreases with temperature, from ~ 0.4 s at 200 K to ~ 0.18 s at 340 K.[239]

Solution NMR investigations were performed on H_2, HD, $H_2@C_{60}$ and HD@C_{60} in toluene-d_8 as a function of temperature (200-340 K). [239] It is found that the ^{1}H T_1 for HD is always slower than H_2 by a factor of ~ 2, in the free form and encapsulated in C_{60}.[239] The ^{1}H T_1's qualitatively follow the same trend in free form and encapsulated inside C_{60}, with the encapsulated species always relaxing 10-20 times faster than the free forms.[239] This slower relaxation in the free form can be explained by having a much shorter correlation time compared to C_{60} encapsulation, i.e. the H_2 and HD have much faster reorientation when in free form due to collisions with the solvent.[239] In endohedral form, the correlation times are longer due to the shielding of the cage - but this results in shorter T_1 relaxation times.[239]

For both free form and C_{60} encapsulation: H_2 has a maximum (at $240-250$ K) in the ^{1}H T_1 with temperature, while HD has a continuous decrease in the ^{1}H T_1 with increasing temperature.[239] This relaxation behaviour can be understood as follows: for H_2 the dominant relaxation mechanisms are dipole-dipole and spin-rotation, the former becoming more important at low temperatures. However, for HD the dipole-dipole mechanism is weak because Deuterium has a gyromagnetic ratio that is 6 times smaller than Hydrogen, so the spin-rotation mechanism dominates at all temperatures.[239]

2. H_2@C_{60} *spin isomer conversion: solution NMR*

Since H_2 has two indistinguishable Hydrogen nuclei, it displays nuclear spin isomerism: ortho-H_2 and para-H_2 (see section II H). Spin isomer conversion of H_2 is extremely slow, up to days/weeks in the gas phase.[240] However, spin isomer conversion can be catalysed by paramagnetic species.[231,240,241]

Singlet molecular oxygen, $^1O_2$, is a highly reactive species that can be quenched by C_{60}. The quenching rate of $^1O_2$ is faster for $D_2@C_{60}$ and even faster for $H_2@C_{60}$ (compared with C_{60}) in a CS_2 solution.[231] Such rates are even faster than for free H_2/D_2 dissolved in solution (CCl_4). This can be explained by assuming that the $^1O_2$ and the C_{60} cage form an exciplex complex, which is rather long lived compared with the free forms. The extended exciplex lifetime allows for longer interaction times, which facilitates the quenching.[231]

The spin catalysed conversion of ortho-$H_2@C_{60}$ to para-$H_2@C_{60}$ was performed at 77 K using liquid Oxygen in a zeolite matrix. O_2 is a very efficient paramagnetic spin catalyst for spin-isomer conversion.[240,241] The para-enriched $H_2@C_{60}$ converts back to ortho-$H_2@C_{60}$ very slowly, with an estimated half-life of ~ 7.5 days. However, the spin isomer conversion is much faster if O_2 is dissolved (saturated solution) in the same sample, obtaining a lifetime of ~ 100 h for $H_2@C_{60}$. Similar conversion rates are observed when nitroxide TEMPO radicals are present in the solution.[240,241]

The spin-isomer conversion of endohedral H_2 can be catalysed by a nitroxide radical covalently attached to the $H_2@C_{60}$ cage. [241,242] Spin-isomer conversion rates faster than 90 s are observed, 4 orders of magnitude faster than for pristine $H_2@C_{60}$. When the nitroxide group ($R-N-O\cdot$) is reduced to a diamagnetic form ($R-N-OH$), the spin-isomer conversion becomes slow again, demonstrating a reversible *magnetic − switch* for interconverting incarcerated nuclear spin isomers.[242] Fast spin isomer conversion rates are also observed for $H_2@C_{60}$ with pyrrolidine anions covalently bonded to the cage.[243]

3. H_2@C_{60} *liquid crystal solution NMR*

NMR measurements of $H_2@C_{60}$ have been performed in the liquid crystal N-(4-methoxybenzylidene)-4-butylaniline (MBBA).[244] The ^{1}H NMR of $H_2@C_{60}$ displays a single peak in the isotropic phase, which splits into two in the nematic phase due to residual dipolar couplings of the two Hydrogen nuclei; see fig. 5. The splitting in the nematic phase becomes larger with decreasing temperature ($\sim$ 1.2 kHz at 300 K), indicating an increasingly larger residual dipolar coupling from a stronger alignment in the magnetic field. Two mechanisms (direct and indirect) are discussed for the alignment of the endohedral species in the liquid crystal solution.[244] The residual dipolar coupling is smaller for $H_2O@C_{60}$, $\sim$ 0.7 kHz at 300 K (section V F 3), because the ^{1}H-^{1}H dipolar coupling is larger in H_2 than in H_2O, due to the shorter ^{1}H-^{1}H distance.

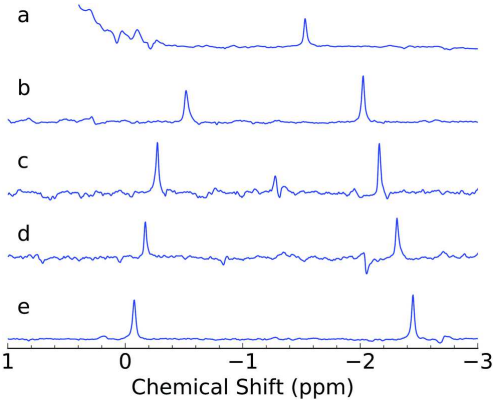

FIG. 5. ^{1}H NMR spectra of $H_2@C_{60}$ dissolved in MBBA, recorded at several temperatures: (a) T = 316 K; (b) T = 312 K; (c) T = 308 K; (d) T = 304 K; (e) T = 300 K. Spectrum (a) was recorded in the isotropic phase using a single pulse excitation and shows a single peak at −1.5 ppm. The intense MBBA signals have been truncated. Spectra (b–e) were observed in the nematic phase using a perfect echo sequence to suppress the liquid crystal background. Used with permission of Royal Society of Chemistry, from (ref. 244) Kouřil *et al.*, Phy. Chem. Chem. Phys., **19**, 11793–11801 (2017); permission conveyed through Copyright Clearance Center, Inc.

4. H_2@C_{60} *solid state NMR*

$H_2@C_{60}$ has been studied using solid state NMR. Initially, NMR measurements were performed on H_2 enclosed in open cage C_{60} fullerenes.[148,245] Cryogenic NMR measurements have been performed on $H_2@C_{70}$, which led to some puzzling results. The ^{1}H signal gave a peculiar Pake pattern, which is consistent with the $H_2@C_{70}$ cages preferentially aligning with the external magnetic field below 10 K, similar to the nematic phase of liquid crystals in magnetic fields.[246]

a. $H_2@C_{60}$ *solid state NMR: static*

Significant broadening is observed for the ^{1}H NMR signal of $H_2@C_{60}$ below 5 K. This broadening is currently unexplained, but has been attributed to magnetic field distortions at low temperatures.[148,178] It must be noted that initial investigations of endofullerenes did not usually employ a sublimation purification step, which may have effects on the sample's behaviour.

Static ^{1}H solid state NMR of $H_2@C_{60}$ at 4.8 K showed a weak but clear Pake pattern with an additional sharp peak superimposed, in a relative ratio 1:1.87 (Pake:sharp peak).[150] The Pake pattern is consistent with a homonuclear dipolar coupling of $\sim$ 116 kHz. The appearance of a Pake pattern at low temperature indicates that the site where H_2 is present has a lower symmetry than Icosahedral.[150,178] The reduced symmetry splits the rotational energy levels, which should be on the order of a few Kelvin (4.8 K).[150]

^{1}H T_1 under static conditions was measured at a variety of magnetic fields.[148] Above 200 K T_1 is field independent, but below 200 K there is a T_1 minimum, which is strongly field dependent. The T_1 minimum appears at lower temperatures in lower fields. The ^{1}H T_1 is still rather fast at all temperatures, reaching a maximum of $\sim$10 s at the lowest temperatures of $\sim$2 K; otherwise, above approximately 50 K the ^{1}H T_1 is around or below 0.1 s.[148]

Some differences were seen between the $\sim$260 K phase transition ($Fm\bar{3}m \rightarrow Pa\bar{3}$) of C_{60} and $H_2@C_{60}$ (see section IV A 2); it was shown to occur $\sim$30 K lower for $H_2@C_{60}$.[148] The $H_2@C_{60}$ does not appear to have been sublimed in this set of experiments, which can have rather strong effects on the phase transition of fullerene crystals.[148]

Ortho-para conversion is negligible in $H_2@C_{60}$ at cryogenic temperatures.[148,245]

b. $H_2@C_{60}$ *solid state NMR: MAS*

^{1}H chemical shift of $H_2@C_{60}$ under MAS (Magic Angle Spinning) is −1.1 ppm, similar to solution NMR (−1.44 ppm).[31,148] The motion of the endohedral H_2 is almost isotropic because the intramolecular ^{1}H-^{1}H dipolar coupling is mostly averaged out at room temperature. Making use of a non-zero dipolar coupling between the two protons, excitation of double quantum (DQ) coherences is possible. This allows filtering of the signal from protons which are coupled together through dipolar couplings (DQ filtering). MAS averages out the dipolar coupling to zero, but it can be recoupled using various NMR sequences (rotor synchronised, symmetry-based recoupling sequences, etc.). The SR26 sequence is used for dipolar recoupling; and by changing the excitation interval, ^{1}H-^{1}H dipolar couplings can be measured.[148] Dipolar coupling was −730 Hz at 293 K and −610 Hz at 175 K, the temperature dependence of the dipolar coupling is very weak between 293-175 K, which reflects the nearly isotropic environment of the C_{60} cage. A non-zero ^{1}H-^{1}H intramolecular dipolar coupling of endohedral H_2, even at room temperature, indicates the motion inside the cage is not perfectly isotropic.[148] However, as Spherical Tensor Analysis (STA)[247] shows, this dipolar coupling could be intermolecular, arising from couplings between H_2 molecules in neighbouring fullerene cages (see below).[148] Larger intramolecular

^{1}H-^{1}H dipolar couplings are seen for H_2 inside open-cage-fullerenes, where the symmetry is drastically lowered from Icosahedral.[148,245]

STA (spherical tensor analysis)[247] performed with small DQ recoupling times (0.4 ms) shows only spin spherical tensor rank 1 components (thermal Zeeman polarisation). Using longer DQ recoupling times (0.8 ms), spin spherical tensors of rank 2 appear – only possible if at least two ^{1}H's are (dipolar) coupled together. At even longer DQ recoupling times (1.6-3.2 ms) ranks higher than 2 are present – only possible if more than two ^{1}H's are coupled. This proves that intermolecular dipolar interactions between H_2's in neighbouring cages are present, since each fullerene cage contains only two ^{1}H atoms.[148] STA effectively shows that the DQ filtered signal (see above) can have components from intermolecular ^{1}H-^{1}H dipolar couplings between H_2 molecules in neighbouring cages.[148]

E. HF@C_{60} NMR

1. HF@C_{60} *solution NMR*

Solution state NMR measurements of HF@C_{60} give the chemical shifts of the endohedral species to be δ_H = −2.68 ppm and δ_F = −219.94 ppm; with a ^{1}H-^{19}F J-coupling ($^1J_{HF}$) of 505.5 ± 0.5 Hz (toluene-d_8). The J-coupling is similar (or smaller) than HF in molecular beams, but is larger than HF in various solvents.[20] For ^{13}C (endohedral) chemical shifts see section V A 1.

2. HF@C_{60} *liquid crystal solution NMR*

NMR measurements of HF@C_{60} have been performed in the liquid crystal N-(4-methoxybenzylidene)-4-butylaniline (MBBA).[244] For HF@C_{60}, the ^{19}F NMR signal is a doublet from the ^{1}H-^{19}F J-coupling in the isotropic phase ($^1J_{HF}$ = 506 Hz). The doublet splitting becomes much larger in the nematic phase, ∼2.71 kHz at room temperature. Indicating a significant ^{1}H-^{19}F residual dipolar coupling is present due to the endohedral HF alignment in the liquid crystal solution. Two mechanisms (direct and indirect) are discussed for the alignment of the endohedral species in the liquid crystal solution.[244]

3. HF@C_{60} *solid state NMR: MAS*

Solid state ^{19}F MAS NMR measurements of HF@C_{60} (263 K) show the presence of anisotropic interactions (broadening), due to ^{19}F chemical shift anisotropy.[20] Most likely, such anisotropic interactions are induced by distortions of the C_{60} cage by the endohedral HF.[20]

F. H_2O@C_{60} NMR

1. H_2O@C_{60} *solution NMR*

The ^{1}H chemical shift of H_2O@C_{60} is −4.81 ppm in ODCB-d_4, which is shielded by 6.2 ppm compared with H_2O dissolved in the same solvent.[98] A $^1J_{HD}$-coupling between the H and D of 0.9 Hz is observed in the HDO@C_{60} isotopologue.[98]

For ^{13}C (endohedral) chemical shifts see section V A 1. The cage ^{13}C NMR signal of H_2O@C_{60} displays two side peaks in the fine structure, HP & HH, arising from secondary isotope shifts when two ^{13}C's are adjacent.[205] Measured shifts and more details are shown in section IV A 1 and V A 2.

The ^{1}H T_1 of H_2O@C_{60} is ∼ 1.5 s in a few organic solvents at 300 K.[236] The ^{1}H T_1 of H_2O@C_{60} does not depend much on the solvent (viscosity and polarity), indicating that the endohedral H_2O is decoupled quite well from the cage motion and is quite electrically isolated from the environment by the cage.[236] The ^{1}H T_1 has a monotonic decrease with increasing temperature, meaning the spin-rotation relaxation mechanism dominates (with dipole-dipole playing a minor role). In H_2@C_{60} the dipole-dipole relaxation mechanism is not negligible, see section V D 1, whereas for H_2O@C_{60} spin-rotation dominates.[236]

Covalently attaching nitroxide radicals to the outside of the cage makes the ^{1}H T_1 much faster.[236]

a. $H_2^{17}O$@C_{60} *solution state NMR*

The ^{1}H solution NMR spectrum of $H_2^{17}O$@C_{60} is composed of 6 peaks, due to the ^{1}H-^{17}O J-coupling ($^1J_{HO}$) of 77.9 Hz (^{17}O is a quadrupolar nucleus with spin $I = \frac{5}{2}$). The line widths of the peaks (full width at half maximum) vary in a peculiar way: 9.1 ± 0.3 Hz ($M_s = \pm\frac{5}{2}$), 13.2 ± 0.3 Hz ($M_s = \pm\frac{3}{2}$) and 10.7 ± 0.1 Hz ($M_s = \pm\frac{1}{2}$), where M_s is the projection quantum number of ^{17}O. The peculiar sequence of ^{1}H linewidths is due to scalar relaxation of the second kind, caused by the fast quadrupolar relaxation of the ^{17}O nucleus.[248] Furthermore, the rotational correlation time of the endohedral $H_2^{17}O$ was determined to be τ_C = 107 ± 9 fs, at room temperature in ODCB-d_4 and 11.7 T.[248]

2. H_2O@C_{60} *spin isomer conversion: solution NMR*

Since H_2O has two indistinguishable Hydrogen nuclei, it displays nuclear spin isomerism: ortho-H_2O and para-H_2O (see section II H).

The ortho-para conversion of H_2O@C_{60} was measured at room temperature in solution.[249] H_2O@C_{60} is enriched in the para spin isomer at low temperature and then rapidly dissolved in ODCB-d_4 at room temperature; then the conversion from para-H_2O to ortho-H_2O is monitored using the ^{1}H NMR signal. The ortho-para spin isomer conversion rate at room temperature in ODCB-d_4 is estimated to be 30 ± 4 s for H_2O@C_{60} and 16 ± 3 s for $H_2^{17}O$@C_{60}.[249] The faster conversion for $H_2^{17}O$ is attributed to ^{1}H-^{17}O dipole-dipole interactions.[249]

3. $H_2O@C_{60}$ *liquid crystal solution: NMR*

NMR measurements of $H_2O@C_{60}$ have been performed in the liquid crystal N-(4-methoxybenzylidene)-4-butylaniline (MBBA).[244] In the ^{1}H NMR of $H_2O@C_{60}$, the single peak in the isotropic phase splits into two in the nematic phase, due to residual dipolar couplings of the two Hydrogens.

The splitting seen in the nematic phase becomes larger with decreasing temperature ($\sim$ 0.7 kHz at 300 K), indicating an increasingly larger residual dipolar coupling from the stronger alignment in the magnetic field. Two mechanisms (direct and indirect) are discussed for the alignment of the endohedral species in the liquid crystal solution.[244] The residual dipolar coupling is larger for $H_2@C_{60}$, $\sim$ 1.2 kHz at 300 K (section V D 3), because the ^{1}H-^{1}H dipolar coupling is larger in H_2 than in H_2O, due to the shorter ^{1}H-^{1}H distance.

a. $H_2^{17}O@C_{60}$ *liquid crystal solution: NMR*

NMR measurements of $H_2^{17}O@C_{60}$ have been performed in the liquid crystal N-(4-methoxybenzylidene)-4-butylaniline (MBBA), see fig. 6 for ^{17}O spectra at different temperatures.[250] In the isotropic phase the ^{17}O signal is split into a triplet (1:2:1) from the ^{1}H-^{17}O scalar J-coupling ($^1J_{HO}$ = 78 Hz). In the nematic phase (MBBA), the splitting of the triplet increases to $150-200$ Hz due to ^{1}H-^{17}O residual dipolar couplings.[250] Furthermore, ^{17}O is a quadrupolar spin $I = 5/2$ nucleus, and ^{17}O residual quadrupolar couplings lead to a pentet with a $5-10$ kHz splitting. Thus, the triplet ^{17}O NMR signal in the nematic phase is split into a pentet of triplets pattern, seen in fig. 6.[250] All residual couplings increase in magnitude with decreasing temperature.

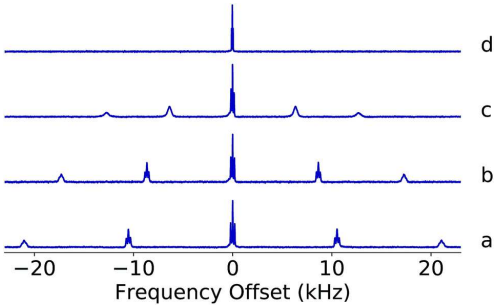

FIG. 6. ^{17}O NMR spectra of $H_2^{17}O@C_{60}$ dissolved in MBBA at four different temperatures: (a) 298 K, (b) 303 K, (c) 307 K, (d) 315 K. Spectra a–c were recorded in the nematic phase. Spectrum d was recorded in the isotropic phase. In the nematic phase the spectrum shows signs of residual quadrupolar coupling and weaker residual dipolar coupling. Details of the nematic-phase spectrum are shown in Fig. 1 of ref. 250. In the isotropic phase the spectrum consists of a 1:2:1 triplet showing a ^{1}H-^{17}O scalar J-coupling ($|^1J_{HO}|$ = 78 Hz). The intensity of spectrum d is scaled down by a factor of 10. Used with permission of Royal Society of Chemistry, from (ref. 250) Kouřil *et al.*, Faraday Discussions, **212**, 517–532 (2018); permission conveyed through Copyright Clearance Center, Inc.

From fitting such residual couplings, the order parameter for $H_2^{17}O$ encapsulated in C_{60} dissolved in MBBA is obtained: water orientations in which the H–O–H plane is perpendicular to the liquid crystal director (and the external magnetic field) are slightly favoured and water orientations in which the H–H internuclear vector is parallel to the liquid crystal director are slightly disfavoured. Two mechanisms (direct and indirect) are discussed for the preferential alignment of the endohedral species in the liquid crystal solution.[250]

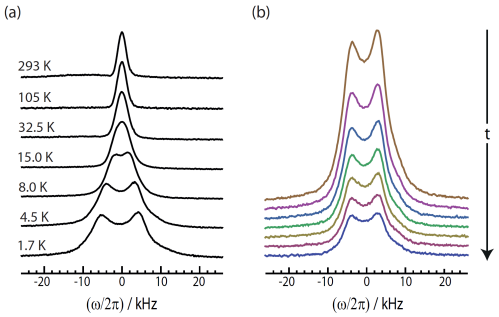

FIG. 7. ^{1}H NMR spectra of $H_2O@C_{60}$. (a) ^{1}H spectra from room temperature down to 1.7 K. (b) ^{1}H spectra recorded at a set temperature of 5 K, taken at intervals of 2.25 h after cooling from 60 K. During all the experiments the temperature was stabilized to 5 K within 0.1 K. The first spectrum (top) was taken after waiting 30 min, in order to allow thermal equilibration of the equipment. Reprinted from (ref. 251) Mamone *et al.*, J. Chem. Phys., **140**, 194306 (2014)., with the permission of AIP Publishing.

4. $H_2O@C_{60}$ *solid state NMR*

a. $H_2O@C_{60}$ *solid state NMR: static*

The ^{1}H NMR spectrum of $H_2O@C_{60}$ in the static solid is composed of a single peak at room temperature, see fig. 7. The peak develops a splitting when the temperature is lowered below $\sim$10 K.[251] The splitting is due to dipolar interactions between the two Hydrogen atoms in ortho-H_2O. The observation of a splitting in the NMR spectrum is consistent with a broken degeneracy of the ground rotational state for ortho-H_2O.[251]

The ^{1}H T_1 spin-lattice relaxation time for $H_2O@C_{60}$ in the static solid was measured to be between $\sim$0.2 s at room temperature and $\sim$5 s at $\sim$4.5 K. There is a T_1 minimum at $\sim$8 K, probably due to the $\sim$0.6 meV splitting of the ortho-H_2O rotational ground state (see section VII H 2).[251]

b. $H_2O@C_{60}$ *solid state NMR: MAS*

^{1}H chemical shift of $H_2O@C_{60}$ under MAS is -4.7 ppm, similar to solution NMR (-4.81 ppm).[221] The presence of a dipole-dipole coupling between the two ^{1}H's has also been observed in cryogenic MAS measurements on $H_2O@C_{60}$.[220] A ^{1}H-^{1}H dipolar coupling of 5.5 kHz is able to explain the observed MAS ^{1}H spectrum at 9.6 K.[220] The splitting of the ortho-H_2O rotational ground state is estimated to be

$\sim$0.9 meV, by calculating the thermal average of the dipolar Hamiltonian.[220] This value is comparable with the 0.6 meV splitting measured by INS (see section VII H 2).[220]

Using double-quantum-filtered dipolar recoupling (DQfDR) techniques, employing symmetry-based sequences ($SR20_2^9$), the dipolar coupling between the two Hydrogens was estimated to be -500 ± 10 Hz at room temperature.[221] With this dipolar coupling and the intensity pattern of the spinning sidebands, the chemical shift anisotropy (CSA) δ^a is determined to be $|\delta^a| = 3.1 \pm 0.3$ ppm ($\delta^a = \delta_{zz} - \delta_{iso}$).[221] Furthermore, the relative angle between the dipole-dipole and CSA tensors is determined to be $90 \pm 40°$ (both tensors assumed to be uniaxial), indicating the two tensors are approximately perpendicular.[221]

The presence of such a residual ^{1}H-^{1}H dipolar coupling and CSA in $H_2O@C_{60}$ at room temperature is significant. At room temperature, the fast rotation of the endohedral H_2O should average out both interactions to zero. The residual interactions allow estimation of an order parameter for second rank spherical tensor interactions. This demonstrates that the observed ^{1}H CSA cannot be the intrinsic ^{1}H CSA of the H_2O molecule and must be caused by the C_{60} encapsulation.[221] Observation of such anisotropic NMR interactions is consistent with a modification of the enclosing C_{60} cage. Either the H_2O disturbs the electronic structure of the cage, or it distorts the C_{60} structure or a combination of the two.[221]

5. $H_2O@C_{60}$ *spin isomer conversion: solid state NMR*

The ortho-para spin isomer conversion rate was measured using low temperature solid state NMR. The ^{1}H NMR signal at low temperature (5 K) decreases with time as $H_2O@C_{60}$ converts to the para spin isomer, see fig. 7 (b).[251]

Using a temperature jump experiment, the ortho-para spin isomer conversion rate of $H_2O@C_{60}$ is observed to follow second-order kinetic behaviour, see fig. 8.[251] The second-order rate constant k_2 is measured to be $120 \pm 25 \times 10^{-5}$ s^{-1}, $23 \pm 5 \times 10^{-5}$ s^{-1} and $10 \pm 2 \times 10^{-5}$ s^{-1} at temperatures of 15 K, 10 K and 5 K respectively.[251] The second-order kinetic behaviour suggests a bimolecular process in which two neighbouring ortho-H_2O molecules are involved in the spin-isomer conversion mechanism.[251]

The presence of ^{13}C nuclei in the fullerene cage is shown to not affect the spin-isomer conversion rate of the endohedral H_2O.[251] Furthermore, the magnetic field strength does not affect the spin-isomer conversion rate.[251]

6. $H_2^{17}O@C_{60}$ *Quantum rotor induced polarisation*

The endofullerene $H_2^{17}O@C_{60}$ has been shown to exhibit quantum rotor induced polarization (QRIP) effects.[249] QRIP is a phenomenon in which nuclei can attain high levels of nuclear spin polarisation in solution, if populations of the nuclear spin isomer states are far from thermal equilibrium (see section II H for spin isomerism). In this case, $H_2^{17}O@C_{60}$ is kept at a low temperature (5 K) in order to enrich the para-$H_2^{17}O$ spin isomer. The sample is then rapidly dissolved in ODCB-d_4 at room temperature and the solution state ^{1}H NMR spectrum is monitored. The 6 ^{1}H peaks of $H_2^{17}O@C_{60}$ display a strange pattern of alternating positive and negative peaks with different intensities, see fig. 9. Some of the signals are enhanced (up to $\times 2$) compared with the thermal polarisation of the nuclear spins.[249]

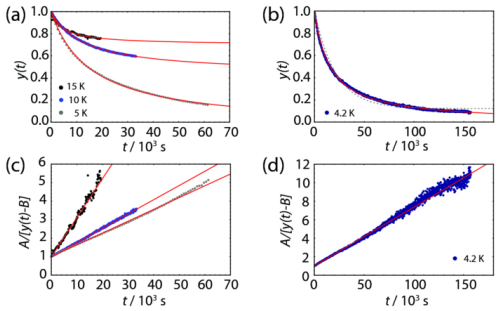

FIG. 8. Integrated normalised ^{1}H NMR signals of $H_2O@C_{60}$, as a function of time, after equilibration at a temperature of 60 K and (a) cooling to 15 K (black dots), 10 K (blue dots), 5 K (gray dots) at a field of 14.1 T and (b) cooling to 4.2 K at a field of 0.86 T. Solid lines are best fits to second order kinetics, eq. 6 in ref. 251. In panel (b), the gray dashed line is the best fit of the experimental points to an exponential decay. Panels (c) and (d) show the data transformed so as to provide straight-line plots for second-order kinetics. Reprinted from (ref. 251) Mamone *et al.*, J. Chem. Phys., **140**, 194306 (2014)., with the permission of AIP Publishing.

This alternating pattern of positive and negative peaks, together with amplitudes larger than thermal polarisation levels, are clear signs of the QRIP effect. The QRIP effect is rather weak here, but in other cases, such as for the rotating methyl group of 4-Methylpyridine (γ-picoline) it can be very strong, enhancing the NMR signal hundreds of times.[252–254] The mechanism of the QRIP effect is complex, involving a combination of nuclear spin isomer imbalance (away from thermal equilibrium) and cross-correlated relaxation effects. Hyperpolarisation builds up in solution as the spin isomer conversion occurs toward thermal equilibrium.[253]

G. $CH_4@C_{60}$ NMR

The chemical shifts of CH_4 in $CH_4@C_{60}$ are $\delta_H = -5.71$ ppm and $\delta_C = -13.63$ ppm (295 K in ODCB-d_4) and the $^1J_{HC}$-coupling of CH_4 is 124.3 ± 0.2 Hz.[103] For ^{13}C (endohedral) chemical shifts of the cage see section V A 1.

The ^{1}H T_1 of $CH_4@C_{60}$ is 1.4904 ± 0.0005 s (295 K in ODCB-d_4) and it decreases monotonically with increasing temperature, indicative of a dominant spin-rotation relaxation mechanism.[103] The ^{13}C T_1 of endohedral CH_4 was measured using polarisation transfer, from ^{1}H to ^{13}C and back to ^{1}H.

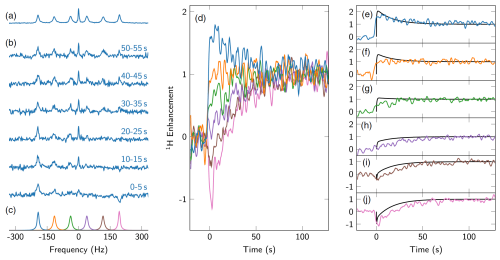

FIG. 9. QRIP Experiment on $H_2^{17}O@C_{60}$. (a) Thermal equilibrium ^{1}H spectrum, recorded after equilibration of the sample (1024 transients averaged). (b) Averages of 20 transients during consecutive intervals after dissolution of the sample. A clear antiphase signal is obtained immediately after the dissolution (0–5 s). The antiphase signal decays, and after approximately one minute the thermal signal is restored. (c) The individual spectra are multiplied with Lorentzian masks that correspond to each of the six peaks, and the product is integrated. (d) Results of the integration after applying a tricube bandwidth reduction of width 2 s. The integrals are normalized by the intensity of the respective thermal ^{17}O peaks. (e)–(j) The same data as in (d), with spin dynamical simulations (black lines). Reprinted figure with permission from (ref. 249) Meier *et al.*, Phys. Rev. Lett., **120**, 266001 (2018). Copyright (2018) by the American Physical Society.

Detection was through the ^{1}H channel, on the two ^{13}C satellites in the ^{1}H spectrum, yielding ^{13}C T_1's of 0.39 ± 0.14 s and 0.55 ± 0.14 s (the difference is likely due to cross-relaxation effects).[103]

The cage ^{13}C T_1 of $CH_4@C_{60}$ was slightly shorter than C_{60}, 17.12 ± 0.05 s and 17.64 ± 0.04 s respectively (298 K, 16.45 T in ODCB-d_4), likely due to additional dipole-dipole relaxation from the endohedral ^{1}H's of CH_4.[110]

1. $^0J_{HC}$ in $CH_4@C_{60}$

Indication of a $^0J_{HC}$ coupling (see section V A 3) is seen in $CH_4@C_{60}$ between the endohedral ^{1}H's and one ^{13}C within the cage.[110] No splitting is observed for the cage ^{13}C resonance of $CH_4@C_{60}$, but the peak linewidth is ∼33% larger than empty C_{60}. Applying weak ^{1}H decoupling on the endohedral protons reduces the broadening of the cage ^{13}C of $CH_4@C_{60}$ by 70 mHz (33%), down to the same linewidth as empty C_{60}. This unambiguously assigns the broadening of the cage ^{13}C in $CH_4@C_{60}$ to a $^0J_{HC}$-coupling interaction with the ^{1}H's on CH_4. The absence of a clear peak splitting is due to the short ^{1}H T_1 of $CH_4@C_{60}$, of 1.465 ± 0.001 s (298 K, ODCB-d_4 and 16.45 T), which "washes" away the spectral splitting due to the scalar relaxation of the second kind mechanism.[110]

H. $CH_2O@C_{60}$ NMR

The solution state NMR of $CH_2O@C_{60}$ is particularly interesting, see fig. 10 for NMR spectra and relaxation measurements. The chemical shifts for endohedral CH_2O are δ_H = 3.75 ppm and δ_C = 197.22 ppm (298 K, ODCB-d_4).[21] Intramolecular $^1J_{HC}$-coupling for endohedral CH_2O is 173.49 ± 0.09 Hz, fig. 10 a. The ^{13}C chemical shift of the $CH_2O@C_{60}$ cage is 143.49 ppm, shifted by +0.684 ppm with respect to empty C_{60} (see section V A 1).[21]

The relaxation behaviour is rather surprising; for endohedral CH_2O the ^{1}H T_1 = 30.65 ± 0.04 s (28.0 ± 0.8 s for $^{13}CH_2O@C_{60}$), whereas the ^{13}C T_1 = 214 ± 13 ms, fig. 10 d & e.[21] The endohedral CH_2O ^{13}C T_1 is monotonically decreasing with increasing temperature (fig. 10 f) and is effectively independent of the magnetic field. From the ^{13}C T_1 field and temperature dependence, it becomes apparent that the dipole-dipole and chemical shift anisotropy relaxation mechanisms play a minor role.[21] This relaxation behaviour can be understood if one considers spin-rotation as the dominant relaxation mechanism. The Frobenius norm, obtained experimentally on gas phase free CH_2O, of the ^{13}C spin-rotation tensor is ∼26 times larger than for ^{1}H. This explains the large difference between the relaxation rates, as the rate is proportional to the square of the Frobenius norm of the tensor. For the cage ^{13}C T_1 there was no significant difference between $CH_2O@C_{60}$ and empty C_{60}.[21]

1. $^0J_{HC}$ in $CH_2O@C_{60}$

A finite ^{0}J-coupling (see section V A 3) is observed in $CH_2O@C_{60}$ between the ^{1}H of CH_2O and the ^{13}C of the cage.[21] No spectral splittings were observed in the ^{1}H or ^{13}C spectra (fig. 10 b) because $^0J_{HC}$ is very small. However, a J-modulated spin echo experiment (fig. 10 c) reveals the magnitude of $^0J_{HC}$ to be 70.6 ± 0.3 mHz at 298 K.[21] This is slightly smaller than the $^0J_{HeC}$ observed in $^3He@C_{60}$ of ∼75 mHz, section V B 2, most likely because each Hydrogen atom in $CH_2O@C_{60}$ has fewer electrons overall to participate in the ^{0}J-coupling compared with the Helium atom in $^3He@C_{60}$. For comparison, the intramolecular $^1J_{HC}$-coupling for endohedral CH_2O is 173.49 ± 0.09 Hz, which is more than three orders of magnitude larger than the $^0J_{HC}$.[21]

VI. EPR

This section discusses EPR (electron paramagnetic resonance) investigations performed on the endohedral species of $N@C_{60}$ and $P@C_{60}$ endofullerenes. C_{60} fullerenes, and corresponding endofullerenes, can be photo-excited to the electronic triplet state, which can be investigated using time-resolved EPR; see section IV D.

Additionally, the NO molecule has been inserted inside open-cage-C_{60}-fullerene and EPR measurements have been carried out on the paramagnetic complex. Since the fullerene

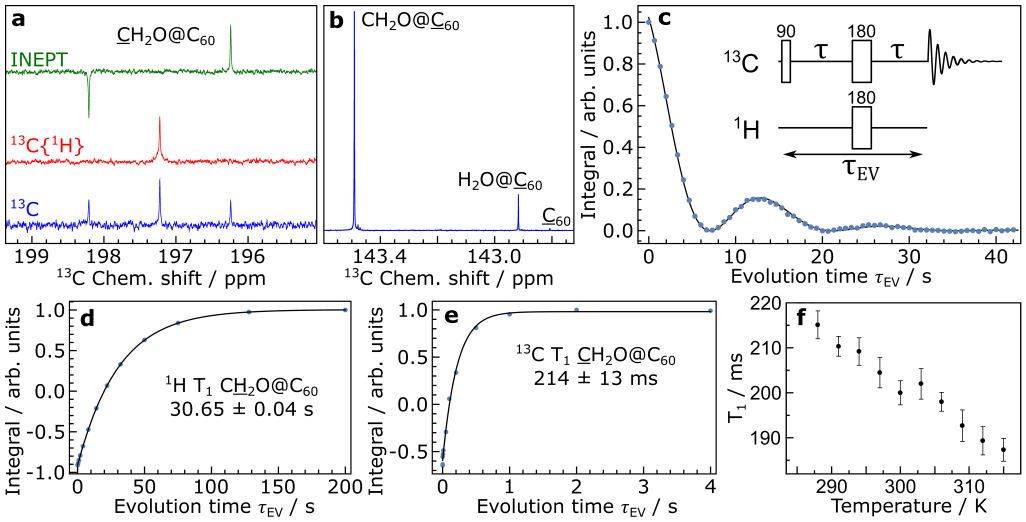

FIG. 10. ^{13}C NMR of natural abundance $CH_2O@C_{60}$ (**a**–**e**). **a** showing the $\underline{C}H_2O$ triplet ^{13}C spectrum, a proton decoupled $^{13}C\{^1H\}$ spectrum and a non-refocused INEPT spectrum with inter-pulse delay of 1.44 ms. **b** expansion of the ^{13}C spectrum around 143 ppm, showing the ^{13}C signals for $CH_2O@\underline{C}_{60}$, $H_2O@\underline{C}_{60}$ and empty $\underline{C}_{60}$. **c** ^{13}C ($CH_2O@\underline{C}_{60}$) NMR signal amplitude modulation following the J-modulated spin-echo sequence shown in the figure [90(^{13}C) – delay – 180(^{13}C, ^{1}H) – delay – Acquire (^{13}C)], acquired with 16 transients. Fitting the modulation gives $|^0J_{HC}| = 70.6 \pm 0.3$ mHz. **d** and **e** Inversion-recovery curves for the T_1 spin-lattice relaxation time constant of CH_2O nuclei in $CH_2O@C_{60}$ for ^{1}H and ^{13}C (central line) respectively. **f** ^{13}C T_1 of the central line of ^{13}C-labelled CH_2O in $^{13}CH_2O@C_{60}$, measured at 16.45 T by inversion recovery as a function of sample temperature, in a 1 mM solution in toluene-d_8. Open access reprint from ref. 21.

was not completely closed back to C_{60} with NO enclosed inside, such studies are not covered in the manuscript; the reader is directed to ref. 106,107 for more information.

A. N@C_{60} EPR

N@C_{60} contains atomic Nitrogen with three unpaired electrons ($S = 3/2$), as P@C_{60} in section VI C. The EPR spectra of ^{14}N@C_{60} and ^{15}N@C_{60} (solid state) can be seen in fig. 11. Sharp lines in the powder EPR spectrum indicate the system is spherically symmetric, so the fine structure and quadrupole interactions are zero, and the g factor and hyperfine interactions are isotropic.[16,82] The hyperfine coupling of N@C_{60} is 1.5 times larger than for the free Nitrogen atom.[16,79] The absence of an electric field gradient indicates the Nitrogen atom is in the centre of the cage, and the electron spin $S = 3/2$ indicates the absence of charge transfer with the cage.[16,255]

1. N@C_{60} *solution EPR*

Pulsed EPR on N@C_{60} in solution (CS_2) at room temperature shows three lines split by the hyperfine interaction of the unpaired electrons with the Nitrogen nucleus (^{14}N I = 1), similar to the solid state EPR spectrum in fig. 11.[255,256] The three lines are very sharp, $0.3 - 1.5\ \mu$T observed experimental linewidth (homogeneous linewidth of $1.5 - 2.5$ kHz), and display unequal intensities due to the second order hyperfine splitting.[255,256] High resolution measurements, instrumental linewidth $< 0.3\ \mu$T, show the outer lines ($M_I = \pm 1$) are further split by 0.9 μT into three lines by the second order hyperfine interaction, $a^2/\omega_e = 26$ kHz.[256] Spectral splittings due to the hyperfine interaction with ^{14}N or ^{15}N are observed, but hyperfine splittings due to ^{13}C nuclei are not detected.[255]

Inversion recovery, of N@C_{60} in CS_2 at room temperature, measured the electron T_1 to be 120(10) μs and a Hahn echo experiment measured the T_2 to be the same.[255] This T_2 corresponds to a 2.5 kHz homogeneous line width, which was approximately a factor of 10 narrower than any observed EPR line until that point.[255] The longest electron T_2 measured for N@C_{60} goes up to 250 μs, being the longest of any molecular electron spin up to that point.[257]

Relaxation measurements (X band) at 300 K in toluene give the electron T_1 120(2) μs and T_2 50(1) μs. Analysing the electron relaxation gives a rotational correlation time of 25 ps and a ZFS (zero field splitting) $|D_{eff}| = 8.5$ MHz.[258]

Modulation of the isotropic hyperfine interaction and spin rotation can be excluded as the dominant relaxation mechanisms. The most likely relaxation mechanism being collision induced cage deformations that lead to fluctuating zero field splittings.[255]

Relaxation measurements of N@C_{60} in CS_2 at different temperatures have been performed.[257] For the central line (M_I = 0) T_1 decreased with increasing temperature ($\sim 500\ \mu$s at 160 K to $\sim 150\ \mu$s at room temperature); and the T_2 was approximately 2/3 of T_1 at all temperatures.[257] The inner and outer peaks ($M_I = 0$ and $M_I = -1$) T_1's are essentially the same at all temperatures. Furthermore, ESEEM (Electron Spin Echo Envelope Modulation) can be used to extract T_2 for the outer coherence ($M_S = \pm 3/2 \leftrightarrow \pm 1/2$), which is approximately 2/3 of the inner coherence ($M_S = +1/2 \leftrightarrow -1/2$) T_2 at all temperatures.[257] The electron T_1 behaviour can be described by an Orbach mechanism; a two phonon mechanism involving a vibrational mode of C_{60} (273 cm^{-1}).[257]

Confining the Nitrogen atom inside C_{60} suppresses most conventional electron relaxation mechanisms: zero-field splitting interaction, anisotropic g matrix, electron-nuclear dipolar coupling and nuclear quadrupole interaction.[257]

The electron T_1 and T_2 of N@C_{60} (toluene at room temperature) become shorter, up to a factor of 10, when in the presence of the nitroxide radical TEMPO.[223]

2. N@C_{60} *solid state EPR*

The Q-band EPR spectrum of N@C_{60} at room temperature is shown in fig. 11. Three lines are seen for endohedral ^{14}N and two lines are seen for ^{15}N, due to the hyperfine splitting with the nuclear spins (I = 1 for ^{14}N and I = 1/2 for ^{15}N).[16] The centre of the ^{14}N@C_{60} triplet has a g factor of 2.0030($\pm$2), which means that there is no orbital contribution to the paramagnetism. The lines are sharp, 16 μT in the X-band and 28 μT in the Q-band at room temperature (22 μT in the X-band at 4 K), indicating that the powder averaging did not lead to significant broadening.[16]

The isotropic hyperfine constants measured in the X-band are 15.97(5) MHz for ^{14}N@C_{60} and 22.35(5) MHz for ^{15}N@C_{60}.[82] The hyperfine coupling of N@C_{60} is 1.5 times larger than for the free Nitrogen atom.[16,79] The hyperfine interaction in atomic Nitrogen (and atomic Phosphorous, section VI C) increases when in confinement. The hyperfine interaction increases monotonically when the confining medium changes as follows: free, Ar matrix, Kr matrix, Xe matrix, C_{70} and C_{60}.[77] The largest hyperfine interaction is observed for N@C_{60}, because the confinement is tightest inside C_{60}, which leads to enhanced orbital overlap between the cage and the endohedral atom.[77]

The g-factor for N@C_{60} (dilute in C_{60}) was measured at room temperature with very high accuracy to be 2.00204(4), with a relative precision of $\sim$20 ppm.[259] This is slightly smaller than gaseous atomic Nitrogen (g = 2.00215) and more similar to matrix-embedded Nitrogen atoms. The deviation from the free electron g-factor is $-138(20)$ ppm, indicating that the Spin-Orbit coupling is mainly responsible for the difference.[259]

Increasing the concentration of N@C_{60} (in C_{60}) leads to much broader EPR lines due to dipolar broadening from interacting (unpaired electrons of the) endohedral N atoms in neighbouring cages.[260] Some weak ($\sim 0.1\%$) sharp peaks are seen on top of the broad features, which are attributed to N@C_{60} cages diffusing on the crystallite surface which average out the dipolar interactions.[260]

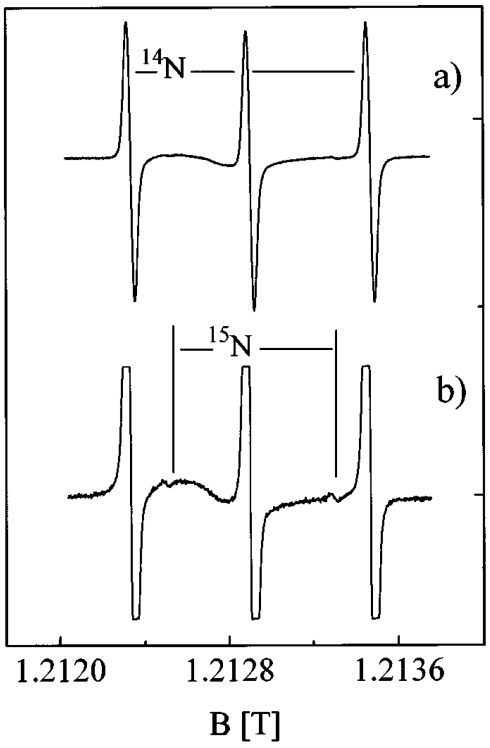

FIG. 11. Q-band EPR spectra of ion bombarded C_{60} measured at room temperature. The lower trace (b) is measured with higher sensitivity than the upper trace (a). The triplet splitting is due to the hyperfine interaction with ^{14}N nucleus I = 1, and the weak doublet to the hyperfine interaction with ^{15}N nucleus I = 1/2. Reprinted figure with permission from (ref. 16) Almeida Murphy *et al.*, Phys. Rev. Lett., **77**, 1075–1078 (1996). Copyright (1996) by the American Physical Society.

At room temperature the C_{60} lattice has $Fm\bar{3}m$ space group symmetry (O_h) and below $\sim$260 K has $Pa\bar{3}$ space group symmetry (S_6), see section IV A 2. Lowering of the symmetry from O_h to S_6 allows for a finite ZFS (zero-field-splitting) interaction. At room temperature (in $Fm\bar{3}m$ space group) the EPR spectrum is composed of sharp lines, but below 258 K a powder spectrum typical for a quartet spin system is observed. The spectrum is fitted with a zero field splitting D = 0.52 MHz.[83,223] At even lower temperatures, the powder features persist but broadening occurs due to the hyperfine interaction with the ^{13}C's, becoming more pronounced as the fullerene cages stop rotating (see section IV A 2). Further-

more, even in the low temperature $Pa\bar{3}$ phase, no quadrupole splittings are observed.[83]

The isotropic hyperfine coupling constant for N@C_{60} increases with temperature. Below 50 K it stays constant at $\sim$ 5.61 Gauss, and above 50 K it increases steadily, up to $\sim$ 5.72 Gauss at 450 K.[82,261] This behaviour can be interpreted as the hyperfine coupling increasing with the mean square displacement of the Nitrogen atom inside the cage. This increases as excited vibrational states of the 3D isotropic harmonic oscillator are populated – i.e. confined translational states, see section II C. This in turn can increase the electron probability at the nucleus, from deformation of the Nitrogen P shell, leading to an increase in the hyperfine coupling.[82,261,262] From this interpretation 18(1) meV is obtained for the energy of the first translational excited state (vibrational states of the 3D isotropic harmonic oscillator); which is comparable with measurements on the other C_{60} endofullerenes, see translational energies in section VII.[82,261]

Relaxation measurements of solid N@C_{60} diluted in C_{60} (W-band) show that the electron T_1 decreases with increasing temperature, from $\sim$ 10 ms at 10 K to $\sim$ 1 ms at 300 K.[263] The electron T_2 also displays a (weak) shortening with increasing temperature ($\sim$20 μs at 50 K to $\sim$10 μs at 300 K). Furthermore, for T_2 there is a sharp drop at 160 K that forms a dip, ascribed to a resonance between the C_{60} molecular reorientation jump frequency and the size of the zero-field splitting.[263]

The electron T_1 of ^{15}N@C_{60} (diluted in C_{60}) is found to depend on the applied magnetic field; relaxing faster at the X-band (9.5 GHz) compared with the W-band (94 GHz).[264] At low temperatures < 30 K the relaxation rates are comparable, and below 20 K the X-band is in fact relaxing a little slower than the W-band. At room temperature, relaxation becomes up to three times faster for X-band.[264]

Relaxation in the solid can be modelled as being dominated by fluctuations of the hyperfine interaction caused by the translational degrees of freedom of N inside the cage (i.e. vibrational motion of the 3D isotropic harmonic oscillator); with the fluctuating fine structure contribution to relaxation playing a minor role.[263]

Another interpretation of the N@C_{60} electron spin relaxation combines the Spin-Orbit interaction of the N 2p electrons and the coupling of these electrons with the C_{60} vibrations (H_g); giving a good match with experiments.[265] Relaxation occurs due to a two-phonon Raman process by absorbing one phonon and emitting another with approximately the same energy.[265] This interpretation is different from the Orbach process seen in section VI A 1.[257,265]

3. N@C_{60} *ENDOR*

The ENDOR (Electron nuclear double resonance, section III A 3)[168,169] spectrum of solid N@C_{60} is reminiscent of solution state measurements, displaying very sharp lines. At 80 K the ENDOR peaks for ^{14}N are very sharp, with a line width of 4 kHz, indicating the absence of anisotropic hyperfine and nuclear quadrupole interactions.[83]

ENDOR measurements on ^{14}N@C_{60} clearly prove that the total electron spin is S = 3/2. ENDOR measurements estimate the hyperfine interaction between the nuclear and electron spins to be 15.730 MHz for ^{14}N@C_{60} and 22.021 MHz for ^{15}N@C_{60}.[16,266] The ^{14}N to ^{15}N hyperfine interaction ratio matches the ratio between the nuclear magnetic moments. The ^{14}N@C_{60} hyperfine coupling is approximately 50% larger than for atomic Nitrogen, which can be understood in terms of admixtures of translational excited states caused by the encapsulation in C_{60}, see also section VI A 2 (and section II C for background).[16]

The ^{13}C nuclei are also detected by ENDOR, and it shows them to be weakly coupled to the electron spins.[16] At room temperature C_{60} rotate rapidly in the lattice (section IV A 2) and average out anisotropic interactions, which allows for an isotropic hyperfine splitting constant of 32(1) kHz to be estimated. This small value indicates that the electron spin density of endohedral nitrogen within the cage is small.[83]

4. N@C_{60} *liquid crystal solution EPR*

EPR measurements of N@C_{60} and N@C_{70} were performed in a liquid crystal matrix of N-(4-methoxybenzylidene)-4-butylaniline (MBBA).[267–270] In both cases the N atom has 3 unpaired electrons with total spin S= $3/2$.

The EPR lines of N@C_{60} and N@C_{70} in liquid crystal solutions are much broader than in isotropic solutions. The most likely explanation is the faster relaxation caused by the appearance of finite fine-structure couplings.[268]

Such measurements show that C_{70} molecules (with endohedral N) can be partially aligned by a liquid crystal matrix, which partially aligns with respect to an externally applied magnetic field.[267–269] This is seen as the appearance of zero-field splittings in the EPR spectrum due to incomplete averaging of fine-structure spin-spin couplings, from the partially aligned endofullerene molecules, see fig. 12. In the nematic phase, spectral splittings of $70 - 170$ kHz are observed (X-band). These change sign with temperature due to the temperature dependence of the order parameter, with the largest splitting seen at the lowest temperature of $\sim$280 K.[267] For C_{70} this is expected since the cage itself has an inherent anisotropic (elongated) shape, which can be aligned by the liquid crystal matrix.[267–269]

However, N@C_{60} also shows a zero-field splitting for the endohedral N in a liquid crystal matrix, regardless of the highly symmetric (nearly spherical) C_{60} cage. This is again due to the partially averaged fine-structure spin-spin interactions of the 3 unpaired electrons. The splittings for N@C_{60} are about $4 - 5$ times smaller than for N@C_{70}.[267–269] Fig. 12 shows the splitting of the central ($M_I = 0$) EPR line for N@C_{60} and N@C_{70} in the nematic phase of MBBA at 296 K: much larger splitting is observed for N@C_{70}.[269]

The icosahedral symmetry of the C_{60} cages should cause the zero-field splitting to vanish. The observation of zero-field splittings for N@C_{60} in a liquid crystal matrix indicates that the environment at the endohedral N atom is anisotropic. This can be achieved through a distortion of the C_{60} by the liquid crystal matrix = indirect effect. Or through a direct effect of

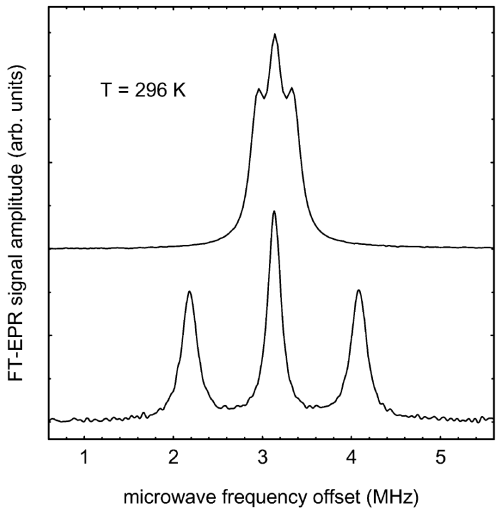

FIG. 12. Comparison of the central EPR ($M_I = 0$) hyperfine component of $N@C_{60}$ (upper trace) and $N@C_{70}$ (lower trace), measured in the nematic phase of MBBA at 296 K. For these transitions line splittings result exclusively from orientational order of the ZFS tensor, thus proving the existence of a non-vanishing order parameter for both compounds. Used with permission of Royal Society of Chemistry, from (ref. 269) Dinse, Phys. Chem. Chem. Phys., **4**, 5442–5447 (2002); permission conveyed through Copyright Clearance Center, Inc.

the liquid crystal matrix onto the endohedral atom, effectively imposing the anisotropic environment regardless of the presence of the C_{60} cage (i.e. through the cage).[267–269] The same observation is made for nuclear spin interactions when molecular C_{60} endofullerenes are placed in a liquid crystal matrix, see section V D 3 & V E 2 & V F 3.

Chemical derivatives of $N@C_{60}$ have also been studied in liquid crystals. These also show preferential alignment in a liquid crystal matrix, with differences depending on the nature of the derivative compound.[270]

5. $N@C_{60}$ *in carbon nanotubes EPR*

$N@C_{60}$ dilute in C_{60} (i.e. $N@C_{60}$:C_{60}) have been inserted inside single wall carbon nanotubes (SWCNT) to form ($N@C_{60}$:C_{60})@SWCNT peapods.[271–276] $N@C_{60}$ is found to be more stable inside the SWCNT than in crystalline form, with the endohedral nitrogen escaping at higher temperatures.[276] The signature $N@C_{60}$ EPR signal is observed from such materials.[271,272] The hyperfine coupling is not changed upon encapsulation in the SWCNT.[271,274] The EPR signals are much broader than pristine $N@C_{60}$; the reason could be due to magnetic impurities in the SWCNT causing inhomogeneous magnetic fields or due to cage distortions induced by the SWCNT.[271,272,274] Sharper EPR lines are obtained when the SWCNT are more pure (prepared by chemical vapour deposition).[275] Electron relaxation is much faster and bi-exponential in ($N@C_{60}$:C_{60})@SWCNT than pristine $N@C_{60}$:C_{60}.[272,273,276] The electron T_1 drops drastically around 100 K, forming a dip in the T_1 curve against temperature. This effect is not explained at the moment, but must involve the dynamics of the fullerene cages encapsulated in SWCNT.[273]

6. $N@C_{60}$ *DNP*

Dynamic Nuclear Polarisation (DNP) is a technique that transfers spin polarisation from the electron to nuclear spins. Thus, hyperpolarisation of the nuclear spins can be achieved, with polarisation levels reaching up to $\sim$100%.

Nuclear spin hyperpolarisation was achieved for endohedral ^{15}N using DNP on $^{15}N@C_{60}$ (in toluene-d_8 at 8.6 T). Using the Overhauser DNP mechanism at 4.2 K, a ^{15}N nuclear polarisation of $21 \pm 2\%$ can be achieved.[277] Employing a new DNP approach called PONSEE (polarisation of nuclear spins enhanced by ENDOR), the ^{15}N polarisation is increased to $62 \pm 2\%$ (enhanced 1100 ± 50 times), at 3 K.[277]

DNP was performed on the ^{13}C nuclei using $^{14}N@C_{60}$ (diluted in C_{60}) under magic angle spinning (MAS). The DNP solid effect is found to be the polarisation transfer mechanism, achieving ^{13}C enhancement factors of approximately 5-fold at 100 K.[278] The enhancement level is found to increase with faster spinning speeds. The electron-driven spin diffusion (EDSD) mechanism is proposed for this system.[278] The DNP enhancement of the ^{13}C nuclei can be up to 12% larger when frequency-chirped microwaves are used for electron decoupling.[279]

B. $(He \cdot N)@C_{60}$ & $(He \cdot N)@C_{70}$ EPR

Multiple species can be inserted inside fullerene cages. This was shown for C_{60} and C_{70} where Helium and atomic Nitrogen are inserted to produce $(He \cdot N)@C_{60}$ and $(He \cdot N)@C_{70}$. In such cases, molecular surgery is used first to make $He@C_{60}$ or $He@C_{70}$, then atomic Nitrogen is introduced using plasma methods.[27]

Both endohedral atoms are detected through single crystal X-ray diffraction measurements, on a co-crystal of $(He \cdot N)@C_{60}$ and nickel(II) octaethylporphyrin.[27]

The EPR spectra of endohedral Nitrogen are broader in $(He \cdot N)@C_{60}$ and $(He \cdot N)@C_{70}$ than in $N@C_{60}$ and $N@C_{70}$. Most likely because the additional Helium atom breaks the symmetry, which can introduce fine-structure splittings of the spin $S = 3/2$ system.[27]

The observed hyperfine couplings of endohedral Nitrogen are 5.99 G for $(He \cdot N)@C_{60}$ (cf. 5.67 G for $N@C_{60}$) and 5.59 G for $(He \cdot N)@C_{70}$ (cf. 5.38 G for $N@C_{70}$). This shows that the hyperfine coupling increases with tighter confinement, since the extra Helium atom is inert and does not interact magnetically with the Nitrogen.[27]

C. P@C_{60} EPR

$P@C_{60}$ contains atomic Phosphorus with three unpaired electrons ($S = 3/2$), as $N@C_{60}$ in section VI A. The hyperfine interaction of endohedral ^{31}P is 2.5 times larger than for the free atom.[78,79]

1. P@C_{60} *solution EPR*

X-band solution EPR of $P@C_{60}$ shows two signals separated by 49.2 G, caused by an isotropic hyperfine interaction of the electron spins with the ^{31}P spin $1/2$ nucleus.[77] The hyperfine interaction of the endohedral ^{31}P is 2.5 times larger than for the free atom.[78,79]

The hyperfine interaction in atomic Phosphorous (and atomic Nitrogen, section VI A) increases when in confinement; the increase is steady when changing the confining medium as follows: free, Ar matrix, Kr matrix, Xe matrix, C_{70} and C_{60}.[77] The largest hyperfine interaction is seen for confinement inside C_{60}, due to the increased orbital overlap between the cage and the endohedral atom.[77] For this reason, since Phosphorus is larger than Nitrogen, confining Phosphorous in C_{60} leads to a larger increase (relative to free atom) in the hyperfine interaction as compared with $N@C_{60}$ (section VI A).[77]

X-band EPR spectrum in toluene shows an additional 36 μT splitting of each signal into 3 components, due to the second order hyperfine interaction of an electron spin $S = 3/2$ system with the ^{31}P nucleus.[77,78] The second order hyperfine coupling is observed because the isotropic hyperfine interaction is large in $P@C_{60}$ and the resulting splitting is larger than the homogeneous line widths of the peaks.[77,78] This second order hyperfine splitting is much smaller in $N@C_{60}$ (by ~ 40) because the hyperfine interaction squared is much smaller for $N@C_{60}$, see section VI C.[77]

The outer components of the three peaks (split by the second order hyperfine coupling) are broader than the central component by a factor of 1.6(2).[78] Lowering the temperature further broadens the outer peaks and they become undetectable.[78] This behaviour is consistent with a relaxation caused by a modulation of the zero field splitting (ZFS).[78] Furthermore, the modulation occurs from collisions of the cage with solvent molecules, and this translational diffusion of the solvent depends on its viscosity.[78] From solution state relaxation measurements the D_{eff} is obtained as 61.7 MHz, which is about an order of magnitude larger than for $N@C_{60}$ (see ref. 255 and section VI C).[78] The electron T_1 in toluene at RT is 1.0(2) μs.[78] No hyperfine splitting from the ^{13}C nuclei was observed, putting an upper limit of 0.05 mT.[78]

2. P@C_{60} *solid state EPR*

For solid state EPR of $P@C_{60}$, dilute in C_{60} powder at RT, only the first order hyperfine splitting with the ^{31}P spin $1/2$ nucleus is observed, of 49.2 G.[77] The outer components of the second order hyperfine splitting are too broad to detect.[78] The hyperfine interaction of the endohedral ^{31}P is 2.5 times larger than the free atom.[78,79]

The hyperfine coupling of $P@C_{60}$ is rather constant below 50 K, but as the temperature increases, the hyperfine coupling steadily increases.[79] This behaviour can be understood as follows: the confined endohedral phosphorous atom behaves like a 3D isotropic harmonic oscillator and as the temperature increases, the excited states become more populated. These excited states (and/or collisions) increase the electron probability at the nucleus, which leads to an increase in the hyperfine coupling; the same phenomenon is observed for $N@C_{60}$ (see section VI A 2). This model for the endohedral phosphorus atom predicts a vibrational splitting of the 3D isotropic harmonic oscillator levels of 125(10) cm^{-1}.[79] This energy is comparable with measurements on the other C_{60} endofullerenes, see translational energies in section VII.[82,261]

Derivatives of $P@C_{60}$ that incorporate side chains, covalently attached to the cage, acquire anisotropic hyperfine interactions.[280]

D. N@C_{60} & P@C_{60} single (co)crystal: EPR

$N@C_{60}$, $N@C_{70}$ and $P@C_{60}$ have been incorporated into a solid state matrix of BrPOT [2,4,6-tris-(4bromophenoxy)-1,3,5-triazine] by co-crystallisation; producing hexagonal and rhombohedral crystals.[281,282] The EPR line-widths are inhomogeneously broadened due to the BrPOT protons and the co-included solvent. The electron relaxation properties of $P@C_{60}$ do not change significantly upon incorporation in BrPOT.[281,282]

Inclusion in the solid state BrPOT matrix lifted, in some cases completely, the degeneracies of the EPR transitions. This allows each state to be accessed individually, with potential applications to quantum computing.[281,282] The splitting is due to the fine-structure interactions, which are non-zero due to symmetry lowering in the BrPOT matrix, probably caused by fullerene cage distortions. Furthermore, the magnitude of the splittings depends on the solvent used for co-crystallisation.[281,282]

E. N@C_{60} & P@C_{60} quantum computing: EPR

Due to their exquisite spin properties, e.g. extremely long relaxation times, $N@C_{60}$ and $P@C_{60}$ have been proposed as ideal qubits for quantum computing – by using the spin states of the unpaired electrons as qubits.[117–124] Many such studies have been published in the literature claiming that $N@C_{60}$ is an ideal qbit for quantum computing; 50 and 30 Rabi oscillations have been observed for $N@C_{60}$ and $P@C_{60}$ respectively.[117–124] These molecules are promising for quantum technologies, and could someday lead to a fullerene based quantum computer.[117–124]

1. $N@C_{60}$ *single molecule detection: NV centres*

Single electron spin readout and control was demonstrated for $N@C_{60}$ using NV (Nitrogen vacancy) centres in diamond (at 4.7 K).[283] The strong electron dipolar interaction between $N@C_{60}$ and the NV centre allowed the detection and control of Rabi oscillations for a single $N@C_{60}$ molecule.[283] Such results can have large implications for the development of quantum computing.

F. $H_2@C_{60}$ EPR

1. *Chemical derivatives of* $H_2@C_{60}$*: ENDOR*

ENDOR (Electron nuclear double resonance, section III A 3)[168,169] measurements have been performed on $H_2@C_{60}$ which has a pyrrolidine radical anion covalently attached to the fullerene cage.[243] Small isotropic and anisotropic hyperfine couplings of the endohedral H_2 with the unpaired electron on the pyrrolidine side chain have been measured at low temperatures ($50-100$ K).[243]

2. $H_2@C_{60}$ & $D_2@C_{60}$ *time-resolved EPR*

The C_{60} fullerene cage can be excited to an electronic triplet state with strong laser irradiation, see section IV D. The same applies to the cage of endofullerene molecules. If the lifetime of the electronic triplet state on the fullerene cage is long enough, time-resolved EPR measurements can be performed on the unpaired electrons.

Time-resolved EPR was performed on the electronic triplet state of the fullerene cage in C_{60}, $H_2@C_{60}$ and $D_2@C_{60}$ (in benzene at 285 K).[231] These measurements do not show any significant differences in the time-resolved EPR spectra between C_{60}, $H_2@C_{60}$ and $D_2@C_{60}$. Furthermore, no differences were observed in the electronic T_1 and T_2 time constants of the three species.[231]

Similarly, no differences are observed between the time-resolved EPR spectra of the photo excited triplet states of C_{60} and $H_2@C_{60}$ at 20 K.[230]

a. $H_2@C_{60}$ & $D_2@C_{60}$ *time-resolved ENDOR*

ENDOR experiments (20 K) detect a small hyperfine coupling tensor of the photo-excited electronic triplet state on the fullerene cage with the endohedral ortho-H_2 molecule. The resulting components of the hyperfine tensor are: $A_{xx} = 0.25$ MHz, $A_{yy} = 0.75$ MHz and $A_{zz} = -1.05$ MHz.[230] Much larger hyperfine couplings are detected between the photo excited triplet state on the fullerene and exohedral ^{1}H & ^{31}P spins when side chains, containing ^{1}H & ^{31}P, are covalently attached to the fullerene cage.[230]

VII. MOLECULAR MOTION SPECTROSCOPIES: THZ, INS, IR AND RAMAN

This section covers spectroscopic investigations that probe molecular (and atomic) motions: translational, rotational and vibrational (see section II). The relevant spectroscopic techniques are: THz spectroscopy, Inelastic Neutron Scattering (INS), Infrared spectroscopy (IR) and Raman spectroscopy (see section III).

INS and IR measurements have been performed on open cage C_{60} endofullerenes with H_2, CH_4 and even NH_3 inside.[149,153] However, only fully closed C_{60} endofullerenes are discussed here.

A. $He@C_{60}$ molecular motion

The simplest noble gas endofullerene, $He@C_{60}$, displays a rich spectral signature of the endohedral Helium atom due to translational quantisation. This effect has been probed using THz (far-IR)[110–112] and INS[110,111,113].

1. $He@C_{60}$ *THz*

Astonishingly, the $He@C_{60}$ molecular complex can absorb THz light and translationally excite the endohedral Helium atom, although neither the C_{60} molecule nor the Helium atom possess permanent electric dipole moments. The $He@C_{60}$ acquires an induced dipole moment that is proportional to the displacement of the Helium atom from the centre of the C_{60} cage. However, THz absorption is weak since the electric dipole moment is induced and not permanent.[110–112]

THz spectra of solid powders are seen in fig. 13 for $^3He@C_{60}$ (a) and $^4He@C_{60}$ (b), at 5 K and 125 K (100 K).[110–112] Both sets of measurements look very similar, with a shift in energy between the $^3He@C_{60}$ and $^4He@C_{60}$ spectra, due to the different masses of the Helium isotopes. This is consistent with the mass of the endohedral Helium atom: higher energy transitions appear for the lighter ^{3}He isotope. At 5 K only the fundamental peak is visible (96.8 cm^{-1} for $^3He@C_{60}$ and 81.4 cm^{-1} for $^4He@C_{60}$), which represents a transition from the translational ground state to the first translational excited state.[110–112]

The fundamental peaks for both $^3He@C_{60}$ and $^4He@C_{60}$ exhibit a very small splitting of < 1 cm^{-1}, see fig. 13. This splitting cannot exist in I_h symmetry, but can be correlated with the different P and H orientations of C_{60} at low temperature, see sections IV A 2 and IV C. The amplitude ratio of the fundamental peak subcomponents matches the P:H ratio of C_{60}.[110–112] Thus, each P and H orientation could give rise to slightly different confining potentials, with slightly different translational eigenstates.[110–112] Therefore, the two subcomponents could arise from two slightly different confining potentials and not from a splitting of translational eigenstates.

As the temperature increases, the fundamental peak decreases in intensity and a comb of other transitions appears;

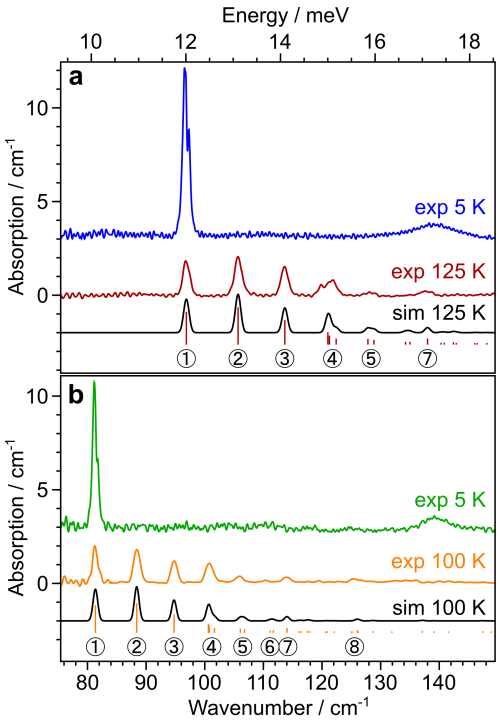

FIG. 13. THz spectra of He@C_{60}. **(a)** THz absorption spectra of ^{3}He@C_{60} at 5 K (blue) and 125 K (red). **(b)** THz absorption spectra of ^{4}He@C_{60} at 5 K (green) and 100 K (orange). Short vertical bars indicate the predicted positions of the terahertz absorption peaks, for the radial potential energy function specified in table V, and their height is proportional to the absorption area. Black curve is the sum of gaussian peaks with position and area defined by the vertical bars. THz peaks are numbered according to the transition assignments in figure 15 (b). Open access reprint from ref. 111.

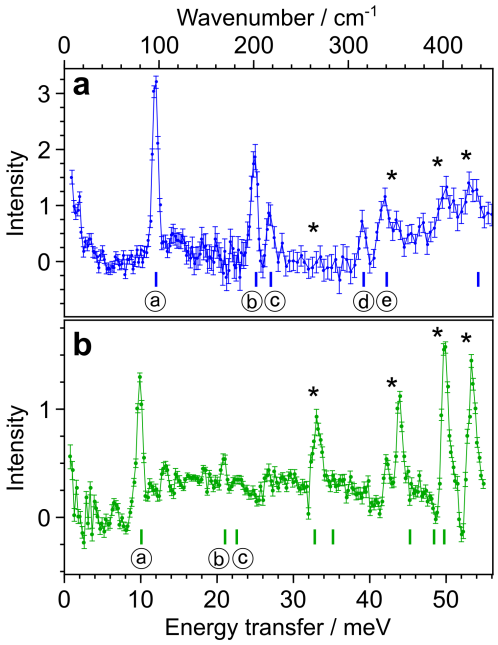

FIG. 14. Inelastic neutron scattering (INS) of He@C_{60}. **(a)** INS spectrum of ^{3}He@C_{60} at 2.7 K (blue). **(b)** INS spectrum of ^{4}He@C_{60} at 2.7 K (green). Spectra are shown as weighted differences between the scattering of He@C_{60} and pure empty C_{60}, with weighting factors adjusted for best subtraction of the C_{60} background. The short vertical bars indicate the predicted position of the INS peaks for the quantised He motion, under the radial potential energy function specified in table V. The INS peaks are labelled according to the transition assignments in figure 15 (b). The peaks above ~ 250 cm^{-1} and marked by asterisks are due to scattering from the C_{60} cages, whose modes are slightly modified in frequency by the presence of endohedral He. Open access reprint from ref. 111.

see fig. 13. Such a comb of transitions would not be possible for a harmonic oscillator (all transitions would have the same energy), so an-harmonic corrections to the confining potential are necessary to explain the spectra.[110–112] In fig. 13 fitted simulations of the THz spectra are shown to reproduce the experimental data very well. Such simulations use a polynomial oscillator, which gives rise to the confining potential and energy level diagram in fig. 15, described in section VII A 3.[110–112] The peaks labelled with numbers in fig. 13 correspond to the transitions shown in fig. 15.

2. He@C_{60} *INS*

Translational quantisation of He@C_{60} can also be probed using INS.[110,111,113,180] Neutron scattering of Helium nuclei is challenging as the scattering cross-section is very small, compared with ^{1}H.[159] Furthermore, ^{3}He is a strong neutron absorber, making INS experiments difficult; such a challenge can be overcome by using thin samples.

The INS spectra are shown in fig. 14 for ^{3}He@C_{60} (a) and ^{4}He@C_{60} (b), at 2.7 K. Similarly to the THz spectra (section VII A 1), a shift in energy is seen due to the difference in mass of the endohedral Helium isotopes (the lighter ^{3}He displays higher energy transitions).[110,111,113,180]

The peaks labelled with letters correspond to translational transitions of the endohedral Helium atom. All transitions originate in the ground state at 2.7 K; and because INS essentially does not have selection rules, transitions to all excited states are possible.[110,111,113] Peak assignment is described in section VII A 3 and fig. 15 where the confining potential and the annotated energy level diagram are shown. Additional

^{3}He@C_{60} INS hot-band transitions and their assignment can be found in ref. 113,180. Modelling the Q-dependence of the fundamental INS transition requires introducing the Debye-Waller factor of the C_{60} lattice.[113,180]

In fig. 14 transitions marked with asterisks correspond to the C_{60} cage modes (phonons, vibrations, etc.). The fig. 14 spectra are obtained by subtracting an empty C_{60} measurement (assumed as background), but some dispersion type features are still visible for the cage modes. This is because the Helium encapsulation leads to a slight change in the vibrational modes of the cage, and the subtraction does not perfectly cancel out the peaks. This seems to scale with the mass of the endohedral Helium, and it appears even more pronounced for Ne@C_{60} which contains the even larger and heavier endohedral Ne, see section VII B 2.[110,179] Similar effects are seen in IR and Raman measurements of Ar@C_{60} (section VII C) and Kr@C_{60} (section VII D).

3. He@C_{60} *confining potential*

For more information on translational quantisation, encountered in endofullerenes, see section II C. The dynamics of the endohedral Helium atom are modelled as a 3D spherically symmetric polynomial oscillator, with the confining potential $V(r)$:

$$V(r) = V_2\, r^2 + V_4\, r^4 + V_6\, r^6 \tag{32}$$

where V_2, V_4, V_6 are coefficients of the potential and r is the distance of the endohedral atom away from the centre of the C_{60} cage.[111–113,179,180]

The energy level structure is obtained by finding the parameters of the potential that best fit the experimental spectra; see fitted THz simulations in fig. 13. Fig. 15 shows: (a) the confining potentials obtained for ^{3}He@C_{60} & ^{4}He@C_{60}, and (b) the energy level diagram annotated with transitions observed experimentally.[111–113] Here the THz transitions are marked with numbers (black) and the INS transitions are marked with letters (blue). THz transitions have the selection rule $\Delta L = \pm 1$, whereas INS does not have any selection rules in this case.[111–113] Additional ^{3}He@C_{60} INS hot-band transitions and their assignment can be found in ref. 113,180.

The confining potential parameters for the endohedral ^{3}He and ^{4}He atoms are fitted separately, from the THz data, with values given in table V. The confining potential parameters are the same for the two isotopes. The only difference in the simulations is the different masses of the endohedral Helium isotopes; this further proves the reliability of the obtained parameters.[110–112]

This procedure allows the non-bonded interaction potential between the endohedral noble gas atom and the inner surface of the C_{60} to be determined experimentally.[110–113] The obtained parametrised confining potential is model-free and has been used to benchmark quantum chemistry calculations; calculations which are aimed at accurately describing non-covalent interactions. [110–113] Such non-covalent interactions are difficult to obtain experimentally; they are usually obtained for gas phase species in molecular beams. Endofullerenes offer the possibility of experimentally extracting non-bonded interactions in condensed phases. Furthermore, the method shown for the He@C_{60} non-bonded potential gives the entire potential energy surface (within the measured range).[110–112]

TABLE V. ^{4}He@C_{60} and ^{3}He@C_{60} THz data fitting results. Best fit polynomial coefficients and confidence limits for the radial potential function $V(r) = V_2\, r^2 + V_4\, r^4 + V_6\, r^6$ and induced dipole moment parameters A_1 and A_3. Reproduced from ref. 111,112 (open access).

Parameter	^{3}He@C_{60}	^{4}He@C_{60}
V_2 / meV pm^{-2}	$(2.500 \pm 0.015) \times 10^{-3}$	$(2.46 \pm 0.04) \times 10^{-3}$
V_4 / meV pm^{-4}	$(3.64 \pm 0.03) \times 10^{-7}$	$(3.77 \pm 0.08) \times 10^{-7}$
V_6 / meV pm^{-6}	$(2.560 \pm 0.017) \times 10^{-11}$	$(2.46 \pm 0.06) \times 10^{-11}$
A_1 / D pm^{-1}	$(3.83 \pm 0.10) \times 10^{-4}$	$(3.73 \pm 0.22) \times 10^{-4}$
A_3 / D pm^{-3}	$(1.7 \pm 0.3) \times 10^{-8}$	$(2.3 \pm 0.6) \times 10^{-8}$

B. Ne@C_{60} molecular motion

1. Ne@C_{60} *THz*

The experimental THz spectrum of Ne@C_{60} displays translational excitations of the endohedral Ne atom, similar to He@C_{60} (section VII A 1). The spectrum is seen in fig. 16, where the fundamental transition appears at 56.6 cm^{-1}, and with increasing temperature the peak broadens on the higher energy side.[179] This is because of the an-harmonicity of the interaction potential between the endohedral Neon atom and the inner carbon surface. Unlike the He@C_{60} case (section VII A 1), a comb of peaks is not seen in the spectrum. This is because the hot-band peaks are not as far apart in energy as for He@C_{60}; and this means that the interaction potential is not as an-harmonic as for He@C_{60}.[110,179]

The frequency of the fundamental transition of Ne@C_{60} shifts to higher energy with increasing temperature (fig. 16 inset).[179] This phenomenon is not currently understood, although it is postulated that the Ne translational modes might be interfering with the inter-molecular lattice phonon modes of the fullerene lattice. The C_{60} inter-molecular lattice modes appear below $\sim$70 cm^{-1} and this shift could be more pronounced for Ne@C_{60} since the fundamental translational transition is at 56.6 cm^{-1}, whereas for all the other noble gases it is above 80 cm^{-1}.[110,111,113,179] This is seen in the INS spectrum of Ne@C_{60}, ref. 110 and the SI of ref. 179, where the fundamental transition of Ne@C_{60} is observed on the edge of the inter-molecular lattice modes of C_{60}.

Fitting the experimental spectrum determines the confining potential parameters for Ne@C_{60}, section VII E.[179]

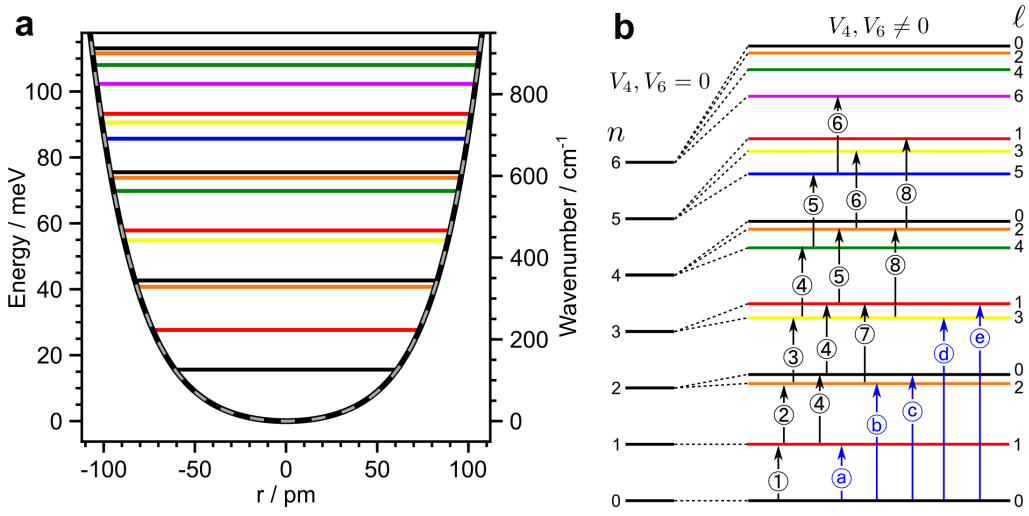

FIG. 15. **(a)** The radial potential energy functions $V(r)$ for ^{3}He in C_{60} (solid black curve) and for ^{4}He in C_{60} (dashed grey curve), together with the quantised energy levels for ^{3}He. The ^{3}He and ^{4}He potential curves are superposed within this energy range. The best-fit polynomial coefficients are given in table V. **(b)** Energy levels of the confined ^{3}He atoms, labelled by the quantum numbers n and ℓ. The energy levels for a harmonic oscillator are shown on the left. The non-zero V_4 and V_6 terms break the degeneracies of states with the same n but with different ℓ. All levels are $(2\ell+1)$-fold degenerate. The transitions observed in THz spectroscopy are labelled by circled numbers in black, and correspond to the peaks in figure 13. The transitions observed in INS are labelled by circled letters in blue, and correspond to the peaks in figure 14. Colours are used to indicate the ℓ values of the energy levels. Open access reprint from ref. 111. To be consistent with the rest of the document, replace $\ell \to L$ and $n \to N$.

2. Ne@C_{60} *INS*

The INS spectrum of Ne@C_{60} is observed experimentally[110,179], despite the weakly scattering Ne nucleus, similar to He@C_{60}. The spectrum shows the fundamental transition of endohedral Neon at ∼7 meV (56.46 cm^{-1}) which perfectly overlaps with the THz transition at 56.6 cm^{-1}, see ref. 110,179 for spectra.

In the INS spectrum of Ne@C_{60} dispersion shapes are seen for the C_{60} modes; which arise when the empty C_{60} INS signal is subtracted from Ne@C_{60}. The dispersion shape appears due to imperfect cancellation of the C_{60} cage modes, because the cage modes for Ne@C_{60} are slightly shifted in energy upon Neon encapsulation.[110,179] The size of this effect seems to scale with the mass of the endohedral noble gas atom: smallest for ^{3}He, in-between for ^{4}He and largest for Ne, see section VII A 2.[110,111,179] Similar shifts of the fullerene cage modes upon noble gas encapsulation are also seen in IR and Raman measurements of Ar@C_{60} (section VII C) and Kr@C_{60} (section VII D).

C. Ar@C_{60} molecular motion

1. Ar@C_{60} *THz*

Ar@C_{60} presents THz absorption peaks due to the endohedral species, just as He@C_{60} and Ne@C_{60}. At low temperature, the fundamental translational transition is observed at 91.1 cm^{-1}.[179] With increasing temperature, the absorption becomes broader and acquires more intensity on the higher energy side. This is because of the an-harmonicity of the interaction potential. The Ar@C_{60} THz spectrum is very similar to Ne@C_{60}, displaying a small an-harmonic contribution compared with He@C_{60}.[179]

Fitting the experimental spectrum determines the confining potential parameters for Ar@C_{60}, section VII E.[179]

2. Ar@C_{60} *IR*

The IR cage vibrations for Ar@C_{60} have been measured at room temperature in the solid powder.[284] The IR active cage modes are shifted for the endofullerenes compared with empty C_{60}. Generally, the lower energy vibrational modes (below ∼600 cm^{-1}) are blue-shifted, whereas the higher energy vibrations are red-shifted. The observed shifts are 0.5 –

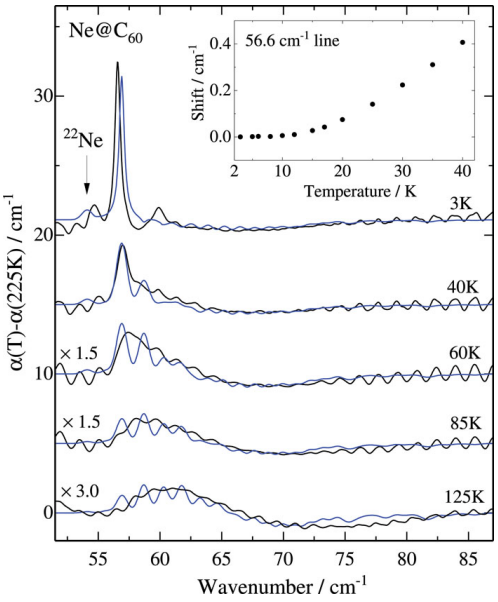

FIG. 16. THz differential absorption spectra of Ne@C_{60} at different temperatures (black) and the differential spectra calculated with the best fit parameters from table VI (blue). The line shape is assumed to be Lorentzian at 3 K (FWHM = 0.5 cm^{-1}) and Gaussian (FWHM = 1.0 cm^{-1}) for temperatures of 40 K and higher. The intensities of the 60, 85, and 125 K differential spectra have been multiplied by factors of 1.5 and 3. The inset shows the temperature dependence of the main peak frequency shift, $\omega_{01}(T) - \omega_{01}(3\ K)$, between 3 and 40 K. Open access reprint from ref. 179.

2.0 cm^{-1} and the sign of the shifts can be correlated with the nature of the C_{60} vibration: vibrations with radial character are blue shifted, whereas vibrations with tangential character are red shifted.[284] Since the shifts are small, they indicate that the endohedral noble gas atoms do not significantly perturb the C_{60} fullerene cage.

Quantum chemistry (DFT) calculations give good predictions for the magnitude of the shifts, but do not correctly predict all the signs.[284] Such cage vibrational shifts induced by the encapsulation have been used to benchmark quantum chemistry calculations involving non-covalent interactions.[108]

3. Ar@C_{60} *Raman*

Raman cage vibrations for Ar@C_{60} have been measured at room temperature in the solid powder.[284] The Raman active cage modes are shifted for the endofullerenes compared with C_{60}. Generally, the lower energy vibrational modes (below ∼600 cm^{-1}) are blue-shifted, whereas the higher energy vibrations are red-shifted. The observed shifts are 0.5 – 2.4 cm^{-1} for Ar@C_{60} and the sign of the shifts can be correlated with the nature of the C_{60} vibrations: vibrations with radial character are blue shifted, whereas vibrations with tangential character are red shifted.[284] Since the shifts are small, they indicate that the endohedral noble gas atoms do not significantly perturb the fullerene cage.

Quantum chemistry (DFT) calculations give good predictions for the magnitude of the shifts, but do not correctly predict all the signs.[284] Such cage vibrational shifts induced by the encapsulation have been used to benchmark quantum chemistry calculations involving non-covalent interactions.[108]

D. Kr@C_{60} molecular motion

1. Kr@C_{60} *THz*

Kr@C_{60} displays a THz absorption spectrum due to the endohedral species, just as the other noble gases. At low temperature, the fundamental translational transition appears around 86 cm^{-1}, but it is rather broad because Kr has a significant fraction of many isotopes in natural abundance.[179] With increasing temperature, the absorption becomes broader and more intense on the higher energy side, because of the an-harmonicity of the potential. The Kr@C_{60} THz spectrum is very similar to Ne@C_{60} and Ar@C_{60}, all are detailed in ref. 179.

Fitting the experimental spectrum determines the confining potential parameters for Kr@C_{60}, section VII E.[179]

2. Kr@C_{60} *IR*

The IR cage vibrations for Kr@C_{60} have been measured at room temperature in the solid powder.[284] The IR active cage modes are shifted for the endofullerenes compared with empty C_{60}. Generally, the lower energy vibrational modes (below ∼600 cm^{-1}) are blue-shifted, whereas the higher energy vibrations are red-shifted. The observed shifts are 0.0 – 2.0 cm^{-1} and the sign of the shifts can be correlated with the nature of the C_{60} vibrations: vibrations with radial character are blue shifted, whereas vibrations with tangential character are red shifted.[284] Since the shifts are small, it indicates that the endohedral noble gas atoms do not significantly perturb the fullerene cage.

Quantum chemistry (DFT) calculations give good predictions for the magnitude of the shifts, but do not correctly predict all the signs.[284] Such cage vibrational shifts induced by the encapsulation have been used to benchmark quantum chemistry calculations involving non-covalent interactions.[108]

The $F_{1u}(1)$ mode of C_{60} (526 cm^{-1}) is observed to unusually soften by ∼0.5 cm^{-1} with decreasing temperature, for both C_{60} and Kr@C_{60}.[285] Furthermore, this vibrational mode of Kr@C_{60} is blue-shifted by ∼2 cm^{-1}, compared with C_{60}. The $F_{1u}(2)$ mode of C_{60} (576 cm^{-1}) exhibits the usual hardening with decreasing temperature; and it is blue-shifted by ∼1 cm^{-1} in Kr@C_{60}.[285] Such results, together with Kr@C_{60}

EXAFS measurements[196] (section IX B), appear to be consistent with C_{60} fullerenes exhibiting negative thermal expansion at low temperatures.[196,285]

3. Kr@C_{60} *Raman*

The Raman cage vibrations for Kr@C_{60} have been measured at room temperature for the solid powder.[284] The Raman active cage modes are shifted for the endofullerene compared with empty C_{60}. Generally, the lower energy vibrational modes (below $\sim$600 cm^{-1}) are blue-shifted, whereas the higher energy vibrations are red-shifted. The observed shifts are $0.5-5.3$ cm^{-1} and the sign of the shifts can be correlated with the nature of the C_{60} vibrations: vibrations with radial character are blue shifted, whereas vibrations with tangential character are red shifted.[284] Since the shifts are small, they indicate that the endohedral noble gas atoms do not significantly perturb the fullerene cage.

Quantum chemistry (DFT) calculations give good predictions for the magnitude of the shifts, but do not correctly predict all the signs.[284] Such cage vibrational shifts induced by the encapsulation have been used to benchmark quantum chemistry calculations involving non-covalent interactions.[108]

E. Noble gas @C_{60} endofullerenes confining potentials

All noble gas C_{60} endofullerenes have been analysed using THz spectroscopy[110–112,179]; for He@C_{60} and Ne@C_{60} INS was also performed.[110,111,113] From these studies, the interaction potentials of the noble gas atoms with the inner carbon surface of C_{60} are experimentally determined, shown in table VI. The interaction potential has the general form $V(r) = V_2\, r^2 + V_4\, r^4 + V_6\, r^6$, with coefficients $\{V_2,\, V_4,\, V_6\}$.

Since only He@C_{60} has a pronounced an-harmonicity, the confining potential for He is composed of three terms (V_2, V_4, V_6), see section VII A 3. For the other noble gases, due to the decreased an-harmonicity only two terms are needed (well defined) for the confining potential (V_2, V_4). The decreasing level of an-harmonicity, in going from Helium to Krypton, is also seen by looking at the degree of an-harmonicity for each system, $\nu_{\rm anh}$ row of table VI.

The confining potential becomes steeper and steeper when switching from Helium to Krypton. This is because the size of the noble gas atom increases, switching from He $\rightarrow$ Kr, which makes the confining potential tighter. The experimentally determined confining potentials for all noble gas C_{60} endofullerenes are shown in fig 17 as solid lines. Dashed lines are the confining potentials obtained by summing 60 interatomic Lennard-Jones potentials (from semi-empirical quantum chemistry calculations[171]) between the noble gas and carbon atoms.[179] The agreement between the experimentally obtained potentials and the computed ones is good. The agreement is expected to deviate at higher energies, but also the experimental potentials lose reliability since these energies are not probed in the experiments.[179]

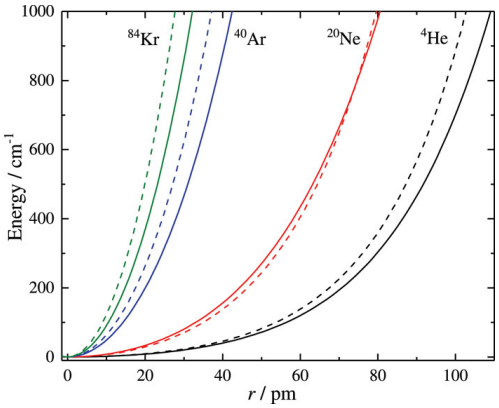

FIG. 17. Comparison of the experimentally determined potential functions V(r) and the LJ (Lennard-Jones) potential functions of ^{4}He@C_{60}, ^{20}Ne@C_{60}, ^{40}Ar@C_{60} and ^{84}Kr@C_{60}. Solid lines: Potential energy curves for the an-harmonic spherical oscillator model, with parameters given in Table VI, which provide the best fit to the experimental data. Dashed lines: Potential energy curves obtained by summing Lennard-Jones two-body potentials, with parameters given in ref. 171. Open access reprint from ref. 179.

As the confining potential becomes tighter, the fundamental translational transition energy should increase significantly. However, this is not observed, it is always between 50-100 cm^{-1} (see the ω_{01} row of table VI). This is because as the noble gas atoms become larger in size they also become heavier, which lowers the energies of all eigenstates and correspondingly the energy separation between them.

F. H_2@C_{60} molecular motion

1. H_2@C_{60} *INS*

H_2 has two indistinguishable Hydrogen nuclei and as a result it displays nuclear spin isomerism: ortho-H_2 and para-H_2 (see section II H). The INS spectrum of H_2@C_{60} at 1.6 K is seen in fig. 18. All possible transitions from the ground states of ortho and para H_2 can be assigned (below 60 meV).[183] An extended INS spectrum of H_2@C_{60} is seen in fig. 19.

Firstly, on the negative side (neutron energy gain) a peak is seen at -14.7 meV, which corresponds to a purely rotational transition from the metastable ortho-H_2 ground state (J = 1) to the para-H_2 ground state (J = 0). This metastable transition is observable because the nuclear spin isomer conversion is very slow for H_2, even when encapsulated inside C_{60} (days or even weeks).[183,240] On the positive side (neutron energy loss), at $+14.7$ meV, the analogous transition from the para-H_2 ground state (J = 0) to the ortho-H_2 ground state (J = 1) is observed.[183]

Interestingly, the peak at 8.08 $\pm$ 0.03 meV corresponds to

TABLE VI. Best fit polynomial coefficients and confidence limits for the radial potential function $V(r) = V_2\ r^2 + V_4\ r^4 + V_6\ r^6$ and induced dipole function $d_{1q} = \sqrt{4\pi/3}(A_1\ r + A_3\ r^3)\ Y_{1q}(\theta,\phi)$ of the confined atoms; see section II C and III B 1 for more details. ω_{01} is the peak frequency of the absorption line at 5 K in the measured THz spectrum corresponding to the n = 0 → n = 1 transition. $\nu_{\rm anh} = (\omega_{01} - \omega_0)/\omega_{01}$ is the fractional contribution of the an-harmonic potential to ω_{01}, where $\omega_0 = \sqrt{2\ V_2/m}$ is the frequency of the harmonic oscillator, m is the mass of the endohedral atom, and c is the speed of light in vacuum. Open access reprint from ref. 179.

Parameter	^{4}He	^{20}Ne	^{40}Ar	^{84}Kr
V_2 / Jm^{-2}	0.39 ± 0.006	1.58 ± 0.04	9.56 ± 0.03	17.81 ± 0.12
V_4 / Jm^{-4}	$(0.60 \pm 0.01) \times 10^{20}$	$(2.28 \pm 0.22) \times 10^{20}$	$(8.19 \pm 0.16) \times 10^{20}$	$(13.20 \pm 1.60) \times 10^{20}$
V_6 / Jm^{-6}	$(3.94 \pm 0.09) \times 10^{39}$	0	0	0
A_1 / C	$(0.68 \pm 0.04) \times 10^{-21}$	$(1.84 \pm 0.13) \times 10^{-21}$	$(3.31 \pm 0.01) \times 10^{-21}$	$(3.30 \pm 0.21) \times 10^{-21}$
A_3 / Cm^{-2}	0.04 ± 0.01	0	0	0
$(2\pi c)^{-1}\ \omega_{01}$ / cm^{-1}	81.4	56.6	91.8	85.4
$\nu_{\rm anh}$	0.29	0.085	0.018	0.007

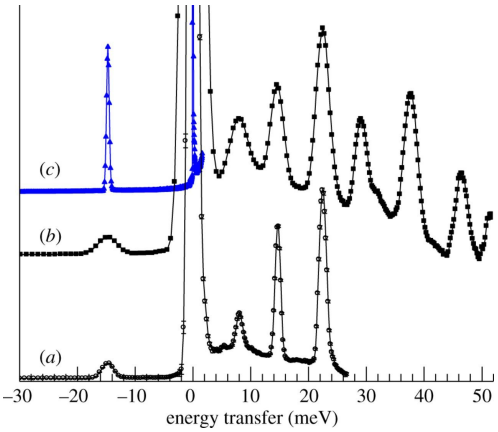

FIG. 18. Low temperature INS spectrum of $H_2@C_{60}$ recorded with two time-of-flight spectrometers. (a) IN4C λ_n = 1.6 Å, T = 1.65 K; (b) IN4C λ_n = 1.2 Å, T = 1.65 K; and (c) IN5 λ_n = 5 Å, T = 1.5 K. Used with permission of The Royal Society (U.K.), from (ref. 192) Horsewill *et al.*, Philos. Trans. R. Soc. A, **371**, 20110627 (2013); permission conveyed through Copyright Clearance Center, Inc.

a transition from the ortho-H_2 ground state to para-H_2 in the first excited translational state, $(J,N,L) = (1,0,0) \rightarrow (0,1,1)$, involving a simultaneous change of rotational and translational states.[183] This in turn gives the energy of the first translational excited state for para-H_2, $(J,N,L) = (0,1,1)$, of 22.78 ± 0.06 meV (not split by the TR coupling because J = 0). The band at 37.8 meV is analogous, corresponding to a transition from para-H_2 ground state to ortho-H_2 in the first excited translational state, $(J,N,L) = (0,0,0) \rightarrow (1,1,1)$.

At ∼23 meV a peak composed of multiple transitions is observed, seen more clearly in fig. 19. The transitions are from the ortho-H_2 ground state to the first translational excited state of ortho-H_2, $(J,N,L) = (1,0,0) \rightarrow (1,1,1)$. The final state is actually split by the TR coupling (see section II E), of ∼ 1 meV magnitude, into three states. $(J,N,L,\Lambda) = (1,1,1,\Lambda)$, where Λ is the true quantum number that describes the system, arising from coupling J & L, and for this case $\Lambda = 0,1,2$.[183,189] This translational peak has a linewidth larger than the instrumental resolution and can accommodate 3 transitions, while most of the other peaks have linewidths equal to the instrument resolution. [183]

An-harmonicity of the confining potential leads to a splitting of the para-H_2 N = 2 states into L = 0 and 2, $(J,N,L) = (0,2,2)$ and $(0,2,0)$, this is visible in the spectrum as a 2.4 meV splitting.[183] Other hot-band and ground state INS transitions are assigned in ref. 172,183.

The INS spectrum can be simulated up to 215 meV with astonishing match to the experimental spectrum, see fig. 19.[189] For such a simulation the unmodified rotational parameters for free H_2 are used and only a few potential parameters are needed: harmonic (V_{00}^{002}), an-harmonic (V_{00}^{004}, V_{00}^{006}) and TR-coupling (V_{00}^{222}), see section II E 1 for details on potential terms.[189] High J rotational states are observed in the spectrum, without significant splittings. Indicating that H_2 rotates freely inside the cage, exhibiting low rotational barriers even at cryogenic temperatures. Furthermore, this shows that including non-spherical potential terms, satisfying Icosahedral symmetry, would only give rise to minor spectral splittings and shifts - which would be obscured by the instrumental resolution. Thus, proving that assuming spherical symmetry for the potential terms is adequate.[189] An alternative simulation approach uses Lennard-Jones interatomic potentials to describe the interaction potential between the endohedral H_2 and C_{60}, with a good match to the experimental INS spectrum.[172,174]

In the temperature range $1.6 - 20$ K a small shift is observed, towards smaller energy transfer, for the −14.7 meV purely rotational transition (J = 0 → J = 1), as temperature is decreased. This is consistent with a small splitting of the J = 1 rotational state of a few tenths of meV.[192]

Very low temperature INS measurements, 60 mK − 35 K, on $H_2@C_{60}$ reveal an apparent shift of the −14.7 meV rotational transition (J = 1 → J = 0).[219] The peak becomes broader, more asymmetric, and it shifts to greater energy transfer with increasing temperature.[219] The peak can be fitted with two components that change in intensity with tempera-

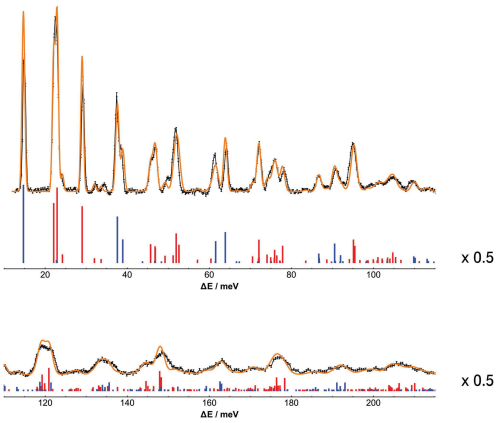

FIG. 19. Comparison between the experimental and calculated spectrum of $H_2@C_{60}$. For clarity the plot is split into two equally wide panels spanning the transfer energy ranges from 10 meV to 215 meV. The black line with error bars represent the spectrum of $H_2@C_{60}$ recorded at 2.5 K on IN1-Lagrange at ILL. The bars represent the calculated stick spectrum of $H_2@C_{60}$ at 2.5 K, where the colours blue and red are used to distinguish transitions originating in the para and ortho ground states, respectively. The orange line overlaid to the experimental spectrum represent the calculated spectrum obtained by convolving the stick spectrum with the instrumental resolution of IN1-Lagrange. For clarity the peaks in the stick spectrum are scaled by a factor 0.5 with respect to the numerical values and vertically shifted. Reprinted from the PCCP Owner Societies (ref. 189): S. Mamone *et al.*, Phys. Chem. Chem. Phys., **18**, DOI: 10.1039/C6CP06059E, 2016; licensed under a Creative Commons Attribution 3.0 Unported Licence (CC BY 3.0) license.

ture, but have constant linewidths and constant energy separation (of 0.135 ± 0.01 meV). Fitting the INS spectra with temperature is consistent with a lower singly degenerate state and a higher doubly degenerate state.[219] Such splitting of the $J = 1$ rotational states cannot be caused by a potential with Icosahedral symmetry and crystal fields with reduced symmetry must be considered.[192,219] Initially ref. 92 suggested this splitting to be due to two different crystal fields arising from two different orientations (P and H) that C_{60} can have in the low temperature phase (i.e. merohedral disorder), see sections IV A 2 and IV C 1.

High pressure (5 kbar) INS measurements on $H_2@C_{60}$ shed light on the effect of pressure on the -14.7 meV purely rotational transition ($J = 1 \rightarrow J = 0$).[219] At ambient pressure, empty C_{60} has two orientations called P and H, in relative ratio 85 : 15, in the $Pa\bar{3}$ phase below $\sim$90 K (section IV A 2). Applying pressure enriches the ratio of H in C_{60} and lowering the temperature (below $\sim$90 K) "locks in" the new P:H ratio even after pressure is released. The energy splitting between the two fitted components, of the -14.7 meV peak, increases by $\sim$40% in the H-rich phase under pressure. It remains $\sim$25% larger when the pressure is released − which relieves the external pressure but locks in the P:H ratio.[219] The high pressure INS results prove that the symmetry breaking of the $J = 1$ rotational state is influenced by the orientation and proximity of neighbouring cages, i.e. crystal field effects.[219]

Simulations of the symmetry breaking effect by making use of the P & H orientations give good correspondence to the experimental splittings.[214,224,225] Such simulations assume 100% pure P and H orientations of the C_{60} fullerene lattice, which induce a crystal field (electric field gradient) in the centre of the cage from its nearest neighbours. It is shown that the 100% pure P orientation leads to a splitting of the $J = 1$ rotational ortho-H_2 state of ~ 1.1 cm^{-1}, whereas the H orientation leads to a splitting an order of magnitude smaller; see section IV C.[214,224,225]

The momentum transfer κ that the neutron imparts on the endohedral H_2 reflects the physical dimension of the H_2 inside the cage.[183] The momentum transfer dependence of the 14.7 meV ($J = 0 \rightarrow J = 1$) transition is the same for the neutron energy loss and the energy gain side. This allows for the determination of $\langle u^2 \rangle$, the mean squared displacement of the hydrogen molecule: 0.126 ± 0.002 Å^2 for NE loss and 0.122 ± 0.002 Å^2 for NE gain. [183] The momentum transfer dependence of the translational peak at 22.5 meV (for ortho-H_2) gives $\langle u^2 \rangle = 0.102 \pm 0.002$ Å^2.[183]

Confined diatomic molecules in fullerene cages exhibit an INS selection rule, resulting from the vector addition of translational and rotational angular momenta (i.e. TR dynamics). This leads to missing peaks in the INS spectra of $H_2@C_{60}$ which can be simulated.[172,174,189] Section IV B explains the INS selection rule in more detail.

2. HD@C_{60} *INS*

The INS spectrum of $HD@C_{60}$ changes greatly with temperature, whereas $H_2@C_{60}$ does not. This is because HD does not display spin isomerisms (see section II H), and for H_2 the ortho-para populations do not change significantly with temperature due to very long spin isomer conversion times.[286] At 1.8 K $HD@C_{60}$ does not have any peaks on the neutron energy gain because it does not have metastable spin isomers; but acquires peaks at higher temperatures from populating TR excited states. Scattering from the ^{1}H nucleus dominates the spectra, but features from ^{2}D are possible.

INS measurements have been performed on a sample containing both $H_2@C_{60}$ and $HD@C_{60}$.[286] INS peaks are observed at 22.3 meV and 19.1 meV, and are assigned to translational excitations of H_2 and HD, respectively (by analysing the reduced masses and their ratio).[286] The $H_2@C_{60}$ rotational peaks are close to the gas phase H_2 but for $HD@C_{60}$ this is not the case; significant differences are seen from the gas phase HD. This is because for the non-centrosymmetric HD, encapsulation inside C_{60} forces HD to rotate about the geometric centre (middle of the bond) and not about the centre of mass. This is not the case for centrosymmetric molecules such as H_2.[286] The same is observed for $H_2@C_{60}$ and $HD@C_{60}$ IR measurements, section VII F 3.

The momentum transfer dependences of the $HD@C_{60}$ INS peaks are quite different from $H_2@C_{60}$. This is because for

HD@C_{60} an extra term is included in the scattering amplitude, since HD is not centrosymmetric.[183] For the rotational (and translational) peak of HD@C_{60} the mean square displacement of the HD molecule, $\langle u^2 \rangle$, is 0.090 ± 0.006 Å^2. This is 26% smaller than $\langle u^2 \rangle$ for H_2@C_{60}, which conforms to the theoretically expected value of 22%.[183]

The theoretical INS spectrum of HD@C_{60} has been simulated using Lennard-Jones interatomic parameters for the interaction potential of the endohedral HD and C_{60}. Such simulations also take into account the INS selection rule, section IV B.[173] The HD@C_{60} simulated spectra remain to be compared with experimental data once available, because so far only a few peaks have been observed in the INS spectrum of HD@C_{60}; acquired on a mixed sample containing both HD@C_{60} and H_2@C_{60}.[286]

3. H_2@C_{60} IR

The H_2@C_{60} endofullerene has been extensively investigated by IR spectroscopy.[150,177,178,181,218] The IR spectra of H_2@C_{60} (solid powder) at different temperatures are shown in fig. 20.[181] At higher temperatures more IR peaks are seen because excited states become more populated, leading to many possible transitions. IR lines are sharp if H_2 is free to rotate inside the C_{60} cage, and this is indeed observed for H_2@C_{60}.[150,177,178,181,218]

The 6 K experimental spectra are shown in more detail in fig. 21, together with peak annotations and fitted simulated spectra.[177] Fig. 22 shows the energy level diagram for H_2@C_{60} with assigned transitions. Absorption lines are seen between 3850-4850 cm^{-1}, corresponding to the stretching mode of H_2 together with rotational/translational sidebands.

Isolated homonuclear diatomic molecules do not display IR absorption. However, H_2 can absorb IR radiation if intermolecular interactions are present.[177,178] IR activity in H_2@C_{60} arises from an induced electric dipole moment caused by the confinement. The induced dipole moment is dependent on the displacement of H_2 from the centre of the cage. Thus, the H_2@C_{60} molecule has zero dipole moment when H_2 is at the centre of the cage, but acquires a dipole moment when H_2 is displaced from it (i.e. translational motion). This leads to the selection rules $\Delta N = \pm 1$ and $\Delta L = \pm 1$ for the translational quantum numbers N and L, see section II C for more details.[177] However, very weak transitions are observed around 4070 cm^{-1} for $\Delta N = 0$, corresponding to pure vibrational excitation (fig. 21 a) − which are formally forbidden in the model used.[177] Electromagnetic radiation cannot induce transitions between H_2 nuclear spin isomers, para-H_2 has even and ortho-H_2 has odd J rotational states. This gives rise to the rotational selection rule $\Delta J = 0, \pm 2$.[177,178,181] The label "Q" or "S" for the transitions corresponds to the change in the J quantum number: Q is for $\Delta J = 0$ and S is for $\Delta J = \pm 2$, and the number in parentheses is the initial J value.[177]

The pure vibrational transition of H_2@C_{60} (fig. 21 a) is red-shifted by 90 cm^{-1} from H_2 in the gas phase.[177] A contribution to the vibrational frequency red-shift represents the translational zero-point energy.[181] It appears that the zero-point translational energies are different for the ground and first excited vibrational states of H_2 encapsulated in C_{60}. This difference leads to a 9 cm^{-1} change in the vibrational excitation energy, from the encapsulation itself and not from changes in the vibrational parameters of H_2 upon encapsulation (e.g. changes in the force constant or bond length).[181] However, the 90 cm^{-1} red-shift cannot be completely disentangled. On the one hand, the shift could be caused by changes in the zero-point vibrational energy; on the other hand, it could be caused by anharmonic corrections to the H_2 vibrational levels caused by the encapsulation. At the moment the two causes cannot be isolated, as the experimental data is limited to $v = 0 \rightarrow 1$ transitions only.[181]

H_2@C_{60} was enriched in the para-H_2 spin isomer by exposing the endofullerene (adsorbed onto a zeolite) to liquid oxygen at 77 K, in order to catalyse the ortho-para conversion, section V D 2. The different peak intensity profile of the para-H_2 enriched sample greatly facilitated the assignment of IR peaks to each spin isomer.[178,181]

IR vibrational transitions must change the vibrational quantum number ($\Delta v = \pm 1$) and at the same time can excite the molecule rotationally or translationally, or both. Fig. 21 (b) shows the peak structure for a vibrational excitation, from the ground rotational ortho and para H_2 states, accompanied by a translational excitation (Q transitions). For ortho-H_2 there are three peaks, Q(1), whereas for para-H_2 only one peak is present, Q(0). The translation-rotational coupling is responsible for splitting Q(1) into three components; because the two sources of angular momentum in ortho-H_2, rotational ($J = 1$) and translational ($L = 1$), couple according to the angular momentum coupling rules (see section II E for more details).[177,178] This gives the total angular momentum that describes the system, represented by the good quantum number Λ. Coupling $J = 1$ and $L = 1$ gives $\Lambda = 0$, 1 and 2 − all three states having different energies. This is the origin of Q(1) being split into three peaks. This is not the case for the para-H_2 Q(0), because the rotational angular momentum $J = 0$ and the translational angular momentum $L = 1$ couple to give a single value of the total angular momentum, $\Lambda = 1$. Fig. 22 shows the energy level diagram of H_2@C_{60}, graphically displaying the TR coupling.

The IR spectrum can be simulated and from the fitting procedure parameters describing the vibration-rotation-translation of H_2 inside C_{60} are obtained.[177,181,218] The parameters are discussed below, for exact values see references 177,178,181,218.

The rotational constant B_e and the vibrational an-harmonic correction term α_e are smaller for H_2@C_{60} than for H_2 in the gas phase; whereas the centrifugal correction term D_e is similar in both cases.[181] The smaller B_e would correspond to a 0.81% stretching of the H-H distance. Indicating that the cage could have an attractive interaction with the H_2, which elongates the H-H bond.[181] However, the smaller α_e indicates that the cage now has a repulsive interaction, reducing the elongation of the H-H bond in excited vibrational states, as compared with H_2 in the gas phase. A repulsive interaction with the cage also follows from the positive an-harmonic translational term ${}^{v}V_{00}^{004}$.[181] See section II E 1 for details on potential terms.

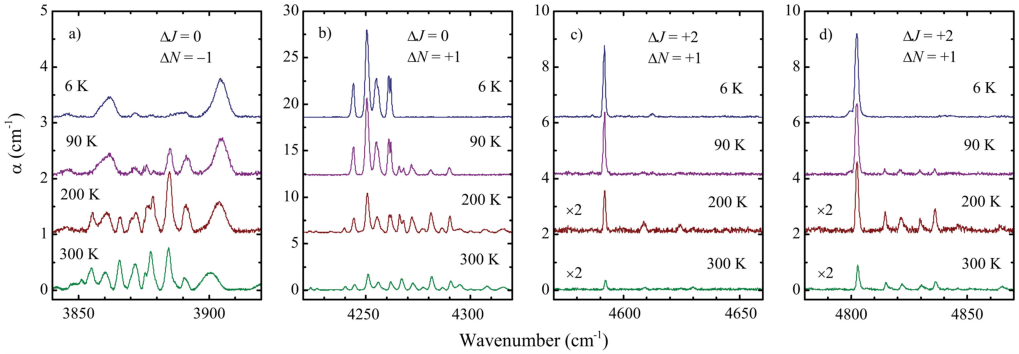

FIG. 20. Temperature dependence of the infrared absorption spectra of $H_2@C_{60}$. Four panels show groups of transitions with the same change of the quantum numbers J and N . An exception is the 4612.5 cm^{-1} line in (c), the fundamental ortho-H_2 transition $\Delta J = 2$, $\Delta N = 0$. Spectra are shifted vertically for clarification. Broad lines that are visible already in the 6 K spectrum below 4000 cm^{-1} in panel (a) are not H_2 absorption lines. The absorption of the 200 and 300 K spectra has been multiplied by 2 in panels (c) and (d). Reprinted from (ref. 181) Ge *et al.*, J. Chem. Phys., **134**, 054507 (2011), with the permission of AIP Publishing.

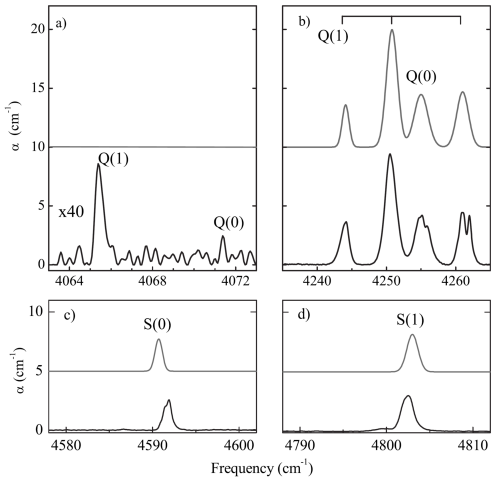

FIG. 21. Baseline-corrected IR absorption spectra of $H_2@C_{60}$ at 6 K (black) and the best fit theoretical spectrum (gray) in panels (a – d). All transitions are from the vibrational state $v = 0$ to $v = 1$. The letter indicates the change in J (Q for $\Delta J = 0$ and S for $\Delta J = 2$) and the number in parentheses is the initial J value. For the assignment inside a rotational branch, see Table I and fig. 2 from ref. 177. (a) Fundamental vibrational transitions; these are forbidden in the first order theory so the calculated spectrum contains no peaks. (b) Q transitions with $\Delta N = +1$ and $\Delta J = 0$. (c) Para-H_2 and (d) ortho-H_2 S transitions with $\Delta N = +1$, $\Delta J = +2$. Reprinted from (ref. 177) Mamone *et al.*, J. Chem. Phys., **130**, 081103 (2009), with the permission of AIP Publishing.

The harmonic TR coupling term in the vibrational excited state ($^1V_{00}^{222}$) is two times larger than in the vibrational ground state ($^0V_{00}^{222}$).[181] However, the trend is opposite for the anharmonic TR coupling term where in the vibrational ground state the $^0V_{00}^{224}$ term is two times larger than $^1V_{00}^{224}$.[181]

A reduction in symmetry is observed for the peaks at 4255 cm^{-1} and 4261 cm^{-1}. This can be due to cage deformations, crystal fields or carbon isotopomers, see section IV C for more information.[177] The same mechanism could allow the observation of "formally forbidden" pure vibrational transitions with $\Delta N = \Delta J = 0$.[177] In icosahedral symmetry, levels with $\Lambda = 3$ will be split; an indication of this effect is observed in ref. 181. However, the magnitude of the splitting would be 2 cm^{-1}, which is too large to arise from I_h symmetry.[181]

4. $HD@C_{60}$ & $D_2@C_{60}$ IR

The endofullerenes $HD@C_{60}$ and $D_2@C_{60}$ have been investigated using IR spectroscopy, discussed below in relation to $H_2@C_{60}$ (previous section).[218] To analyse the $HD@C_{60}$ IR spectrum, some results from INS measurements on $HD@C_{60}$ are used (section VII F 2).[218,286]

The IR data of $HD@C_{60}$ and $D_2@C_{60}$ is analysed and fitted analogously to $H_2@C_{60}$. The exact fitting parameters for $H_2@C_{60}$, $HD@C_{60}$ and $D_2@C_{60}$ are found in ref. 218.

The isotropic confining potential parameters $^vV_{00}^{002}$ and $^vV_{00}^{004}$ are similar for all isotopomers, with a slight trend to increase with the mass of the endohedral species (see section II E 1 for details on the potential terms).[218]

The relative change in the rotational constant B_e is the same for H_2 and D_2 (with respect to free H_2 and D_2), being mass independent.[218]

The most surprising result is for $HD@C_{60}$, where in order to match the experimental results, the potential terms $^vV_{00}^{111}$

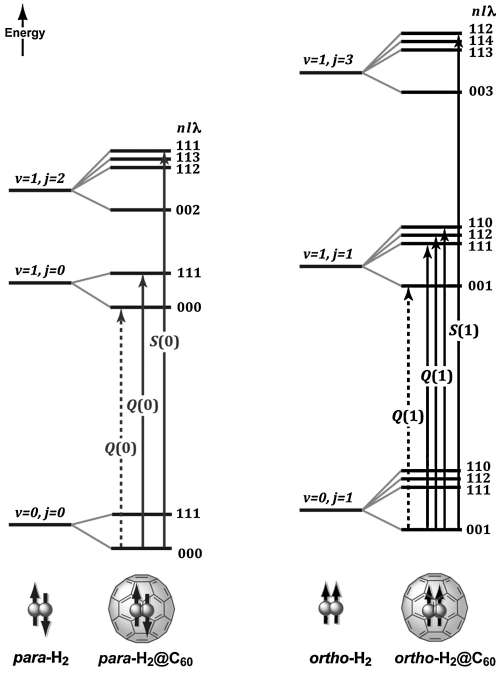

FIG. 22. Diagrammatic scheme showing the transitions and the corresponding energy levels that are relevant for IR spectroscopy on $H_2@C_{60}$ at temperatures near 4 K: para-H_2 is on the left and ortho-H_2 is on the right. The dotted lines stand for formally forbidden transitions in the isolated $H_2@C_{60}$. The effect of confinement in C_{60} is to split the vibrational–rotational energy manifold of free H_2 in translational sublevels labelled by the set of quantum numbers n, l, λ. In the ground $v = 0$ state the $j = 2$ and $j = 3$ energy levels are not shown. Reprinted from (ref. 150) Mamone *et al.*, Coord. Chem. Rev., **255**, 938–948 (2011), Copyright (2011), with permission from Elsevier.

and ${}^{\nu}V_{00}^{113}$ were invoked. Such terms mix different rotational and translational states of the endohedral HD, effectively shifting the centre of rotation away from its centre of mass.[218] This does not apply to $H_2@C_{60}$ or $D_2@C_{60}$, because the centre of mass and geometric centre coincide for homonuclear diatomics (centrosymmetric molecules). Encapsulation in the cage forces the HD to rotate about an axis much closer to its geometric centre than its centre of mass, which intuitively makes sense. The distances of H and D from the rotation centre are 0.3854 Å and 0.3560 Å, respectively. In contrast, the distances of H and D from the centre of mass are 0.49428 Å and 0.24714 Å, respectively.[218]

For $H_2@C_{60}$ and $D_2@C_{60}$ the rotational quantum number J is still a good quantum number, however, for $HD@C_{60}$ this is not the case. As the centre of rotation is shifted significantly from the gas phase HD, this strongly mixes different J rotational states.[218]

Another striking feature of $HD@C_{60}$ is the large centrifugal distortion term D_e. The reason is most likely because the Deuterium atom is farther away from the centre of rotation, causing a larger centrifugal force (larger deformation) when HD rotates faster in the cage.[218]

For heteronuclear diatomics, since the inversion symmetry is broken, the dipole moment expansion contains more terms.[218] For $HD@C_{60}$ the dipole moment A^{010} corresponding to the $v = 0 \rightarrow 1$, $J = 0 \rightarrow 1$ transition is enhanced by two orders of magnitude compared with the permanent dipole moment of the free HD molecule.[218]

Small additional splittings are observed for some IR peaks for all molecules studied, $H_2@C_{60}$, $HD@C_{60}$ and $D_2@C_{60}$. Icosahedral symmetry cannot generate such splittings, so the symmetry must be lower. The splittings are independent of the endohedral isotopomer and depend on the initial and/or final states.[218] More about this symmetry breaking effect in section IV C.

5. $H_2@C_{60}$ *Raman*

Raman measurements on solid $H_2@C_{60}$ did not show much difference to empty C_{60} measurements. The cage signals (peak positions) for both agree within 0.4 cm^{-1}, and no signal was observed for the endohedral H_2 in the measured range (200 − 1800 cm^{-1}).[13] So far, endohedral species have not been detected by Raman spectroscopy in C_{60} endofullerenes, only cage vibrations (excluding metallo-endofullerenes). However, a weak and broad Raman vibration of H_2 was detected in open cage fullerenes $H_2@$ATOCF at 4135 cm^{-1} (small red-shift compared with gas phase H_2).[287]

6. $H_2@C_{60}^+$ *IR*

$H_2@C_{60}$ has been investigated using IR spectroscopy in the gas phase, in ionic form using Helium tagging (see section VIII A), namely the $H_2@C_{60}^+ - He$ species. IR measurements are performed at 3.7 K between 1100 − 1600 cm^{-1}. The observed transitions belong to the encapsulating cage.[13]

Electronic (near-IR) spectroscopy on $H_2@C_{60}^+$ is discussed in section VIII E 4.

The IR spectrum of $H_2@C_{60}^+ - He$ is slightly blue-shifted and displays smaller spectral splittings compared to $C_{60}^+ - He$. $H_2@C_{60}^+ - He$ IR spectrum is more similar to C_{60}^+ in a cryogenic Neon matrix than gas phase $C_{60}^+ - He$.[13] The C_{60}^+ interacts more strongly with the endoehdral H_2 than neutral C_{60}, since there was no difference (within 0.4 cm^{-1}) in the Raman frequencies between $H_2@C_{60}$ and C_{60}.[13] Furthermore, C_{60}^+ has D_{5d} symmetry and not I_h like C_{60}, meaning the cage is more anisotropic in cationic form.[13]

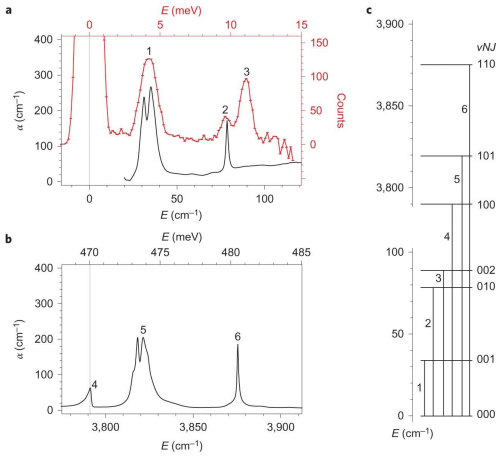

FIG. 23. Molecular motion spectroscopy of HF@C_{60}. (a) INS at 1.6 K (red) and THz/far-infrared spectra at 5 K (black) of polycrystalline HF@C_{60}. (b) Mid-infrared spectrum of HF@C_{60} at 5 K. (a) and (b) have the same energy width across the horizontal scale and (b) is aligned so that the fundamental vibrational transition at 3791.1 cm^{-1} falls in line with the zero-energy position in (a). (c) energy levels and the assignments of the transitions using the vibrational (v), translational (N) and rotational (J) quantum numbers. Reproduced from (ref. 20) Krachmalnicoff *et al.*, Nat. Chem., **8**, 953–957 (2016), with permission from Springer Nature.

G. HF@C_{60} molecular motion

1. HF@C_{60} *THz*

The THz spectrum of HF@C_{60} (5 K) can be seen in fig. 23 (a), black curve, and the energy level diagram in fig. 23 (c). Two transitions are seen at 31.1 cm^{-1} and 35.0 cm^{-1} (peak label 1) corresponding to the fundamental rotational excitation of endohedral HF ($J = 0 \rightarrow J = 1$); compared with 41.11 cm^{-1} for gas phase HF.[20] The splitting is due to a symmetry breaking effect that lifts the degeneracy of the $J = 1$ rotational state, which is not possible in I_h symmetry. This symmetry breaking effect is also observed in other molecular C_{60} endofullerenes, see section IV C for more details. The presence of weakly perturbed rotational peaks demonstrates that HF is essentially rotating freely (small hindering potential) inside the C_{60} cage, even at cryogenic temperatures.

A sharp peak is seen at 78.6 cm^{-1} (peak label 2) which corresponds to a purely translational excitation (section II C) of the endohedral HF centre of mass.[20] For HF@C_{60} at cryogenic temperatures (5 K) only these two transitions can be observed with THz spectroscopy, because only the ground state is populated and the transitions must satisfy the selection rules $\Delta J = \pm 1$ and $\Delta L = \pm 1$.

2. HF@C_{60} *INS*

The INS spectrum of HF@C_{60} is seen in fig. 23 (a) red curve; with the energy level diagram in fig. 23 (c). Three peaks are observed: fundamental rotational excitation $J = 0 \rightarrow J = 1$ (peak 1), purely translational excitation (peak 2) and overtone rotational excitation $J = 0 \rightarrow J = 2$ (peak 3).[20]

The spectrum is similar to the THz spectrum (section VII G 1 and fig. 23 a − black curve) with the addition of peak 3, assigned as overtone rotational excitation, at 88.72 cm^{-1} (compared with 122.5 cm^{-1} for gas phase HF).[20] However, simulations of the INS spectrum using LJ (Lennard-Jones) parameters[175] for the interaction potential between the endohedral HF and C_{60} assign this transition as $(N, L, J, \Lambda) = 0, 0, 0, 0 \rightarrow 1, 1, 1, 2$; a final state with $J = 1$ and $L = 1$ rotational and translational (orbital) angular momentum respectively.[175,228] The same simulations predict the overtone transition $J = 0 \rightarrow J = 2$ to be at ∼15 meV (∼121 cm^{-1}). This is consistent with the HF@C_{60} INS spectrum acquired with a neutron wavelength of 1.6 Å, which displays a strong peak at ∼15 meV, see ref. 175. This interpretation does not explain why peak 3 (fig. 23) is absent from the THz spectrum.

The INS selection rule for confined diatomic molecules, see section IV B for details, is shown to hold for HF@C_{60}.[175]

3. HF@C_{60} *IR*

The IR spectrum of endohedral HF in HF@C_{60} at 5 K is seen in fig. 23 (b), with energy level diagram in panel (c). The pure vibrational excitation $v = 0 \rightarrow v = 1$ is seen at 3791.1 cm^{-1} (peak 4), and is red shifted by 170.5 cm^{-1} compared with the gas phase HF (3961.64 cm^{-1}).[20] The rotational excitation (peak 5) displays a spectral splitting due to the symmetry breaking effect (see section IV C for details), whereas the translational excitation is very sharp (peak 6). The IR spectrum is consistent with the THz spectrum in fig. 23 (a), section VII G 1.[20] The observation of a mostly unperturbed ro-vibrational transition (peak 5) demonstrates mostly free unhindered rotation of the endohedral HF inside C_{60}.

H. H_2O@C_{60} molecular motion

Since H_2O has two indistinguishable Hydrogen nuclei, it displays nuclear spin isomerism: ortho-H_2O and para-H_2O (more details in section II H).

1. H_2O@C_{60} *THz & spin isomer conversion*

The THz spectrum of H_2O@C_{60} is seen in fig. 24, where three peaks are observed below 60 cm^{-1} − corresponding to rotational transitions of the endohedral H_2O.[187] The THz/far-IR spectra are unambiguously assigned to the ortho or para spin isomer through a temperature jump experiment, by making use of the rather slow ortho-para conversion of endohedral H_2O, fig. 24. If the sample is cooled quickly, the ortho/para

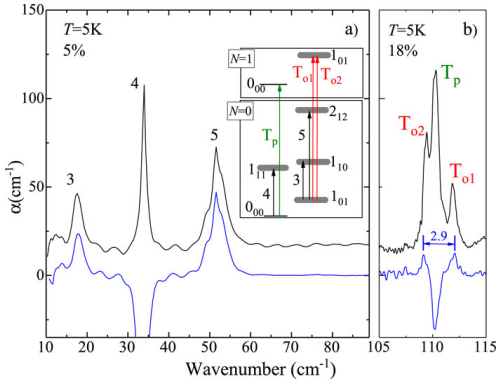

FIG. 24. THz (far-IR) absorption spectra of $H_2O@C_{60}$ at 5 K. Spectrum $\alpha(0)$ was measured after the temperature jump from 30 to 5 K (**black**) and the difference spectrum (**blue**), $\Delta\alpha = \alpha(0) - \alpha(\Delta t)$, with $\Delta t = 44$ h in (a) and $\Delta t = 5$ h in (b). The sample filling factors are f = 0.05 in (a) and f = 0.18 in (b). Water rotational transitions corresponding to the absorption lines numbered 3 and 5 (ortho-water) and 4 (para-water) are shown in the inset. The translational transitions $N = 0 \rightarrow N = 1$ for para (T_p) and ortho (T_{o1}, T_{o2}) $H_2O@C_{60}$ are shown in the inset of panel (a). N is the quantum number of the spherical harmonic oscillator, section II C. Open access reprint from ref. 187.

fraction at high temperature is "locked in" at low temperature. As time goes on, ortho↔para conversion occurs and the relative intensities of the peaks at low temperature will change. Monitoring this change with time gives the ortho-para conversion time constant.[187,288]

The ortho-para nuclear spin isomer conversion time of $H_2O@C_{60}$, measured using continuous wave THz spectroscopy, is 12.0 ± 1.3 h at 3.5 K.[220] Using pulsed THz spectroscopy the conversion time is ∼12 hours at 4 K.[288]

The rotational peaks of H_2O are slightly red-shifted inside the C_{60} cage compared with the gas phase H_2O, by <5 cm^{-1}.[187] Only these three rotational peaks are observed at 5 K (fig. 24). As expected considering the populations of the ortho and para H_2O ground states and the selection rules for electromagnetic excitation of an asymmetric top with a permanent electric dipole moment. From the intensities of the rotational peaks, the permanent dipole moment of endohedral H_2O is determined to be 0.50 ± 0.05 D; compared with 1.85 D for free H_2O.[187] The same value is obtained through dielectric constant measurements of $H_2O@C_{60}$, 0.51 ± 0.05 D, section X D 2.[289] This reduction of the dipole moment can be attributed to the screening by the π electrons of the cage: an endohedral electric dipole moment induces a rather strong polarisation of the π electrons inside the cage, which leads to a significant cancellation of the endohedral water dipole moment.[290]

Red-shifts of the rotational frequencies are due to changes in the rotational constants of the H_2O molecule upon encapsulation. Comparing the rotational constants for endohedral and free H_2O gives relative shifts of −13%, +5.5% and −8.7% for A_0, B_0 and C_0 respectively (in the ground vibrational state).[187] The change in the rotational constants for endohedral H_2O can be explained through the confinement inside C_{60}. Because H_2O is a non-centrosymmetric molecule, when confined inside a spherical cavity, H_2O is forced to rotate about the "centre of interaction" (geometric centre) and not about the centre of mass – like in the gas phase.[187] The same effect was observed in $HD@C_{60}$ but not $H_2@C_{60}$ because the latter endohedral molecule is centrosymmetric, see sections VII F 1 and VII F 3 (also section VII G 1 for $HF@C_{60}$). Another reason for the change in rotational constants could be geometric changes (changes in bond lengths and/or bond angles) induced in H_2O by the confinement. However, the latter is likely not dominant, see ref. 187.

The peaks at 110 cm^{-1}, fig. 24, correspond to pure translational excitations of the endohedral water, for both ortho and para spin isomers.[187] The ortho translational excitation has a splitting of 2.9 cm^{-1} due to the translational-rotational (TR) coupling. This coupling arises when non-spherical molecules are rotating inside the *almost spherical* C_{60} cage, see section II E for more on TR coupling. The para-H_2O pure translational peak does not display a TR splitting because $J = 0$ in both the initial and final states (i.e. para H_2O ground state is not rotating).[187]

From the translational transitions the confining potential of $H_2O@C_{60}$ can be estimated, see section II C for background. From current experimental data only the harmonic term (V_2) of the potential can be determined, with the an-harmonicity being undefined.[187] The harmonic term in $H_2O@C_{60}$ is found to be ∼3.4 times larger than for $H_2@C_{60}$, which reflects the larger size of H_2O compared to H_2.[187]

The THz spectrum of $H_2O@C_{60}$ was also measured using pulsed THz techniques.[288,291] It provides similar information to the continuous wave THz results (ref. 187), with the addition of unassigned hot band transitions (thermally populated initial state which ≠ ground state) at ∼75 cm^{-1} and ∼ 120 cm^{-1}.[288,291] Simulations of $H_2O@C_{60}$ IR results (section VII H 3), using the confined rotor model, provide possible assignments for these peaks.[292] Simulations predict transitions at 77 cm^{-1} for $(|J_{Ka\ Kc}\ N\ L\rangle)$ $|1_{10}\ 0\ 0\rangle \rightarrow |2_{21}\ 0\ 0\rangle$ and at 121.0 cm^{-1} & 121.1 cm^{-1} for $|1_{10}\ 0\ 0\rangle \rightarrow |1_{10}\ 1\ 1\rangle$ & $|1_{11}\ 0\ 0\rangle \rightarrow |1_{11}\ 1\ 1\rangle$.[292]

2. $H_2O@C_{60}$ *INS*

Neutron scattering measurements of $H_2O@C_{60}$ revealed rich INS spectra composed of sharp peaks, with resolution mostly limited by the instrument, which is unusual and special. An INS spectrum of $H_2O@C_{60}$ at 1.6 K is seen in fig. 25.[193]

The INS spectrum shows peaks on both the neutron energy gain (positive energy transfer) and the neutron energy loss side (negative energy transfer). A peak is seen around −2.5 meV, in the neutron energy gain, proving that there are populated metastable states at 1.6 K.[193] The energy matches the energy difference between the J = 1 ortho and the J = 0 para H_2O

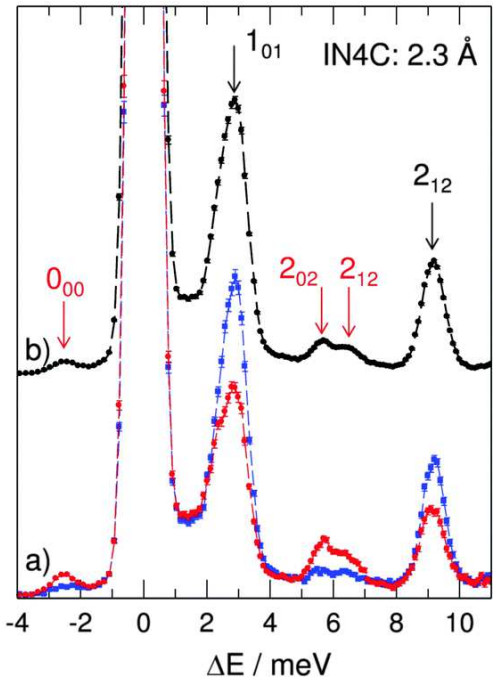

FIG. 25. INS spectrum of $H_2O@C_{60}$ recorded at 1.6 K on IN4C ($\lambda_n = 2.3$ Å): (a) spectrum recorded in the first hour (red) and 8th hour (blue) after cooling; (b) the sum of all neutrons recorded during a period of 8 hours after cooling. Labels identify the final states for the transitions: transitions originating in 1_{01} (red text) and transitions originating in 0_{00} (black text). Used with permission of Royal Society of Chemistry, from (ref. 193) Goh *et al.*, Phys. Chem. Chem. Phys., **16**, 21330–21339 (2014); permission conveyed through Copyright Clearance Center, Inc.

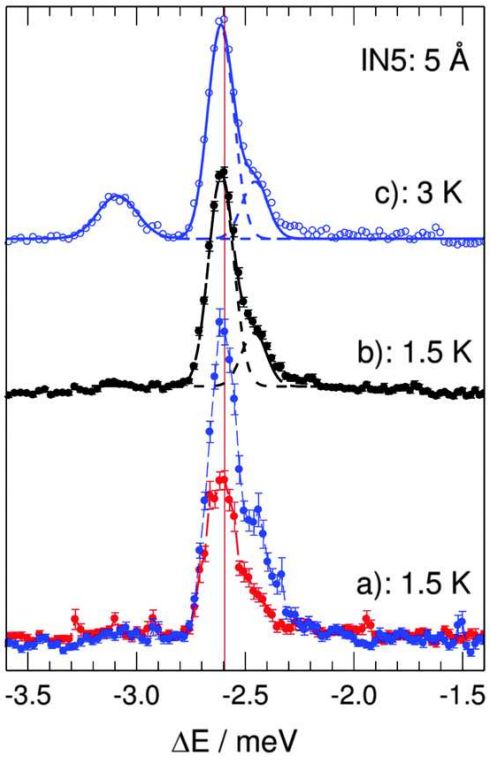

FIG. 26. INS spectrum of $H_2O@C_{60}$ recorded at 1.5 K on IN5 ($\lambda_n = 5$ Å): (a) spectrum recorded in the 1st hour (red) and 5th hour (blue) after cooling; (b) the sum of all neutrons recorded during a period of 5 hours after cooling. (c) the sum of scattered neutrons recorded during 3 hours after cooling to 3 K. The spectra reveal the splitting of the 1_{01} ortho-water state arising from a symmetry breaking interaction. Used with permission of Royal Society of Chemistry, from (ref. 193) Goh *et al.*, Phys. Chem. Chem. Phys., **16**, 21330–21339 (2014); permission conveyed through Copyright Clearance Center, Inc.

states. A temperature jump experiment is seen in fig. 25 a, where spectra are taken in the first hour and after 8 h following fast cooling to 1.6 K. This experiment assigns the negative energy peak to originate in the ortho-H_2O J = 1 state and corresponds to the $1_{01} \rightarrow 0_{00}$ transition. The temperature jump also assigns the initial state of all neutron energy loss transitions to be either para or ortho, depending on if they increase or decrease in intensity with time. Thus, the peaks around 2.5 meV and 9 meV are para-H_2O, while the peaks around 6 meV are ortho-H_2O.[193] The energies of the transitions correspond to H_2O in the gas phase, with small modifications. Additional higher energy peaks are observed and described in ref. 193.

Higher resolution INS measurements have been performed on $H_2O@C_{60}$ (fig. 26).[193] This reveals the peak on the neutron energy gain around −2.5 meV ($1_{01} \rightarrow 0_{00}$) to be composed of three peaks: −3.09 meV, −2.61 meV and a shoulder at −2.46 meV, see fig. 26.[193] This additional splitting of the ortho-H_2O J=1 state must arise from a symmetry breaking mechanism which lowers the Icosahedral symmetry of the C_{60} cage, see section IV C.

The peak at −3.09 meV (fig. 26) is absent at 1.5 K, but it quickly increases as the temperature increases, becoming visible at just 3 K. This peak is ∼40% broader than the instrument resolution, whereas the other two have the linewidth equal to the instrument resolution. This indicates that the −3.09 meV peak displays an unresolved structure.[193]

From the temperature dependence of the neutron energy gain peaks it becomes clear that the J = 1 ortho-H_2O state is split into a lower lying singly degenerate state (−2.61 meV)

and a higher energy doubly degenerate state (−3.09 meV). In ref. 193 there is a typo that switched the labels of the degeneracies. The nature of the −2.46 meV peak is a little unclear, since it does not appear to change with temperature. However, it is closely related to the other two peaks and it certainly originates in the J = 1 ortho-H_2O state.[193]

Part of the $H_2O@C_{60}$ INS peaks are assigned with some uncertainty. It is unclear which is the pure translational excitation for the centre of mass displacement of the endohedral H_2O.[193,220] However, the THz measurements of $H_2O@C_{60}$ (section VII H 1) unambiguously assign the pure translational excitation energy to be around 110 cm^{-1} (13.638 meV).

The $H_2O@C_{60}$ INS spectra can be simulated using interatomic LJ (Lennard-Jones) potentials for the interaction potential between the endohedral H_2O and C_{60}.[176] The computed energy of the translational excited state for para-H_2O is 21.4 meV.[176] A symmetry breaking mechanism is included in these INS simulations; assuming pure 100% P or 100% H orientations of C_{60} to generate crystal fields at the centre of the fullerene, more details in section IV C. The rotational INS spectrum of $H_2O@C_{60}$ is simulated, showing good agreement with the experiment on the neutron energy loss side (<10 meV). The simulated pattern for the 1_{01} peak (see ref. 193 for better resolution) shows a good match with the experiment on the neutron energy loss side (fig. 25); the symmetry breaking on the neutron energy gain is not discussed (fig. 26).[176]

3. $H_2O@C_{60}$ IR

IR spectroscopy investigations have been performed on $H_2O@C_{60}$ in the solid state.[187,290,293] Related computational studies are found in ref. 187,292,294,295. The IR spectra of $H_2O@C_{60}$ are similar to the gas phase H_2O, with some differences. Temperature jump experiments clearly identify the IR peaks belonging either to the ortho or para water spin isomer.[187,293] Since H_2O has two indistinguishable Hydrogen nuclei it displays nuclear spin isomerism: ortho-H_2O and para-H_2O (see section II H).

Around 3600 cm^{-1} the symmetric (ν_1) and anti-symmetric (ν_3) stretching modes of water in $H_2O@C_{60}$ are observed,[187,290,293] see fig. 27. Pure vibrational excitation (Q-band transition), nominally forbidden, is observed for ν_1 at $\sim$ 3573 cm^{-1}, red-shifted compared with free isolated H_2O ν_1 at 3657 cm^{-1}.[187,290,293] A splitting of 0.5 − 0.6 cm^{-1} is observed between the para-H_2O (peak 1) and ortho-H_2O (peak 2) ν_1 Q-band.[187,293] No Q-band is observed for ν_3, because this requires changing the nuclear spin state from para to ortho H_2O.[187,293] On average the redshifts for the ν_1 and ν_3 peaks (including rotational excitations) are 86.9 cm^{-1} and 96.4 cm^{-1} respectively.[293] Translational transitions are expected as side peaks accompanying vibrations, but are obscured by other peaks in the spectrum.[187]

The pure vibrational excitation (Q-band) of the ν_2 bending mode is observed at $\sim$ 1570 cm^{-1}. Red-shifted, by 29.3 cm^{-1},[293] compared with the free isolated H_2O ν_2 at 1595 cm^{-1}.[187,290] Spectral splittings are observed between the para-H_2O and ortho-H_2O ν_2 Q-band, of 1.8 cm^{-1} in ref. 187 and 0.1 − 4.4 cm^{-1} in ref. 293. Approximately 110 cm^{-1} higher than the pure ν_2 bending mode, the translational excitations in the excited ν_2 vibrational state are observed.[187,293] It displays a small 2.7 cm^{-1} splitting for the ortho-H_2O due to the TR coupling.[187,293] The same is observed for $H_2O@C_{60}$ in the ground vibrational state with THz spectroscopy (section VII H 1), but the splitting is slightly larger, 2.9 cm^{-1}.[187]

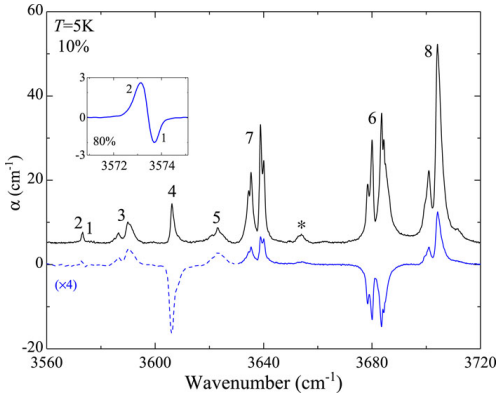

FIG. 27. IR absorption spectra of $H_2O@C_{60}$ vibrational, rovibrational, and vibration-translational transitions of the symmetric stretching, ν_1, and anti-symmetric stretching, ν_3, vibrations at 5 K. The spectrum $\alpha(0)$ was measured after the temperature jump from 30 to 5 K (**black**), and the difference $\Delta\alpha = \alpha(0) - \alpha(\Delta t)$ was measured $\Delta t = 3$ h later (**blue dashed** line multiplied by 4 and **blue** line). The sample filling factor f = 0.1. Lines numbered 1 and 2 are pure vibrational transitions and 3-5 are rovibrational transitions of mode ν_1, and lines 6-8 are rovibrational transitions of ν_3 [see Fig. 1(c) of ref. 187]. (*) marks the ν_3 rovibrational transition at 3654 cm^{-1}, $|\nu_1,\nu_2,\nu_3\rangle|J_{Ka,Kc}\rangle = |000\rangle|1_{10}\rangle \rightarrow |001\rangle|1_{11}\rangle$. The inset shows the para, line 1, and ortho, line 2, components of the pure vibrational transition of mode ν_1, of a f = 0.8 sample, as the difference spectrum with time delay 1 h. Open access reprint from ref. 187

Overtone transitions for the bending mode and further combinations of vibrational modes are observed for $H_2O@C_{60}$.[187] Even a three-quantum transition is observed around 6700 cm^{-1}, from the combination of the bending mode overtone with the anti-symmetric stretch.[187]

The vibrational frequencies for the endohedral H_2O are redshifted compared with the free H_2O: by $\sim$2.4% for the stretching modes and by $\sim$1.6% for the bending mode (and by 1.5% for the bending mode overtone).[187]

From the translational transitions, the confining potential of $H_2O@C_{60}$ can be estimated, see section II C for background. From the current experimental data, only the harmonic term (V_2) of the potential can be determined, with the an-harmonicity being undefined.[187] The harmonic term in $H_2O@C_{60}$ is found to be $\sim$3.4 times larger than for $H_2@C_{60}$, reflecting the larger size of H_2O compared to H_2.[187] Fit-

ting the experimental IR spectra[293], using the confined rotor model (CRM)[292], the force constant k ($V_2 = \frac{k}{2}$) is determined $k = 11.86 \pm 0.03$ J m^{-2}.

Rotational peaks of $H_2O@C_{60}$ that accompany vibrational excitations have a similar pattern to the vibrational ground state (see section VII H 1 for THz results).[187,290,293]

Shifts in the rotational frequencies are observed, due to changes in the rotational constants of the H_2O molecule upon encapsulation. The change in rotational constants for endohedral H_2O can be explained through the confinement inside C_{60}. Because H_2O is not centrosymmetric, when confined within a spherical cavity, H_2O is forced to rotate about the "centre of interaction" (geometric centre) and not about the centre of mass like in the gas phase.[187,292] This interaction leads to mixing of the rotational and translational states. Fitting the experimental IR spectra[293], using the confined rotor model (CRM)[292], determines the distance between the centre of mass and the centre of interaction in $H_2O@C_{60}$ to be 7.55 ± 0.07 pm. The same effect was observed in $HD@C_{60}$ but not in $H_2@C_{60}$, because the latter endohedral molecule is centrosymmetric, see sections VII F 1 and VII F 3.

Another reason for the change in rotational constants could be geometric changes (different bond lengths and bond angles) induced in H_2O by the confinement. However, the latter is likely not dominant according to ref. 187. The rotational constants for the endohedral H_2O in the excited vibrational states are similar to the ground vibrational state; see ref. 187 for a detailed discussion. Assignments of the IR rotational and translational peaks of $H_2O@C_{60}$, based on simulations, for most of the observed transitions are found in ref. 187,292,293.

Peaks 6 and 7 in fig. 27, $|J_{Ka\,Kc}\ N\ L\rangle = |0_{00}\ 0\ 0\rangle \leftrightarrow |1_{01}\ 0\ 0\rangle$, display a multiplet of at least 4 sub-components, seen more clearly in ref. 293 − where symmetric and asymmetric doublets are observed. The large splitting between the doublets is 4.2 cm^{-1} and the small splitting is ~ 1 cm^{-1} (0.8 cm^{-1} & 1.45 cm^{-1}).[293] This is a symmetry breaking effect that leads to a splitting of the J = 1 rotational state (section IV C). Transitions to $J = 2$ states display much more convoluted splitting patterns.[293] Such symmetry breaking effects are seen irrespective of the sample f.f. (filling factor = percentage of filled cages) or the spin isomer ratio; indicating they originate from interactions of endohedral H_2O with the confinement medium.[293]

A quadrupolar interaction can lead to a splitting of the J = 1 rotational state. The quadrupolar interaction arises from an electric field gradient (EFG) at the centre of the C_{60} − which can couple to the molecular quadrupole moment of the H_2O.[214,224,225] The EFG likely originates from the merohedral disorder, see section IV C for background. However, it is not possible to determine the electric field gradient and the molecular quadrupole moment of endohedral H_2O separately.[187]

Four sub-components are seen, whereas the maximum number should be 3 − from the degeneracy of $J = 1$. Thus, there should be at least two sites with different electric field gradients present, leading to different quadrupole splittings.[187] The quadrupole interaction splits $J = 1$ into $M_\Lambda = 0$ lower and $M_\Lambda = \pm 1$ upper states ($\Lambda = J$ if $L = 0$).[187,293] The P-orientation of fullerene cages, 85% abundant (sections IV A 2 and IV C), is shown to give a ~ 4 cm^{-1} splitting − explaining quite well the large 4.2 cm^{-1} splitting of peaks 6 & 7.[187,214,224,225,293] However, the small ~ 1 cm^{-1} splitting, the asymmetry of the doublet and the apparent absence of the 15% H-orientation in the IR spectra cannot be explained.[187,293]

A possible explanation for the small splitting could be given by an electric dipolar interaction.[187,293] A finite electric field, induced by the merohedral disorder, can be observed at the centre of empty C_{60} cages − which can couple to the electric dipole moment of endohedral H_2O.[187] An electric dipole interaction can split the $M_\Lambda = \pm 1$ rotational states − which could explain the small ~ 1 cm^{-1} splitting.[187,293]

Pure vibrational transitions, Q band, of the symmetric modes ν_1 and ν_2 are forbidden if J is a good quantum number (i.e. free gas phase H_2O).[187,290,293] An electric field inside the C_{60} mixes rotational states of the endohedral molecule (within a vibrational state). This mixing can transfer enough amplitude to the pure vibrational transitions (Q-band) to make them observable.[187] However, the translational-rotational coupling can also relax the selection rules through the induced dipole moment of the translational motion.[187] The former is more likely according to ref. 187.

Another explanation for why Q-band transitions are observed for $H_2O@C_{60}$ is electric dipole-dipole interactions between H_2O molecules in adjacent cages.[293] Experimental IR spectra show the absence of observable Q-band transitions in $H_2O@C_{60}$ samples with low filling factors: visible for 75% f.f. but invisible for 15% and 1.5% f.f.[293] Increasing the nearest-neighbour contacts between endohedral H_2O molecules in the $H_2O@C_{60}$ lattice leads to the observation of nominally forbidden Q-band transitions[293] Intermolecular electric dipole-dipole interactions between $H_2O@C_{60}$ molecules in adjacent cages can allow ro-translational states to couple − which could be the reason for relaxing the Q-band selection rules.[293]

Furthermore, higher filling factors (f.f.) lead to significant changes to the IR peak line-shape, see fig. 28. Broader asymmetric features containing multiple sub-components are seen for 75% f.f., whereas only sharp components are seen for 15% and 1.5% f.f.[293]

The broad feature changes shape/evolves significantly with temperature between $5 - 60$ K, middle panel fig 28, which can be expected. However, similar changes are seen during spin isomer conversion at 5 K, bottom panel fig 28. Changes in the intensity and frequency of the shape components during the spin isomer conversion process indicate some interactions between neighbouring endohedral H_2O molecules are present; and perturbations must be associated with populations of the para/ortho-H_2O ground states.[293] Furthermore, the absence of such effects at low filling factors further supports this observation, as the average distance between H_2O's is smaller for larger filling factors.[293]

The line-shapes in fig. 28 **a** and **b** appear as mirror images of each other, which is still a mystery, as they originate in the same para-$H_2O@C_{60}$ ground state and end up in the same rotational state; only the vibrational excitation is different between the two.[293] Additionally, during the spin isomer conversion process, the line-shapes develop a blue-shift for

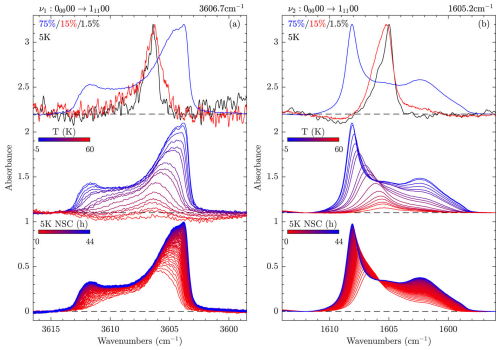

FIG. 28. Details of the $|J_{Ka\ Kc}\ N\ L\rangle = |0_{00}\ 0\ 0\rangle \rightarrow |1_{11}\ 0\ 0\rangle$ transition from para-H_2O@C_{60} in the ν_1 (a) and ν_2 (b) ranges of solid H_2O@C_{60}. (Top) Normalized IR spectra from samples having a fill ratio of 75% (blue), 15% (red), and 1.5% (black). They were acquired at thermodynamic equilibrium at 5 K for para-H_2O@C_{60}. (Middle) Normalized IR spectra from solid H_2O@C_{60} samples having a fill ratio of 75%, obtained at thermodynamic equilibrium for temperatures of 5, 6, 7.5, 8, 9, 10, 12.5, 13.5, 15, 20, 25, 30, 35, 40, 45, and 60 K. IR spectra are normalized to the intensity maximum of each transition over the temperature range. They are colour-coded from the coolest (blue) to the warmest (red). (Bottom) Normalized IR spectra from solid H_2O@C_{60} samples having a fill ratio of 75% acquired during nuclear spin isomer conversion at 5 K. IR spectra are normalized to the intensity maximum of each transition at thermodynamic equilibrium at 5 K. They are colour-coded from their warmest (red) to their coolest (blue) nuclear spin isomer populations. Reprinted from (ref. 293) Chartrand *et al.*, J. Chem. Phys., **162**, 144312 (2025), with the permission of AIP Publishing.

ν_1 and a red-shift for ν_2 (bottom panel fig. 28), currently unexplained.[293] Additional research is required to elucidate and characterise such collective dynamics in endofullerenes.

I. CH_4@C_{60} INS

INS investigations have been performed on CH_4@C_{60}.[180] At 1.6 K on the neutron energy loss side, peaks are observed at: 1.3 meV for $J = 0 \rightarrow 1$ and 3.87 meV for $J = 0 \rightarrow 2$. These transitions match very well with the free CH_4 rotor model: 1.3 meV for $J = 0 \rightarrow 1$ and 3.9 meV for $J = 0 \rightarrow 2$. However, the $J = 0 \rightarrow 3$ transition displays two peaks at 7.05 meV and 8.9 meV, and the free rotor model predicts only one peak at 7.8 meV.[180] This splitting is most likely caused by the I_h symmetry of the confining potential, caused by the enclosing C_{60} cage. In I_h symmetry, the allowed values for λ (which describe the symmetry of the potential) are $\lambda = 0, 6, 10, ...$, see section II E 1 for more information. The rank $\lambda = 6$ term is capable of causing a splitting of the $J = 3$ rotational state.[133,150,155,180] At 1.6 K on the neutron energy gain side, only one peak is observed at -1.3 meV, corresponding to the $J = 1 \rightarrow 0$ transition.[180] This peak originates in a metastable state of the CH_4 (the ortho-CH_4, see below), because significant time has passed during cooling before the data acquisition began. Additional neutron energy loss peaks are observed originating from this metastable state, completely analogous to the $J = 0$ transitions above, see ref. 180.

1. CH_4@C_{60} *INS: nuclear spin isomer conversion*

CH_4 displays three nuclear spin isomers: meta (total nuclear spin $I = 2$), ortho ($I = 1$) and para ($I = 0$).[180] Temperature jump experiments measured the ortho-CH_4 $\leftrightarrow$ meta-CH_4 nuclear spin isomer conversion time. At 10 K the conversion time is 723 ± 195 min for the $J = 1 \rightarrow 0$ transition and 662 ± 122 min for $J = 0 \rightarrow 1$; at 15 K the conversion time is 175 ± 79 min for the $J = 1 \rightarrow 0$ transition and 121 ± 26 min for $J = 0 \rightarrow 1$.[180] No metastable state was observed for para-CH_4, concluding that its lifetime must be too short to be detected on the timescale of the INS experiments.

J. CH_2O@C_{60} molecular motion

1. CH_2O@C_{60} *THz*

The THz (far-IR) spectrum of CH_2O@C_{60} consists of two peaks ($5 - 80$ K), at 166.8 cm^{-1} and 231.1 cm^{-1}.[21] They correspond to transitions between the quantised translational modes of CH_2O confined in C_{60}, see section II C. The qualitative explanation for the two modes involves the anisotropic shape of the CH_2O molecule. Translation along the long axis of the molecule (along the CO bond) experiences a tighter fit in the cage compared with translation perpendicular to the long axis. Thus, translation along the long axis is expected at higher energy (231 cm^{-1}) and perpendicular to it at lower energy (167 cm^{-1}). Quantum chemistry calculations are in good agreement with the experiment for the translational modes.[21]

2. CH_2O@C_{60} *IR: spin isomer conversion*

Nuclear spin isomers of endohedral CH_2O have been observed in CH_2O@C_{60}.[21] CH_2O has two identical Hydrogens, which through the Pauli exclusion principle lead to two spin isomers: Ortho and Para, same as H_2 and H_2O (see section II H). The nuclear spin isomer conversion of CH_2O@C_{60} was measured for the first time in the solid state, at cryogenic temperatures using the IR active CH_2O vibration at $\sim$1255 cm^{-1}.[21] The spin isomer conversion rate is measured to be 13.3 ± 0.4 min at 5 K. Observing the spin isomer conversion in endohedral CH_2O indicates that the rotation exchanging the two Hydrogen atoms (around the CO bond) is mostly unhindered even at cryogenic temperatures.[21]

VIII. ELECTRONIC STRUCTURE SPECTROSCOPIES

This section is about electronic structure spectroscopies, involving higher energies than in the previous sections. They

represent transitions involving rearrangements of electronic structure (section II G), i.e. electronic transitions, usually falling in the visible range of light. At the lower end is the near-IR range and at higher energy is the UV or near-UV. Common is UV-vis spectroscopy, which measures the absorbance against frequency for visible and UV light – mostly probing electronic transitions. Other techniques usually employ light excitation using a laser.

A. $He@C_{60}^+$ electronic (near-IR) spectroscopy

Electronic (near-IR) spectroscopy has been performed on the $He@C_{60}$ endofullerene (^{4}He isotope). On the cationic species in the gas phase, and with helium tagging. The $He@C_{60}^+ - He_n$ species have been investigated, where $n = 1-4$, between 9300 – 9700 Å (10752.7 – 10309.3 cm^{-1}) at 3.9 K.[14] The electronic spectra are obtained by photofragmentation of the (endo)fullerene cage – Helium complex, upon laser irradiation. The observed transitions belong to the encapsulating fullerene cage.[14]

The effect of tagging (exohedral adsorption) the fullerene cages with Helium is revealed. Upon tagging one Helium atom, the absorption lines of the C_{60} fullerene are redshifted by 0.7 Å. Furthermore, the effect is linear, redshifting by 0.7 Å with each adsorbed Helium atom.[14] Using this effect, the absorption frequencies of $He@C_{60}^+$ can be determined by extrapolating the $He@C_{60}^+ - He_n$ experimental results to $n = 0$.[14]

Firstly, the electronic spectrum of $He@C_{60}^+ - He$ is blueshifted by 2 – 3 Å compared to $C_{60}^+ - He$. Thus, endohedral He encapsulation leads to the opposite effect of exohedral adsorption, blueshift vs. redshift.[14] Secondly, there is no significant difference in the absorption cross-section between the filled and empty fullerene cages – so the endohedral Helium does not significantly affect the near-IR absorption of the fullerene cage.[14]

Implications for detecting the $He@C_{60}^+$ molecule in space are discussed in ref. 14. Furthermore, refs. 7–13 discuss more about detecting (endo)fullerenes in space.

B. $Ar@C_{60}$ UV-vis

No observable differences are observed between the UV-vis spectra of $Ar@C_{60}$ and C_{60} (room temperature in toluene).[101,233,296]

C. $Kr@C_{60}$ electronic spectroscopy

1. $Kr@C_{60}$ *UV-vis*

UV-vis measurements of $Kr@C_{60}$ (dissolved in methylcyclohexane/isopentane glasses at 77 K), compared with C_{60}, reveal a red-shift of ∼45 cm^{-1} for the bands around 600 nm ($^1T_{1g} \leftarrow^1 A_{1g}$) and a blue-shift of $10-15$ cm^{-1} for the bands around 400 nm ($1^1T_{1u} \leftarrow^1 A_{1g}$).[73] However, in toluene at room temperature the UV-vis spectrum of $Kr@C_{60}$ is almost identical to C_{60}, with some uncertain small red-shifts around 600 nm.[102]

2. $Kr@C_{60}$ *photoexcited electronic triplet: lifetime*

C_{60} can be excited to an electronic triplet state by strong laser irradiation, see section IV D. Transient absorbance decay kinetics can measure the lifetime of the photoexcited electronic triplet state. The electronic triplet state lifetime of $Kr@C_{60}$ at 77 K is found to be 12% faster than that of empty C_{60}, 4760 s^{-1} compared with 4240 s^{-1} respectively.[73]

D. $N@C_{60}$ electronic spectroscopy

1. $N@C_{60}$ *UV-vis*

UV-vis measurements of dilute $N@C_{60}$ (2×10^{-5} M) and C_{60} in hexane effectively show no difference between the two.[297] Also, in toluene there is no observable difference from 300 – 1000 nm.[232]

2. $N@C_{60}$ *photoexcited electronic triplet: lifetime*

C_{60} can be excited to an electronic triplet state by strong laser irradiation, see section IV D. Transient absorbance decay kinetics can measure the lifetime of the photoexcited electronic triplet state. The photo excited electronic triplet lifetime of $N@C_{60}$ (in toluene at room temperature) is measured to be mono-exponential with a lifetime of 2.3 μs, whereas C_{60} is 51 μs under the same conditions.[232] This 22-fold difference in the lifetimes (decay constants 1.9×10^4 s^{-1} for C_{60} and 4.4×10^5 s^{-1} for $N@C_{60}$) indicates the C_{60} electronic triplet decay rate is drastically enhanced by the endohedral Nitrogen atom; likely due to the unpaired electrons on N ($S = 3/2$).[232]

E. $H_2@C_{60}$ electronic spectroscopy

1. $H_2@C_{60}$ *UV-vis*

The UV-vis spectrum of $H_2@C_{60}$ is the same as that of C_{60} (cyclohexane, room temperature).[234]

2. $H_2@C_{60}$ & $D_2@C_{60}$ *photoexcited electronic triplet: lifetimes*

C_{60} can be excited to an electronic triplet state by strong laser irradiation, see section IV D. Transient absorbance decay kinetics can measure the lifetime of the photoexcited electronic triplet state. The triplet lifetimes of C_{60}, $H_2@C_{60}$ and $D_2@C_{60}$ were measured in toluene at 285 K to be 110 ± 8 μs, with no measurable difference between them.[231]

3. H_2@C_{60} photoexcited electronic triplet state: spin isomer conversion

Since H_2 has two indistinguishable Hydrogen nuclei, it displays nuclear spin isomerism: ortho-H_2 and para-H_2 (see section II H). Photo-exciting the C_{60} cage leads to an electronic triplet state on the fullerene (see section IV D).

As a result of photo-excitation, the "paramagnetic skin" of the fullerene molecule could act as a spin catalyst for the nuclear spin isomer conversion of endohedral H_2.[298] Unfortunately, this did not work for $H_2@C_{60}$ which displayed no observable ortho-para conversion; but it was very efficient for $H_2@C_{70}$ (77 K in toluene-d_8).[298] The reason is believed to be the triplet lifetime of the fullerene cages, for $H_2@C_{70}$ the triplet lifetime is long, 49 ± 2 ms, whereas for $H_2@C_{60}$ is much shorter, 0.21 ± 0.01 ms at 77 K in toluene-d_8 (similar values are seen for empty C_{70} and C_{60}).[298] Interestingly, no significant spin isomer conversion occurred in $H_2@C_{70}$ when generating the electronic triplet state at room temperature, most likely due to very short C_{70} triplet lifetimes at room temperature.[298]

4. H_2@C_{60}^+ electronic (near-IR) spectroscopy

$H_2@C_{60}$ has been investigated using electronic (near-IR) spectroscopy in the gas phase, in ionic form using Helium tagging (more details in section VIII A), namely the $H_2@C_{60}^+ - He$ species. Measurements are performed at 3.7 K between $860 - 970$ nm ($11627.9 - 10309.3$ cm^{-1}). The observed transitions belong to the encapsulating cage.[13]

IR spectroscopy on $H_2@C_{60}^+$ is shown in section VII F 6.

When comparing the $H_2@C_{60}^+ - He$ electronic spectra with $C_{60}^+ - He$ some distinct differences are observed. The $H_2@C_{60}^+ - He$ signals are blue-shifted by about 1.5 nm and exhibit additional splittings.[13] The endohedral H_2 significantly perturbs the electronic excited states of C_{60}^+.

The electronic blue-shift caused by endohedral H_2 encapsulation is much larger than the shifts caused by exohedral adsorption of Ne, Ar, N_2, H_2 or D_2 onto C_{60}^+. Furthermore, exohedral adsorption generally causes red-shifts and not blue-shifts like endohedral encapsulation.[13,299]

The upper limit for the interstellar $H_2@C_{60}^+/C_{60}^+$ ratio is determined to be ~ 0.1.[13] Furthermore, refs. 7–12,14 discuss more about detecting (endo)fullerenes in space.

F. HF@C_{60} UV-vis

UV-vis measurements on $HF@C_{60}$, at room temperature in toluene and hexane, show no detectable difference from the empty C_{60} measurement.[20]

G. $H_2O@C_{60}$ electronic spectroscopy

1. $H_2O@C_{60}$ UV-vis

The UV-vis spectrum of $H_2O@C_{60}$ is essentially indistinguishable from that of empty C_{60} in toluene. Indicating that there is no detectable interaction between H_2O and C_{60}.[98]

2. $H_2O@C_{60}^+$ & $D_2O@C_{60}^+$ electronic (near-IR) spectroscopy

Electronic (near-IR) spectroscopy has been performed on the cationic species $C_{60}^+ - He$, $H_2O@C_{60}^+ - He$ and $D_2O@C_{60}^+ - He$ in the gas phase.[300] Performed using Helium tagging (Helium atoms exohedrally adsorbed on the fullerene), more details in section VIII A. The near-IR data are obtained from photofragmentation of the complexes (expulsion of the adsorbed Helium) upon laser irradiation, in the range $10400 - 10700$ cm^{-1} at 4 K. Mostly transitions corresponding to the cage are seen, but transitions of the endohedral H_2O are also observed.[300]

Minor perturbations of the electronic transitions are present due to the exohedrally adsorbed Helium atoms. $H_2O@C_{60}^+ - He_n$ displays a red-shift of 0.77 cm^{-1} per Helium, which scales linearly with n the number of He atoms. The adsorbed He atom is ignored in the analysis and $H_2O@C_{60}^+ - He$ is treated as $H_2O@C_{60}^+$; same for $D_2O@C_{60}^+$ and C_{60}^+.[300]

Comparing the electronic transitions of C_{60}^+ and $H_2O@C_{60}^+$ shows striking differences. C_{60}^+ should be Jahn-Teller distorted and it has two electronic transitions around 10400 cm^{-1} ($^2B_g \leftarrow \tilde{X}^2A_u$ and $^2A_g \leftarrow \tilde{X}^2A_u$), whereas $H_2O@C_{60}^+$ shows only one such transition. Besides the strong absorption peaks, additional weaker signals are seen $9 - 250$ cm^{-1} away from the electronic transition of $H_2O@C_{60}^+$, peaks a-f in fig. 29.[300] These frequencies match the energies for rotations or translations of endohedral water in $H_2O@C_{60}$, but are too low for vibrations – see section VII H. Most of the weak transitions are assigned to rotations or translations of the endohedral water, with some uncertainties. This demonstrates that it is possible to have electronic transitions of the C_{60}^+ fullerene cage accompanied by rotations/translations of the endohedral water.[300] Other such examples are seen for $H_2O@C_{60}^-$ and $H_2O@C_{59}N^-$, in section IX E 3.

Electronic (near-IR) spectra of individual spin isomers of $H_2@C_{60}^+$ and $D_2O@C_{60}^+$ (see section II H for spin isomerism) are observed by employing a two colour hole burning method; see fig. 29 for $H_2O@C_{60}^+$.[300] The assignment of the spin isomers is done based on the proportion of leftover signal upon hole burning. For $H_2O@C_{60}^+$ the leftover signal is 25% for para and 75% for ortho; whereas for $D_2O@C_{60}^+$ it is 33.3% for para and 66.6% for ortho. Thus, rotations/translations of endohedral water (inside electronic excited state C_{60}^+) are unambiguously associated with each spin isomer.[300]

For $H_2O@C_{60}^+$ it appears that if $K_a + K_c$ (rotational quantum numbers of H_2O) is even that corresponds to ortho water, which is opposite to neutral $H_2O@C_{60}$ (or free H_2O).[300] This

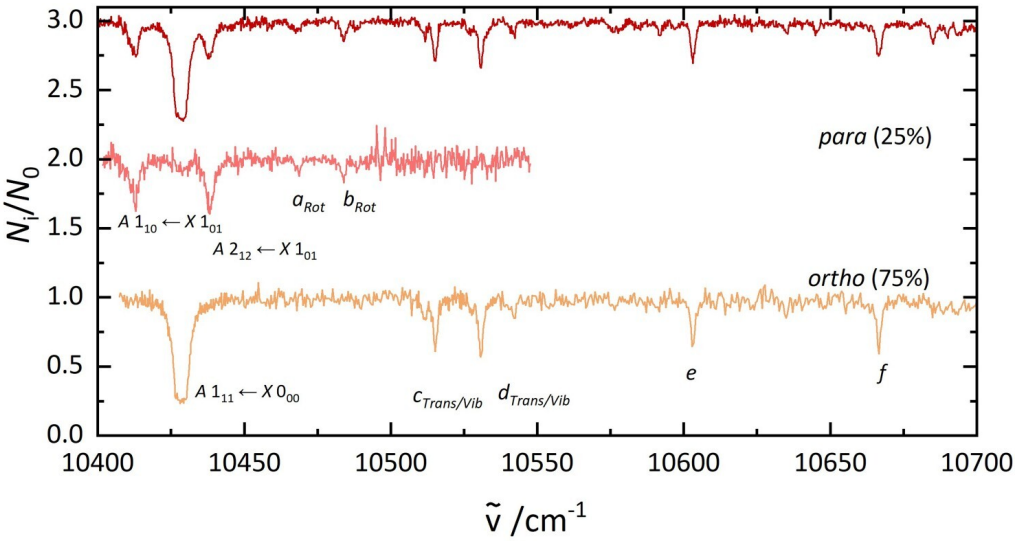

FIG. 29. Electronic (near-IR) spectra of $H_2O@C_{60}^+$ (top), para-$H_2O@C_{60}^+$ (middle), and ortho-$H_2O@C_{60}^+$ (bottom). The lower two traces were obtained in 2 colour experiments. The middle spectrum was recorded by fragmenting all complexes that absorb at 10429 cm^{-1}. The bottom spectrum was recorded after irradiation at 10438 cm^{-1}. Open access reprint from ref. 300.

indicates that the electronic wavefunction of $H_2O@C_{60}^+$ is antisymmetric with respect to the exchange of the Hydrogen nuclei, since all other wavefunctions (vibrational, rotational and nuclear) are the same as for neutral $H_2O@C_{60}$.[300]

The spectrum of $D_2O@C_{60}^+$ differs significantly from $H_2O@C_{60}^+$.[300] First, the intensity pattern of the peaks is different. Second, the separation between the peaks is smaller because of the isotope effect (as expected). Furthermore, the isotope effect is used to confirm the assignments. Most of the observed transitions are assigned, although some are uncertain due to the difficulty in modelling electronic transitions of C_{60}^+.[300]

H. $CH_2O@C_{60}$ UV-vis

The UV-vis spectrum of $CH_2O@C_{60}$ (toluene, room temperature) is red-shifted by -6 nm with respect to empty C_{60} (corresponds to -18 meV).[21] This difference between the electronic orbitals of C_{60} filled with CH_2O and empty C_{60} is the largest observed to date for non-metallic endofullerenes.[21]

IX. IONISATION SPECTROSCOPIES AND TECHNIQUES

This section involves high energy spectroscopical methods, performed with UV or X-ray radiation, that lead to ionisation of the endohedral species or the fullerene cage. For more background information see section III D.

A. $Ar@C_{60}$ ionisation spectroscopy

1. $Ar@C_{60}$ *XPS*

X-ray photoelectron spectroscopy (XPS), section III D, has been performed on low filling factor ($\sim 0.1\%$) $Ar@C_{60}$.[70] The XPS spectrum displays a multiplet corresponding to the 2p orbital of Ar: $2p_{1/2}$ at ~ 245 eV and $2p_{3/2}$ at ~ 243 eV.[70]

A similar XPS spectrum is obtained for Ar inserted into graphite by ion implantation; but redshifted by ~ 2 eV compared with $Ar@C_{60}$.[70]

2. $Ar@C_{60}$ *VB-XPS*

Valence-band X-ray photoemission spectra (VB-XPS), section III D 1, show no difference between the cage molecular orbitals of $Ar@C_{60}$ and C_{60}.[195] However, at 15 eV the Ar $3p$ orbital of $Ar@C_{60}$ is observed. This ionisation potential is higher for Ar in the gas phase, 15.76 eV, and it also displays an observable 177 meV spin-orbit splitting − which is absent in $Ar@C_{60}$.[195]

Through DFT calculations, the Ar $3p$ orbital is shown to interact with the C_{60} $6T_{1u}$ orbital of the same symmetry and similar energy. This leads to hybridisation of the Ar $3p$ and

C_{60} $6T_{1u}$ orbitals, resulting in bonding and anti-bonding orbitals, 1.6 ± 0.2 eV apart in energy.[195]

3. Ar@C_{60} *EXAFS*

EXAFS (extended X-ray absorption fine structure), section III D 2, experiments have been performed on Ar@C_{60} at the Ar K-edge.[301] The EXAFS analysis gives the average Ar−C distance of ∼3.55 Å; and this distance is shown to decrease by a small amount with increasing temperature. However, the Debye-Waller factor for the Ar−C distance increases with increasing temperature.[301]

4. Ar@C_{60} *NIXSW*

Normal incidence X-ray standing wave (NIXSW), section III D 3, measurements have been performed on Ar@C_{60} adsorbed on a Ag(111) surface.[302] Interpretation of the NIXSW results estimates the position of the endohedral Ar atom to be 5.54 ± 0.04 Å above the Ag(111) surface.[302] For NIXSW measurements of HF@C_{60} and H_2O@C_{60} see section IX D and IX E 2.

The position of the endohedral atom inside the cage differs between bulk endofullerenes and endofullerenes adsorbed on a surface. When fullerenes are chemisorbed on a surface, charge redistribution occurs, which produces an electric field inside the cage. The distance of the Ar above the Ag(111) surface is consistent with Ar@C_{60} PAW-DFT calculations and LEED measurements on empty C_{60}.[302]

5. Ar@C_{60} *core hole clock measurements*

The Auger-Meitner resonant Raman variant of the core clock technique was used to measure the delocalisation (tunnelling) time of a photoexcited Ar electron in Ar@C_{60}.[302–304] This core clock technique is an energy domain variant of ultrafast pump-probe spectroscopy, capable of measuring the rate of electron transfer from tens of attoseconds to hundreds of femtoseconds.[302,304] The photoexcited electron can be a spectator during an Auger-Meitner process or it can delocalise beforehand (i.e. the electron tunnelled away before the core hole decay). The characteristic delocalisation (charge transfer) time τ_D is measured from the ratio of these two processes.[302,304]

X-ray irradiation was used to excite an Ar electron (in Ar@C_{60}) from a core $2p$ orbital to a $4s$ orbital. The core hole clock technique then probes the characteristic delocalisation time of the $4s$ electron. The full width at half-maximum of the $2p_{3/2} \rightarrow 4s$ absorption peak is 280 ± 10 meV, compared with ∼ 120 meV for gas phase Ar.[302] Furthermore, the Ar $2p_{3/2} \rightarrow 4s$ resonance is found to be 4.80 ± 0.15 eV above the HOMO.[302]

The characteristic delocalisation time τ_D is 6.6 ± 0.3 fs for bulk Ar@C_{60} and $\lesssim 500$ attoseconds for a monolayer of Ar@C_{60} adsorbed on a Ag(111) surface.[302] Compared with a few fs for Ar directly adsorbed on a metal, $3 - 16$ fs when a graphene monolayer is present in between the Ar & the metal surface and over 50 fs for Ar decoupled from the substrate by an underlying layer of Ar/Xe.[302] The enclosing C_{60} cage seems to facilitate the electron transfer to the metal surface. Furthermore, the delocalisation time τ_D becomes shorter as a function of increasing X-ray energy; which is entirely opposite to Ar directly adsorbed on metal surfaces.[302]

Quantum chemistry calculations predict that the Ar $4s$ orbital extends beyond the C_{60} cage for both the ground and excited states.[302] More than 80% of the density lies beyond the fullerene cage. The ground state unoccupied $4s$ orbital has 92% Ar character, whereas the excited state only has 13%. The excited state Ar-C_{60} hybrid orbital appears to couple substantially with the Ag(111) electronic structure, shortening the delocalisation time. This diffuse nature of the excited state combined with the dominant C_{60} character is indicative of superatomic molecular orbitals.[302]

B. Kr@C_{60} EXAFS

EXAFS (extended X-ray absorption fine structure), section III D 2, experiments were performed on Kr@C_{60} at the Kr K-edge.[196] Some differences are seen in the Kr@C_{60} EXAFS response between low and high temperature, indicating the rotation of the fullerene cages at room temperature affects the EXAFS response.[196] Furthermore, the Kr−C path distance is estimated to be 3.540(7) Å and 3.537(10) Å at 80 K and 300 K respectively.[196,285]

Such results, together with Kr@C_{60} IR measurements[285] (section VII D 2), appear to be consistent with C_{60} fullerenes exhibiting negative thermal expansion at low temperatures.[196,285]

C. Xe@C_{60}^+ Confinement resonances photoionisation

Confinement resonances, section III D 4, have been observed in endofullerenes, specifically in the Xe@C_{60}^+ molecular ion.[199–201]

Xe@C_{60}^+ ions in the gas phase were irradiated with synchrotron radiation (vacuum ultra-violet to soft X-rays). Performed by counter-propagating a beam of Xe@C_{60}^+ molecular ions with a monochromatic synchrotron beam of $60 - 150$ eV (ionisation energy of the Xe $4d$ electrons).[199–201]

A significant increase in the photoionisation cross section is observed in the range $70 - 140$ eV when Xe is present inside C_{60}^+ as compared with empty C_{60}^+.[199–201] Oscillations in the energy dependence of the photoionisation cross section for Xe@C_{60}^+ prove the observation of confinement resonances (multipath interference); since photoionisation of free Xe or empty C_{60}^+ does not present such oscillations.[199] Fig. 30 displays such oscillations in the photoionisation cross section of Xe@C_{60}^+, with the contribution from free Xe removed.[200] Interference is pronounced here because the de Broglie wavelength of $5 - 70$ eV photoelectrons (ionised by $70 - 140$ eV

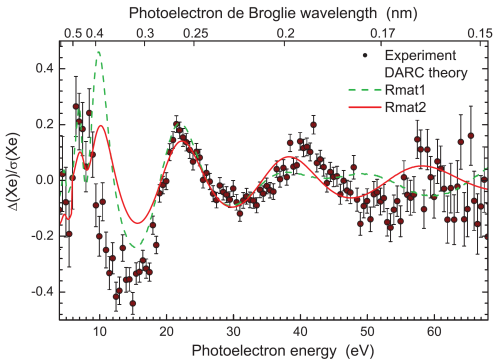

FIG. 30. Oscillatory structure of the encapsulated Xe photoionization cross section made visible by displaying the ratio $\Delta(Xe)/\sigma(Xe) = [\sigma(Xe@C_{60}^+) - \sigma(Xe)]/\sigma(Xe)$ as a function of the photoelectron energy and the photoelectron de Broglie wavelength, respectively. More details about the experiment and theoretical analysis are found in ref. 200. At a 4*d* photoelectron energy of 21 eV, about five de Broglie half waves fit inside the inner diameter of the C_{60} cage. Reprinted figure with permission from (ref. 200) Phaneuf *et al.*, Phys. Rev. A, **88**, 053402 (2013). Copyright (2013) by the American Physical Society.

synchrotron radiation) is comparable with the ∼0.7 nm diameter of the C_{60} cage.[200]

Using a simplified model, treating the fullerene cage as a hard sphere (which has limitations), and interpreting the confinement resonance data (fig. 30) gives reasonable results: a 0.35 nm radius for C_{60}^+ and a carbon shell thickness of 0.09 nm.[200]

Furthermore, analysing the different ion channels after photoionisation indicates that the presence of Xe inside the fullerene cage leads to enhanced fragmentation of the C_{60}. The endohedral Xe atom converts the photon energy to molecular vibrational energy − displaying potential practical applications.[200]

D. HF@C_{60} Normal incidence X-ray standing wave (NIXSW)

Normal incidence X-ray standing wave (NIXSW), section III D 3, measurements have been performed on HF@C_{60} adsorbed on a Ag(111) surface.[198] Interpretation of the NIXSW results estimates the position of the Fluorine (in HF@C_{60}) to be 5.7 ± 0.1 Å above the Ag(111) surface.[198] For NIXSW measurements of Ar@C_{60} and H_2O@C_{60} see sections IX A 4 and IX E 2.

The position of the endohedral molecule inside the cage differs between bulk endofullerenes and endofullerenes adsorbed on a surface. When fullerenes are chemisorbed on a surface, charge redistribution occurs, which produces an electric field inside the cage. Endohedral molecules are affected by this intra-cage electric field and can have different positions inside the cage, compared with the bulk endofullerene material.[198]

E. H_2O@C_{60} ionisation spectroscopy

1. H_2O@C_{60} *VB-XPS*

Valence band X-ray photoemission spectroscopy (VB-XPS), section III D 1, acquired with 110 eV photon energy, effectively shows no difference between C_{60} and H_2O@C_{60}.[198] This further strengthens the argument that upon encapsulation, endohedral species are electrostatically screened and decoupled from the environment.[198] However, there is evidence that the endohedral H_2O molecule "senses" the change in electrostatic potential when H_2O@C_{60} is adsorbed on a Ag(111) surface. Adsorption leads to charge transfer into the LUMO of the fullerene cage, changing the electrostatic potential inside the cage, see section IX E 2.[198]

2. H_2O@C_{60} *NIXSW*

Normal incidence X-ray standing wave (NIXSW), section III D 3, measurements have been performed on H_2O@C_{60} adsorbed on a Ag(111) surface.[198] Interpretation of the NIXSW results estimates the position of the Oxygen (in H_2O@C_{60}) to be 5.57 ± 0.03 Å above the Ag(111) surface.[198] For NIXSW measurements of Ar@C_{60} and HF@C_{60} see sections IX A 4 and IX D.

The position of the endohedral molecule inside the cage differs between bulk endofullerenes and endofullerenes adsorbed on a surface. When fullerenes are chemisorbed on a surface, charge redistribution occurs, which produces an electric field inside the cage. Adsorption leads to charge transfer into the LUMO of the C_{60} cage, changing the electrostatic potential inside the cage.[198] Endohedral molecules are affected by this intra-cage electric field and can have different positions inside the cage, compared with the bulk endofullerene material.[198]

3. H_2O@C_{60}^- & H_2O@$C_{59}N^-$: *Electron affinity (EA) and ionisation potential*

High resolution photoelectron (section III D) imaging studies have been performed on H_2O@C_{60}^- and H_2O@$C_{59}N^-$ in the gas phase.[105] In the photoelectron (PE) spectrum of H_2O@C_{60}^-, a sharp peak (0_0^0) is seen for the transition from the anion H_2O@C_{60}^- to the neutral species H_2O@C_{60}, corresponding to the electron affinity (EA) energy. Above the EA energy, multiple peaks are observed, corresponding to transitions from the ground vibrational state of the anion to the excited vibrational states of the neutral species. Small differences are seen between the empty and filled cages, most of the peaks corresponding to the fullerene cage. However, a few peaks are observed that are not present in the empty species at: 35 cm^{-1} & 95 cm^{-1} (away from the EA energy) for H_2O@C_{60}^- and at 74 cm^{-1} & 128 cm^{-1} for H_2O@$C_{59}N^-$.[105]

Such transitions correspond to rotations of the water molecule inside the cage, although the differences in energy are rather large between $H_2O@C_{60}^-$ and $H_2O@C_{59}N^-$.[105] Very similar energies are observed for the neutral species $H_2O@C_{60}$, see section VII H. This shows that it is possible to have transitions of the C_{60}^- & $C_{59}N^-$ fullerene cages accompanied by rotations/translations of the endohedral H_2O.[105] Other such examples are seen for $H_2O@C_{60}^+$ and $D_2O@C_{60}^+$ in section VIII G 2.

Measuring the PE spectra and EA's for all C_{60}^-, $H_2O@C_{60}^-$, $C_{59}N^-$ and $H_2O@C_{59}N^-$, gives the difference in EA's when an endohedral species is present.[105] The EA for $H_2O@C_{60}$ was measured to be 2.6923 ± 0.0008 eV, which is 8.8 meV higher than C_{60}; and the EA for $H_2O@C_{59}N$ is 3.0058 ± 0.0007 eV, 9.2 meV lower than $C_{59}N$.[105]

The opposite shifts of the EA's for $H_2O@C_{60}$ and $H_2O@C_{59}N$ can be understood from a simple electrostatic model between the HOMO of the fullerene anion and the partial charges on H_2O.[105] For C_{60}^- the electron is delocalised over the whole cage, whereas $C_{59}N^-$ has the electron mostly localised around the Nitrogen atom. DFT calculations show that for $H_2O@C_{59}N^-$ the water molecule has the Oxygen atom pointing towards the Nitrogen.[105] This will destabilise the complex because of electrostatic repulsion between the electronegative Oxygen and the extra electron centred on the Nitrogen atom. Whereas for $H_2O@C_{60}^-$, there is no preferred orientation and the interaction between H_2O and C_{60}^- is attractive (the complex is stabilised). Thus, for $H_2O@C_{59}N$ one expects the EA to be lower than $C_{59}N$, and for $H_2O@C_{60}$ and C_{60} the opposite, as observed.[105]

X. OTHER NON-SPECTROSCOPICAL TECHNIQUES

A. Crystallography

Performing crystallographic experiments on (endo)fullerenes is notoriously challenging because of the difficulty in making single crystals. Some powder X-ray (PXRD) crystallographic measurements of pristine endofullerenes are presented in the following sections. Single crystal measurements performed on co-crystals of (endo)fullerenes are briefly mentioned below.

1. *Single crystal diffraction of endofullerene co-crystals*

Single crystal measurements have been performed on co-crystals of (endo)fullerenes, usually porphyrin complexes.[305] Single crystal diffraction measurements can be found for co-crystals containing the following endofullerenes: $He@C_{60}$[27], $Ne@C_{60}$[100], $Kr@C_{60}$[102,305], $HF@C_{60}$[20], $H_2O@C_{60}$[98], $CH_4@C_{60}$[103], $CH_2O@C_{60}$[21], $(He \cdot N)@C_{60}$[27], $H_2O@C_{70}$[26] and $(HF \cdot H_2O)@C_{70}$[29].

2. $Ar@C_{60}$ *crystallography*

Powder X-ray diffraction (PXRD) measurements performed on $Ar@C_{60}$ show that the unit cell parameter of $Ar@C_{60}$ is 0.022 Å larger than empty C_{60} at room temperature. However, at low temperature, they switch: at 100 K the $Ar@C_{60}$ unit cell parameter is slightly smaller than C_{60}, with the crossover appearing around 200 K.[233,296]

PXRD of $Ar@C_{60}$ clearly shows the presence of the (200) reflection, corresponding to the Ar atom in the centre of the cage. Furthermore, the electronic density of $Ar@C_{60}$ simulated using the maximum entropy method (MEM), clearly shows significant electronic density for the carbon cage framework and for the endohedral Ar atom at the centre of the C_{60} cage.[233]

a. $K_3(Ar@C_{60})$ crystallography

PXRD measurements show a slightly smaller unit cell parameter for $K_3(Ar@C_{60})$ than K_3C_{60} .[233,296]

3. $H_2@C_{60}$ *crystallography*

Powder X-ray diffraction measurements have been performed on $H_2@C_{60}$.[92] Maximum Entropy Method (MEM) Rietveld analysis gives the electron density of the $H_2@C_{60}$ endofullerene. Such results determine the position of the endohedral H_2 to be at the centre of the fullerene cage.[92]

4. $H_2O@C_{60}$ *crystallography*

Powder X-ray diffraction measurements have been performed on $H_2O@C_{60}$ $(20 - 300$ K$)$.[306] The lattice constant for $H_2O@C_{60}$ at 300 K is slightly larger than empty C_{60}, but at 252 K they are almost equal. The $Fm\bar{3}m \rightarrow Pa\bar{3}$ fullerene phase transition (see section IV A 2) occurs at 257(1) K for $H_2O@C_{60}$, same as for empty C_{60}.[306]

At 20 K the mean square displacement of the Oxygen atom is three times larger than the Carbon. This demonstrates the, mostly unhindered, translational and rotational mobility of H_2O inside the C_{60} cage.[306]

Maximum Entropy Method (MEM) Rietveld analysis gives the electron density of the $H_2O@C_{60}$ endofullerene. Such results determine the position of the endohedral H_2O to be at the centre of the fullerene cage.[306]

B. Superconductivity

The fulleride materials M_3C_{60} (M = K, Rb, Cs, etc.) become type 2 superconductors at low temperatures, displaying superconducting transitions (T_c) below 40 K.[126,233,296] The fulleride cage can contain endohedral species leading to endofulleride materials. The superconducting transition T_c can be measured by bulk magnetisation measurements, usually employed using SQUID magnetometers.

1. $Rb_3(^3He@C_{60})$ superconductivity

$Rb_3(^3He@C_{60})$ with a filling factor of 22% displays a T_c of 30.7 ± 0.1 K.[126] This is comparable with the T_c of Rb_3C_{60} which is between $25-30$ K. The presence of endohedral ^3He does not disturb the superconducting transition temperature significantly.[126] The $Rb_3(^3He@C_{60})$ displays interesting ^3He NMR results, see section V B 4.

2. $K_3(Ar@C_{60})$ & $Rb_3(Ar@C_{60})$ superconductivity

The endofullerides $K_3(Ar@C_{60})$ and $Rb_3(Ar@C_{60})$ have been obtained in small quantities (<1 mg).[233,296] For the endofulleride $K_3(Ar@C_{60})$ T_c is 17.6 K and for K_3C_{60} T_c is 19.2 K, displaying a ~ 1.6 K difference.[233,296] For the endofulleride $Rb_3(Ar@C_{60})$ T_c is 26.8 K and for Rb_3C_{60} T_c is 29.3 K, displaying a ~ 2.5 K difference.[233,296]

However, impurities are detected in these samples. Thus, it cannot be ruled out that the observed differences between the T_c values are due to impurities, non-stoichiometry or inhomogeneities.

C. Voltammetry

Cyclic Voltammetry (CV) and Differential Pulse Voltammetry (DPV) experiments measure the redox potentials of a molecule, i.e. at which electrochemical potential the molecule can accept/donate electrons. In all the cases discussed here, small or no differences are observed between the empty C_{60} and the endofullerene analogue. Indicating that the interactions between the endohedral species and the cage are small, and that charge transfer does not occur between them or is very small.

1. $H_2@C_{60}$ Voltammetry

CV and DPV measurements on $H_2@C_{60}$, at room temperature in ODCB and in 1,1,2,2-tetrachloroethane, do not show measurable differences from empty C_{60}.[234] However, when performed in a mixture of toluene and acetonitrile at -10 °C, the $H_2@C_{60}$ reduction potentials increase in magnitude as more electrons are added to the cage. The measured reduction potentials are -0.95 V, -1.37 V, -1.89 V, -2.39 V, -2.95 V and ~ -3.5 V for $H_2@C_{60}$; and -0.95 V, -1.37 V, -1.88 V, -2.35 V, -2.88 V and -3.35 V for empty C_{60}.[234]

2. $HF@C_{60}$ Voltammetry

CV and DPV measurements on $HF@C_{60}$, at room temperature in toluene : acetonitrile $= 4:1$, do not show detectable differences from the empty C_{60} measurements.[20]

3. $H_2O@C_{60}$ Voltammetry

CV and DPV measurements of $H_2O@C_{60}$ in ODCB, with 0.1 M Bu_4NPF_6 as supporting electrolyte, give the redox potentials (vs. ferrocene) as: $+1.32$ V (irreversible), -1.08 V, -1.46 V, -1.91 V and -2.38 V.[98] These are almost the same as determined for empty C_{60}: $+1.32$ V (irreversible), -1.08 V, -1.47 V, -1.92 V and -2.39 V.[98] Furthermore, no difference was seen in the electrical conductance between $H_2O@C_{60}$ and C_{60}.[307]

4. $CH_2O@C_{60}$ Voltammetry

Voltammetry measurements have been performed on $CH_2O@C_{60}$ in toluene : acetonitrile $= 4:1$, containing 0.1 M Bu_4NPF_6 as the supporting electrolyte. CV and DPV measurements reveal that the first 4 reduction potentials of $CH_2O@C_{60}$ are shifted by -30 mV relative to empty C_{60}.[21] This difference between the electronic orbitals of C_{60} filled with CH_2O and empty C_{60} is the largest observed to date for non-metallic endofullerenes.[21]

D. Dielectric constant measurements

Measurements of the dielectric constants of $HF@C_{60}$ and $H_2O@C_{60}$ have been performed as a function of temperature. From such results, electric dipole moments and molecular polarizabilities can be determined.

1. $HF@C_{60}$ Dielectric constant measurements

Temperature dependent dielectric constant measurements of $HF@C_{60}$ can estimate the dipole moment of the endohedral HF molecule.[20] This is possible by using the gas phase free HF model in the temperature range $0-100$ K; because above 100 K the free HF model cannot reproduce the experimental data. The determined dipole moment for the endohedral HF is 0.45 ± 0.05 D, which is approximately 4 times smaller than for the gas phase HF.[20] A similar reduction in the dipole moment by a factor of four is seen for $H_2O@C_{60}$ below (section X D 2).

2. $H_2O@C_{60}$ dielectric constant & spin isomer conversion

The bulk dielectric permittivities of $H_2O@C_{60}$ and C_{60} have been measured as a function of temperature.[306] For C_{60} the permittivity is temperature independent, but for $H_2O@C_{60}$ it increases significantly as the temperature decreases (Curie−Weiss law). An upper limit for the dipole moment of the endohedral H_2O is estimated to be $\mu < 0.7$ D.[306]

Furthermore, for $H_2O@C_{60}$ the bulk dielectric constant is shown to depend on the ortho/para ratio of endohedral H_2O (see section II H for spin isomerism).[289] The capacitance (bulk

dielectric constant) of $H_2O@C_{60}$ follows the ortho/para ratio and can be used to measure the ortho-para conversion rate: of a few hours and following bi-molecular kinetics.[289] This ortho-para conversion rate is shown to be the same as measured by NMR (section V F 5).[289] From such measurements, the dipole moment of endohedral water in $H_2O@C_{60}$ is measured to be 0.51 ± 0.05 D, approximately four times smaller than for free H_2O.[289] The same value is obtained from THz spectroscopy of $H_2O@C_{60}$, 0.50 ± 0.05 D (section VII H 1).[187] Furthermore, by combining the capacitance and NMR measurements on $H_2O@C_{60}$, the polarizability volumes for the two endohedral spin isomers can be estimated: $\alpha^{\text{ortho}'} = 43 \pm 4$ Å^3 and $\alpha^{\text{para}'} = 29 \pm 3$ Å^3.[289]

E. Heat capacity measurements

Measurements of the specific heat capacity of endofullerene materials can detect significant contributions (to the heat capacity) from endohedral species.

1. $Ar@C_{60}$ & $Kr@C_{60}$ *differential scanning calorimetry*

Differential scanning calorimetry (DSC) measurements have been performed on C_{60}, $Ar@C_{60}$ and $Kr@C_{60}$ (0.9 mg, 0.205 mg and 0.05 mg respectively) between -50 °C and 110 °C.[233] The DSC measurements display a peak around $250-260$ K, corresponding to the rotational disordered $\rightarrow$ rotational ordered phase transition of the fullerene lattice $Fm\bar{3}m \rightarrow Pa\bar{3}$ (see section IV A 2). The phase transition of $Ar@C_{60}$ appears ~ 1.5 K lower than for C_{60}; and for $Kr@C_{60}$ the difference is larger, appearing ~ 5 K lower than for C_{60}.[233] However, the endofullerene samples do not appear to have been sublimed in this case, which can lead to changes in the phase transition temperature.

2. $H_2@C_{60}$ *specific heat capacity*

The specific heat capacity (or heat capacity) of $H_2@C_{60}$ is measured to be larger than C_{60} at all temperatures, attributed to additional contributions from endohedral H_2, see fig. 31.[92]

A peak is seen in the specific heat capacity against temperature around 260 K for both $H_2@C_{60}$ and empty C_{60}, fig. 31 (a). The peak appears due to the phase transition of the C_{60} or $H_2@C_{60}$ lattice from a rotational disordered to a rotational ordered phase, $Fm\bar{3}m \rightarrow Pa\bar{3}$, more details in section IV A 2.

For $H_2@C_{60}$ an anomaly is seen at 0.6 K, where a peak is observed in the specific heat against temperature (not present for C_{60}), fig. 31 (b). This is attributed to a small splitting of the triply degenerate $J = 1$ rotational ortho-H_2 state, with an energy separation of $0.1 - 0.2$ meV.[92] This splitting is due to a symmetry breaking effect seen for C_{60} endofullerenes, more details in section IV C. Merohedral disorder of the C_{60} lattice (section IV A 2) lowers the symmetry from Icosahedral to S_6, which can lift the degeneracy of the H_2 $J = 1$ rotational state.[92]

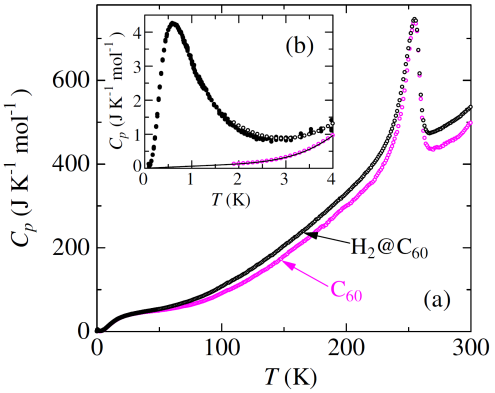

FIG. 31. Specific heat of C_{60} and $H_2@C_{60}$. Full temperature range in (a) and low temperature range in (b). Open circles are measured by a PPMS, and solid black circles are measured by a home-made calorimeter. The solid line was obtained by extrapolation. Reprinted figure with permission from (ref. 92) Kohama *et al.*, Phys. Rev. Lett., **103**, 073001 (2009). Copyright (2009) by the American Physical Society.

3. $H_2O@C_{60}$ *specific heat capacity & spin isomer conversion*

The specific heat capacity of $H_2O@C_{60}$ is measured to be larger than C_{60} at all temperatures, attributed to additional contributions from endohedral H_2O.[222]

An anomaly is seen for $H_2O@C_{60}$ at ~ 2 K where a shoulder is visible in the heat capacity.[222] The shoulder slowly disappears if the sample is kept at low temperature for a long time, during which the spin isomer conversion from ortho to para H_2O occurs. This proves the anomaly to be due to the ortho-H_2O spin isomer (see section II H for spin isomerism).[222]

The results are consistent with a split $J = 1$ ortho-H_2O rotational state (section IV C). However, the results suggest there should be two distinct environments for the endohedral H_2O, with different energy level structures and different spin isomer conversion rates.[222]

The spin isomer conversion rate can be measured from the time dependence of the $H_2O@C_{60}$ heat capacity at a given temperature. The endohedral H_2O spin isomer conversion rate is temperature independent below 13 K and above 13 K it becomes faster with increasing temperature.[222] Below 13 K the spin isomer conversion rate is bi-exponential and the two conversion times are estimated to be 1.5 h and 11 h. Above 13 K, the spin isomer conversion is mono-exponential and follows an Arrhenius type behaviour with temperature, yielding an activation energy of ~ 3.2 meV. This is comparable to the energy difference between the para and ortho H_2O ground states of $2.2 - 2.8$ meV (section VII H).[222]

The spin isomer conversion appears to involve 2 processes: one thermally active and one thermally inactive. The thermally activated process above 13 K could be due to thermal

excitations, and the thermally inactive process below 13 K could be due to tunnelling.[222]

From the heat capacity measurements, the $H_2O@C_{60}$ spin isomer conversion rate is shown to be bi-exponential below 13 K.[222] This conflicts with the bi-molecular kinetic process identified through the NMR measurements (section V F 5).[251] However, upon close inspection of the two models, see SI of ref. 222, the two calculated decay curves are very similar and it is difficult to distinguish between them. For the heat capacity measurements, the bi-exponential model provides a more satisfactory match with the experimental data.[222]

F. STM and ncAFM of $H_2O@C_{60}$ & $HF@C_{60}$

The endofullerenes $H_2O@C_{60}$ and $HF@C_{60}$, adsorbed on a Cu(111) surface, have been probed using scanning tunnelling microscopy (STM) and non-contact atomic force microscopy (ncAFM).[198] STM and ncAFM did not detect any difference between filled and empty fullerene cages, suggesting that the frontier orbitals of the adsorbed C_{60} are unperturbed by the presence of endohedral H_2O or HF.[198]

G. Electron beam chemical modifications (ChemTEM): endofullerene peapods

ChemTEM is a tunnelling electron microscopy (TEM) technique in which the electrons are used to obtain TEM images but also to generate chemical modifications of the imaged sample. By providing the right kinetic energy to dissociate chemical bonds, the electron beam acts as both the pump (kinetic energy transfer) and the probe (imaging).[308,309]

1. $HF@C_{60}$ & $H_2O@C_{60}$ *peapods: ChemTEM*

The endofullerenes $HF@C_{60}$ and $H_2O@C_{60}$ have been inserted into single walled carbon nanotubes (SWCNT) to form $(HF@C_{60})$@SWCNT and $(H_2O@C_{60})$@SWCNT peapods, filling the entire SWCNT without gaps.[308] Upon electron irradiation, the empty C_{60} fullerene peapods (i.e. C_{60}@SWCNT) did not show observable damage, with electron beam energy of up to 40 keV. However, $(HF@C_{60})$@SWCNT is less stable and $(H_2O@C_{60})$@SWCNT even less, where damage is observed at energies of 30 keV or below.[308] The "damage" is observed as oligomerisation of the fullerene cages inside the SWCNT. The presence of hydrogen atoms in the sample increases the effective energy transfer from the electron beam to heavier atoms. The hydrogen acts as an intermediate in the momentum transfer process, effectively amplifying the impact of electrons onto heavier atoms. This explains why $(H_2O@C_{60})$@SWCNT is the least stable, since it has double the number of hydrogen atoms compared with $(HF@C_{60})$@SWCNT.[308]

2. $Kr@C_{60}$ *peapods &* Kr *1-dimensional gas: ChemTEM*

$Kr@C_{60}$ has been inserted into single walled carbon nanotubes (SWCNT) to form $(Kr@C_{60})$@SWCNT "peapod" structures, confirmed by TEM.[309] Using heat of $\sim$1200 °C, the endofullerene molecules, while inside the SWCNT, fuse together to form almost perfect nanotubes containing Kr atoms (the Kr atoms did not leave the parent fullerene cage when fusing). Thus, generating $(nKr@C_{n\cdot 60})$@SWCNT, nested carbon nanotubes, where the Kr atoms are delocalised and form a 1D gas.[309] Furthermore, fusion of the (endo)fullerene "peas" into nanotubes (inside the SWCNT "pods") is also observed under ChemTEM electron irradiation of 80 keV beam energy. This is shown to affect (endo)fullerenes inside the SWCNT, causing them to fuse, but leaving the SWCNT "pods" essentially unaffected.[309]

H. Molecular junctions: electron transport measurements

Electron transport measurements can be performed on molecular junctions containing endofullerene molecules. Molecular junctions represent electric contacts between molecular species and electrodes (usually made of noble metals). Electron transport measurements through a junction refer to current – voltage (I – V) analysis, where a voltage is applied and the (tunnelling) current is measured. Such junctions can be constructed to contain a single molecule, and transport measurements can be performed on single molecules. Thus, this section mainly involves single molecule junctions and single molecule transistors (SMT).[115,307,310,311]

Molecular junctions can be simple 2 terminal devices, with a molecular species sandwiched between 2 electrodes. I – V analysis of 2 terminal molecular junctions gives information about conductivity (conductance), electronic structure of the molecule & electrodes, the electronic coupling Γ between the molecule and the metal electrode and the energy difference between the Fermi level of the electrode & the conduction orbital on the molecule (ΔE).[307,310,311]

More complex junctions have 3 terminals, i.e. transistor geometry, where the molecular species is connected to the source and drain electrodes (both electrically connected to provide a bias voltage) and to a gate electrode (which controls the charge flow through the junction).[310] For SMT, the (tunnelling) current can flow through the device/single molecule depending on the bias voltage V_B (or V_{DS}) and the gate voltage V_G. Current flow is possible if the molecule has energy levels close to the Fermi energy, and it generates excitations of such energy levels. Differential conductance $\partial I/\partial V_{DS}$ spectra (or tunnelling conductance spectra or Coulomb stability diagrams) are obtained as a function of the bias and gate voltages and contain spectroscopic information.[312] Furthermore, differential conductance spectra can be obtained at different magnetic fields.[114,115]

1. $N@C_{60}$ *single molecule transistor*

Electron transport measurements have been performed on $N@C_{60}$ using a single molecule transistor (SMT) geometry. Tunnelling conductance spectra ($\partial I/\partial V_{DS}$) through $N@C_{60}$ have been acquired as a function of the bias and gate voltage at mK temperatures.[114,115]

By measuring spectra at different magnetic fields, the magnetic properties (spin dynamics) of the system can be investigated, and spin excitation energies can be measured. The spin and charge states of $N@C_{60}$ have been detected, and the tunnelling electrons are observed to generate spin excitations of the three unpaired electrons on the endohedral N ($S = 3/2$).[114,115] Such investigations demonstrate that it is possible to construct and control $N@C_{60}$ single molecule transistors for practical applications.[114,115] Furthermore, co-tunnelling processes have been observed in $N@C_{60}$ SMT.[115]

2. $H_2O@C_{60}$ *single molecule junction*

Molecular junctions constructed from a single $H_2O@C_{60}$ or C_{60} molecule bridging Au electrodes have been investigated using the mechanically controllable break junction (MCBJ) technique.[307]

Both molecules show essentially the same molecular conductance of 0.25 ± 0.05 G_0, which is close to a typical metal atomic contact. The same conductance for $H_2O@C_{60}$ and C_{60} suggests that the interaction between H_2O and C_{60} is very small, i.e. there is no electrostatic contact between H_2O and the carbon wall of C_{60}.[307]

$I-V$ analysis performed on C_{60} and $H_2O@C_{60}$ single molecule junctions gives the electronic coupling between the metal & the molecule (Γ) and the energy difference between the Fermi level of the electrode & the conduction orbital on the molecule (ΔE).[307] For $H_2O@C_{60}$ and C_{60}: $\Gamma = 0.2 \pm 0.1$ eV and $\Delta E = 0.5 \pm 0.1$ eV. ΔE indicates that the LUMO of $H_2O@C_{60}$ and C_{60} is 0.5 eV above the Fermi level of the gold electrodes. Furthermore, the $I-V$ analysis shows that the metal-molecule coupling is as large as 0.5 eV for both $H_2O@C_{60}$ and C_{60}, which is much larger than conventional single molecular junctions.[307]

3. $H_2O@C_{60}$ *scanning tunnelling microscope break junction (STM-BJ)*

Charge transport measurements have been performed on a scanning tunnelling microscope break junction (STM-BJ) containing a single molecule of: C_{60} or $H_2O@C_{60}$ or $Li^+@C_{60}$. An Au STM tip is brought into contact with the fullerene junction and $I-V$ measurements are performed.[311]

The conductivity of $H_2O@C_{60}$ is slightly decreased compared with C_{60}; whereas $Li^+@C_{60}$ sees a $2-4$ fold increase in conductivity.[311]

For all, C_{60}, $H_2O@C_{60}$ and $Li^+@C_{60}$ two states are observed in the conductance measurements. Corresponding to two metastable structures of the fullerene molecule with respect to the Au electrode separation: small separation = high conductance state and large separation = low conductance state.[311] The measured high & low conductances are: 34 ± 3 mG_0 & 3.1 ± 0.4 mG_0 for C_{60}, 26 ± 8 mG_0 & 2.7 ± 0.7 mG_0 for $H_2O@C_{60}$ and 81 ± 10 mG_0 & 13 ± 3 mG_0 for $Li^+@C_{60}$.[311]

For the high and low conductance states, encapsulation does not have a significant effect on the electronic coupling Γ. For the energy difference ΔE, the low conductance states are not significantly affected by the encapsulation. Whereas for the high conductance state, ΔE is significantly perturbed by endohedral insertion: for $H_2O@C_{60}$ ΔE increases slightly ($+0.01$ eV) and for $Li^+@C_{60}$ ΔE decreases significantly (-0.16 eV).[311]

As a result of the $I-V$ analysis, the zero-bias conductances for C_{60}, $H_2O@C_{60}$ and $Li^+@C_{60}$ are 1.2 mG_0, 2.6 mG_0 and 2.4 mG_0 respectively.[311]

4. $H_2O@C_{60}$ *single molecule transistor*

Single molecule transistors (SMT) containing a single $H_2O@C_{60}$ molecule have been constructed using the electrical break-junction (EBJ) method.[116] Electron transport measurements through a single $H_2O@C_{60}$ molecule, at 4.2 K and ~ 100 mK, obtain differential conductance $\partial I/\partial V_{DS}$ maps (Coulomb stability diagrams) which can reveal spectroscopic information, see fig. 32.[116]

Multiple excited states are observed in the tunnelling spectra as conductance peaks, which are attributed to rotational & translational excitations of the endohedral H_2O and vibrations of the C_{60}. Such excitation spectra are most likely for the neutral $H_2O@C_{60}$ or positively charged $H_2O@C_{60}^+$, depending on the positive or negative bias drain-source voltage V_{DS}.[116] C_{60} displays excited states at ~ 30 meV and ~ 60 meV in the Coulomb stability diagram, corresponding to the $H_g(1)$ and $A_g(1)$ vibrations.[116]

Tunnelling peaks in the differential conductance are observed at 2.0 meV & 7.2 meV for ortho-H_2O and 4.4 meV for para-H_2O, see fig. 32.[116] Corresponding to rotational excitations of endohedral H_2O, with excellent match to the $H_2O@C_{60}$ THz results (section VII H 1).[187,288] Furthermore, translational excitation of endohedral H_2O is observed at 13.8 meV,[116] with excellent match to the $H_2O@C_{60}$ THz results (section VII H 1).[187,288]

The measurements in fig. 32 are performed on a single molecule of $H_2O@C_{60}$, and one scan takes ~ 1 min. Since both ortho and para H_2O transitions are visible, the spin isomer conversion (section II H) in the endohedral H_2O must be fast (< 1 min), most likely due to interactions with the conduction electrons.[116]

a. $H_2O@C_{60}$ *SMT THz-induced photocurrent*

THz type spectroscopy was performed on the $H_2O@C_{60}$ SMT at 4.6 K. Performed by illuminating the molecule with broadband blackbody radiation and then measuring the THz-induced photocurrent I_{DS}.[116]

When THz irradiation is turned on, it will excite molecular vibrations/rotations/translations. An electron in the electrode

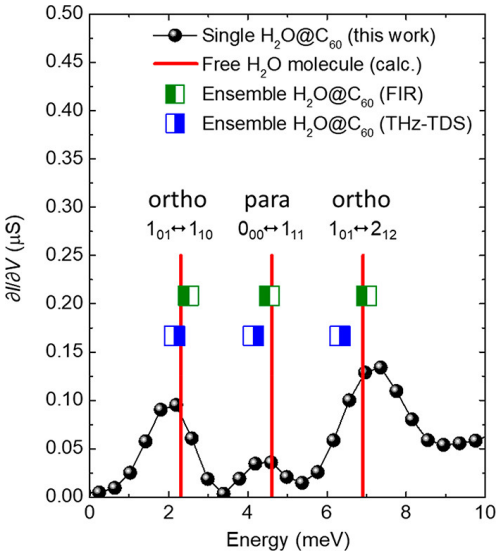

FIG. 32. $\partial I/\partial V_{DS}$ spectrum of the $H_2O@C_{60}$ single molecule transistor (black dots) measured at the Coulomb peak ($V_G = -12.63$ V). The energy positions of the rotational modes of an isolated water molecule are indicated by red lines. The rotational energies determined by continuous wave THz/far-infrared spectroscopy and time-domain THz spectroscopy on ensembles of $H_2O@C_{60}$ molecules (section VII H 1) are also plotted. Reprinted with permission from (ref. 116) Du *et al.*, Nano Lett., **21**, 10346–10353 (2021). Copyright 2021 American Chemical Society.

will absorb the vibration/rotation/translation quantum, jumping into the LUMO and generating a photocurrent (vibron-assisted tunnelling).[116]

The THz-induced photocurrent peaks seen in the THz measurements appear at 5 meV and 7 meV, which are the same as observed in the tunnelling spectra shown in fig. 32 – corresponding to rotational excitations of ortho and para H_2O.[116]

XI. CONCLUDING REMARKS

The physico-chemical investigations of non-metallic C_{60} endofullerenes have been presented. A small introduction was given for the different types of endofullerenes and how they are produced, together with their natural occurrences. Theoretical background is provided for the quantum behaviour encountered in the presented studies and for the methods used to probe them (mostly spectroscopic methods). All spectroscopic studies are reviewed, together with other experimental techniques related to structure, voltammetry, electron transport, heat capacity, etc. The spectroscopic methods include nuclear magnetic resonance (NMR), electron paramagnetic resonance (EPR), inelastic neutron scattering (INS), Raman, THz & infrared (IR), electronic structure and ionisation techniques. The sections are organised in order of ascending energy probed by, or required by, the experimental techniques.

The encapsulated species display quantisation of their translational degrees of freedom. Such translational eigenstates define the non-bonded (non-covalent) interaction between the host (C_{60} fullerene) and the guest (endohedral species). Molecules encapsulated in fullerenes behave as quantum rotors, displaying essentially free rotation even at cryogenic temperatures. This allows observation of nuclear spin isomerisms for symmetric molecules. The translational and rotational motion can interact rather strongly, leading to translational-rotational coupling, which can also couple to the vibrational degrees of freedom. Endofullerenes offer the advantage of investigating such degrees of freedom, and the coupling between them, in the condensed phase. Endofullerenes act as nano-laboratories that isolate the atoms/molecules of interest from the environment, protecting the encapsulated species from strong external interactions. This feature makes endofullerenes ideal for spectroscopic investigations into the quantum behaviour of the endohedral species, and its interaction with the enclosing cage and with other encapsulated species.

ACKNOWLEDGMENTS

This work was supported by the Engineering and Physical Sciences Research Council UK, EP/Y010515/1. The author would particularly like to thank Malcolm H. Levitt, Richard J. Whitby, Toomas Rõõm, Stéphane Rols, Klaus-Peter Dinse, Philip Moriarty and Anthony J. Horsewill for valuable comments and constructive feedback on the manuscript.

REFERENCES

[1]H. W. Kroto, J. R. Heath, S. C. O'Brien, R. F. Curl, and R. E. Smalley, "C 60 : Buckminsterfullerene," Nature **318**, 162–163 (1985).
[2]M. S. Dresselhaus, G. Dresselhaus, and P. C. Eklund, *Science of Fullerenes and Carbon Nanotubes* (Academic Press, 1996).
[3]J. R. Heath, S. C. O'Brien, Q. Zhang, Y. Liu, R. F. Curl, F. K. Tittel, and R. E. Smalley, "Lanthanum complexes of spheroidal carbon shells," Journal of the American Chemical Society **107**, 7779–7780 (1985).
[4]Z. Farmani, A. Vetere, C. Poidevin, A. A. Auer, and W. Schrader, "Studying Natural Buckyballs and Buckybowls in Fossil Materials," Angewandte Chemie International Edition **59**, 15008–15013 (2020).
[5]Z. Farmani, A. Vetere, N. Pfänder, C. W. Lehmann, and W. Schrader, "Naturally Occurring Allotropes of Carbon," Analytical Chemistry **96**, 2968–2974 (2024).
[6]L. Becker, R. J. Poreda, and T. E. Bunch, "Fullerenes: An extraterrestrial carbon carrier phase for noble gases," Proceedings of the National Academy of Sciences **97**, 2979–2983 (2000).
[7]E. K. Campbell, M. Holz, D. Gerlich, and J. P. Maier, "Laboratory confirmation of C60+ as the carrier of two diffuse interstellar bands," Nature **523**, 322–323 (2015).
[8]M. A. Cordiner, H. Linnartz, N. L. J. Cox, J. Cami, F. Najarro, C. R. Proffitt, R. Lallement, P. Ehrenfreund, B. H. Foing, T. R. Gull, P. J. Sarre, and S. B. Charnley, "Confirming Interstellar C60+ Using the Hubble Space Telescope," The Astrophysical Journal Letters **875**, L28 (2019).
[9]E. K. Campbell, M. Holz, J. P. Maier, D. Gerlich, G. A. H. Walker, and D. Bohlender, "GAS PHASE ABSORPTION SPECTROSCOPY OF

\rmC_60^+ AND \rmC_70^+ IN A CRYOGENIC ION TRAP: COMPARISON WITH ASTRONOMICAL MEASUREMENTS*," The Astrophysical Journal **822**, 17 (2016).
[10]A. O. Lykhin, S. Ahmadvand, and S. A. Varganov, "Electronic Transitions Responsible for C60+ Diffuse Interstellar Bands," The Journal of Physical Chemistry Letters **10**, 115–120 (2019).
[11]G. A. H. Walker, D. A. Bohlender, J. P. Maier, and E. K. Campbell, "IDENTIFICATION OF MORE INTERStelLAR \rmC_60^+ BANDS*," The Astrophysical Journal Letters **812**, L8 (2015).
[12]A. Omont, "Interstellar fullerene compounds and diffuse interstellar bands," Astronomy & Astrophysics **590**, A52 (2016).
[13]D. V. Strelnikov, J. Jašík, D. Gerlich, M. Murata, Y. Murata, K. Komatsu, and J. Roithová, "Near- and Mid-IR Gas-Phase Absorption Spectra of H2@C60+-He," The Journal of Physical Chemistry A **122**, 8162–8166 (2018).
[14]E. K. Campbell, E. S. Reedy, J. Rademacher, R. J. Whitby, and G. Hoffman, "Electronic Spectroscopy of \bfHe@\rmC_60^+ for Astrochemical Consideration," The Astrophysical Journal **897**, 88 (2020).
[15]R. Shimshi, A. Khong, H. A. Jiménez-Vázquez, R. J. Cross, and M. Saunders, "Release of noble gas atoms from inside fullerenes," Tetrahedron **52**, 5143–5148 (1996).
[16]T. Almeida Murphy, Th. Pawlik, A. Weidinger, M. Höhne, R. Alcala, and J.-M. Spaeth, "Observation of Atomlike Nitrogen in Nitrogen-Implanted Solid ${\mathrm{C}}_{60}$," Physical Review Letters **77**, 1075–1078 (1996).
[17]M. Waiblinger, B. Pietzak, K. Lips, and A. Weidinger, "Thermal stability of N@C60," AIP Conference Proceedings **442**, 388–391 (1998).
[18]A. Iwasiewicz-Wabnig, K. Porfyrakis, G. A. D. Briggs, and B. Sundqvist, "Investigations of N@C60 and N@C70 stability under high pressure and high temperature conditions," physica status solidi (b) **246**, 2767–2770 (2009).
[19]M. Waiblinger, K. Lips, W. Harneit, A. Weidinger, E. Dietel, and A. Hirsch, "Corrected Article: Thermal stability of the endohedral fullerenes ${\mathrm{N}\mathrm{@}\mathrm{C}}_{60},$ ${\mathrm{N}\mathrm{@}\mathrm{C}}_{70},$ and ${\mathrm{P}\mathrm{@}\mathrm{C}}_{60}$ [Phys. Rev. B 63, 045421 (2001)]," Physical Review B **64**, 159901 (2001).
[20]A. Krachmalnicoff, R. Bounds, S. Mamone, S. Alom, M. Concistrè, B. Meier, K. Kouřil, M. E. Light, M. R. Johnson, S. Rols, A. J. Horsewill, A. Shugai, U. Nagel, T. Rõõm, M. Carravetta, M. H. Levitt, and R. J. Whitby, "The dipolar endofullerene HF@C 60," Nature Chemistry **8**, 953–957 (2016).
[21]V. K. Vyas, G. R. Bacanu, M. Soundararajan, E. S. Marsden, T. Jafari, A. Shugai, M. E. Light, U. Nagel, T. Rõõm, M. H. Levitt, and R. J. Whitby, "Squeezing formaldehyde into C60 fullerene," Nature Communications **15**, 2515 (2024).
[22]J. Laskin, T. Peres, C. Lifshitz, M. Saunders, R. J. Cross, and A. Khong, "An artificial molecule of Ne2 inside C70," Chemical Physics Letters **285**, 7–9 (1998).
[23]T. Sternfeld, R. E. Hoffman, M. Saunders, R. J. Cross, M. S. Syamala, and M. Rabinovitz, "Two Helium Atoms Inside Fullerenes: Probing the Internal Magnetic Field in C606- and C706-," Journal of the American Chemical Society **124**, 8786–8787 (2002).
[24]R.-F. Peng, S.-J. Chu, Y.-M. Huang, H.-J. Yu, T.-S. Wang, B. Jin, Y.-B. Fu, and C.-R. Wang, "Preparation of He@C60 and He2@C60 by an explosive method," Journal of Materials Chemistry **19**, 3602–3605 (2009).
[25]M. Murata, S. Maeda, Y. Morinaka, Y. Murata, and K. Komatsu, "Synthesis and Reaction of Fullerene C70 Encapsulating Two Molecules of H2," Journal of the American Chemical Society **130**, 15800–15801 (2008).
[26]R. Zhang, M. Murata, T. Aharen, A. Wakamiya, T. Shimoaka, T. Hasegawa, and Y. Murata, "Synthesis of a distinct water dimer inside fullerene C 70," Nature Chemistry **8**, 435–441 (2016).
[27]Y. Morinaka, S. Sato, A. Wakamiya, H. Nikawa, N. Mizorogi, F. Tanabe, M. Murata, K. Komatsu, K. Furukawa, T. Kato, S. Nagase, T. Akasaka, and Y. Murata, "X-ray observation of a helium atom and placing a nitrogen atom inside He@C60 and He@C70," Nature Communications **4**, 1554 (2013).
[28]Y. Morinaka, R. Zhang, S. Sato, H. Nikawa, T. Kato, K. Furukawa, M. Yamada, Y. Maeda, M. Murata, A. Wakamiya, S. Nagase, T. Akasaka, and Y. Murata, "Fullerene C70 as a Nanoflask that Reveals the Chemical Reactivity of Atomic Nitrogen," Angewandte Chemie International Edition **56**, 6488–6491 (2017).
[29]R. Zhang, M. Murata, A. Wakamiya, T. Shimoaka, T. Hasegawa, and Y. Murata, "Isolation of the simplest hydrated acid," Science Advances **3**, e1602833 (2017).
[30]K. Fujiwara, K. Komatsu, G.-W. Wang, T. Tanaka, K. Hirata, K. Yamamoto, and M. Saunders, "Derivatization of Fullerene Dimer C120 by the Bingel Reaction and a 3He NMR Study of 3He@C120 Monoadducts," Journal of the American Chemical Society **123**, 10715–10720 (2001).
[31]K. Komatsu, M. Murata, and Y. Murata, "Encapsulation of Molecular Hydrogen in Fullerene C60 by Organic Synthesis," Science **307**, 238–240 (2005).
[32]R. Zhang, M. Murata, A. Wakamiya, and Y. Murata, "Synthesis and X-ray Structure of Endohedral Fullerene C60 Dimer Encapsulating a Water Molecule in Each C60 Cage," Chemistry Letters **42**, 879–881 (2013).
[33]E. J. Ansaldo, C. Niedermayer, and C. E. Stronach, "Muonium in fullerite," Nature **353**, 121–121 (1991).
[34]R. F. Kiefl, T. L. Duty, J. W. Schneider, A. MacFarlane, K. Chow, J. Elzey, P. Mendels, G. D. Morris, J. H. Brewer, E. J. Ansaldo, C. Niedermayer, D. R. Noakes, C. E. Stronach, B. Hitti, and J. E. Fischer, "Evidence for endohedral muonium in ${\mathrm{K}}_{\mathit{x}}$ ${\mathrm{C}}_{60}$ and consequences for electronic structure," Physical Review Letters **69**, 2005–2008 (1992).
[35]Ch. Niedermayer, I. D. Reid, E. Roduner, E. J. Ansaldo, C. Bernhard, U. Binninger, H. Glückler, E. Recknagel, J. I. Budnick, and A. Weidinger, "Simultaneous observation of muonium and multiple free radicals in muon-implanted ${\mathrm{C}}_{70}$," Physical Review B **47**, 10923–10926 (1993).
[36]A. Khong, R. J. Cross, and M. Saunders, "From 3He@C60 to 3H@C60: Hot-Atom Incorporation of Tritium in C60," The Journal of Physical Chemistry A **104**, 3940–3943 (2000).
[37]Y. Matsuo, H. Okada, and H. Ueno, *Endohedral Lithium-containing Fullerenes* (Springer, Singapore, 2017).
[38]C. G. Joslin, J. Yang, C. G. Gray, S. Goldman, and J. D. Poll, "Infrared rotation and vibration—rotation bands of endohedral fullerene complexes. Absorption spectrum of Li+ @C60 in the range 1–1000 cm-1," Chemical Physics Letters **208**, 86–92 (1993).
[39]C. G. Joslin, C. G. Gray, S. Goldman, J. Yang, and J. D. Poll, "Raman spectra of endohedral fullerenes. Li+ @C60," Chemical Physics Letters **215**, 144–150 (1993).
[40]R. Tellgmann, N. Krawez, S.-H. Lin, I. V. Hertel, and E. E. B. Campbell, "Endohedral fullerene production," Nature **382**, 407–408 (1996).
[41]T. Akasaka, S. Nagase, K. Kobayashi, M. Wälchli, K. Yamamoto, H. Funasaka, M. Kako, T. Hoshino, and T. Erata, "13C and 139La NMR Studies of La2@C80: First Evidence for Circular Motion of Metal Atoms in Endohedral Dimetallofullerenes," Angewandte Chemie International Edition in English **36**, 1643–1645 (1997).
[42]E. E. B. Campbell, R. Tellgmann, N. Krawez, and I. V. Hertel, "Production and LDMS characterisation of endohedral alkalifullerene films," Journal of Physics and Chemistry of Solids **58**, 1763–1769 (1997).
[43]H. Shinohara, "Endohedral metallofullerenes," Reports on Progress in Physics **63**, 843 (2000).
[44]C.-R. Wang, T. Kai, T. Tomiyama, T. Yoshida, Y. Kobayashi, E. Nishibori, M. Takata, M. Sakata, and H. Shinohara, "A Scandium Carbide Endohedral Metallofullerene: (Sc2C2)@C84," Angewandte Chemie International Edition **40**, 397–399 (2001).
[45]A. Gromov, D. Ostrovskii, A. Lassesson, M. Jönsson, and E. E. B. Campbell, "Fourier Transform Infrared and Raman Spectroscopic Study of Chromatographically Isolated Li@C60 and Li@C70," The Journal of Physical Chemistry B **107**, 11290–11301 (2003).
[46]M. N. Chaur, F. Melin, A. L. Ortiz, and L. Echegoyen, "Chemical, Electrochemical, and Structural Properties of Endohedral Metallofullerenes," Angewandte Chemie International Edition **48**, 7514–7538 (2009).
[47]A. Rodríguez-Fortea, A. L. Balch, and J. M. Poblet, "Endohedral metallofullerenes: A unique host–guest association," Chemical Society Reviews **40**, 3551–3563 (2011).
[48]H. Okada, T. Komuro, T. Sakai, Y. Matsuo, Y. Ono, K. Omote, K. Yokoo, K. Kawachi, Y. Kasama, S. Ono, R. Hatakeyama, T. Kaneko, and H. Tobita, "Preparation of endohedral fullerene containing lithium (Li@C 60) and isolation as pure hexafluorophosphate salt ([Li + @C 60][PF 6 -]),"

RSC Advances **2**, 10624–10631 (2012).
[49]H. Ueno, K. Kokubo, Y. Nakamura, K. Ohkubo, N. Ikuma, H. Moriyama, S. Fukuzumi, and T. Oshima, "Ionic conductivity of [Li+@C60](PF6-) in organic solvents and its electrochemical reduction to Li+@C60˙-," Chemical Communications **49**, 7376–7378 (2013).
[50]J. Zhang and H. C. Dorn, "NMR Studies of the Dynamic Motion of Encapsulated Ions and Clusters in Fullerene Cages: A Wheel Within a Wheel," Fullerenes, Nanotubes and Carbon Nanostructures **22**, 35–46 (2014).
[51]H. Shinohara and N. Tagmatarchis, *Endohedral Metallofullerenes: Fullerenes with Metal Inside* (John Wiley & Sons, 2015).
[52]H. Ueno, S. Aoyagi, Y. Yamazaki, K. Ohkubo, N. Ikuma, H. Okada, T. Kato, Y. Matsuo, S. Fukuzumi, and K. Kokubo, "Electrochemical reduction of cationic Li+@C60 to neutral Li+@C60˙-: Isolation and characterisation of endohedral [60]fulleride," Chemical Science **7**, 5770–5774 (2016).
[53]H. Suzuki, M. Ishida, M. Yamashita, C. Otani, K. Kawachi, Y. Kasama, and E. Kwon, "Rotational dynamics of Li+ ions encapsulated in C60 cages at low temperatures," Physical Chemistry Chemical Physics **18**, 31384–31387 (2016).
[54]A. A. Popov, ed., *Endohedral Fullerenes: Electron Transfer and Spin*, Nanostructure Science and Technology (Springer International Publishing, Cham, 2017).
[55]W. Cai, R. Morales-Martínez, X. Zhang, D. Najera, E. L. Romero, A. Metta-Magaña, A. Rodríguez-Fortea, S. Fortier, N. Chen, J. M. Poblet, and L. Echegoyen, "Single crystal structures and theoretical calculations of uranium endohedral metallofullerenes (U@C2n, 2n = 74, 82) show cage isomer dependent oxidation states for U," Chemical Science **8**, 5282–5290 (2017).
[56]I. Jeon, H. Ueno, S. Seo, K. Aitola, R. Nishikubo, A. Saeki, H. Okada, G. Boschloo, S. Maruyama, and Y. Matsuo, "Lithium-Ion Endohedral Fullerene (Li+@C60) Dopants in Stable Perovskite Solar Cells Induce Instant Doping and Anti-Oxidation," Angewandte Chemie International Edition **57**, 4607–4611 (2018).
[57]S. Aoyagi, K. Miwa, H. Ueno, H. Okada, Y. Matsuo, and K. Kokubo, "Structure of [60]fullerene with a mobile lithium cation inside," Royal Society Open Science **5**, 180337 (2018).
[58]M. Stefanou, H. J. Chandler, B. Mignolet, E. Williams, S. A. Nanoh, J. O. F. Thompson, F. Remacle, R. Schaub, and E. E. B. Campbell, "Angle-resolved photoelectron spectroscopy and scanning tunnelling spectroscopy studies of the endohedral fullerene Li@C 60," Nanoscale **11**, 2668–2678 (2019).
[59]H. Okada, H. Ueno, Y. Takabayashi, T. Nakagawa, M. Vrankić, J. Arvanitidis, T. Kusamoto, K. Prassides, and Y. Matsuo, "Chemical reduction of Li+@C60 by decamethylferrocene to produce neutral Li+@C60•–," Carbon **153**, 467–471 (2019).
[60]H. J. Chandler, M. Stefanou, E. E. B. Campbell, and R. Schaub, "Li@C60 as a multi-state molecular switch," Nature Communications **10**, 2283 (2019).
[61]E. Kwon, T. Matsukawa, A. Hoshikawa, T. Ishigaki, S. Aoyagi, K. Kawachi, and Y. Kasama, "Direct observation of nucleus of lithium in a C60 fullerene cage by neutron diffraction study," Chemical Physics Letters **801**, 139678 (2022).
[62]X. Lu, T. Akasaka, and Z. Slanina, *Handbook of Fullerene Science and Technology* (Springer Nature, 2022).
[63]H. Ueno, D. Kitabatake, T. Mabuchi, S. Aoyagi, T. Itoh, T. Deng, and F. Misaizu, "Synthesis and Characterization of Ionic Li+@C70 Endohedral Fullerene," Chemistry – A European Journal **30**, e202303908 (2024).
[64]M. Saunders, H. A. Jiménez-Vázquez, R. J. Cross, and R. J. Poreda, "Stable Compounds of Helium and Neon: He@C60 and Ne@C60," Science **259**, 1428–1430 (1993).
[65]M. Saunders, H. A. Jiménez-Vázquez, R. J. Cross, S. Mroczkowski, D. I. Freedberg, and F. A. L. Anet, "Probing the interior of fullerenes by 3He NMR spectroscopy of endohedral 3He@C60 and 3He@C70," Nature **367**, 256–258 (1994).
[66]M. Saunders, H. A. Jimenez-Vazquez, B. W. Bangerter, R. J. Cross, S. Mroczkowski, D. I. Freedberg, and F. A. L. Anet, "3He NMR: A Powerful New Tool for Following Fullerene Chemistry," Journal of the American Chemical Society **116**, 3621–3622 (1994).
[67]M. Saunders, H. A. Jimenez-Vazquez, R. J. Cross, S. Mroczkowski, M. L. Gross, D. E. Giblin, and R. J. Poreda, "Incorporation of helium, neon, argon, krypton, and xenon into fullerenes using high pressure," Journal of the American Chemical Society **116**, 2193–2194 (1994).
[68]A. B. I. Smith, R. M. Strongin, L. Brard, W. J. Romanow, M. Saunders, H. A. Jimenez-Vazquez, and R. J. Cross, "Synthesis and 3He NMR Studies of C60 and C70 Epoxide, Cyclopropane, and Annulene Derivatives Containing Endohedral Helium," Journal of the American Chemical Society **116**, 10831–10832 (1994).
[69]M. Saunders, R. J. Cross, H. A. Jiménez-Vázquez, R. Shimshi, and A. Khong, "Noble Gas Atoms Inside Fullerenes," Science **271**, 1693–1697 (1996).
[70]B. A. DiCamillo, R. L. Hettich, G. Guiochon, R. N. Compton, M. Saunders, H. A. Jiménez-Vázquez, A. Khong, and R. J. Cross, "Enrichment and Characterization of a Noble Gas Fullerene: Ar@C60," The Journal of Physical Chemistry **100**, 9197–9201 (1996).
[71]A. Khong, H. A. Jiménez-Vázquez, M. Saunders, R. J. Cross, J. Laskin, T. Peres, C. Lifshitz, R. Strongin, and A. B. Smith, "An NMR Study of He2 Inside C70," Journal of the American Chemical Society **120**, 6380–6383 (1998).
[72]E. Shabtai, A. Weitz, R. C. Haddon, R. E. Hoffman, M. Rabinovitz, A. Khong, R. J. Cross, M. Saunders, P.-C. Cheng, and L. T. Scott, "3He NMR of He@C606- and He@C706-. New Records for the Most Shielded and the Most Deshielded 3He Inside a Fullerene1," Journal of the American Chemical Society **120**, 6389–6393 (1998).
[73]K. Yamamoto, M. Saunders, A. Khong, R. J. Cross, M. Grayson, M. L. Gross, A. F. Benedetto, and R. B. Weisman, "Isolation and Spectral Properties of Kr@C60, a Stable van der Waals Molecule," Journal of the American Chemical Society **121**, 1591–1596 (1999).
[74]G.-W. Wang, B. R. Weedon, M. S. Meier, M. Saunders, and R. J. Cross, "3He NMR Study of 3He@C60H6 and 3He@C70H2-10," Organic Letters **2**, 2241–2243 (2000).
[75]M. S. Syamala, R. J. Cross, and M. Saunders, "129Xe NMR Spectrum of Xenon Inside C60," Journal of the American Chemical Society **124**, 6216–6219 (2002).
[76]T. Peres, B. Cao, W. Cui, A. Khong, R. J. Cross, M. Saunders, and C. Lifshitz, "Some new diatomic molecule containing endohedral fullerenes1," International Journal of Mass Spectrometry **210–211**, 241–247 (2001).
[77]A. Weidinger, B. Pietzak, M. Waiblinger, K. Lips, B. Nuber, and A. Hirsch, "Study of N@C60 and P@C60," AIP Conference Proceedings **442**, 363–367 (1998).
[78]C. Knapp, N. Weiden, H. Kass, K.-P. Dinse, B. Pietzak, M. Waiblinger, and A. Weidinger, "Electron paramagnetic resonance study of atomic phosphorus encapsulated in [60]fullerene," Molecular Physics **95**, 999–1004 (1998).
[79]J. A. Larsson, J. C. Greer, W. Harneit, and A. Weidinger, "Phosphorous trapped within buckminsterfullerene," The Journal of Chemical Physics **116**, 7849–7854 (2002).
[80]S. Zhou and K. Porfyrakis, "Preparation and Chemistry of N@C60," in *Endohedral Fullerenes: Electron Transfer and Spin*, edited by A. A. Popov (Springer International Publishing, Cham, 2017) pp. 265–295.
[81]S. Zhou and K. Porfyrakis, "Endohedral Nitrogen Fullerenes," in *Handbook of Fullerene Science and Technology*, edited by X. Lu, T. Akasaka, and Z. Slanina (Springer Nature, Singapore, 2022) pp. 725–752.
[82]A. Weidinger, M. Waiblinger, B. Pietzak, and T. Almeida Murphy, "Atomic nitrogen in C60:N@C60," Applied Physics A **66**, 287–292 (1998).
[83]N. Weiden, H. Käss, and K.-P. Dinse, "Pulse Electron Paramagnetic Resonance (EPR) and Electron-Nuclear Double Resonance (ENDOR) Investigation of N@C60 in Polycrystalline C60," The Journal of Physical Chemistry B **103**, 9826–9830 (1999).
[84]T. Suetsuna, N. Dragoe, W. Harneit, A. Weidinger, H. Shimotani, S. Ito, H. Takagi, and K. Kitazawa, "Separation of N2@C60 and N@C60," Chemistry – A European Journal **8**, 5079–5083 (2002).
[85]S. Ito, H. Shimotani, H. Takagi, and N. Dragoe, "On the Synthesis Conditions of N and N2 Endohedral Fullerenes," Fullerenes, Nanotubes and Carbon Nanostructures **16**, 206–213 (2008).
[86]T. Weiske, D. K. Böhme, J. Hrušák, W. Krätschmer, and H. Schwarz, "Endohedral Cluster Compounds: Inclusion of Helium within C and C through Collision Experiments," Angewandte Chemie International Edition in English **30**, 884–886 (1991).
[87]M. M. Ross and J. H. Callahan, "Formation and characterization of car-

bon mol.-helium (C60He+)," The Journal of Physical Chemistry **95**, 5720–5723 (1991).
[88]K. A. Caldwell, D. E. Giblin, and M. L. Gross, "High-energy collisions of fullerene radical cations with target gases: Capture of the target gas and charge stripping of C60.bul.+, C70.bul.+, and C84.bul.+," Journal of the American Chemical Society **114**, 3743–3756 (1992).
[89]Z. Wan, J. F. Christian, and S. L. Anderson, "Ne++C60: Collision energy and impact parameter dependence for endohedral complex formation, fragmentation, and charge transfer," The Journal of Chemical Physics **96**, 3344–3347 (1992).
[90]J. A. Mosely, H. J. Cooper, R. T. Gallagher, and P. J. Derrick, "Letter: Target Capture of Argon by Fullerene Radical Cations in High-Energy Collisions," European Mass Spectrometry **1**, 501–502 (1995).
[91]M. Murata, Y. Murata, and K. Komatsu, "Surgery of fullerenes," Chemical Communications **0**, 6083–6094 (2008).
[92]Y. Kohama, T. Rachi, J. Jing, Z. Li, J. Tang, R. Kumashiro, S. Izumisawa, H. Kawaji, T. Atake, H. Sawa, Y. Murata, K. Komatsu, and K. Tanigaki, "Rotational Sublevels of an Ortho-Hydrogen Molecule Encapsulated in an Isotropic ${\mathbf{C}}_{60}$ Cage," Physical Review Letters **103**, 073001 (2009).
[93]G. C. Vougioukalakis, M. M. Roubelakis, and M. Orfanopoulos, "Open-cage fullerenes: Towards the construction of nanosized molecular containers," Chemical Society Reviews **39**, 817–844 (2010).
[94]M. Murata, Y. Murata, and K. Komatsu, "Molecular Surgery toward Organic Synthesis of Endohedral Fullerenes," in *Chemistry of Nanocarbons* (John Wiley & Sons, Ltd, 2010) Chap. 8, pp. 215–237.
[95]M. Murata, Y. Murata, and K. Komatsu, "Organic Synthesis of Endohedral Fullerenes Encapsulating Helium, Dihydrogen, and Water," in *Organic Nanomaterials* (John Wiley & Sons, Ltd, 2013) Chap. 11, pp. 225–239.
[96]S. Bloodworth and R. J. Whitby, "Synthesis of endohedral fullerenes by molecular surgery," Communications Chemistry **5**, 1–14 (2022).
[97]Y. Hashikawa and Y. Murata, "Water in Fullerenes," Bulletin of the Chemical Society of Japan **96**, 943–967 (2023).
[98]K. Kurotobi and Y. Murata, "A Single Molecule of Water Encapsulated in Fullerene C60," Science **333**, 613–616 (2011).
[99]Y. Morinaka, F. Tanabe, M. Murata, Y. Murata, and K. Komatsu, "Rational synthesis, enrichment, and 13C NMR spectra of endohedral C60 and C70 encapsulating a helium atom," Chemical Communications **46**, 4532–4534 (2010).
[100]G. Hoffman, M. C. Walkey, J. Gräsvik, G. R. Bacanu, S. Alom, S. Bloodworth, M. E. Light, M. H. Levitt, and R. J. Whitby, "A Solid-State Intramolecular Wittig Reaction Enables Efficient Synthesis of Endofullerenes Including Ne@C60, 3He@C60, and HD@C60," Angewandte Chemie International Edition **60**, 8960–8966 (2021).
[101]S. Bloodworth, G. Hoffman, M. C. Walkey, G. R. Bacanu, J. M. Herniman, M. H. Levitt, and R. J. Whitby, "Synthesis of Ar@C60 using molecular surgery," Chemical Communications **56**, 10521–10524 (2020).
[102]G. Hoffman, G. R. Bacanu, E. S. Marsden, M. C. Walkey, M. Sabba, S. Bloodworth, G. J. Tizzard, M. H. Levitt, and R. J. Whitby, "Synthesis and 83Kr NMR spectroscopy of Kr@C60," Chemical Communications **58**, 11284–11287 (2022).
[103]S. Bloodworth, G. Sitinova, S. Alom, S. Vidal, G. R. Bacanu, S. J. Elliott, M. E. Light, J. M. Herniman, G. J. Langley, M. H. Levitt, and R. J. Whitby, "First Synthesis and Characterization of CH4@C60," Angewandte Chemie International Edition **58**, 5038–5043 (2019).
[104]Y. Hashikawa, M. Murata, A. Wakamiya, and Y. Murata, "Synthesis and Properties of Endohedral Aza[60]fullerenes: $H_2O@C_{59}N$ and $H_2@C_{59}N$ as Their Dimers and Monomers," Journal of the American Chemical Society **138**, 4096–4104 (2016).
[105]G.-Z. Zhu, Y. Liu, Y. Hashikawa, Q.-F. Zhang, Y. Murata, and L.-S. Wang, "Probing the interaction between the encapsulated water molecule and the fullerene cages in H2O@C60- and H2O@C59N-," Chemical Science **9**, 5666–5671 (2018).
[106]S. Hasegawa, Y. Hashikawa, T. Kato, and Y. Murata, "Construction of a Metal-Free Electron Spin System by Encapsulation of an NO Molecule Inside an Open-Cage Fullerene C60 Derivative," Angewandte Chemie International Edition **57**, 12804–12808 (2018).
[107]K.-P. Dinse, T. Kato, S. Hasegawa, Y. Hashikawa, Y. Murata, and R. Bittl, "EPR study of NO radicals encased in modified open C_{60} fullerenes," Magnetic Resonance **1**, 197–207 (2020).
[108]B. Frecus, C. M. Buta, C. I. Oprea, A. Stroppa, M. V. Putz, and F. Cimpoesu, "Noble gas endohedral fullerenes, Ng@C60 (Ng=Ar, Kr): A particular benchmark for assessing the account of non-covalent interactions by density functional theory calculations," Theoretical Chemistry Accounts **135**, 133 (2016).
[109]G. R. Bacanu, J. Rantaharju, G. Hoffman, M. C. Walkey, S. Bloodworth, M. Concistrè, R. J. Whitby, and M. H. Levitt, "An Internuclear J-Coupling of 3He Induced by Molecular Confinement," Journal of the American Chemical Society **142**, 16926–16929 (2020).
[110]G. Bacanu, *Spectroscopic Investigations of C60 Fullerene and Its Endohedral Derivatives.*, Ph.D. thesis, University of Southampton, School of Chemistry (2021).
[111]G. R. Bacanu, T. Jafari, M. Aouane, J. Rantaharju, M. Walkey, G. Hoffman, A. Shugai, U. Nagel, M. Jiménez-Ruiz, A. J. Horsewill, S. Rols, T. Rõõm, R. J. Whitby, and M. H. Levitt, "Experimental determination of the interaction potential between a helium atom and the interior surface of a C60 fullerene molecule," The Journal of Chemical Physics **155**, 144302 (2021).
[112]T. Jafari, G. R. Bacanu, A. Shugai, U. Nagel, M. Walkey, G. Hoffman, M. H. Levitt, R. J. Whitby, and T. Rõõm, "Terahertz spectroscopy of the helium endofullerene He@C60," Physical Chemistry Chemical Physics **24**, 9943–9952 (2022).
[113]M. Aouane, J. Armstrong, M. Walkey, G. Hoffman, G. R. Bacanu, R. J. Whitby, M. H. Levitt, and S. Rols, "A combined inelastic neutron scattering and simulation study of the 3He@C60 endofullerene," Physical Chemistry Chemical Physics **25**, 20295–20301 (2023).
[114]J. E. Grose, E. S. Tam, C. Timm, M. Scheloske, B. Ulgut, J. J. Parks, H. D. Abruña, W. Harneit, and D. C. Ralph, "Tunnelling spectra of individual magnetic endofullerene molecules," Nature Materials **7**, 884–889 (2008).
[115]N. Roch, R. Vincent, F. Elste, W. Harneit, W. Wernsdorfer, C. Timm, and F. Balestro, "Cotunneling through a magnetic single-molecule transistor based on N@C${}_{60}$," Physical Review B **83**, 081407 (2011).
[116]S. Du, Y. Hashikawa, H. Ito, K. Hashimoto, Y. Murata, Y. Hirayama, and K. Hirakawa, "Inelastic Electron Transport and Ortho–Para Fluctuation of Water Molecule in H2O@C60 Single Molecule Transistors," Nano Letters **21**, 10346–10353 (2021).
[117]C. Meyer, W. Harneit, M. Waiblinger, K. Lips, and A. Weidinger, "Electron spin quantum computing with N@C60," AIP Conference Proceedings **591**, 101–104 (2001).
[118]C. Meyer, W. Harneit, B. Naydenov, K. Lips, and A. Weidinger, "N@C60 and P@C60 as quantum bits," Applied Magnetic Resonance **27**, 123–132 (2004).
[119]J. J. L. Morton, A. M. Tyryshkin, A. Ardavan, S. C. Benjamin, K. Porfyrakis, S. A. Lyon, and G. A. D. Briggs, "The N@C60 nuclear spin qubit: Bang-bang decoupling and ultrafast phase gates," physica status solidi (b) **243**, 3028–3031 (2006).
[120]S. C. Benjamin, A. Ardavan, G. A. D. Briggs, D. A. Britz, D. Gunlycke, J. Jefferson, M. A. G. Jones, D. F. Leigh, B. W. Lovett, A. N. Khlobystov, S. A. Lyon, J. J. L. Morton, K. Porfyrakis, M. R. Sambrook, and A. M. Tyryshkin, "Towards a fullerene-based quantum computer," Journal of Physics: Condensed Matter **18**, S867 (2006).
[121]A. Ardavan, J. J. L. Morton, S. C. Benjamin, K. Porfyrakis, G. A. D. Briggs, A. M. Tyryshkin, and S. A. Lyon, "Manipulation of quantum information in N@C60 using electron and nuclear magnetic resonance," physica status solidi (b) **244**, 3874–3878 (2007).
[122]W. Harneit, K. Huebener, B. Naydenov, S. Schaefer, and M. Scheloske, "N@C60 quantum bit engineering," physica status solidi (b) **244**, 3879–3884 (2007).
[123]W. L. Yang, Z. Y. Xu, H. Wei, M. Feng, and D. Suter, "Quantum-information-processing architecture with endohedral fullerenes in a carbon nanotube," Physical Review A **81**, 032303 (2010).
[124]W. Harneit, "Spin Quantum Computing with Endohedral Fullerenes," in *Endohedral Fullerenes: Electron Transfer and Spin*, edited by A. A. Popov (Springer International Publishing, Cham, 2017) pp. 297–324.
[125]R. T. Harding, S. Zhou, J. Zhou, T. Lindvall, W. K. Myers, A. Ardavan, G. A. D. Briggs, K. Porfyrakis, and E. A. Laird, "Spin Resonance Clock Transition of the Endohedral Fullerene $^{15}\mathrm{N}@{\mathrm{C}}_{60}$," Physical Review Letters **119**, 140801 (2017).

[126]M. Soundararajan, G. R. Bacanu, F. Giustiniano, M. C. Walkey, G. Hoffman, M. Carravetta, M. R. Lees, R. J. Whitby, and M. H. Levitt, "Solid-State $$\mathrm {^3He}$$NMR of the Superconducting Rubidium Endofulleride $$\mathrm {Rb_3(^3He@C_{60})}$$," Applied Magnetic Resonance **54**, 1177–1192 (2023).
[127]S. Guha and K. Nakamoto, "Electronic structures and spectral properties of endohedral fullerenes," Coordination Chemistry Reviews **249**, 1111–1132 (2005).
[128]M. Straka and J. Vaara, "Density Functional Calculations of 3He Chemical Shift in Endohedral Helium Fullerenes: Neutral, Anionic, and Di-Helium Species," The Journal of Physical Chemistry A **110**, 12338–12341 (2006).
[129]P. Pyykkö, C. Wang, M. Straka, and J. Vaara, "A London-type formula for the dispersion interactions of endohedral A@B systems," Physical Chemistry Chemical Physics **9**, 2954–2958 (2007).
[130]M. Xu, F. Sebastianelli, Z. Bačić, R. Lawler, and N. J. Turro, "H2, HD, and D2 inside C60: Coupled translation-rotation eigenstates of the endohedral molecules from quantum five-dimensional calculations," The Journal of Chemical Physics **129**, 064313 (2008).
[131]M. Straka, P. Lantto, and J. Vaara, "Toward Calculations of the 129Xe Chemical Shift in Xe@C60 at Experimental Conditions: Relativity, Correlation, and Dynamics," The Journal of Physical Chemistry A **112**, 2658–2668 (2008).
[132]S. Taubert, M. Straka, T. O. Pennanen, D. Sundholm, and J. Vaara, "Dynamics and magnetic resonance properties of Sc3C2@C80 and its monoanion," Physical Chemistry Chemical Physics **10**, 7158–7168 (2008).
[133]M. Xu, F. Sebastianelli, Z. Bačić, R. Lawler, and N. J. Turro, "Quantum dynamics of coupled translational and rotational motions of H2 inside C60," The Journal of Chemical Physics **128**, 011101 (2008).
[134]M. Xu, F. Sebastianelli, B. R. Gibbons, Z. Bačić, R. Lawler, and N. J. Turro, "Coupled translation-rotation eigenstates of H2 in C60 and C70 on the spectroscopically optimized interaction potential: Effects of cage anisotropy on the energy level structure and assignments," The Journal of Chemical Physics **130**, 224306 (2009).
[135]S. Ye, M. Xu, S. FitzGerald, K. Tchernyshyov, and Z. Bačić, "H2 in solid C60: Coupled translation-rotation eigenstates in the octahedral interstitial site from quantum five-dimensional calculations," The Journal of Chemical Physics **138**, 244707 (2013).
[136]G. A. Dolgonos and G. H. Peslherbe, "Encapsulation of diatomic molecules in fullerene C 60 : Implications for their main properties," Physical Chemistry Chemical Physics **16**, 26294–26305 (2014).
[137]P. M. Felker and Z. Bačić, "Translation-rotation states of H2 in C60: New insights from a perturbation-theory treatment," J. Chem. Phys. **145**, 0845310 (2016).
[138]Z. Slanina, F. Uhlík, S. Nagase, T. Akasaka, L. Adamowicz, and X. Lu, "A computational characterization of CO@C60," Fullerenes, Nanotubes and Carbon Nanostructures **25**, 624–629 (2017).
[139]P. M. Felker and Z. Bačić, "Accurate quantum calculations of translation-rotation eigenstates in electric-dipole-coupled H2O@C60 assemblies," Chemical Physics Letters Ahmed Zewail (1946-2016) Commemoration Issue of Chemical Physics Letters, **683**, 172–178 (2017).
[140]J. Roukala, M. Straka, S. Taubert, J. Vaara, and P. Lantto, "Ratcheting rotation or speedy spinning: EPR and dynamics of Sc3C2@C80," Chemical Communications **53**, 8992–8995 (2017).
[141]P. M. Felker and Z. Bačić, "Electric-dipole-coupled H2O@C60 dimer: Translation-rotation eigenstates from twelve-dimensional quantum calculations," The Journal of Chemical Physics **146**, 084303 (2017).
[142]S. Jalife, J. Arcudia, S. Pan, and G. Merino, "Noble gas endohedral fullerenes," Chemical Science **11**, 6642–6652 (2020).
[143]N. Sathyamurthy, "Atoms and molecules confined inside C60," Proceedings of the Indian National Science Academy **87**, 311–319 (2021).
[144]O. Carrillo-Bohórquez, Á. Valdés, and R. Prosmiti, "Encapsulation of a Water Molecule inside C60 Fullerene: The Impact of Confinement on Quantum Features," Journal of Chemical Theory and Computation **17**, 5839–5848 (2021).
[145]C. Wespiser, T. Putaud, Y. Kalugina, A. Soldera, P.-N. Roy, X. Michaut, and P. Ayotte, "Ro-translational dynamics of confined water. I. The confined asymmetric rotor model," The Journal of Chemical Physics **156**, 074304 (2022).
[146]A. W. Hauser and J. V. Pototschnig, "Vibronic Coupling in Spherically Encapsulated, Diatomic Molecules: Prediction of a Renner–Teller-like Effect for Endofullerenes," The Journal of Physical Chemistry A **126**, 1674–1680 (2022).
[147]J. Vícha, J. Vaara, and M. Straka, "The essential role of symmetry in understanding 3He chemical shifts in endohedral helium fullerenes," Physical Chemistry Chemical Physics **25**, 10620–10627 (2023).
[148]M. Carravetta, A. Danquigny, S. Mamone, F. Cuda, O. G. Johannessen, I. Heinmaa, K. Panesar, R. Stern, M. C. Grossel, A. J. Horsewill, A. Samoson, M. Murata, Y. Murata, K. Komatsu, and M. H. Levitt, "Solid-state NMR of endohedral hydrogen–fullerene complexes," Physical Chemistry Chemical Physics **9**, 4879–4894 (2007).
[149]A. J. Horsewill, K. S. Panesar, S. Rols, M. R. Johnson, Y. Murata, K. Komatsu, S. Mamone, A. Danquigny, F. Cuda, S. Maltsev, M. C. Grossel, M. Carravetta, and M. H. Levitt, "Quantum Translator-Rotator: Inelastic Neutron Scattering of Dihydrogen Molecules Trapped inside Anisotropic Fullerene Cages," Physical Review Letters **102**, 013001 (2009).
[150]S. Mamone, J. Y. C. Chen, R. Bhattacharyya, M. H. Levitt, R. G. Lawler, A. J. Horsewill, T. Rõõm, Z. Bačić, and N. J. Turro, "Theory and spectroscopy of an incarcerated quantum rotor: The infrared spectroscopy, inelastic neutron scattering and nuclear magnetic resonance of H2@C60 at cryogenic temperature," Coordination Chemistry Reviews A Celebration of Harry B. Gray's 75th Birthday, **255**, 938–948 (2011).
[151]M. H. Levitt, "Spectroscopy of light-molecule endofullerenes," Philosophical Transactions of the Royal Society A: Mathematical, Physical and Engineering Sciences **371**, 20120429 (2013).
[152]Y. Murata, "Open-Cage Fullerene Derivatives: Synthesis, Reactions, and Encapsulation of a Small Molecule," in *Chemical Science of π-Electron Systems*, edited by T. Akasaka, A. Osuka, S. Fukuzumi, H. Kandori, and Y. Aso (Springer Japan, Tokyo, 2015) pp. 117–131.
[153]S. Bloodworth, J. Gräsvik, S. Alom, K. Kouřil, S. J. Elliott, N. J. Wells, A. J. Horsewill, S. Mamone, M. Jiménez-Ruiz, S. Rols, U. Nagel, T. Rõõm, M. H. Levitt, and R. J. Whitby, "Synthesis and Properties of Open Fullerenes Encapsulating Ammonia and Methane," ChemPhysChem **19**, 266–276 (2018).
[154]J. Y.-C. Chen, Y. Li, M. Frunzi, X. Lei, Y. Murata, R. G. Lawler, and N. J. Turro, "Nuclear spin isomers of guest molecules in H2@C60, H2O@C60 and other endofullerenes," Philosophical Transactions of the Royal Society A: Mathematical, Physical and Engineering Sciences **371**, 20110628 (2013).
[155]T. Rõõm, L. Peedu, M. Ge, D. Hüvonen, U. Nagel, S. Ye, M. Xu, Z. Bačić, S. Mamone, M. H. Levitt, M. Carravetta, J.-C. Chen, X. Lei, N. J. Turro, Y. Murata, and K. Komatsu, "Infrared spectroscopy of small-molecule endofullerenes," Philosophical Transactions of the Royal Society A: Mathematical, Physical and Engineering Sciences **371**, 20110631 (2013).
[156]H. Nie, C. Zhao, Z. Shi, C. Jia, and X. Guo, "Single-Molecule Fullerenes: Current Stage and Perspective," ACS Materials Letters **4**, 1037–1052 (2022).
[157]G. Herzberg, *Molecular Spectra and Molecular Structure: 1 Spectra of Diatomic Molecules*, 2nd ed., Vol. 1 (Van Nostrand, 1950).
[158]M. Mehring, *Principles of High Resolution NMR in Solids*, 2nd ed. (Springer-Verlag, Berlin Heidelberg, 1983).
[159]S. W. Lovesey, *Theory of Neutron Scattering from Condensed Matter: Volume I: Nuclear Scattering*, International Series of Monographs on Physics (Oxford University Press, Oxford, New York, 1986).
[160]R. N. Zare, *Angular Momentum: Understanding Spatial Aspects in Chemistry and Physics* (John Wiley & Sons, 1988).
[161]S. Flügge, *Practical Quantum Mechanics*, Classics in Mathematics (Springer-Verlag, Berlin Heidelberg, 1999).
[162]B. H. Bransden and C. J. Joachain, *Quantum Mechanics*, 2nd ed. (Pearson Prentice Hall, 2000).
[163]M. H. Levitt, *Spin Dynamics: Basics of Nuclear Magnetic Resonance*, 2nd ed. (John Wiley & Sons, 2007).
[164]D. J. Griffiths and D. F. Schroeter, *Introduction to Quantum Mechanics*, 3rd ed. (Cambridge University Press, Cambridge, 2018).
[165]A. Abragam and A. Abragam, *The Principles of Nuclear Magnetism*, International Series of Monographs on Physics (Oxford University Press, Oxford, New York, 1983).
[166]R. R. Ernst, G. Bodenhausen, A. Wokaun, R. R. Ernst, G. Bodenhausen, and A. Wokaun, *Principles of Nuclear Magnetic Resonance in One and Two Dimensions*, International Series of Monographs on Chemistry (Oxford University Press, Oxford, New York, 1990).

[167]E. J. L. McInnes and D. Collison, "EPR Interactions – Coupled Spins," eMagRes , 1445–1458 (2016).
[168]D. Goldfarb and S. Stoll, *EPR Spectroscopy: Fundamentals and Methods* (John Wiley & Sons, 2018).
[169]N. Wili, "A primer in pulse EPR-based hyperfine spectroscopy for NMR spectroscopists," Journal of Magnetic Resonance Open **16–17**, 100108 (2023).
[170]A. J. Pell, G. Pintacuda, and C. P. Grey, "Paramagnetic NMR in solution and the solid state," Progress in Nuclear Magnetic Resonance Spectroscopy **111**, 1–271 (2019).
[171]L. Pang and F. Brisse, "Endohedral energies and translation of fullerene-noble gas clusters G@Cn (G = helium, neon, argon, krypton and xenon; n = 60 and 70)," The Journal of Physical Chemistry **97**, 8562–8563 (1993).
[172]M. Xu, S. Ye, A. Powers, R. Lawler, N. J. Turro, and Z. Bačić, "Inelastic neutron scattering spectrum of H2@C60 and its temperature dependence decoded using rigorous quantum calculations and a new selection rule," The Journal of Chemical Physics **139**, 064309 (2013).
[173]M. Xu, S. Ye, R. Lawler, N. J. Turro, and Z. Bačić, "HD in C60: Theoretical prediction of the inelastic neutron scattering spectrum and its temperature dependence," Philosophical Transactions of the Royal Society A: Mathematical, Physical and Engineering Sciences **371**, 1471–2962 (2013).
[174]M. Xu, M. Jiménez-Ruiz, M. R. Johnson, S. Rols, S. Ye, M. Carravetta, M. S. Denning, X. Lei, Z. Bačić, and A. J. Horsewill, "Confirming a Predicted Selection Rule in Inelastic Neutron Scattering Spectroscopy: The Quantum Translator-Rotator ${\mathrm{H}}_{2}$ Entrapped Inside ${\mathrm{C}}_{60}$," Physical Review Letters **113**, 123001 (2014).
[175]M. Xu, P. M. Felker, S. Mamone, A. J. Horsewill, S. Rols, R. J. Whitby, and Z. Bačić, "The Endofullerene HF@C60: Inelastic Neutron Scattering Spectra from Quantum Simulations and Experiment, Validity of the Selection Rule, and Symmetry Breaking," The Journal of Physical Chemistry Letters **10**, 5365–5371 (2019).
[176]M. Xu, P. M. Felker, and Z. Bačić, "H2O inside the fullerene C60: Inelastic neutron scattering spectrum from rigorous quantum calculations," The Journal of Chemical Physics **156**, 124101 (2022).
[177]S. Mamone, M. Ge, D. Hüvonen, U. Nagel, A. Danquigny, F. Cuda, M. C. Grossel, Y. Murata, K. Komatsu, M. H. Levitt, T. Rõõm, and M. Carravetta, "Rotor in a cage: Infrared spectroscopy of an endohedral hydrogen-fullerene complex," The Journal of Chemical Physics **130**, 081103 (2009).
[178]M. Salvatore, *Theory and Spectroscopy of Dihydrogen Endofullerenes*, Ph.D. thesis, University of Southampton, School of Chemistry (2011).
[179]T. Jafari, A. Shugai, U. Nagel, G. R. Bacanu, M. Aouane, M. Jiménez-Ruiz, S. Rols, S. Bloodworth, M. Walkey, G. Hoffman, R. J. Whitby, M. H. Levitt, and T. Rõõm, "Ne, Ar, and Kr oscillators in the molecular cavity of fullerene C60," The Journal of Chemical Physics **158**, 234305 (2023).
[180]M. Aouane, *Endofullerenes: Dynamics in Confinement Probed by Neutron Spectroscopy*, Ph.D. thesis, Grenoble Alpes University (2022).
[181]M. Ge, U. Nagel, D. Hüvonen, T. Rõõm, S. Mamone, M. H. Levitt, M. Carravetta, Y. Murata, K. Komatsu, J. Y.-C. Chen, and N. J. Turro, "Interaction potential and infrared absorption of endohedral H2 in C60," The Journal of Chemical Physics **134**, 054507 (2011).
[182]P. R. Bunker and P. Jensen, *Molecular Symmetry and Spectroscopy*, 2nd ed. (NRC Research Press, 2006).
[183]A. J. Horsewill, K. S. Panesar, S. Rols, J. Ollivier, M. R. Johnson, M. Carravetta, S. Mamone, M. H. Levitt, Y. Murata, K. Komatsu, J. Y.-C. Chen, J. A. Johnson, X. Lei, and N. J. Turro, "Inelastic neutron scattering investigations of the quantum molecular dynamics of a H${}_{2}$ molecule entrapped inside a fullerene cage," Physical Review B **85**, 205440 (2012).
[184]S. McArdle, S. Endo, A. Aspuru-Guzik, S. C. Benjamin, and X. Yuan, "Quantum computational chemistry," Reviews of Modern Physics **92**, 015003 (2020).
[185]F. Jensen, *Introduction to Computational Chemistry*, 3rd ed. (Wiley, Chichester, 2017).
[186]I. Levine, *Quantum Chemistry*, 7th ed. (Pearson, Boston Columbus Indianapolis New York San Francisco Upper Saddle River Amsterdam Cape Town Dubai London, 2013).
[187]A. Shugai, U. Nagel, Y. Murata, Y. Li, S. Mamone, A. Krachmalnicoff, S. Alom, R. J. Whitby, M. H. Levitt, and T. Rõõm, "Infrared spectroscopy of an endohedral water in fullerene," The Journal of Chemical Physics **154**, 124311 (2021).
[188]D. L. Dexter, "Absorption of Light by Atoms in Solids," Physical Review **101**, 48–55 (1956).
[189]S. Mamone, M. Jiménez-Ruiz, M. R. Johnson, S. Rols, and A. J. Horsewill, "Experimental, theoretical and computational investigation of the inelastic neutron scattering spectrum of a homonuclear diatomic molecule in a nearly spherical trap: H2@C60," Physical Chemistry Chemical Physics **18**, 29369–29380 (2016).
[190]M. Xu, L. Ulivi, M. Celli, D. Colognesi, and Z. Bačić, "Quantum calculation of inelastic neutron scattering spectra of a hydrogen molecule inside a nanoscale cavity based on rigorous treatment of the coupled translation-rotation dynamics," Physical Review B **83**, 241403 (2011).
[191]M. Xu and Z. Bačić, "Inelastic neutron scattering spectra of a hydrogen molecule in a nanocavity: Methodology for quantum calculations incorporating the coupled five-dimensional translation-rotation eigenstates," Physical Review B **84**, 195445 (2011).
[192]A. J. Horsewill, K. Goh, S. Rols, J. Ollivier, M. R. Johnson, M. H. Levitt, M. Carravetta, S. Mamone, Y. Murata, J. Y.-C. Chen, J. A. Johnson, X. Lei, and N. J. Turro, "Quantum rotation and translation of hydrogen molecules encapsulated inside C60: Temperature dependence of inelastic neutron scattering spectra," Philosophical Transactions of the Royal Society A: Mathematical, Physical and Engineering Sciences **371**, 20110627 (2013).
[193]K. S. K. Goh, M. Jiménez-Ruiz, M. R. Johnson, S. Rols, J. Ollivier, M. S. Denning, S. Mamone, M. H. Levitt, X. Lei, Y. Li, N. J. Turro, Y. Murata, and A. J. Horsewill, "Symmetry-breaking in the endofullerene H2O@C60 revealed in the quantum dynamics of ortho and para-water: A neutron scattering investigation," Physical Chemistry Chemical Physics **16**, 21330–21339 (2014).
[194]J. Als-Nielsen and D. McMorrow, *Elements of Modern X-ray Physics*, 2nd ed. (John Wiley & Sons, 2011).
[195]M. Morscher, A. P. Seitsonen, S. Ito, H. Takagi, N. Dragoe, and T. Greber, "Strong $3p$-${T}_{1u}$ hybridization in ${\mathrm{Ar@C}}_{60}$," Physical Review A **82**, 051201 (2010).
[196]S. Ito, A. Takeda, T. Miyazaki, Y. Yokoyama, M. Saunders, R. J. Cross, H. Takagi, P. Berthet, and N. Dragoe, "Kr Extended X-ray Absorption Fine Structure Study of Endohedral Kr@C60," The Journal of Physical Chemistry B **108**, 3191–3195 (2004).
[197]D. P. Woodruff, "Normal incidence X-ray standing wave determination of adsorbate structures," Progress in Surface Science **57**, 1–60 (1998).
[198]S. P. Jarvis, H. Sang, F. Junqueira, O. Gordon, J. E. A. Hodgkinson, A. Saywell, P. Rahe, S. Mamone, S. Taylor, A. Sweetman, J. Leaf, D. A. Duncan, T.-L. Lee, P. K. Thakur, G. Hoffman, R. J. Whitby, M. H. Levitt, G. Held, L. Kantorovich, P. Moriarty, and R. G. Jones, "Chemical shielding of H2O and HF encapsulated inside a C60 cage," Communications Chemistry **4**, 1–7 (2021).
[199]A. L. D. Kilcoyne, A. Aguilar, A. Müller, S. Schippers, C. Cisneros, G. Alna'Washi, N. B. Aryal, K. K. Baral, D. A. Esteves, C. M. Thomas, and R. A. Phaneuf, "Confinement Resonances in Photoionization of $\mathrm{Xe}@{\mathrm{C}}_{60}^{+}$," Physical Review Letters **105**, 213001 (2010).
[200]R. A. Phaneuf, A. L. D. Kilcoyne, N. B. Aryal, K. K. Baral, D. A. Esteves-Macaluso, C. M. Thomas, J. Hellhund, R. Lomsadze, T. W. Gorczyca, C. P. Ballance, S. T. Manson, M. F. Hasoglu, S. Schippers, and A. Müller, "Probing confinement resonances by photoionizing Xe inside a C${}_{60}^{+}$ molecular cage," Physical Review A **88**, 053402 (2013).
[201]A. Müller, A. L. D. Kilcoyne, S. Schippers, and R. A. Phaneuf, "Experimental studies on photoabsorption by endohedral fullerene ions with a focus on Xe@C60+ confinement resonances," Physica Scripta **96**, 064004 (2021).
[202]R. Taylor, J. P. Hare, A. K. Abdul-Sada, and H. W. Kroto, "Isolation, separation and characterisation of the fullerenes C60 and C70: The third form of carbon," Journal of the Chemical Society, Chemical Communications , 1423–1425 (1990).
[203]H. W. Kroto, A. W. Allaf, and S. P. Balm, "C60: Buckminsterfullerene," Chemical Reviews **91**, 1213–1235 (1991).
[204]C. S. Yannoni, R. D. Johnson, G. Meijer, D. S. Bethune, and J. R. Salem, "Carbon-13 NMR study of the C60 cluster in the solid state: Molecular motion and carbon chemical shift anisotropy," The Journal of Physical Chemistry **95**, 9–10 (1991).
[205]G. R. Bacanu, G. Hoffman, M. Amponsah, M. Concistrè, R. J. Whitby, and M. H. Levitt, "Fine structure in the solution state 13C-NMR spectrum

of C60 and its endofullerene derivatives," Physical Chemistry Chemical Physics **22**, 11850–11860 (2020).
[206]C. J. Jameson, "The isotope shift in NMR," The Journal of Chemical Physics **66**, 4983–4988 (1977).
[207]P. E. Hansen, "Isotope effects in nuclear shielding," Progress in Nuclear Magnetic Resonance Spectroscopy **20**, 207–255 (1988).
[208]R. Tycko, G. Dabbagh, R. M. Fleming, R. C. Haddon, A. V. Makhija, and S. M. Zahurak, "Molecular dynamics and the phase transition in solid ${\mathrm{C}}_{60}$," Physical Review Letters **67**, 1886–1889 (1991).
[209]R. D. Johnson, C. S. Yannoni, H. C. Dorn, J. R. Salem, and D. S. Bethune, "C60 Rotation in the Solid State: Dynamics of a Faceted Spherical Top," Science **255**, 1235–1238 (1992).
[210]W. I. F. David, R. M. Ibberson, T. J. S. Dennis, J. P. Hare, and K. Prassides, "Structural Phase Transitions in the Fullerene C 60," Europhysics Letters (EPL) **18**, 219–225 (1992).
[211]W. I. F. David, R. M. Ibberson, J. C. Matthewman, K. Prassides, T. J. S. Dennis, J. P. Hare, H. W. Kroto, R. Taylor, and D. R. M. Walton, "Crystal structure and bonding of ordered C 60," Nature **353**, 147–149 (1991).
[212]W. I. F. David and R. M. Ibberson, "High-pressure, low-temperature structural studies of orientationally ordered C60," Journal of Physics: Condensed Matter **5**, 7923 (1993).
[213]M. Xu, S. Ye, and Z. Bačić, "General Selection Rule in the Inelastic Neutron Scattering Spectroscopy of a Diatomic Molecule Confined Inside a Near-Spherical Nanocavity," The Journal of Physical Chemistry Letters **6**, 3721–3725 (2015).
[214]Z. Bačić, "Perspective: Accurate treatment of the quantum dynamics of light molecules inside fullerene cages: Translation-rotation states, spectroscopy, and symmetry breaking," The Journal of Chemical Physics **149**, 100901 (2018).
[215]M. Xu, P. M. Felker, and Z. Bačić, "Light molecules inside the nanocavities of fullerenes and clathrate hydrates: Inelastic neutron scattering spectra and the unexpected selection rule from rigorous quantum simulations," International Reviews in Physical Chemistry **39**, 425–463 (2020).
[216]B. Poirier, "Communication: The H2@C60 inelastic neutron scattering selection rule: Expanded and explained," The Journal of Chemical Physics **143**, 101104 (2015).
[217]L. W. Poirier, "Effect of Confinement on the Translation-Rotation Motion of Molecules: The Inelastic Neutron Scattering Selection Rule," in *Chemical Reactivity in Confined Systems* (John Wiley & Sons, Ltd, 2021) Chap. 1, pp. 1–24.
[218]M. Ge, U. Nagel, D. Hüvonen, T. Rõõm, S. Mamone, M. H. Levitt, M. Carravetta, Y. Murata, K. Komatsu, X. Lei, and N. J. Turro, "Infrared spectroscopy of endohedral HD and D2 in C60," The Journal of Chemical Physics **135**, 114511 (2011).
[219]S. Mamone, M. R. Johnson, J. Ollivier, S. Rols, M. H. Levitt, and A. J. Horsewill, "Symmetry-breaking in the H2@C60 endofullerene revealed by inelastic neutron scattering at low temperature," Physical Chemistry Chemical Physics **18**, 1998–2005 (2016).
[220]C. Beduz, M. Carravetta, J. Y.-C. Chen, M. Concistrè, M. Denning, M. Frunzi, A. J. Horsewill, O. G. Johannessen, R. Lawler, X. Lei, M. H. Levitt, Y. Li, S. Mamone, Y. Murata, U. Nagel, T. Nishida, J. Ollivier, S. Rols, T. Rõõm, R. Sarkar, N. J. Turro, and Y. Yang, "Quantum rotation of ortho and para-water encapsulated in a fullerene cage," Proceedings of the National Academy of Sciences **109**, 12894–12898 (2012).
[221]M. Concistrè, S. Mamone, M. Denning, G. Pileio, X. Lei, Y. Li, M. Carravetta, N. J. Turro, and M. H. Levitt, "Anisotropic nuclear spin interactions in H2O@C60 determined by solid-state NMR," Philosophical Transactions of the Royal Society A: Mathematical, Physical and Engineering Sciences **371**, 20120102 (2013).
[222]H. Suzuki, M. Nakano, Y. Hashikawa, and Y. Murata, "Rotational Motion and Nuclear Spin Interconversion of H2O Encapsulated in C60 Appearing in the Low-Temperature Heat Capacity," The Journal of Physical Chemistry Letters **10**, 1306–1311 (2019).
[223]K. P. Dinse, H. Käß, C. Knapp, and N. Weiden, "EPR investigation of atoms in chemical traps," Carbon Fullerenes '99, **38**, 1635–1640 (2000).
[224]P. M. Felker, V. Vlček, I. Hietanen, S. FitzGerald, D. Neuhauser, and Z. Bačić, "Explaining the symmetry breaking observed in the endofullerenes H2@C60, HF@C60, and H2O@C60," Physical Chemistry Chemical Physics **19**, 31274–31283 (2017).
[225]Z. Bačić, V. Vlček, D. Neuhauser, and P. M. Felker, "Effects of symmetry breaking on the translation–rotation eigenstates of H2, HF, and H2O inside the fullerene C60," Faraday Discussions **212**, 547–567 (2018).
[226]J. L. Dunn and E. Rashed, "Evidence for Jahn-Teller effects in endohedral fullerenes," Journal of Physics: Conference Series **1148**, 012003 (2018).
[227]E. Rashed and J. L. Dunn, "Interactions between a water molecule and C60 in the endohedral fullerene H2O@C60," Physical Chemistry Chemical Physics **21**, 3347–3359 (2019).
[228]Y. N. Kalugina and P.-N. Roy, "Potential energy and dipole moment surfaces for HF@C60: Prediction of spectral and electric response properties," The Journal of Chemical Physics **147**, 244303 (2017).
[229]O. Carrillo-Bohórquez, Á. Valdés, and R. Prosmiti, "Unraveling the Origin of Symmetry Breaking in H2O@C60 Endofullerene Through Quantum Computations," ChemPhysChem **23**, e202200034 (2022).
[230]V. Filidou, S. Mamone, S. Simmons, S. D. Karlen, H. L. Anderson, C. W. M. Kay, A. Bagno, F. Rastrelli, Y. Murata, K. Komatsu, X. Lei, Y. Li, N. J. Turro, M. H. Levitt, and J. J. L. Morton, "Probing the C60 triplet state coupling to nuclear spins inside and out," Philosophical Transactions of the Royal Society A: Mathematical, Physical and Engineering Sciences **371**, 20120475 (2013).
[231]J. López-Gejo, A. A. Martí, M. Ruzzi, S. Jockusch, K. Komatsu, F. Tanabe, Y. Murata, and N. J. Turro, "Can H2 Inside C60 Communicate with the Outside World?" Journal of the American Chemical Society **129**, 14554–14555 (2007).
[232]H. Nikawa, Y. Araki, Z. Slanina, T. Tsuchiya, T. Akasaka, T. Wada, O. Ito, K.-P. Dinse, M. Ata, T. Kato, and S. Nagase, "The effect of atomic nitrogen on the C 60 cage," Chemical Communications **46**, 631–633 (2010).
[233]K. Yakigaya, A. Takeda, Y. Yokoyama, S. Ito, T. Miyazaki, T. Suetsuna, H. Shimotani, T. Kakiuchi, H. Sawa, H. Takagi, K. Kitazawa, and N. Dragoe, "Superconductivity of doped Ar@C 60," New Journal of Chemistry **31**, 973–979 (2007).
[234]M. Murata, Y. Murata, and K. Komatsu, "Synthesis and Properties of Endohedral C60 Encapsulating Molecular Hydrogen," Journal of the American Chemical Society **128**, 8024–8033 (2006).
[235]E. Sartori, M. Ruzzi, N. J. Turro, J. D. Decatur, D. C. Doetschman, R. G. Lawler, A. L. Buchachenko, Y. Murata, and K. Komatsu, "Nuclear Relaxation of H2 and H2@C60 in Organic Solvents," Journal of the American Chemical Society **128**, 14752–14753 (2006).
[236]Y. Li, J. Y.-C. Chen, X. Lei, R. G. Lawler, Y. Murata, K. Komatsu, and N. J. Turro, "Comparison of Nuclear Spin Relaxation of H2O@C60 and H2@C60 and Their Nitroxide Derivatives," The Journal of Physical Chemistry Letters **3**, 1165–1168 (2012).
[237]E. Sartori, M. Ruzzi, N. J. Turro, K. Komatsu, Y. Murata, R. G. Lawler, and A. L. Buchachenko, "Paramagnet Enhanced Nuclear Relaxation of H2 in Organic Solvents and in H2@C60," Journal of the American Chemical Society **130**, 2221–2225 (2008).
[238]Y. Li, X. Lei, R. G. Lawler, Y. Murata, K. Komatsu, and N. J. Turro, "Distance-Dependent Paramagnet-Enhanced Nuclear Spin Relaxation of H2@C60 Derivatives Covalently Linked to a Nitroxide Radical," The Journal of Physical Chemistry Letters **1**, 2135–2138 (2010).
[239]J. Y.-C. Chen, A. A. Martí, N. J. Turro, K. Komatsu, Y. Murata, and R. G. Lawler, "Comparative NMR Properties of H2 and HD in Toluene-d8 and in H2/HD@C60," The Journal of Physical Chemistry B **114**, 14689–14695 (2010).
[240]N. J. Turro, A. A. Martí, J. Y.-C. Chen, S. Jockusch, R. G. Lawler, M. Ruzzi, E. Sartori, S.-C. Chuang, K. Komatsu, and Y. Murata, "Demonstration of a Chemical Transformation Inside a Fullerene. The Reversible Conversion of the Allotropes of H2@C60," Journal of the American Chemical Society **130**, 10506–10507 (2008).
[241]N. J. Turro, J. Y.-C. Chen, E. Sartori, M. Ruzzi, A. Marti, R. Lawler, S. Jockusch, J. López-Gejo, K. Komatsu, and Y. Murata, "The Spin Chemistry and Magnetic Resonance of H2@C60. From the Pauli Principle to Trapping a Long Lived Nuclear Excited Spin State inside a Buckyball," Accounts of Chemical Research **43**, 335–345 (2010).
[242]Y. Li, X. Lei, S. Jockusch, J. Y.-C. Chen, M. Frunzi, J. A. Johnson, R. G. Lawler, Y. Murata, M. Murata, K. Komatsu, and N. J. Turro, "A Magnetic Switch for Spin-Catalyzed Interconversion of Nuclear Spin Isomers," Journal of the American Chemical Society **132**, 4042–4043 (2010).
[243]A. Zoleo, R. G. Lawler, X. Lei, Y. Li, Y. Murata, K. Komatsu, M. Di Valentin, M. Ruzzi, and N. J. Turro, "ENDOR Evidence of Electron–H2 Interaction in a Fulleride Embedding H2," Journal of the

American Chemical Society **134**, 12881–12884 (2012).
[244]K. Kouřil, C. Wickens, B. Meier, S. Alom, J. Gräsvik, R. J. Whitby, and M. H. Levitt, "NMR of molecular endofullerenes dissolved in a nematic liquid crystal," Physical Chemistry Chemical Physics **19**, 11793–11801 (2017).
[245]M. Carravetta, O. G. Johannessen, M. H. Levitt, I. Heinmaa, R. Stern, A. Samoson, A. J. Horsewill, Y. Murata, and K. Komatsu, "Cryogenic NMR spectroscopy of endohedral hydrogen-fullerene complexes," The Journal of Chemical Physics **124**, 104507 (2006).
[246]S. Mamone, M. Concistrè, I. Heinmaa, M. Carravetta, I. Kuprov, G. Wall, M. Denning, X. Lei, J. Y.-C. Chen, Y. Li, Y. Murata, N. J. Turro, and M. H. Levitt, "Nuclear Magnetic Resonance of Hydrogen Molecules Trapped inside C70 Fullerene Cages," ChemPhysChem **14**, 3121–3130 (2013).
[247]J. D. van Beek, M. Carravetta, G. C. Antonioli, and M. H. Levitt, "Spherical tensor analysis of nuclear magnetic resonance signals," The Journal of Chemical Physics **122**, 244510 (2005).
[248]S. J. Elliott, C. Bengs, K. Kouril, B. Meier, S. Alom, R. J. Whitby, and M. H. Levitt, "NMR Lineshapes and Scalar Relaxation of the Water-Endofullerene H217O@C60," ChemPhysChem **19**, 251–255 (2018).
[249]B. Meier, K. Kouřil, C. Bengs, H. Kouřilová, T. C. Barker, S. J. Elliott, S. Alom, R. J. Whitby, and M. H. Levitt, "Spin-Isomer Conversion of Water at Room Temperature and Quantum-Rotor-Induced Nuclear Polarization in the Water-Endofullerene ${\mathrm{H}}_{2}\mathrm{O}@{\mathrm{C}}_{60}$," Physical Review Letters **120**, 266001 (2018).
[250]K. Kouřil, B. Meier, S. Alom, R. J. Whitby, and M. H. Levitt, "Alignment of 17O-enriched water–endofullerene H2O@C60 in a liquid crystal matrix," Faraday Discussions **212**, 517–532 (2018).
[251]S. Mamone, M. Concistrè, E. Carignani, B. Meier, A. Krachmalnicoff, O. G. Johannessen, X. Lei, Y. Li, M. Denning, M. Carravetta, K. Goh, A. J. Horsewill, R. J. Whitby, and M. H. Levitt, "Nuclear spin conversion of water inside fullerene cages detected by low-temperature nuclear magnetic resonance," The Journal of Chemical Physics **140**, 194306 (2014).
[252]M. Icker and S. Berger, "Unexpected multiplet patterns induced by the Haupt-effect," Journal of Magnetic Resonance **219**, 1–3 (2012).
[253]J.-N. Dumez, P. Håkansson, S. Mamone, B. Meier, G. Stevanato, J. T. Hill-Cousins, S. S. Roy, R. C. D. Brown, G. Pileio, and M. H. Levitt, "Theory of long-lived nuclear spin states in methyl groups and quantum-rotor induced polarisation," The Journal of Chemical Physics **142**, 044506 (2015).
[254]C. Dietrich, J. Wissel, J. Knoche, O. Lorenz, and J. Matysik, "Simple device for dissolution and sample transfer for applications in spin-hyperpolarization," Molecular Physics **117**, 2772–2776 (2019).
[255]C. Knapp, K. P. Dinse, B. Pietzak, M. Waiblinger, and A. Weidinger, "Fourier transform EPR study of N@C60 in solution," Chemical Physics Letters **272**, 433–437 (1997).
[256]J. J. L. Morton, A. M. Tyryshkin, A. Ardavan, K. Porfyrakis, S. A. Lyon, and G. A. D. Briggs, "A new mechanism for electron spin echo envelope modulation," The Journal of Chemical Physics **122**, 174504 (2005).
[257]J. J. L. Morton, A. M. Tyryshkin, A. Ardavan, K. Porfyrakis, S. A. Lyon, and G. Andrew D. Briggs, "Electron spin relaxation of N@C60 in CS2," The Journal of Chemical Physics **124**, 014508 (2006).
[258]A. Gruss, C. Knapp, N. Weiden, K.-P. Dinse, E. Dietel, A. Hirsch, B. Pietzak, M. Waiblinger, and A. Weidinger, "EPR studies of N@C60 and its adducts," AIP Conference Proceedings **442**, 396–399 (1998).
[259]J. J. Wittmann, T. V. Can, M. Eckardt, W. Harneit, R. G. Griffin, and B. Corzilius, "High-precision measurement of the electron spin *g* factor of trapped atomic nitrogen in the endohedral fullerene N@C60," Journal of Magnetic Resonance **290**, 12–17 (2018).
[260]M. Waiblinger, B. Goedde, K. Lips, W. Harneit, P. Jakes, A. Weidinger, and K.-P. Dinse, "Magnetic interaction in diluted N@C60," AIP Conference Proceedings **544**, 195–198 (2000).
[261]H. Kuzmany, J. Fink, M. Mehring, and S. Roth, *Molecular Nanostructures* (World Scientific, 1998) https://www.worldscientific.com/doi/pdf/10.1142/3592.
[262]E. Roduner, P. W. Percival, P. Han, and D. M. Bartels, "Isotope and temperature effects on the hyperfine interaction of atomic hydrogen in liquid water and in ice," The Journal of Chemical Physics **102**, 5989–5997 (1995).
[263]S. Knorr, A. Grupp, M. Mehring, M. Waiblinger, and A. Weidinger, "Electron spin relaxation rates T1-1 and T2-1 in diluted solid N@C60," AIP Conference Proceedings **544**, 191–194 (2000).
[264]S. Knorr, A. Grupp, M. Mehring, M. Waiblinger, and A. Weidinger, "Frequency-dependent spin-lattice relaxation in 15N@C60," AIP Conference Proceedings **591**, 105–108 (2001).
[265]Z. G. Yu, "Microscopic theory of electron spin relaxation in N@${\text{C}}_{60}$," Physical Review B **77**, 205439 (2008).
[266]N. Weiden, B. Goedde, H. Käß, K.-P. Dinse, and M. Rohrer, "Squeezing of Nitrogen Atomic Orbitals in a Chemical Trap," Physical Review Letters **85**, 1544–1547 (2000).
[267]C. Meyer, W. Harneit, K. Lips, A. Weidinger, P. Jakes, and K.-P. Dinse, "Alignment of the endohedral fullerenes $\mathrm{N}@{\mathrm{C}}_{60}$ and $\mathrm{N}@{\mathrm{C}}_{70}$ in a liquid-crystal matrix," Physical Review A **65**, 061201 (2002).
[268]P. Jakes, N. Weiden, R. A. Eichel, A. Gembus, K. P. Dinse, C. Meyer, W. Harneit, and A. Weidinger, "Electron Paramagnetic Resonance Investigation of Endohedral Fullerenes N@C60 and N@C70 in a Liquid Crystal," Journal of Magnetic Resonance **156**, 303–308 (2002).
[269]K.-P. Dinse, "EPR investigation of atoms in chemical traps," Physical Chemistry Chemical Physics **4**, 5442–5447 (2002).
[270]G. Liu, M. d. C. Gimenez-Lopez, M. Jevric, A. N. Khlobystov, G. A. D. Briggs, and K. Porfyrakis, "Alignment of N@C60 Derivatives in a Liquid Crystal Matrix," The Journal of Physical Chemistry B **117**, 5925–5931 (2013).
[271]F. Simon, H. Kuzmany, H. Rauf, T. Pichler, J. Bernardi, H. Peterlik, L. Korecz, F. Fülöp, and A. Jánossy, "Low temperature fullerene encapsulation in single wall carbon nanotubes: Synthesis of N@C60@SWCNT," Chemical Physics Letters **383**, 362–367 (2004).
[272]A. Gembus, F. Simon, A. Jánossy, H. Kuzmany, and K.-P. Dinse, "Properties Of N@C60-Derived Peapods," AIP Conference Proceedings **723**, 259–262 (2004).
[273]B. Corzilius, A. Gembus, K.-P. Dinse, F. Simon, and H. Kuzmany, "Carbon Nanotubes Investigated by N@C60 and N@C70 Spin Probes," AIP Conference Proceedings **786**, 291–295 (2005).
[274]B. Corzilius, A. Gembus, N. Weiden, and K.-P. Dinse, "Preparation and EPR characterization of N@C60 and N@C70 based peapods," AIP Conference Proceedings **786**, 317–320 (2005).
[275]B. Corzilius, A. Gembus, N. Weiden, K.-P. Dinse, and K. Hata, "EPR characterization of catalyst-free SWNT and N@C60-based peapods," physica status solidi (b) **243**, 3273–3276 (2006).
[276]S. Tóth, D. Quintavalle, B. Náfrádi, L. Korecz, L. Forró, and F. Simon, "Enhanced thermal stability and spin-lattice relaxation rate of N@${\text{C}}_{60}$ inside carbon nanotubes," Physical Review B **77**, 214409 (2008).
[277]G. W. Morley, J. van Tol, A. Ardavan, K. Porfyrakis, J. Zhang, and G. A. D. Briggs, "Efficient Dynamic Nuclear Polarization at High Magnetic Fields," Physical Review Letters **98**, 220501 (2007).
[278]J. J. Wittmann, M. Eckardt, W. Harneit, and B. Corzilius, "Electron-driven spin diffusion supports crossing the diffusion barrier in MAS DNP," Physical Chemistry Chemical Physics **20**, 11418–11429 (2018).
[279]N. Alaniva, E. P. Saliba, P. T. Judge, E. L. Sesti, W. Harneit, B. Corzilius, and A. B. Barnes, "Electron-decoupled MAS DNP with N@C60," Physical Chemistry Chemical Physics **25**, 5343–5347 (2023).
[280]M. Scheloske, B. Naydenov, C. Meyer, and W. Harneit, "Synthesis and Functionalization of Fullerenes Encapsulating Atomic Phosphorus," Israel Journal of Chemistry **46**, 407–412 (2006).
[281]B. Naydenov, Ch. Spudat, M. Scheloske, H. I. Suess, J. Hulliger, and W. Harneit, "N@C60 and N@C70 oriented in a single-crystalline matrix," physica status solidi (b) **243**, 2995–2998 (2006).
[282]B. Naydenov, C. Spudat, W. Harneit, H. I. Süss, J. Hulliger, J. Nuss, and M. Jansen, "Ordered inclusion of endohedral fullerenes N@C60 and P@C60 in a crystalline matrix," Chemical Physics Letters **424**, 327–332 (2006).
[283]D. Pinto, D. Paone, B. Kern, T. Dierker, R. Wieczorek, A. Singha, D. Dasari, A. Finkler, W. Harneit, J. Wrachtrup, and K. Kern, "Readout and control of an endofullerene electronic spin," Nature Communications **11**, 6405 (2020).
[284]F. Cimpoesu, S. Ito, H. Shimotani, H. Takagi, and N. Dragoe, "Vibrational properties of noble gas endohedral fullerenes," Physical Chemistry

Chemical Physics **13**, 9609–9615 (2011).
[285]S. Brown, J. Cao, J. L. Musfeldt, N. Dragoe, F. Cimpoesu, S. Ito, H. Takagi, and R. J. Cross, "Search for microscopic evidence for molecular level negative thermal expansion in fullerenes," Physical Review B **73**, 125446 (2006).
[286]A. J. Horsewill, S. Rols, M. R. Johnson, Y. Murata, M. Murata, K. Komatsu, M. Carravetta, S. Mamone, M. H. Levitt, J. Y.-C. Chen, J. A. Johnson, X. Lei, and N. J. Turro, "Inelastic neutron scattering of a quantum translator-rotator encapsulated in a closed fullerene cage: Isotope effects and translation-rotation coupling in ${\text{H}}_{2}@{\text{C}}_{60}$ and $\text{HD}@{\text{C}}_{60}$," Physical Review B **82**, 081410 (2010).
[287]P. M. Rafailov, C. Thomsen, A. Bassil, K. Komatsu, and W. Bacsa, "Inelastic light scattering of hydrogen containing open-cage fullerene ATOCF," physica status solidi (b) **242**, R106–R108 (2005).
[288]S. S. Zhukov, V. Balos, G. Hoffman, S. Alom, M. Belyanchikov, M. Nebioglu, S. Roh, A. Pronin, G. R. Bacanu, P. Abramov, M. Wolf, M. Dressel, M. H. Levitt, R. J. Whitby, B. Gorshunov, and M. Sajadi, "Rotational coherence of encapsulated ortho and para water in fullerene-C 60 revealed by time-domain terahertz spectroscopy," Scientific Reports **10**, 18329 (2020).
[289]B. Meier, S. Mamone, M. Concistrè, J. Alonso-Valdesueiro, A. Krachmalnicoff, R. J. Whitby, and M. H. Levitt, "Electrical detection of ortho – para conversion in fullerene-encapsulated water," Nature Communications **6**, 8112 (2015).
[290]H. Torii, S. Sadai, Y. Hashikawa, Y. Murata, and Y. Ikemoto, "Single-Sided Delocalized Polarization of the C60 Cage and Reduced Infrared Intensities and Dipole Moment of H2O@C60," The Journal of Physical Chemistry A **128**, 10867–10874 (2024).
[291]A. Melentev, S. Zhukov, V. Balos, G. Hoffman, S. Alom, M. Belyanchikov, E. Zhukova, M. Dressel, G. Bacanu, P. Abramov, M. Levitt, R. Whitby, B. Gorshunov, and M. Sajadi, "THz and IR spectroscopy of endofullerene H2O@C60," Journal of Physics: Conference Series **1984**, 012012 (2021).
[292]T. Putaud, J.-C. Chartrand, Y. Kalugina, X. Michaut, P.-N. Roy, and P. Ayotte, "A simple confined rotor model to describe the ro-translational dynamics of water endofullerenes and to assign the ro-vibrational spectra of solid H2O@C60," The Journal of Chemical Physics **162**, 144313 (2025).
[293]J.-C. Chartrand, T. Putaud, G. Bélanger, M. Bertin, J.-H. Fillion, P. Léveillé, X. Michaut, and P. Ayotte, "Signatures of rotation–translation couplings, symmetry-breaking, and intermolecular interactions in the rovibrational spectra of solid H2O@C60," The Journal of Chemical Physics **162**, 144312 (2025).
[294]P. M. Felker and Z. Bačić, "Communication: Quantum six-dimensional calculations of the coupled translation-rotation eigenstates of H2O@C60," The Journal of Chemical Physics **144**, 201101 (2016).
[295]P. M. Felker and Z. Bačić, "Flexible water molecule in C_{60} : Intramolecular vibrational frequencies and translation-rotation eigenstates from fully coupled nine-dimensional quantum calculations with small basis sets," The Journal of Chemical Physics **152**, 014108 (2020).
[296]A. Takeda, Y. Yokoyama, S. Ito, T. Miyazaki, H. Shimotani, K. Yakigaya, T. Kakiuchi, H. Sawa, H. Takagi, K. Kitazawa, and N. Dragoe, "Superconductivity of doped Ar@C60," Chemical Communications , 912–914 (2006).
[297]P. Jakes, K.-P. Dinse, C. Meyer, W. Harneit, and A. Weidinger, "Purification and optical spectroscopy of N@C 60," Physical Chemistry Chemical Physics **5**, 4080–4083 (2003).
[298]M. Frunzi, S. Jockusch, J. Y.-C. Chen, R. M. K. Calderon, X. Lei, Y. Murata, K. Komatsu, D. M. Guldi, R. G. Lawler, and N. J. Turro, "A Photochemical On–Off Switch for Tuning the Equilibrium Mixture of H2 Nuclear Spin Isomers as a Function of Temperature," Journal of the American Chemical Society **133**, 14232–14235 (2011).
[299]M. Holz, E. K. Campbell, C. A. Rice, and J. P. Maier, "Electronic absorption spectra of C60+<math><mrow is="true"><msubsup is="true"><mrow is="true"><mtext is="true">C</mtext></mrow><mrow is="true"><mn is="true">60</mn></mrow><mrow is="true"><mo is="true">+</mo></mrow></msubsup></mrow></math>–*L* (*L* = He, Ne, Ar, Kr, H2, D2, N2) complexes," Journal of Molecular Spectroscopy Molecular Spectroscopy in Traps, **332**, 22–25 (2017).
[300]J. Rademacher, E. S. Reedy, F. Negri, S. Alom, R. J. Whitby, M. H. Levitt, and E. K. Campbell, "Gas-phase electronic spectroscopy of nuclear spin isomer separated H2O@C60+ and D2O@C60+," Molecular Physics **122**, e2173507 (2024).
[301]N. Dragoe, A. M. Flank, P. Lagarde, S. Ito, H. Shimotani, and H. Takagi, "Molecular thermal contraction of the Ar@C${}_{60}$ endohedral fullerene," Physical Review B **84**, 155448 (2011).
[302]C. Fields, A. Foerster, S. Ghaderzadeh, I. Popov, B. Huynh, F. Junqueira, T. James, S. Alonso Perez, D. A. Duncan, T.-L. Lee, Y. Wang, S. Bloodworth, G. Hoffman, M. Walkey, R. J. Whitby, M. H. Levitt, B. Kiraly, J. N. O'Shea, E. Besley, and P. Moriarty, "Timing the escape of a photoexcited electron from a molecular cage," Nature Communications **16**, 5062 (2025).
[303]F. Gel'mukhanov and H. Ågren, "Resonant X-ray Raman scattering," Physics Reports **312**, 87–330 (1999).
[304]P. A. Brühwiler, O. Karis, and N. Mårtensson, "Charge-transfer dynamics studied using resonant core spectroscopies," Reviews of Modern Physics **74**, 703–740 (2002).
[305]H. Man Lee, M. M. Olmstead, T. Suetsuna, H. Shimotani, N. Dragoe, R. James Cross, K. Kitazawa, and A. L. Balch, "Crystallographic characterization of Kr@C 60 in (0.09Kr@C 60 /0.91C 60)·{Ni II (OEP)}·2C 6 H 6," Chemical Communications **0**, 1352–1353 (2002).
[306]S. Aoyagi, N. Hoshino, T. Akutagawa, Y. Sado, R. Kitaura, H. Shinohara, K. Sugimoto, R. Zhang, and Y. Murata, "A cubic dipole lattice of water molecules trapped inside carbon cages," Chemical Communications **50**, 524–526 (2013).
[307]S. Kaneko, Y. Hashikawa, S. Fujii, Y. Murata, and M. Kiguchi, "Single Molecular Junction Study on H2O@C60: H2O is "Electrostatically Isolated"," ChemPhysChem **18**, 1229–1233 (2017).
[308]J. Biskupek, S. T. Skowron, C. T. Stoppiello, G. A. Rance, S. Alom, K. L. Y. Fung, R. J. Whitby, M. H. Levitt, Q. M. Ramasse, U. Kaiser, E. Besley, and A. N. Khlobystov, "Bond Dissociation and Reactivity of HF and H2O in a Nano Test Tube," ACS Nano **14**, 11178–11189 (2020).
[309]I. Cardillo-Zallo, J. Biskupek, S. Bloodworth, E. S. Marsden, M. W. Fay, Q. M. Ramasse, G. A. Rance, C. T. Stoppiello, W. J. Cull, B. L. Weare, R. J. Whitby, U. Kaiser, P. D. Brown, and A. N. Khlobystov, "Atomic-Scale Time-Resolved Imaging of Krypton Dimers, Chains and Transition to a One-Dimensional Gas," ACS Nano **18**, 2958–2971 (2024).
[310]J. M. Thijssen and H. S. J. Van der Zant, "Charge transport and single-electron effects in nanoscale systems," physica status solidi (b) **245**, 1455–1470 (2008).
[311]S. Fujii, H. Cho, Y. Hashikawa, T. Nishino, Y. Murata, and M. Kiguchi, "Tuneable single-molecule electronic conductance of C60 by encapsulation," Physical Chemistry Chemical Physics **21**, 12606–12610 (2019).
[312]N. Roch, S. Florens, V. Bouchiat, W. Wernsdorfer, and F. Balestro, "Out-of-Equilibrium Singlet-Triplet Kondo Effect in a Single C60 Quantum Dot," Journal of Low Temperature Physics **153**, 350–358 (2008).